SOILS and ROCKS

An International Journal of Geotechnical and Geoenvironmental Engineering

Soils and Rocks publishes papers in English in the broad fields of Geotechnical Engineering, Engineering Geology, and Geoenvironmental Engineering. The Journal is published quarterly in March, June, September and December. The first issue was released in 1978, under the name *Solos e Rochas*, being originally published by the Graduate School of Engineering of the Federal University of Rio de Janeiro. In 1980, the Brazilian Association for Soil Mechanics and Geotechnical Engineering took over the editorial and publishing responsibilities of *Solos e Rochas*, increasing its reach. In 2007, the journal was renamed Soils and Rocks and acquired the status of an international journal, being published jointly by the Brazilian Association for Soil Mechanics and Geotechnical Engineering, by the Portuguese Geotechnical Society, and until 2010 by the Brazilian Association for Engineering Geology and the Environment.

Soils and Rocks

1978,	1 (1, 2)
1979,	1 (3), 2 (1,2)
1980-1983,	3-6 (1, 2, 3)
1984,	7 (single number)
1985-1987,	8-10 (1, 2, 3)
1988-1990,	11-13 (single number)
1991-1992,	14-15 (1, 2)
1993,	16 (1, 2, 3, 4)
1994-2010,	17-33 (1, 2, 3)
2011,	34 (1, 2, 3, 4)
2012-2019,	35-42 (1, 2, 3)
2020,	43 (1, 2, 3, 4)
2021,	44 (1,

ISSN 1980-9743
ISSN-e 2675-5475 CDU 624.131.1

Soils and Rocks
An International Journal of Geotechnical and Geoenvironmental Engineering
ISSN 1980-9743 ISSN-e 2675-5475

Publication of
ABMS - Brazilian Association for Soil Mechanics and Geotechnical Engineering
SPG - Portuguese Geotechnical Society
Volume 44, N. 1, January-March 2021

Table of Contents

Articles

Soils and Rocks

An International Journal of Geotechnical and Geoenvironmental Engineering

www.soilsandrocks.com

ISSN 1980-9743
ISSN-e 2675-5475

Geotechnical and other characteristics of cement-treated low plasticity clay

Ibrahim M. Alkiki[1], Mohammed D. Abdulnafaa[2], Abdulrahman Aldaood[3#]

Article

Keywords:
Clay soil
Cement stabilization
Strength behavior
Microstructure
Curing time
Water retention behavior

Abstract

This research work examines the utilization of cement in order to improve low plasticity clay soil. The soil samples treated with 2, 4 and 6% cement percents and cured for different curing times extended to 90 days. Laboratory investigations include unconfined compression, indirect tensile, gas permeability and microstructural tests, which were conducted on the tested samples. The soil-water retention behavior has been also investigated. The test results showed that the cement addition improved both the compressive and tensile strength properties of soil specimens. These strength properties were also increased with curing times. pH and electrical conductivity values were good indicators for the enhancement in the strengths properties. The results of micro structural tests illustrated that the natural soil specimens contain voids and the open structure. Further, these tests showed the cementation of soil grains and filling the voids among soil grains with cementing compounds. Gas permeability and soil-water retention behavior of soil specimens are strongly related to the variations in the soil structures. Further examination illustrated that in the case of low cement content, the pore size distribution (PSD) and the efficiency of gas permeability are more sensitive to curing times.

1. Introduction and past studies

The successive urban development in various parts of the world necessitated further improvement of the infrastructure accompanying the constructed facilities. Compacted fine-grained soils are used in the infrastructure earthworks such as the construction embankment of roads, highways, road foundations. Fine-grained soils (especially clayey soils) consider as a problematic soil and can induce damages to roads founded on them, due to their volume changes, higher water content and/or low bearing capacity. The use of ordinary Portland cement; its components or residues; has been widely used in stabilizing cohesionless and some types of problematic soils like clayey soil. Studies conducted in this field may be classified into three main categories: use byproduct from cement production operations, direct use of cement alone or mixed with other materials, and recycling of cement as concrete waste. The use of cement byproduct, especially cement kiln dust to stabilize or improve clay soil was cover by many studies (Adeyanju & Okeke, 2019; Amadi & Osu, 2018; Miller & Azad, 2000; Naseem et al., 2019). The mixing of cement with fly ash become commonly used to reduce the amount of cement used or improve specific geotechnical properties of soil (Amu et al., 2008; Chenari et al., 2018; Khemissa & Mahamedi, 2014). Portland cement was also used with other stabilizing materials to improve the soil engineering properties. Lime is used with cement to improve the soil strength and reduce the swelling and settlement (Amu et al., 2008; Joel & Agbede, 2010; Lemaire et al., 2013; Mousavi & Leong Sing, 2015; Riaz et al., 2014; Saeed et al., 2015; Sharma et al., 2018; Umesha et al., 2009; Wei et al., 2014). Nayak & Sarvade (2012) used cement and quarry dust to improve the shear strength and hydraulic features of lithomarge clay. Ayeldeen & Kitazume (2017) utilized fiber, and liquid polymer to enhance the strength of cement-soft clay blends. The fibers and liquid polymers displayed a notable mechanically, economically and environmentally prospects to be used as an additive to cement in improving the soft clay. Also, organic soils have become the target of many studies that have addressed improving the properties of these soils by adding cement and other materials (Kalantari & Huat, 2008; Kalantari & Prasad, 2014). Moreover, Osinubi et al. (2011) used ordinary Portland cement –Locust bean waste ash mixture to enhance the engineering properties such as (UCS) and California bearing ratio (CBR) for black cotton clayey soil. Crushed concrete waste, which represents the last form of cement used, has been used in many studies to improve the properties of clay soils (Abdulnafaa et al., 2019;

[#]Corresponding author. E-mail address: abdulrahman.aldaood@uomosul.edu.iq
[1]University of Mosul, College of Engineering, Department of Dams &Water Resources Engineering, Mosul, Iraq.
[2]University of Mosul, College of Engineering, Department of Environmental Engineering, Mosul, Iraq.
[3]University of Mosul, College of Engineering, Department of Civil Engineering, Mosul, Iraq.

Submitted on June 27, 2020; Final Acceptance on October 21, 2020; Discussion open until May 31, 2021

DOI: https://doi.org/10.28927/SR.2021.053120

Cabalar et al., 2016, 2017, 2019a, b; İşbuğa et al., 2019). The main purpose of adding ordinary Portland cement to cohesionless soils is to provide strong bonds between soil particles (Consoli et al., 2011, 2017). Al-Aghbari et al. (2009) used cement and cement dust to stabilize desert sands. The results showed that the cement and cement by-pass dust could be used to improve the compressibility and shear strength characteristics of desert sands. Also, Saberian et al. (2018) studied the stabilization of marine and desert sands with deep mixing of cement and sodium bentonite and found an improvement in the geotechnical properties of these soils. Shooshpasha & Shirvani (2015) reported that the use of cement to stabilize sandy soils resulting in increased strength parameters, reduced strain at failure, and changed soil behavior to a noticeable brittle behavior. Iravanian & Bilsel (2016) studied the sand-bentonite landfill barrier material with and without cement additive, at different periods of aging. The strength characterization of mixtures was a marked improvement with cement inclusion and that the effect of aging has been very effective.

The clay-cement reaction produce primary and secondary cementations materials in the soil-cement matrix (chew et al., 2004). Cement has two chemical reactions; the first one begins at the time of adding the water to the fine soil-cement mixture and the second one is the secondary reaction occurs as the calcium ions diffuse through the soil (Chen & Wang, 2006; Chew et al., 2004). These chemical reactions are responsible for the strength development in cement-treated soils. The geotechnical properties of cement-treated clay soils have been investigated by different researchers (Consoli et al., 2010; Goodary et al., 2012; Kalıpcılar et al., 2016; Kasama et al., 2000; Kenai et al., 2006; Lorenzo & Bergado, 2004; Okyay & Dias, 2010; Park, 2011; Petchgate et al., 2001; Saadeldin & Siddiqua, 2013; Zhang et al., 2014). Common Portland cement was used to improve shear resistance and durability of clay soils. The unsaturated properties of cement-treated clay soils were observed by different studies (Attom et al., 2000; Azam & Cameron, 2013; Nahlawi et al., 2004). Horpibulsuk et al. (2012) found that the strength of clay is governed by the clay-water/cement ratio. The strength increases with the decrease in the clay-water/cement ratio. (Horpibulsuk et al., 2012) studied the microstructural characteristics of cement-stabilized soils and found that soil behavior enhanced significantly. The optimum dosages of cement added to clay soil to improve some geotechnical properties were investigated by Rojas-Suárez et al. (2019a, b). Korf et al. (2017) observed the hydraulic and diffusive behavior of compact clay soil, with and without cement addition. The results of the reactive behavior analysis showed that the retention by adsorption increased with the increase of pH, but it was not affected by the applied static load.

In summary, many interesting results indicating the potential of the use of ordinary Portland cement to improve clayey soils have been reported. This study aims to extend and increase the knowledge of the clayey soil-cement stabilization technique.

2. Materials and testing methods

2.1 Materials

Two materials were used in this experimental work: clayey soil and cement. The soil was obtained from a depth of 1.5 m from the ground surface. The soil samples were oven-dried for 2 days at 60 C° and passed through a 4 mm sieve before use in various tests. The soil specific gravity was 2.68, the liquid limit was 35% and the plasticity index was 16%. All the chemical and physical properties tests were carried out following the ASTM standards and test procedures adopted by Aldaood et al. (2014a). The sample is categorized as CL following the Unified Soil Classification System (USCS). The X-ray diffraction test results presented that the main clay mineral was kaolinite and the non-clay minerals were quartz and calcite. Table 1 presents some properties of the clay soil used in the experimental program.

The stabilizing agent used for this study was ordinary Portland cement. The specific gravity is 3.13 and the specific surface is 3790 (cm^2/gm). The main composition of cement is (CaO is 63.1%, SiO_2 is 19.4% and Al_2O_3 is 5.4%). The loss on the ignition of the cement is 2.33%.

2.2 Sample preparation

An oven-dried soil was mixed with a pre-determined quantity of ordinary Portland cement (2%, 4% and 6% of dry soil weight) in dry condition. The soil specimens were prepared at the optimum moisture content of natural soil (i.e. 11%). The formation of lumps was avoided when the water was added to the soil-cement mixture. The soil-cement mixture kept in the plastic bags then left for 10 minutes

Table 1. Chemical and physical properties of the natural soil.

Properties		Value
Liquid Limit (%)		35
Plastic Limit (%)		19
Plasticity Index (%)		16
Total Soluble Salts (%)		3
Specific Gravity		2.68
pH		8.2
Electrical Conductivity (mS/cm)		0.42
Gravel (%)		7
Sand (%)		18
Silt (%)		56
Clay (%)		19
Wave Velocity (m/sec)		540
Gas Permeability (m^2)		2.20E-13
Unified Soil Classification System (USCS)		CL
Standard Compaction	Optimum Moisture Content (OMC)	11%
	Max. Dry Unit Weight (kN/m^3)	17.5

for homogeneity (Khattab & Aljobouri, 2012). After that, the soil specimens were statically compacted in a specific rigid mold related to the type of the test. A standard Proctor compaction test (ASTM, 2003) was adopted in the preparation of soil-cement specimens to obtain the maximum dry density of natural soil. All treated and untreated specimens were compacted statically to dry density of (17.5 kN/m^3), which is the maximum dry density of natural soil. After compaction, the treated soil specimens were wrapped in cling film and coated with paraffin wax to prevent moisture loss, then specimens were left at room temperature of 20 C$^\circ$ for different periods of 3, 10, 30, 60 and 90 days to be cured.

2.3 Testing methods

The pore size distribution and microstructural characteristics of the natural soil and cement-treated soil specimen were measured using a scanning electron microscope (SEM) and porosity tests. These tests were conducted on the natural and cement-treated soil specimens, following the test procedures suggested by Aldaood et al. (2014b)

To conduct the UCS, a cylindrical (50 mm diameter × 100 mm height) soil specimens were statically compacted at the optimum moisture content and maximum dry unit weight obtained from the standard compaction curve of natural soil. The rate of compaction was (1 mm/min) to obtain a uniform unit weight of the soil sample. The UCS has been determined according to the ASTM D-2166 and D-1633 (ASTM 2000). procedures for untreated and cement-treated soil samples, respectively. Before testing, the wave velocity of the soil specimens was determined using A PUNDIT device with a frequency of 82 kHz.

The commonly used alternative procedure for the determination of tensile strength is the Brazilian tensile test, which is generally referred to as the (ITS) (Das et al., 1995). The soil specimens were prepared in a metal mold with dimensions of (50 mm high and 25 mm diameter). The soil specimens were compacted statically, at the same rate as for preparing the UCS specimens. After the preparation of the natural soil specimens, they were extracted from the stacking mold and tested. While the cement-treated specimens are encapsulated as in the UCS test and exposed to the same curing time before tested. The ITS test was performed according to the method approved by the ASTM (2011), by applying compressive strength along the diameter of the model and with the rate of the unconfined compressive resistance test (1.27 mm/min) until the specimens fail. The (ITS) is calculated using Equation 1

$$S_t = \frac{2P_{\max}}{\pi\, t\, d} \tag{1}$$

where S_t is the indirect tensile strength and $P_{max.}$; is the maximum applied load on the sample; t is the average height of the sample with d as diameter.

For For pH and electrical conductivity test (EC), a portion of failed (tested) samples in the UCS test was used to determine the pH and EC values, following the tests procedures suggested by (Eades & Grim, 1966; Aldaood et al. 2014a).

For gas permeability, the test procedure suggested by Aldaood et al. (2016) was adopted to measure the gas permeability of cylindrical soil specimens of 50 mm diameter and 50 mm height. The soil specimens were statically compacted inside a cylindrical metal mold so that it reached the maximum dry unit weight of natural soil. The gas permeability specimens were exposed to different curing times as the specimens for UCS and ITS tests. The coefficient of gas permeability was estimated using the modified Darcy's equation as follows:

$$K_A = \frac{Q}{A} \times \frac{2\,\mu\, L\, P_{atm}}{\left(P_i^2 - P_{atm}^2\right)} \tag{2}$$

where: Q is the volume flow rate (m^3/sec), L is the thickness of the sample (m), μ is the viscosity (1.76*10^{-5} Pa.s for nitrogen gas at 20 °C), P_{atm} is the atmospheric pressure (Pa) and P_i is the injection pressure (Pa), A is the cross-sectional area of the sample (m^2).

It worth noting that, the measurements of permeability were conducted in an air-conditioned room having a constant temperature of 20 °C. Each permeability test involved four measurements of apparent permeability at various injection pressures.

The soil–water retention curve (SWRC) of natural and cement-treated soil specimens was determined by using the vapor equilibrium technique, osmotic membrane, and tensiometric plates. The vapor equilibrium technique was used to evaluate the SWRC in suction pressure more than 1500 kPa. The osmotic membrane determined the SWRC in the suction pressure range of 100 kPa and 1500 kPa. The evaluation of the SWRC continued in low suction pressure ranging between 10-20 kPa by using tensiometric plates. The required time to reach the balance condition (in the determination of the SWRC) varied between 20-35 days, depending on the desired technique. More details about these techniques can be found in Aldaood et al. (2015). It worth noting that, all the previous SWRC determination techniques were carried at room temperature of (20 °C).

3. Results and discussion

3.1 Assessment of pH and Electrical Conductivity (EC)

The pH values of cement-treated soil specimens before and after curing were determined. Cement addition increases the pH value from (8.2) for natural soil to 12.5 for 6% cement-treated soil specimens, which promotes cation exchange (due to increasing calcium Ca^{++} ions). In the literature (Al-Mukhtar et al., 2014; Eades & Grim, 1966; Feng et al., 2001), it was agreed that the pH value of 12.5 represent the necessary value to get a favorable environment for producing the cementing materials, and thus, the development of acceptable mechanical performance. Table 2 shows the changes in pH and EC values of cement-treated soil specimens after various curing times. It is observed that

Table 2. Variation of pH and electrical conductivity values of soil specimens with cement content and curing times.

Curing Time (day)	pH value			EC (mS/cm)		
	2% Cement	4% Cement	6% Cement	2% Cement	4% Cement	6% Cement
3	12.2	12.3	12.4	2.5	3	3.7
10	12.1	12.2	12.3	2.18	2.63	3.44
30	11.85	12.0	12.1	1.9	2.21	3
60	11.5	11.8	11.9	1.66	2	2.76
90	11.2	11.65	11.7	1.43	1.8	2.57

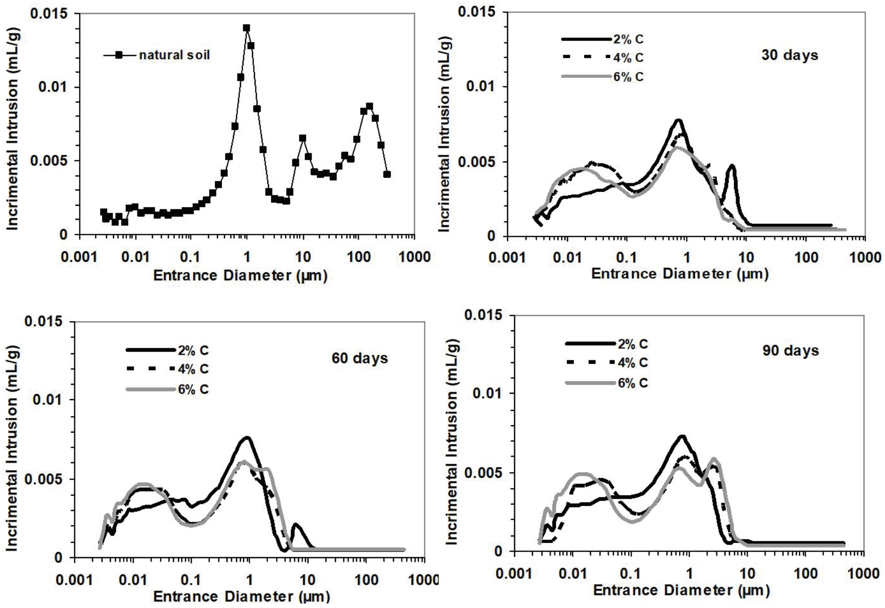

Figure 1. PSD of natural and cement-treated soil specimens with different cement content and curing times.

the pH values of soil specimens decreased slightly as the curing time increased. More reduction in pH occurs for low cement content and high curing time and the value reached 11.2. At this level of pH value, the pozzolanic products such as (CSH and CAH) will continue. (Al-Mukhtar et al., 2014) reported that, as calcium cation is existed and the pH is high enough (more than 10.5), the pozzolanic reaction continues. Moreover, Chen & Wang (2006) documented that, when pH value (≤ 9) low level of hardening will produce or even no hardening. The reduction in pH values of soil specimens related to the reduced amount of Ca^{++} and $(OH)^{-}$ ions due to the development of the pozzolanic reactions.

The electrical conductivity values (EC) of soil specimens followed the same trend as pH values. Cement addition causes an increasing in EC values from (0.42 mS/cm) for natural soil to (3.9 mS/cm) for 6% cement-treated soil specimens. This increasing related to the existing high calcium ions in adding cement (CaO is 63.1%). As the curing time increases, the EC value of soil specimens continues to down, but slightly. The reduction in EC values related to the consumption of calcium ions during the pozzolanic reactions. Finally, obtaining pH and EC values corroborate the next-obtained results of unconfined compressive and indirect tensile strengths, where significant cementing materials (such as CSH and CAH) were formed.

3.2 Microstructural characterization

Microstructural analyses were carried out to investigate the variations in the microstructure of the cured specimens and for natural soil as a comparison. These analyses helped in understanding the increase in strength of cemented soil specimens at a microscopic level. The analysis focused on the formation of cementing materials named calcium silicate hydrates (CSH) and calcium aluminate hydrates (CAH); which normally presented in lime and cement stabilized soils (Aldaood et al., 2014a; Mengue et al., 2017). Figure 1 presents the pore size distribution (PSD) of natural and cement-treated soil specimens. The natural soil specimens exhibited a tri-modal PSD with a large number of macrospores centered at (1–200 μm) and with a less pronounced peak centered at (0.01 μm). The PSD curve of natural soil supported the SEM results, where the texture of the natural soil specimens exhibited a fairly open type of microstructure, as illustrated in Figure 2. Besides, many coarse grains (sand grains) relatively well calibrate and assembled with fine grains (clay grains) in a dispersed arrangement, resulting to form many voids in different dimensions.

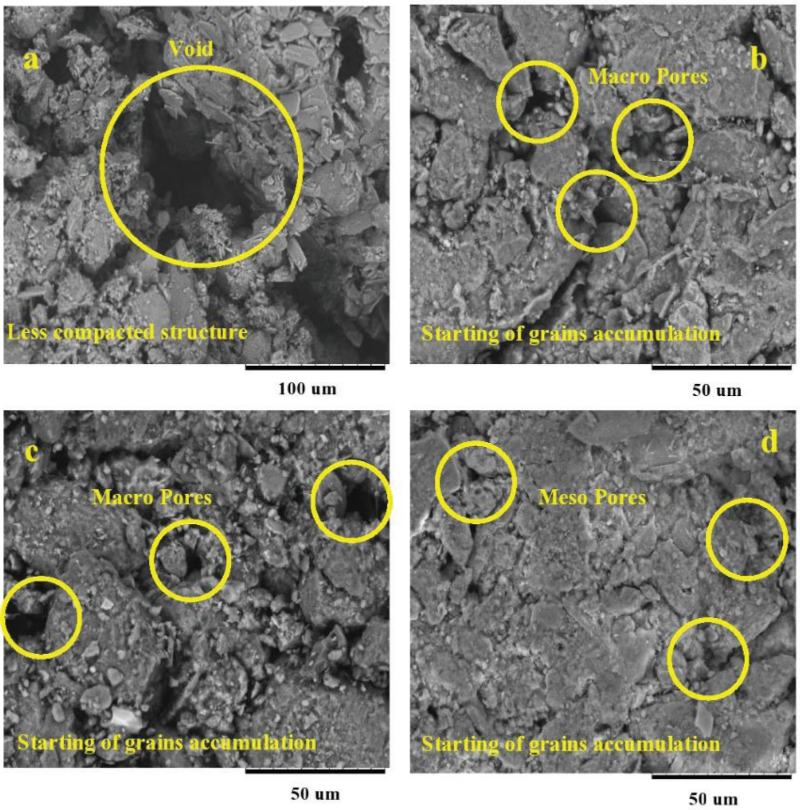

Figure 2. SEM images (a) natural soil (b, c, d) 30 days cured specimens treated with 2, 4 and 6% cement content, respectively.

Cement addition enhanced the PSD of soil specimens by decreasing the amount of macropores (> 10 μm) and increasing the micropores (≤ 0.01 μm), see Figure 1. The changes in the PSD of cemented soil specimens related to that, the pores (especially macrospores) covered and filled by the hydrated cement. During cement addition and with the presence of water, the clay and cement particles grow together to large clusters. Then cement gel is stable in macropores and micropores due to the attractive forces, leading to enhance PSD of cemented soil specimens (Horpibulsuk et al., 2009, 2010). Further, as the curing times increase the hydration products grow and cause more reduction in the macropores. An investigation of the structure of the cemented soil specimens allowed to reflect the changes in the structure of specimens from open structure to denser one with fewer voids formation (Figure 2). Further, as the cement content increase, the soil structure became tighter than the structure of natural soil and the cluster of grains become more effective (Mengue et al., 2017). It is noting that the cement addition was more affected on the PSD of soil specimens than curing times, as presented in Figure 1.

3.3 Unconfined Compressive Strength characteristics (UCS)

The results of USC for cement-treated soil specimens were illustrated in Figure 3. This figure also presents the effect of curing time on the UCS. The results suggest that

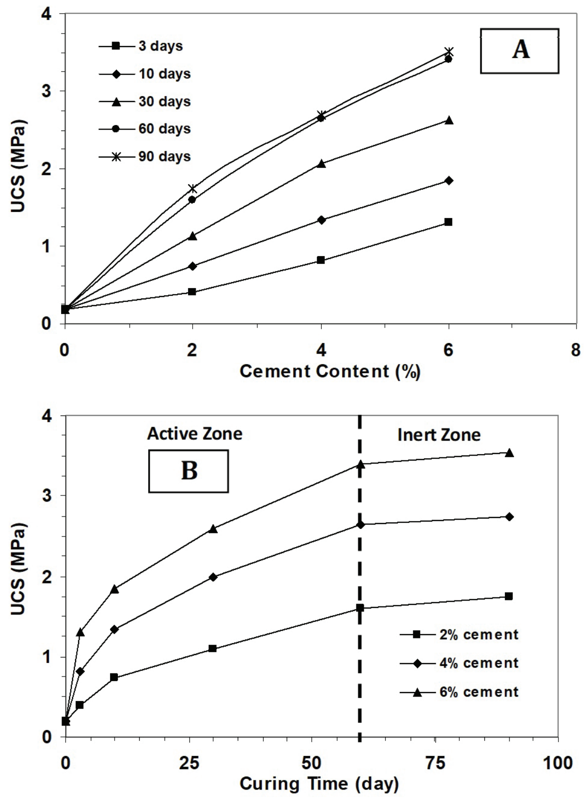

Figure 3. UCS of soil specimens with (A) cement content and (B) curing times.

the cement content has a significant effect on the strength characteristics of soil specimens and the UCS of soil specimens increase with cement content. The increase in the UCS was approximately linearly with the increase in the cement content. This finding is consistent with the findings of previous studies by (Chenari et al. (2018) and Pakbaz & Alipour (2012). The increase in USC with increasing cement content was attributed to the pozzolanic reactions between soil and cement mixtures. The pozzolanic reactions resulting in the formation of cementing compounds named calcium silicate hydrate (CSH) and calcium aluminate hydrates (CAH). These cementing compounds enhanced the inter-cluster bonding strength and filled the pore space between soil particles (see Figure 1). As a result, the strength values (i.e. UCS and ITS) of the soil specimens increased with an increase in cement content (Sharma et al., 2018). Moreover, as the cement content increases, the contact points among cement and soil particles increases and, upon hardening, gives a suitable amount of bonding at these points. Further, during cement addition, the flat and smooth particles of soil disintegrate into rough and crumbled portions and this behavior improves the cohesion value among the particles, which then increases the strength values. It worth noting that, the development of white cementing compounds (CSH and CAH) on the surfaces of soil particles aids as an indicator of the pozzolanic reactions, as illustrated in Figure 4. Similar results have been noticed for various types of soil (Lemaire et al., 2013; Sharma et al., 2018).

The role of curing time on the strength improvement of the cement-treated soil specimens was illustrated in Figure 3B. It is observed that as the curing times increased, the UCS increased. At specific cement content, the UCS increased significantly until a curing time of 60 days. After 60 days of curing, the UCS increases gently as shown in Figure 3B. The UCS increase can be classified into two zones. As the curing times increase up to 60 days, the UCS increased and this zone is referred to as the active zone. After this zone, the UCS improvement slows down while still gradually increasing and this zone is designated as the inert zone. This behavior may be due to that kaolinite is exhausted by the pozzolanic reactions, which lead to reducing the action of pozzolanic reaction with increasing curing time. Besides, the continuous reduction in water content during curing times could affect the pozzolanic reactions. Great attention has been given to calculating the residual water content (RWC) of the soil samples, as shown in Figure 5. RWC means the water content of soil samples after the end of specific curing time. The RWC decreased with the increasing of curing time and cement percentages. Most reduction in water content occurs during the first times of curing until 60 days, after that the reduction in water content continued slightly. The reduction in the RWC could be due to the hydration process of cement and to completion of the pozzolanic reactions. It worth noting that, all the UCS curves (for all cement content) follow the same pattern with curing times.

The stress-strain of UCS test results is presented in Figure 6. Results showed that the failure strain decreases considerably as the cement content and curing time increases. While the slope of the stress-strain curves (before and after the maximum stress value), increases with increasing both cement content and curing times. This means that the utilization of cement addition increased the UCS, reduced the strain at failure, and changed the soil behavior from ductile to brittle behavior. The influence of curing times on the stress-strain curves was more pronounced for higher cement content. Many researchers reported that the natural soil specimen exhibited ductile behavior; while the stabilized soil specimen posed brittle behavior (Horpibulsuk et al., 2012; Mousavi & Leong Sing, 2015). It worth noting that, all the stress-strain curves were similar, except the difference in the maximum stress values.

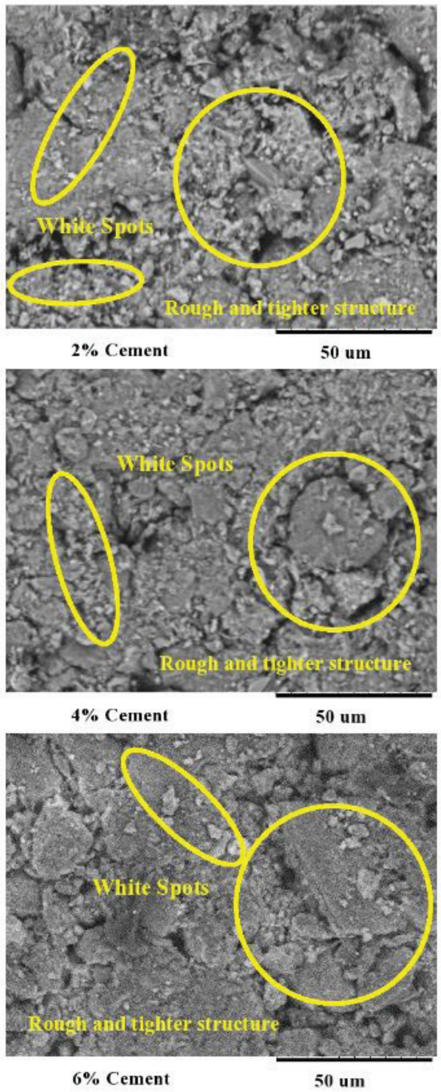

Figure 4. SEM images of cement-treated soil specimens cured for 90 days showing the roughness of the soil structure.

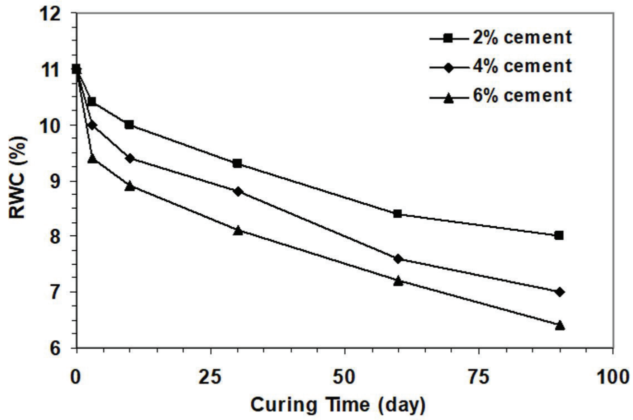

Figure 5. RWC of cement-treated soil specimens cured for different curing times.

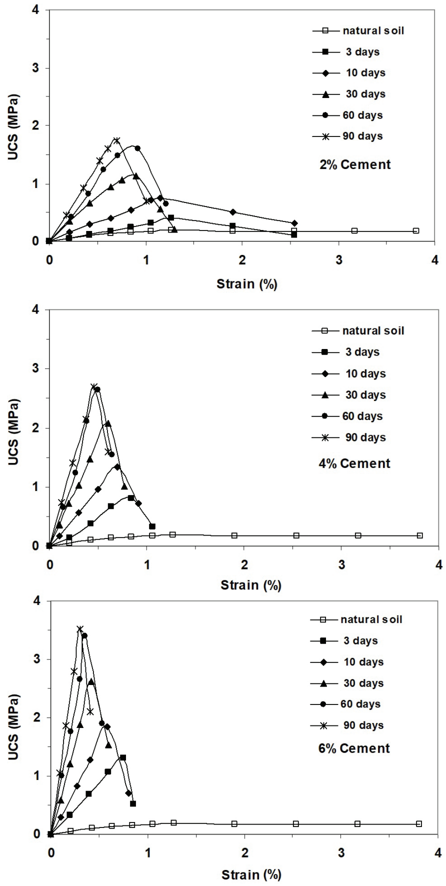

Figure 6. Stress-strain curves of cement-treated soil specimens cured for different curing times.

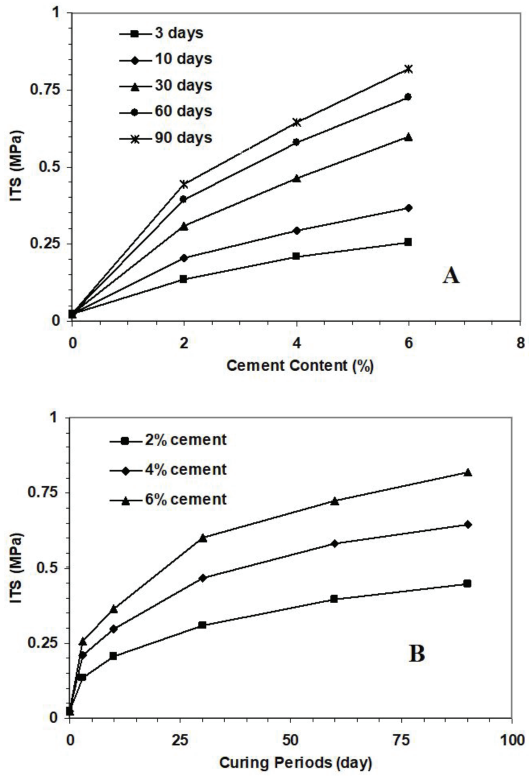

Figure 7. ITS of soil specimens with (A) cement content and (B) curing times.

3.4 Indirect Tensile Strength characteristics (ITS)

The ITS test results of cement-treated soil specimens were shown in Figure 7. The data show a significant increase in the ITS of treated soils in comparison to the natural soil. It is also shown that the tensile strength increases linearly with the increase of both cement content and the curing times. The linear increase in ITS with a high slope at 3 days of curing was attributed to the short-term reactions and cement hydration. Further, this behavior largely depended on the cement content. As the curing times increase the ITS was likely to be more reliant upon the pozzolanic reactions. Also, Figure 7B implies that ITS improvement for all cement contents starts to moderate beyond 60 days of curing. This is consistent with the steady of the pozzolanic reaction at high curing times (more than 60 days). The most obvious explanation for this significant increase in the ITS is that this strength is indirectly calculated and is based on the compression pressure ($P_{max.}$) used in Equation 1. Thus, the same reasons considered to explain the increase in UCS can be used to illustrate the significant increase in ITS values.

3.5 Wave velocity results

A wave velocity test was performed on natural and cement-treated soil specimens, and the results were presented in Table 3. The results show that the wave velocity increases with increasing both cement content and curing times and followed the same trend as UCS. In general, the increase in wave velocity from the value of natural specimens to the 3 days of curing was more pronounced than the increase from 3 days to 10 days of curing. Sequentially, this value was more than other intervals of curing times (i.e. the interval between 10 to 30 days, etc.). As the curing times increase, the reactions between the soil particles and cement increased and result to increase the stiffness of the soil specimens. As a result, the wave velocity propagation increased with increasing

Table 3. Variation of wave velocity values of soil specimens with cement content and curing times.

Curing Time (day)	Wave Velocity (m/sec)		
	2% Cement	4% Cement	6% Cement
3	890	965	1115
10	1045	1200	1385
30	1350	1625	1880
60	1550	1780	2060
90	1620	1850	2170

both cement content and curing times. Mandal et al. (2016) documented similar test results. Besides, Yesiller et al. (2000) reported that the wave velocity of cement-treated soil specimens was higher than the wave velocity of the natural specimens.

Further, the cementing compounds and the unreacted cement help to filling the voids among soil particles, resulting to create other paths with short traveling times. This behavior increases the wave velocity values of soil specimens.

3.6 Gas permeability results

Gas permeability is the capacity of soil to allow air to flow in the existence of a pressure gradient. In this research, gas permeability is used as a pointer of the structural changes of soil specimens. The use of gas permeability rather than water permeability avoids the interaction of water with the soil-cement mixtures. The variations of coefficient of gas permeability (Ka) values with both cement content and curing times were illustrated in Figure 8. In general, the Ka of soil specimens decreased with increasing both cement content and curing times. The values of Ka decreased from (2.2×10^{-13} m^2) of natural soil to (8.9×10^{-14}, 7.6×10^{-14} and 6.8×10^{-14} m^2) of soil specimens treated with 2, 4 and 6% cement content respectively, and cured for 3 days. While the values of soil specimens cured for 90 days were (4.9×10^{-15}, 2.4×10^{-15}, and 8.4×10^{-16} m^2) of soil specimens treated with 2, 4, and 6% cement content respectively. It is well known that the voids and pores (macropores and micropores) of soil specimens play a major role in the gas permeability values (Aldaood et al., 2016; Wang et al., 2017). As discussed previously in section (3.2), the PSD of soil specimens mainly affected by cement content and curing times. Before cement addition (i.e. natural soil), the pores available for gas flow are larger (see Figures 1 and 2), resulting in larger values of Ka. Again, the Ka is a function of two parameters: the porosity and the interconnectivity between the pores (Aldaood et al., 2016). When the cement was added and the soil specimens cured for different times, both porosity and the interconnectivity between the pores decreased due to the formation of cementing compounds during the pozzolanic reactions. As a result, the Ka decreased with both cement content and curing times. Further, it is observed that the decrease in Ka values from the value of natural specimens to the 60 days of curing was more pronounced than the decrease from 60 days to 90 days of curing. This behavior is attributed to the formation of most cementing compounds (as discussed previously) and these compounds will bound the soil grains and hinder the gas flow in soil specimens. Therefore, the Ka values of soil specimens decreased. Another reason to decrease the Ka values (especially at short curing times) of soil specimens was the unreacted cement particles which act as a filler and fill the voids among soil particles, leading to enclosed the voids and decreasing the gas permeability.

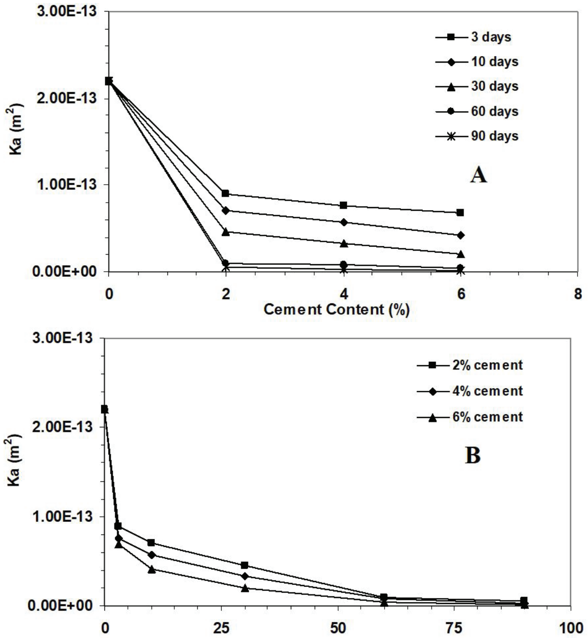

Figure 8. Gas permeability of soil specimens with (A) cement content and (B) curing times.

3.7 Soil-water retention behavior

The soil-water retention curves (SWRC) referring to both cement content and curing times were plotted together to comment on the general shape of the SWRCs and whether these curves affected by the cement content and curing times. Figure 9 presents the influence of the cement content and curing times on the SWRCs in terms of suction pressure and volumetric water content. In general, the cement addition and curing times have an insignificant influence on the shape of the SWRC, and all curves having an S-shape curve. For all cement contents, the SWRCs of soil specimens cured for 90 days were lie above the other curves (see Figure 9). This behavior was attributed to high capillary and absorptive forces resulting from finer soil structure (Aldaood, 2020). Moreover, the influence of curing times on the SWRCs was larger at low suction pressure than at high suction pressure. Another interesting observation from Figure 9 is that there was a continuous reduction in the volumetric water content of soil specimens with increasing suction pressure. This reduction was found to be dependent

Table 4. Variation of volumetric water content values of soil specimens with cement content and curing times.

Curing Time (day)	θ at 10 kPa (%)			θ at 1500 kPa (%)		
	2% Cement	4% Cement	6% Cement	2% Cement	4% Cement	6% Cement
30	35.7	39.0	46.5	25.3	27.2	29.6
60	42.4	45.3	51.0	29.1	31.5	35.2
90	54.2	59.2	66.0	33.8	35.7	40.2

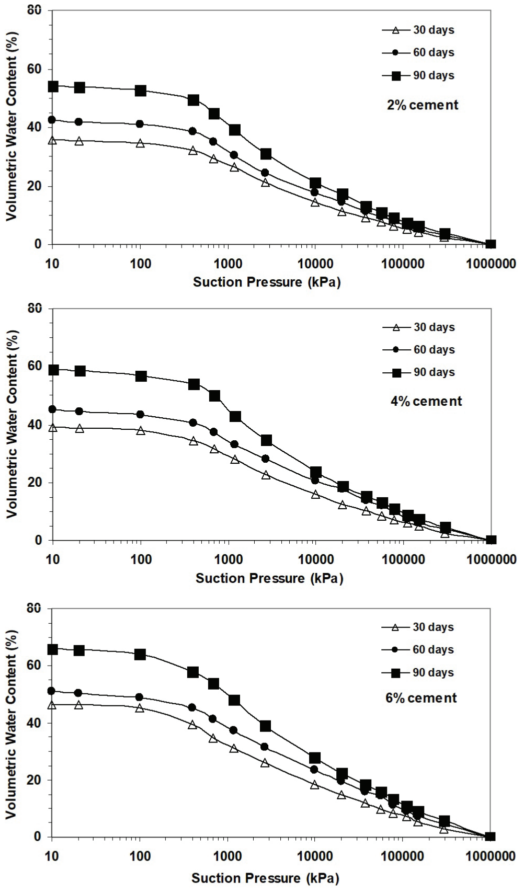

Figure 9. SWRCs of soil specimens with various cement content and curing times.

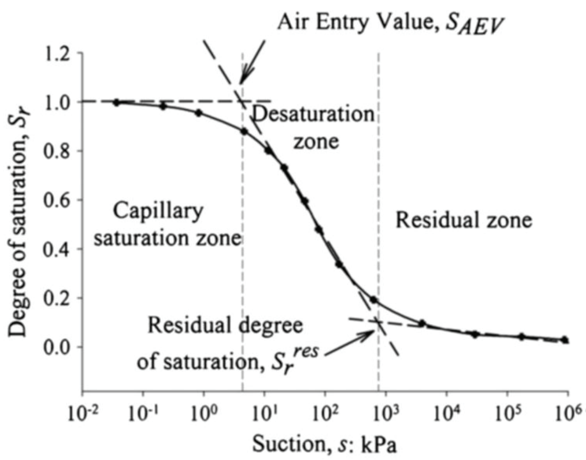

Figure 10. Typical SWCC showing the saturation, desaturation and residual zones (Vanapalli et al., 1999).

on both cement content and curing times as presented in Table 4. The differences between the volumetric water content values of soil specimens were obvious at suction pressure lower than 1500 kPa. While at suction pressure larger than 1500 kPa the differences in values were slight particularly for soil specimens cured at 60 and 90 days. This behavior is attributed to the more pozzolanic reactions in the soil specimens. Certainly, increasing curing time promotes the pozzolanic reaction within the soil mixture and resulting to the development of cementing materials (i.e. CSH and CAH), so that they help to the change in the PSD of soil specimens as discussed previously. Moreover, cement addition can help to enhance the microstructure properties of soil specimens, thus make the PSD more uniform and improving the water-holding performance of treated soil specimens (Jiang et al., 2019).

The key parameters of SWRC were established using the method suggested by Vanapalli et al. (1999), as illustrated in Figure 10. The main zones (states) of the SWRC are saturated and residual zones. The saturation volumetric water content (θ_a) and the air entry value AEV (Ψ_a) represented the saturation state. While the residual volumetric water content (θ_r) and the corresponding residual suction pressure (Ψ_r) represented the residual state. As the suction pressures of soil specimens increased from 10 kPa to the AEV the volumetric water content of the soil specimens was approximately constant. Beyond the AEV, there was a continuous reduction in the volumetric water content of the soil specimens with increasing suction pressure. Further, the slope of the SWRCs of soil specimens cured for 90 days in part between the AEV and the residual water content was larger than the slope of other parts. This means that the soil structure was uniform and compact then resulting in better water holding capacity (Aldaood et al., 2014). Table 5 presents the saturation and residual state values of soil specimens with all cement contents and curing times. It is observed that both (θ_a) and (θ_r) increased with increasing cement content and curing times. The increase in (θ_a) was greater than the increase in (θ_r). The AEV showed insignificant changes with cement addition and curing times. Further, no obvious relationship was observed for the residual suction pressure with cement content and curing times. The difference in saturated and residual states values with cement content and curing times reveals the mineralogical and microstructural variations in soil specimens as discussed in section 3.2.

Table 5. Saturation and residual states values of soil specimens with cement content and curing times.

Curing Time (day)	Cement Content (%)	Saturation State		Residual State	
		Air-Entry Value, Ψ_a (kPa)	θ_a (%) corresponding to Ψ_a	Residual Suction, Ψ_r (kPa)	θ_r (%) corresponding to Ψ_r
30	**2**	200	35.7	30000	8
	4	240	39.0	12000	11
	6	255	46.5	20000	13
60	**2**	205	42.4	17000	10
	4	245	45.3	13000	13
	6	255	51.0	18000	15
90	**2**	210	54.2	16000	12
	4	260	59.2	28000	14
	6	270	66.0	14000	21

4. Conclusions

The following conclusions can be driven from this study:

- Increasing both cement content and curing times increased the strengths properties and wave velocity values of soil specimens. On the other hand, the gas permeability, pH, electrical conductivity values, and the failure strain were decreased with increasing curing times;
- The strength improvement of cement-treated soil specimens with curing times is divided into two zones: active and inert zones. Inactive zone the soil structure became compactness rather than the structure of natural soil and the cluster of grains become more effective. In the inert zone, there were insignificant changes in soil structure, thus there was a slight increase in strength value;
- Cement addition and curing times considerably modified the microstructural behavior of soil specimens. Cement content enhanced the volume and the morphology of pores (particularly the macropores), suggesting more cementing compounds formed and its action was more than the curing times;
- Interesting agreements between the microstructural, mechanical, and unsaturated hydraulic properties were obtained. Whereas the states of pores over time mainly affect the strength, gas permeability, and soil-water retention behavior;
- The AEV of soil specimens did not affect considerably with cement content and curing times. While the water holding capacity of soil specimens increased with these parameters. The most influences of cement content and curing times were on the part of SWRC with suction pressure smaller than 1500 kPa.

Declaration of interest

The authors declare that there are no known conflicts of interest associated with this publication and there has been no significant financial support for this work that could have influenced its outcome.

Author's contributions

Ibrahim M. Alkiki: investigation, methodology, validation. Mohammed D. Abdulnafaa: data curation, writing - original draft preparation. Abdulrahman Aldaood: writing - reviewing and editing.

References

Abdulnafaa, M.D., Cabalar, A.F., & Arabash, Z. (2019). Shear strength characteristics of clay with waste solid construction and demolition materials. In *Shear Strength Characteristics of Clay with Construction and Demolition Solid Waste Materials*, Turkey.

Adeyanju, E.A., & Okeke, C.A. (2019). Clay soil stabilization using cement kiln dust. *IOP Conference Series: Materials Science and Engineering*, 640, 012080. http://dx.doi.org/10.1088/1757-899X/640/1/012080

Al-Aghbari, M.Y., Mohamedzein, Y.E.A., & Taha, R. (2009). Stabilisation of desert sands using cement and cement dust. *Proceedings of the Institution of Civil Engineers: Ground Improvement*, 162(3), 145-151. http://dx.doi.org/10.1680/grim.2009.162.3.145.

Aldaood, A. (2020). Impact of fine materials on the saturated and unsaturated behavior of silty sand soil. *Ain Shams Engineering Journal*, 11(3), 717-725. http://dx.doi.org/10.1016/j.asej.2019.11.005.

Aldaood, A., Bouasker, M., & Al-Mukhtar, M. (2014). Soil-water characteristic curve of lime treated gypseous soil. *Applied Clay Science*, 102, 128-138. http://dx.doi.org/10.1016/j.clay.2014.09.024.

Aldaood, A., Bouasker, M., & Al-Mukhtar, M. (2014a). Geotechnical properties of lime-treated gypseous soils. *Applied Clay Science*, 88–89, 39-48. http://dx.doi.org/10.1016/j.clay.2013.12.015.

Aldaood, A., Bouasker, M., & Al-Mukhtar, M. (2014b). Impact of wetting-drying cycles on the microstructure and mechanical properties of lime-stabilized gypseous soils. *Engineering Geology*, 174, 11-21. http://dx.doi.org/10.1016/j.enggeo.2014.03.002.

Aldaood, A., Bouasker, M., & Al-Mukhtar, M. (2015). Soil-water characteristic curve of gypseous soil. *Geotechnical* *and Geological Engineering*, 33(1), 123-135. http://dx.doi.org/10.1007/s10706-014-9829-5.

Aldaood, A., Bouasker, M., & Al-Mukhtar, M. (2016). Effect of water during freeze-thaw cycles on the performance and durability of lime-treated gypseous soil. *Cold Regions Science and Technology*, 123, 155-163. http://dx.doi.org/10.1016/j.coldregions.2015.12.008.

Al-Mukhtar, M., Lasledj, A., & Alcover, J.F. (2014). Lime consumption of different clayey soils. *Applied Clay Science*, 95, 133-145. http://dx.doi.org/10.1016/j.clay.2014.03.024.

Amadi, A.A., & Osu, A.S. (2018). Effect of curing time on strength development in black cotton soil: quarry fines composite stabilized with cement kiln dust (CKD). *Journal of King Saud University - Engineering Sciences*, 30(4), 305-312. http://dx.doi.org/10.1016/j.jksues.2016.04.001.

Amu, O., Fajobi, A., & Afekhuai, S. (2008). Stabilizing potential of cement-fly ash mixture on expansive clay Soil. *Journal of Technology and Education in Nigeria*, 12(2), http://dx.doi.org/10.4314/joten.v12i2.35698.

ASTM 6931. (2011). *Standard Test Method for Indirect Tensile (IDT) Strength of Bituminous Mixtures* (Vol. 1, pp. 3-7). ASTM International, West Conshohocken, PA. https://doi.org/10.1520/D6931-17.2.

ASTM D 698. (2003). Standard test methods for laboratory compaction characteristics of soil using standard effort (12 400 ft-lbf/ft^3 (600 kN-m/m^3)). In ASTM International, *The annual book of ASTM standards* (Vol. 3, pp. 1-11). ASTM, West Conshohocken, PA. https://doi.org/10.1520/D0698-12E01.1.

ASTM (2000). *Annual book of ASTM standards. Soil and rock, Vol. 04.08.* Philadelphia: American Society for Testing and Materials.

Attom, M.F., Taqieddin, S.A., & Mubeideen, T. (2000). Shear strength and swelling stabilization of unsaturated clayey soil using pozzolanic material. In C.D. Shackelford, S.L. Houston & N.-Y. Chang (Eds.), *Advances in unsaturated geotechnics* (pp. 275-288). Reston, VA: American Society of Civil Engineers.

Ayeldeen, M., & Kitazume, M. (2017). Using fiber and liquid polymer to improve the behaviour of cement-stabilized soft clay. *Geotextiles and Geomembranes*, 45(6), 592-602. http://dx.doi.org/10.1016/j.geotexmem.2017.05.005.

Azam, A.M., & Cameron, D.A. (2013). Geotechnical properties of blends of recycled clay masonry and recycled concrete aggregates in unbound pavement construction. *Journal of Materials in Civil Engineering*, 25(6), 788-798. http://dx.doi.org/10.1061/(ASCE)MT.1943-5533.0000634.

Cabalar, A., Abdulnafaa, M., & Isik, H. (2019a). The role of construction and demolition materials in swelling of a clay. *Arabian Journal of Geosciences*, 12(11), 361. http://dx.doi.org/10.1007/s12517-019-4552-4.

Cabalar, A., Zardikawi, O., & Abdulnafaa, M. (2019b). Utilisation of construction and demolition materials with clay for road pavement subgrade. *Road Materials and Pavement Design*, 20(3), 702-714. http://dx.doi.org/10.1080/14680629.2017.1407817.

Cabalar, A.F., Abdulnafaa, M.D., & Karabash, Z. (2016). Influences of various construction and demolition materials on the behavior of a clay. *Environmental Earth Sciences*, 75(9), 841. http://dx.doi.org/10.1007/s12665-016-5631-4.

Cabalar, A.F., Hassan, D.I., & Abdulnafaa, M.D. (2017). Use of waste ceramic tiles for road pavement subgrade. *Road Materials and Pavement Design*, 18(4), 882-896. http://dx.doi.org/10.1080/14680629.2016.1194884.

Chen, H., & Wang, Q. (2006). The behaviour of organic matter in the process of soft soil stabilization using cement. *Bulletin of Engineering Geology and the Environment*, 65(4), 445-448. http://dx.doi.org/10.1007/s10064-005-0030-1.

Chenari, R.J., Fatahi, B., Ghorbani, A., & Alamoti, M.N. (2018). Evaluation of strength properties of cement stabilized sand mixed with EPS beads and fly ash. *Geomechanics and Engineering*, 14(6), 533-544. http://dx.doi.org/10.12989/gae.2018.14.6.533.

Chew, S.H., Kamruzzaman, A.H.M., & Lee, F.H. (2004). Physicochemical and engineering behavior of cement treated clays. *Journal of Geotechnical and Geoenvironmental Engineering*, 130(7), 696-706. http://dx.doi.org/10.1061/(ASCE)1090-0241(2004)130:7(696).

Consoli, N., Arcari Bassani, M., & Festugato, L. (2010). Effect of fiber-reinforcement on the strength of cemented soils. *Geotextiles and Geomembranes*, 28(4), 344-351. http://dx.doi.org/10.1016/j.geotexmem.2010.01.005.

Consoli, N., Cruz, R., & Floss, M. (2011). Variables controlling strength of artificially cemented sand: influence of curing time. *Journal of Materials in Civil Engineering*, 23(5), 692-696. http://dx.doi.org/10.1061/(ASCE)MT.1943-5533.0000205.

Consoli, N., Faro, V., Schnaid, F., & Born, R. (2017). Stabilised soil layers enhancing performance of transverse-loaded flexible piles on lightly bonded residual soils. *Soils and Rocks*, 40(3), 219-228. http://dx.doi.org/10.28927/SR.403219.

Das, B.M., Yen, S.C., & Dass, R.N. (1995). Brazilian tensile strength test of lightly cemented sand. *Canadian Geotechnical Journal*, 32(1), 166-171. http://dx.doi.org/10.1139/t95-013.

Eades, J.L., & Grim, R.E. (1966). A quick test to determine lime requirements for lime stabilization. *Highway Research Record*, (139), 61-72.

Feng, T.W., Lee, J.Y., & Lee, Y.J. (2001). Consolidation behavior of a soft mud treated with small cement content. *Engineering Geology*, 59(3-4), 327-335. http://dx.doi.org/10.1016/S0013-7952(01)00021-7.

Goodary, R., Lecomte-Nana, G.L., Petit, C., & Smith, D.S. (2012). Investigation of the strength development in cement-stabilised soils of volcanic origin. *Construction & Building Materials*, 28(1), 592-598. http://dx.doi.org/10.1016/j.conbuildmat.2011.08.054.

Horpibulsuk, S., Phojan, W., Suddeepong, A., Chinkulkijniwat, A., & Liu, M.D. (2012). Strength development in blended cement admixed saline clay. *Applied Clay Science*, 55, 44-52. http://dx.doi.org/10.1016/j.clay.2011.10.003.

Horpibulsuk, S., Rachan, R., & Raksachon, Y. (2009). Role of fly ash on strength and microstructure development in blended cement stabilized silty clay. *Soil and Foundation*, 49(1), 85-98. http://dx.doi.org/10.3208/sandf.49.85.

Horpibulsuk, S., Rachan, R., Chinkulkijniwat, A., Raksachon, Y., & Suddeepong, A. (2010). Analysis of strength development in cement-stabilized silty clay from microstructural considerations. *Construction & Building Materials*, 24(10), 2011-2021. http://dx.doi.org/10.1016/j.conbuildmat.2010.03.011.

Iravanian, A., & Bilsel, H. (2016). Strength characterization of sand-bentonite mixtures and the effect of cement additives. *Marine Georesources and Geotechnology*, 34(3), 210-218. http://dx.doi.org/10.1080/1064119X.2014.991463.

İşbuğa, V., Çabalar, A., & Abdulnafaa, M. (2019). Large-scale testing of a clay soil improved with concrete pieces. *Proceedings on Engineering Sciences B*, 2, 95-100.

Jiang, X., Huang, Z., Ma, F., & Luo, X. (2019). Large-scale testing of clay soil improved with concrete pieces. *Materials*, 12(23), 3873. http://dx.doi.org/10.3390/ma12233873.

Joel, M., & Agbede, I.O. (2010). Cement stabilization of Igumale shale lime admixture for use as flexible pavement construction material. *The Electronic Journal of Geotechnical Engineering*, 15, 1661-1673.

Kalantari, B., & Huat, B.B.K. (2008). Peat soil stabilization, using ordinary portland cement, polypropylene fibers, and air curing technique. *The Electronic Journal of Geotechnical Engineering*, 13, 1-13.

Kalantari, B., & Prasad, A. (2014). A study of the effect of various curing techniques on the strength of stabilized peat. *Transportation Geotechnics*, 1(3), 119-128. http://dx.doi.org/10.1016/j.trgeo.2014.06.002.

Kalıpcılar, İ., Mardani-Aghabaglou, A., Sezer, G.İ., Altun, S., & Sezer, A. (2016). Assessment of the effect of sulfate attack on cement stabilized montmorillonite. *Geomechanics and Engineering*, 10(6), 807-826. http://dx.doi.org/10.12989/gae.2016.10.6.807.

Kasama, K., Ochiai, H., & Yasufuku, N. (2000). On the stress-strain behaviour of lightly cemented clay based on an extended critical state concept. *Soil and Foundation*, 40(5), 37-47. http://dx.doi.org/10.3208/sandf.40.5_37.

Kenai, S., Bahar, R., & Benazzoug, M. (2006). Experimental analysis of the effect of some compaction methods on mechanical properties and durability of cement stabilized soil. *Journal of Materials Science*, 41(21), 6956-6964. http://dx.doi.org/10.1007/s10853-006-0226-1.

Khattab, S.I., & Aljobouri, M.M. (2012). Effect of Combined Stabilization by Lime and Cement on Hydraulic Properties of Clayey Soil Selected From Mosul Area. *Al-Rafidain Engineering Journal*, 20(6), 139-153.

Khemissa, M., & Mahamedi, A. (2014). Cement and lime mixture stabilization of an expansive overconsolidated clay. *Applied Clay Science*, 95, 104-110. http://dx.doi.org/10.1016/j.clay.2014.03.017.

Korf, E.P., Prietto, P.D.M., & Consoli, N.C. (2017). Hydraulic and diffusive behavior of a compacted cemented soil. *Soils and Rocks*, 39(3), 325-331.

Lemaire, K., Deneele, D., Bonnet, S., & Legret, M. (2013). Effects of lime and cement treatment on the physicochemical, microstructural and mechanical characteristics of a plastic silt. *Engineering Geology*, 166, 255-261. http://dx.doi.org/10.1016/j.enggeo.2013.09.012.

Lorenzo, G.A., & Bergado, D.T. (2004). Fundamental parameters of cement-admixed clay - New approach. *Journal of Geotechnical and Geoenvironmental Engineering*, 130(10), 1042-1050. http://dx.doi.org/10.1061/(ASCE)1090-0241(2004)130:10(1042).

Mandal, T., Tinjum, J.M., & Edil, T.B. (2016). Non-destructive testing of cementitiously stabilized materials using ultrasonic pulse velocity test. *Transportation Geotechnics*, 6, 97-107. http://dx.doi.org/10.1016/j.trgeo.2015.09.003.

Mengue, E., Mroueh, H., Lancelot, L., & Medjo Eko, R. (2017). Physicochemical and consolidation properties of compacted lateritic soil treated with cement. *Soil and Foundation*, 57(1), 60-79. http://dx.doi.org/10.1016/j.sandf.2017.01.005.

Miller, G.A., & Azad, S. (2000). Influence of soil type on stabilization with cement kiln dust. *Construction & Building Materials*, 14(2), 89-97. http://dx.doi.org/10.1016/S0950-0618(00)00007-6.

Mousavi, S., & Leong Sing, W. (2015). Utilization of brown clay and cement for stabilization of clay. *Jordan Journal of Civil Engineering*, 9(2), 163-174.

Nahlawi, H., Chakrabarti, S., & Kodikara, J. (2004). A direct tensile strength testing method for unsaturated geomaterials. *Geotechnical Testing Journal*, 27(4), 356-361. http://dx.doi.org/10.1520/GTJ11767.

Naseem, A., Mumtaz, W., Fazal-e-Jalal, & De Backer, H. (2019). Stabilization of expansive soil using tire rubber powder and cement kiln dust. *Soil Mechanics and Foundation Engineering*, 56(1), 54-58. http://dx.doi.org/10.1007/s11204-019-09569-8.

Nayak, S., & Sarvade, P.G. (2012). Effect of cement and quarry dust on shear strength and hydraulic characteristics of lithomargic Clay. *Geotechnical and Geological Engineering*, 30(2), 419-430. http://dx.doi.org/10.1007/s10706-011-9477-y.

Okyay, U.S., & Dias, D. (2010). Use of lime and cement treated soils as pile supported load transfer platform. *Engineering Geology*, 114(1-2), 34-44. http://dx.doi.org/10.1016/j.enggeo.2010.03.008.

Osinubi, K.J., Oyelakin, M.A., & Eberemu, A.O. (2011). Improvement of black cotton soil with ordinary portland cement - locust bean waste ash blend. *The Electronic Journal of Geotechnical Engineering*, 16, 619-627.

Pakbaz, M.S., & Alipour, R. (2012). Influence of cement addition on the geotechnical properties of an Iranian clay. *Applied Clay Science*, 67-68, 1-4. http://dx.doi.org/10.1016/j.clay.2012.07.006.

Park, S.S. (2011). Unconfined compressive strength and ductility of fiber-reinforced cemented sand. *Construction & Building Materials*, 25(2), 1134-1138. http://dx.doi.org/10.1016/j.conbuildmat.2010.07.017.

Petchgate, K., Sukmongkol, W., & Voottipruex, P. (2001). Effect of height and diameter ratio on the strength of cement stabilized soft Bangkok clay. *Journal of Geotechnical Engineering*, 31(3), 227-239.

Riaz, S., Aadil, N., & Waseem, U. (2014). Stabilization of subgrade soils using cement and lime: a case study of Kala Shah Kaku, Lahore, Pakistan. *Pakistan Journal of Science*, 66(1), 39-44. Retrieved in March 1, 2014, from http://aplicacionesbiblioteca.udea.edu.co:3653/ehost/detail/detail?vid=11&sid=9827d053-420e-4669-9575-5e6211a04bbc@sessionmgr112&hid=125&bdata=Jmxhbmc9ZXMmc2l0ZT1laG9zdC1saXZl#db=a9h&AN=98360899

Rojas-Suárez, J.P., Orjuela-Abril, M.S., & Prada-Botía, G. (2019a). Study of low plasticity clay for optimum dosage of the soil-cement. *Journal of Physics: Conference Series*, 1386(1), 012078. http://dx.doi.org/10.1088/1742-6596/1386/1/012078.

Rojas-Suárez, J.P., Orjuela-Abril, M.S., & Prada-Botía, G.C. (2019b). Determination of the adequate dosage of the soil-cement, using clay of high plasticity. *Journal of Physics: Conference Series*, 1386(1), 012077. http://dx.doi.org/10.1088/1742-6596/1386/1/012077.

Saadeldin, R., & Siddiqua, S. (2013). Geotechnical characterization of a clay-cement mix. *Bulletin of Engineering Geology and the Environment*, 72(3-4), 601-608. http://dx.doi.org/10.1007/s10064-013-0531-2.

Saberian, M., Moradi, M., Vali, R., & Li, J. (2018). Stabilized marine and desert sands with deep mixing of cement and sodium bentonite. *Geomechanics and Engineering*, 14(6), 553-562. http://dx.doi.org/10.12989/gae.2018.14.6.553.

Saeed, K.A., Kassim, K.A., Nur, H., & Yunus, N.Z.M. (2015). Strength of lime-cement stabilized tropical lateritic clay contaminated by heavy metals. *KSCE Journal of Civil Engineering*, 19(4), 887-892. http://dx.doi.org/10.1007/s12205-013-0086-6.

Sharma, L.K., Sirdesai, N.N., Sharma, K.M., & Singh, T.N. (2018). Experimental study to examine the independent roles of lime and cement on the stabilization of a mountain soil: a comparative study. *Applied Clay Science*, 152, 183-195. http://dx.doi.org/10.1016/j.clay.2017.11.012.

Shooshpasha, I., & Shirvani, R.A. (2015). Effect of cement stabilization on geotechnical properties of sandy soils. *Geomechanics and Engineering*, 8(1), 17-31. http://dx.doi.org/10.12989/gae.2015.8.1.017.

Umesha, T.S., Dinesh, S.V., & Sivapullaiah, P.V. (2009). Control of dispersivity of soil using lime and cement. *International Journal of Geology*, 3(1), 8-16.

Vanapalli, S.K., Fredlund, D.G., & Pufahl, D.E. (1999). The influence of soil structure and stress history on the soil-water characteristics of a compacted till. *Geotechnique*, 49(2), 143-159. http://dx.doi.org/10.1680/geot.1999.49.2.143.

Wang, Y., Cui, Y.J., Tang, A.M., Benahmed, N., & Duc, M. (2017). Effects of aggregate size on the compressibility and air permeability of lime-treated fine-grained soil. *Engineering Geology*, 228, 167-172. http://dx.doi.org/10.1016/j.enggeo.2017.08.005.

Wei, D., Zhu, B., Wang, T., Tian, M., & Huang, X. (2014). Effect of Cationic Exchange Capacity of Soil on Strength of Stabilized Soil. *Procedia: Social and Behavioral Sciences*, 141, 399-406. http://dx.doi.org/10.1016/j.sbspro.2014.05.070.

Yesiller, N., Hanson, J.L., & Usmen, M.A. (2000). Ultrasonic assessment of stabilized soils. In *Soft Ground Technology Conference* (Vol. 301, pp. 170-181), Noordwijkerhout, the Netherlands. http://dx.doi.org/10.1061/40552(301)14.

Zhang, T., Yue, X., Deng, Y., Zhang, D., & Liu, S. (2014). Mechanical behaviour and micro-structure of cement-stabilised marine clay with a metakaolin agent. *Construction & Building Materials*, 73, 51-57. http://dx.doi.org/10.1016/j.conbuildmat.2014.09.041.

Soils and Rocks
An International Journal of Geotechnical and Geoenvironmental Engineering
www.soilsandrocks.com
ISSN 1980-9743
ISSN-e 2675-5475

Seismic zoning of Tabriz area by stochastic finite fault model considering site-specific soil effects

Armin Sahebkaram Alamdari[1], Rouzbeh Dabiri[1#], Rasoul Jani[1], Fariba Behrouz Sarand[1]

Article

Keywords
Tabriz
Tabriz North Fault
Seismic zonation
Peak ground acceleration
Stochastic finite fault

Abstract

Tabriz, as one of the most earthquake-prone cities in the Iran plateau, has experienced enormous earthquakes that have even destroyed the city altogether. Considering this seismological background and the vicinity of Tabriz's northwestern fault, reducing the possible earthquake losses can be highly useful by scrutinizing the strong ground motion resulting from the fault activation. To this end, a stochastic finite-fault ground motion simulation (EXSIM) method was applied as an important means for predicting the ground motion near the epicenter of the earthquake. EXSIM is an open-source stochastic finite-fault simulation algorithm that generates the time-series of the earthquake's ground motion. Based on the findings, the peak horizontal acceleration reached 0.83 g in the northern parts by creating artificial accelerograms and Tabriz's seismic zonation. In comparison, it reduced by 0.48 g by departing from the fault in the city's southern parts. Additionally, providing a seismic zonation map in Tabriz revealed that stopping the construction in the north parts while extending the settlement construction to the south part of the city are considered vital and unavoidable. Also, by applying the magnification and effects of the soil layers above the bedrock, it was further found that the existence of the loose layer with low strength and compaction intensify the application of seismic acceleration on the near-surface structures in the central, west, and southwest parts of the target area.

1. Introduction

The earthquake is regarded as one of the natural hazards that puts an end to many people's lives. Various studies have globally delved into finding appropriate methods to counteract and reduce the caused damage by predicting the amount of the released energy by fault activation. The Iranian plateau is formed by the active tectonics of the Alpine-Himalayan seismic belt and is located between the tectonic plates of Eurasia and Arabia. This plateau is also considered one of the most seismic-prone regions in the world that face many earthquakes per year (Mirzaei, 1997). Several parameters contribute to the need for special attention to this natural risk, including the active tectonic conditions, the presence of faults, and numerous seismogenic sources, along with the high population density in areas susceptible to the earthquake (Zaré et al., 1999; Uyanık, 2015). Given the above-mentioned seismic conditions regarding the Iran plateau, many studies have extensively focused on this area (e.g., Nowroozi, 1996; Shoja-Taheri, 1984; Nogol-Sadat, 1994; Jackson at al., 1995; Tavakoli, 1996; Mirzaei et al., 1998; Berberian & Yeats, 1999; Zaré & Memarian, 2000; Masson et al., 2006; Ansari et al., 2009; Karimiparidari et al., 2011; Hamzehloo et al., 2012; Mojarab et al., 2013; Khoshnevis et al., 2017).

Besides, numerous cities have been expanded in the range of active faults despite this vast area's seismicity. Among these metropolises, Tabriz is located in a seismicity area and has frequently been faced with earthquakes throughout its history. According to Berberian (1976), Tabriz's most dramatic earthquake occurred in the 1780 with a magnitude of 7.7, leading to the city's destruction. This city is surrounded by the mountains and plains of Tabriz from the North, South, and East, the Talkhehrood salt marshland (Ajichai) from the West, and is shaped like a fairly large hole or a hinterland plain. Besides, the North Tabriz Fault is the most dangerous in Iran due to extensive construction volume and population density. Moreover, this fault is even more dangerous than the North Tehran Fault, Alborz and Zagros, and other Iran faults. The city of Tabriz shakes if the earthquake occurs, but the landslide and rupture occur in the north and east of the metropolis, located on the fault.

Similarly, the North Tabriz Fault with the right-lateral strike-slip mechanism of pressure component (such that in most parts, northern limb raises more compared to the southern limb) is considered a seismic and active fault with at least 16 historical earthquake occurrences (Zaré, 2000). Moreover, as one of the most prominent faults in Azerbaijan, this fault

#Corresponding author. E-mail address: rouzbeh_dabiri@iaut.ac.ir
[1]Department of Civil Engineering, Tabriz Branch, Islamic Azad University, Tabriz, Iran.

Submitted on January 20, 2020; Final Acceptance on November 20, 2020; Discussion open until May 31, 2021.

DOI: https://doi.org/10.28927/SR.2021.047220

is extended along the main road of Tabriz-Boustanabad up to Miyaneh and has caused an earthquake with a magnitude of 7.6 Richter scale in 1721 (Berberian, 1976; Berberian & Yeats, 1999). Although the fault has no definite activity in the current century, there is some evidence on its possible remotion. Statistical data also show that the return period of severe and destructive earthquakes in Tabriz can reach about 260 years. We can refer to some studies that have addressed the above issue (e.g., Zaré, 2001; Zaré et al., 2009; Manafi, 2012; Farahani, 2015). The geometry of the fault was determined based on geological information, seismology, and existent equations (Ambraseys & Melville, 1982; Wells & Coppersmith, 1994; Siahkali Moradi et al., 2008). It has been mentioned in Table 1.

The study area of Tabriz is selected in this work because the earthquake system record does not record any destructive event for Tabriz fault, and the estimation of strong ground motion predicts based on the hypothetical stochastic model in this region. Simulating the earthquakes scenario is the best method for getting more knowledge of the Tabriz region's earthquake event.

Accordingly, in the research regarding the significance of the seismicity of Tabriz and its location in the vicinity of the Tabriz fault, the peak horizontal acceleration was calculated, and the seismic zonation map of the study area due to the activation of Tabriz fault provided using the stochastic finite-fault method by selecting appropriate parameters. Then, the peak horizontal acceleration near the surface was computed utilizing the seismic zonation results of Tabriz urban area and collecting geotechnical and geophysical down hole sampling from different points of the target area by applying the soil's magnification effects layer.

2. Literature review

2.1 Stochastic finite fault

Given the issues mentioned above and the importance of the subject in this research, Tabriz's seismic zonation considering due to the activation of the North Tabriz Fault. For this purpose, the stochastic finite fault method is employing to predict the strong ground motion.

The stochastic finite-fault model is an important instrument for predicting the earth's motion near the epicenter of the earthquake. In strong ground motion modeling, the earthquake can be regarded as a point source when the target area is far from the earthquake source (fault). However, cases such as fault geometry, heterogeneous slip distribution on the fault surface, and directivity can greatly impact motion content in the near field (Boore, 2005, 2009). To investigate the effects of these finite faults on the ground motion modeling Hartzell (1978) suggested that an earthquake's fault surface is divided into a network of sub-faults, each of which can be considered a point source. Moreover, a fault surface is categorized into an array of sub-faults based on the determined magnitude according to its seismic moment, each one of which is treated as a point source.

Table 1. The Geometry of North Fault of Tabriz.

Section	Value
Length and width of the fault (km)	19.9×150
Strike slope	85 310

Additionally, the sub-faults' time-series employs a serialized point-source stochastic model, developed by Boore (1983, 2003), using the stochastic method simulated by generalized computer code (Boore, 2003, 2005). Various studies have sought to obtain the maximum strong ground motion utilizing a stochastic finite fault in recent years. For instance, Scandella et al. (2011) investigated the earthquake scenario in Vicoforte, Italy, applying the kinematic source developed by Hisada & Bielak (2003) and the stochastic finite fault. Similarly, Zonno et al. (2012) presented the high-frequency maximum observable shaking map of Italy for the fault source. Besides, Yazdani & Kowsari (2013) provided the earthquake ground-motion prediction equation for northern Iran using the same method. Using the stochastic finite fault method, Samaei et al. (2014) also conducted a study on the strong ground motion from Niavaran fault in Tehran. Likewise, Wang et al. (2015) simulated the 2013 Lushan earthquake in China with a 7 Richter scale by the field acceleration approach.

Moreover, Amiranlou et al. (2016) predicted the strong ground motion of Tabriz's north fault utilizing the stochastic finite fault model based on a dynamic corner frequency simulation. Eventually, Karimzadeh et al. (2019) simulated a vast range of ground motion, followed by simulating a large collection of simulated earth movements. They then studied the effects of various parameters on the seismic behavior of a single degree of freedom systems in terms of energy, applying a nonlinear time history analysis. Finally, stochastic finite fault simulations were conducted on the western parts of the Northern Anatolian Fault zone in Turkey.

2.2 Seismic amplification

Destructions resulted from the recent earthquakes reveal the effect of site conditions and topography on the severity and extent of destructions. Therefore, investigating these factors on the seismic wave response is of great importance in earthquake engineering. Complex topographic feature patterns cause significant differences in arriving the waves to the ground surface. Furthermore, surface and sub-fault ruggedness increase the range of ground motion. The influence of local soil conditions on ground motion characteristics has long been revealed while the earthquake waves travel through the soil layers and arrive at the ground surface. Previous studies demonstrated soil layer characteristics, including the type, depth, and profile of the soil effect on the ground response domain, even in moderate earthquakes, and highlighted them as important factors for ground motion estimation (Yaghmaei-Sabegh & Motallebzade, 2012).

For example, Rodríguez-Marek et al. (2001) introduced a simple empirical approach based on the seismic site response, including the dynamic stiffness of surficial material measurement and the bedrock's depth. This geotechnical site classification scheme provides an alternative to the geologic-based and shear wave. Similarly, Pitilakis et al. (2004) conducted a study on the environmental regulation setting's design response spectra and soil classification. Moreover, Park & Hashash (2005) evaluated seismic site factors in the Mississippi Embayment and analyzed the probabilistic seismic hazard with nonlinear site effects. Hashash et al. (2010), besides reviewed recent advances in nonlinear site response analysis focusing on 1-D site response commonly used in engineering practice. He described material models' developments for both total and effective stress considerations and the challenges of capturing the measured small and large strain damping within these models. Additionally, Eker et al. (2012) investigated local site characteristics, and seismic classification study using active and inactive wave approaches in the north of Ankara, Turkey. Likewise, in their study, Drennov et al. (2013) examined the acceleration response spectra of earthquakes with M=4-6.5 in the southwestern part of the Baikal Rift Zone. Also, Uyanık et al. (2013) determined from shear wave velocity the soil liquefaction locations of soils in Kumluca district with assuming an earthquake to be M=7 in the Finike–Kaş–Elmalı triangle in the southwest of Antalya, Turkey. Also, Groholski et al. (2014) conducted a study regarding the dynamic soil behavior and pore pressure response from Downhole array measurements. More, Atesh & Uyanık (2019) applied the spectral ratio and horizontal to vertical spectral ratio techniques to earthquake signals using the reference and single station methods to determine the amplification of the building and ground in Kocaeli, Turkey. Verdugo et al. (2019) also presented an alternative method to establish seismic site classification. It is noteworthy that the use of the new spectral parameters named "Spectral Threshold Displacement (STD)" and "Spectral Threshold Acceleration (STA)" allow identifying the relevance of the displacement spectrum with the structural damage, which is also related to the stiffness and drift of the structure. Besides, Shreyasvi et al. (2019) attempted to combine the local site response with the standard probabilistic seismic hazard analysis. The site response was computed by performing an equivalent linear analysis in the frequency domain. Yaghmaei-Sabegh & Hassani (2020) developed a new site amplification model for Iran based on the site fundamental frequency obtained from the horizontal-to-vertical spectral ratio.

3. Method

3.1 Stochastic finite-fault modeling

Possible simulation methods are of two types: in the first type, the seismic source is a point source; in the second type, which is called finite fault simulation, the seismic source is a rectangular fault that in its longitudinal and transverse directions as sources the point is of the same elements. The point source method cannot consider the main parameters of an earthquake in a massive earthquake, such as the long duration and the slopes' dependence on the observation station (orientation effect). Due to these limitations, the modeling method based on finite faults proposed by Hartzel and has become very popular in the last two decades (Boore, 2009).

The finite fault modeling method combines the plane source aspects with the point source seismic model, and since the mentioned limitations do not naturally exist in the limited fault modeling method, this geometry method fails and considers the effect of orientation and gives good results. For simulation using finite faults, the time delay method, and addition of related accelerometers of a two-dimensional network containing elements, are used. The stochastic point source method is using in cases where the distance of the fault from the study area is so far that the fault can study as a point relative to the case study, but in cases where the distance from the fault is very close or the part of the study area located on the fault, it is better to use the stochastic finite fault method (Boore, 2009).

Motazedian & Atkinson (2005) proposed simulating earthquake seismogram using the stochastic finite-fault method relying on dynamic corner frequency. Based on their findings, high accurate results were obtained by improving the approach and increasing more parameters. In this model, the corner frequency was a function of time, and the rupture history controlled the frequency content of the simulated time series of each sub-fault. A large fault was also divided into N sub-faults, where each sub-fault was considered a small point source (Figure 1).

EXSIM is an open-source stochastic finite-fault simulation algorithm, which is written in FORTRAN that generates the time series of the ground motion for the earthquakes (Atkinson & Assatourians, 2015). In the finite fault modeling of the ground motion, a large fault is categorized into N sub-faults, where each sub-fault is considered a small point-source. The ground motion that contributed to each sub-fault can be calculated by the stochastic point-source method and then summed at the observation point with a proper time delay to obtain the ground motion from the entire fault.

The time series from the sub-faults are modeled using the point-source stochastic model developed by Boore (1983, 2003) and popularized by the Stochastic-Method Simulation computer code (Boore, 2003, 2005). Furthermore, each sub-fault's ground motion is treated as the random Gaussian noise of a specified duration by having an underlying spectrum as given by the point-source model (Brune, 1970) for shear radiation. This basic idea was implemented in many studies (e.g., Irikura 1983, 1992; Schneider et al., 1993; Irikura & Kamae, 1994; Atkinson & Silva, 1997; Bour & Cara, 1997; Beresnev & Atkinson, 1998; Motazedian & Atkinson, 2005; Boore, 2009). Motazedian & Atkinson (2005) introduced the new variety of this method based on dynamic corner frequency. Their implementation had a significant advantage

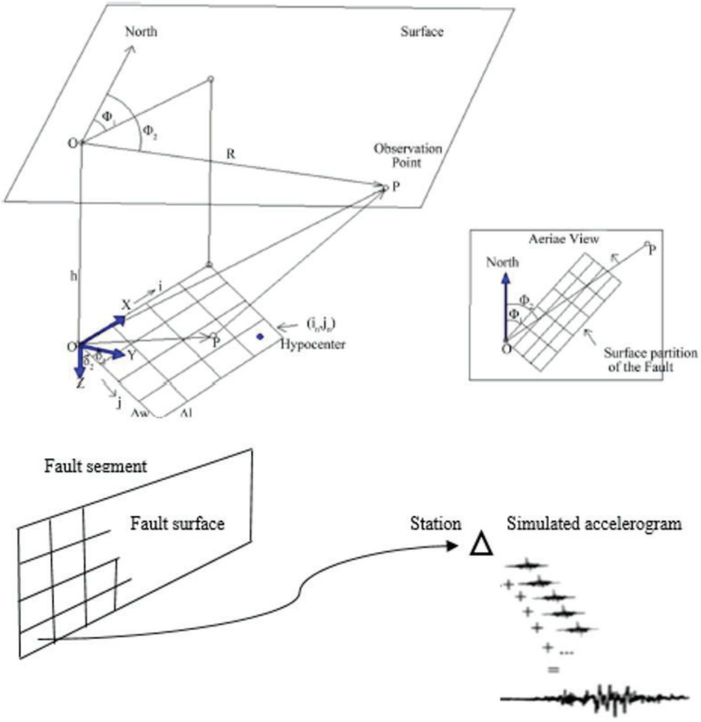

Figure 1. An illustration of finite-fault modeling. The fault surface divides into smaller fault segments, and each subfault is treating as a point source (Motazedian & Atkinson, 2005).

over previous algorithms such that it made the simulation results relatively insensitive to the sub-fault size and thus eliminated the need for the multiple triggering of the sub-events (Atkinson & Assatourians, 2015). Boore (2009) moreover improved the algorithm with modifications to the sub-event normalization procedures that eliminated the remaining dependency on sub-fault size and improved the treatment of low-frequency amplitudes. In this model, the corner frequency is a function of time, and the rupture history controls the frequency content of the simulated time series of each sub-fault.

Moreover, the rupture begins with a high corner frequency and progresses to lower corner frequencies as the ruptured area grows. Additionally, limiting the number of active sub-faults in calculating dynamic corner frequency can control the amplitude of lower frequencies. In the revised EXSIM algorithm, properly normalized and delayed sub-fault contributions are summed in the time domain as

$$A(t)=\sum_{i=1}^{N}H_i \times Y_i\left(t-\Delta t_i-T_i\right) \tag{1}$$

$$H_i=\frac{M_0}{M_{0_i}}\sqrt{\frac{\sum_j\left(\frac{f_0^2 f_i}{f_0^2+f_j^2}\right)^2}{N\sum_j\left(\frac{f_{0_i}^2 f_i}{f_{0_i}^2+f_j^2}\right)^2}} \tag{2}$$

A(t) is the total seismic signal at the site, which incorporates the sub-faults' delays. Besides, H_i denotes a normalization factor for *i*th sub-fault that aims to conserve high-frequency amplitudes. Further, Y_i (t), N, and Δt_i indicate the signal of the *i*th sub-fault (the inverse Fourier transform of the sub-fault spectrum), the total number of sub-faults, and the delay time of the sub-fault, respectively. Furthermore, T_i and M_0 are a fraction of the rise time and the total seismic moment. Finally, M_{0i} displays the seismic moment of *i*th sub-fault, which is internally calculated by the EXSIM based on the sub-fault size (Atkinson & Assatourians, 2015; Atkinson et al., 2011). The final version of EXSIM named "EXSIM12" by Atkinson & Assatourians (2015) was used in the present research.

3.2 Site response analysis

Various evidence were reported regarding the site effect and nonlinear behavior of the local soil in previous earthquakes. The soil type and thus the dynamic characteristics of the soil profile (e.g., attenuation and shear modulus, soil liquefaction, soil amplification, porosity, moisture content, the number of layers, and their thickness) were all mentioned as factors that affect the nonlinear behavior of the soil (Uyanık et al., 2006; Eker et al., 2012; Drennov et al., 2013).

Many researchers investigated the effects of different parameters on seismic magnification. For example, Park & Hashash (2005) and Rodríguez-Marek et al. (2001) highlighted soil thickness as one of the most significant parameters for the seismic response. Pitilakis et al. (2004) and Uyanık (2015) also considered the very high effect of different variables on seismic bedrock, including the soil type, soil classification and thickness, the dominant period of the local soil, and the average velocity of shear wave in the alluvial layer.

It is noteworthy that in the current study, the DEEPSOIL software, which is applied for site response analysis, was used for seismic magnification. DEEPSOIL is a unified one-dimensional program utilized for the dynamic analysis of the site response in linear, equivalent-linear, and nonlinear approaches. Moreover, this software provides the user with the required outputs by accelerograms and the applying site conditions (Hashash et al., 2016). The linear approach was utilized in this research, as well.

In this method, a conversion function with dynamic and force properties was determined based on one of the bedrock's dynamic properties. This approach, based on the principle of force summation, is a very simple method and is based on complex number calculation. The bedrock motion, which is considered accelerograms, can be converted to the Fourier series that can be changed into the Fourier series of the used conversion function's ground motion. Thus, the conversion function easily determines the resonance or damping of the bedrock motion when it arrives at the surface.

In this study, we first investigate the input parameters for the stochastic finite fault model by investigating the North Tabriz Fault and the Tabriz city area survey. Then, due to the importance of correctly selecting input parameters using empirical reduction relationships, the selected input parameters have been validated. By obtaining modeling results using stochastic finite fault, maximum acceleration seismic zonation due to activation of North Tabriz Fault over the studied area is presented.

Finally, by collecting geotechnical (to obtain general and soil strength characteristics) and geophysical (to obtain the shear wave velocity of the soil) data by Downhole sampling, from reputable and active laboratories in this field (Like the results of geotechnical and geophysical experiments that have been done in the study phase of different lines of Tabriz metro.), and experiments have performed in areas where there is not enough data seismic magnification is carrying out by transferring seismic acceleration from bedrock to ground level using Deepsoil software. The calculation of the results will show us the maximum seismic acceleration at ground level. The aggregation of results provides a zoning map for maximum seismic acceleration at ground level for the Tabriz city area. Figure 2 schematically illustrates the present study.

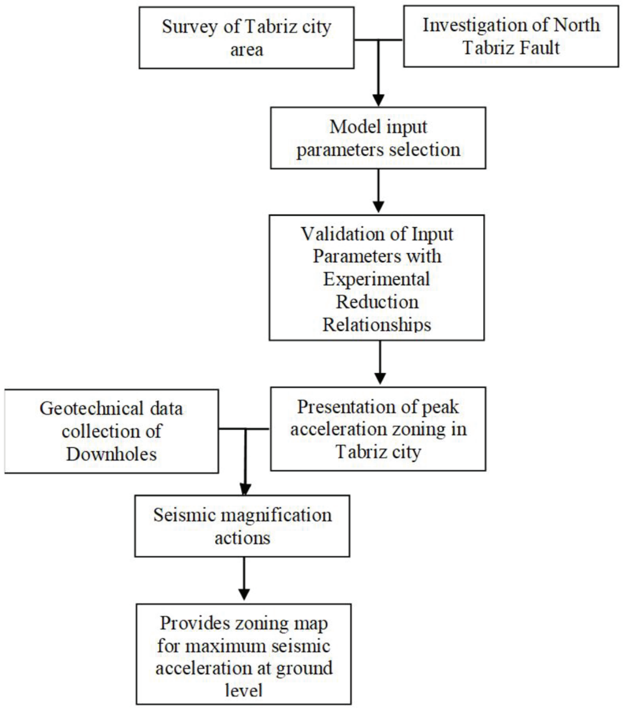

Figure 2. Schematic of progressive research.

4. Case study

4.1 Tabriz boundary

Tabriz city is located in the northwest of Iran, near one of the most important and known seismic faults of the Iranian Plateau (North Tabriz Fault). The North Tabriz Fault with its right-lateral strike-slip mechanism of pressure component (such that in most parts, the northern limb has raised more than the southern limb) is regarded as a seismic and active fault with at least 16 historical earthquakes occurring. Additionally, it is a well-known fault of Iran's seismic faults due to the historical earthquake occurring and the destruction of Tabriz for 12 times. The fault is currently laying on through the settlements in the north of Tabriz, owing to the expansion of construction and settlement construction on the fault zone. The losses and massive damages for an earthquake of a magnitude of 6.5 or more are predicted based on the risk of the direct rupture in the city, the faulting within Tabriz boundary, and the effects of the near-field fault. Besides, the evaluation of seismic potential and seismic zoning is of great importance due to Tabriz's significance in the northwestern parts of Iran, the history of seismicity, the existence of marl-clay deposits, and the potential for landslides (Zaré, 2001).

4.2 Geotechnical conditions of the study area

Based on the studies done on alluvial sediments and the data obtained from drilled wells in Tabriz, the thickness of alluvial sediments in different parts of the city is different. The thickness of these sediments increases from east to west. Most of which are the clay, silt, and sand. The thickness of the alluvium decreases from the city center to the north and south of the city. North and northeast towns of Tabriz (Eram and Baghmisheh) on Miocene units and several neighbourhoods and towns east, south, northeast of Tabriz (Valiasr town, El Goli, Sahand's Villashahr and Andisheh) on lignite layers and Miocene and Miocene-

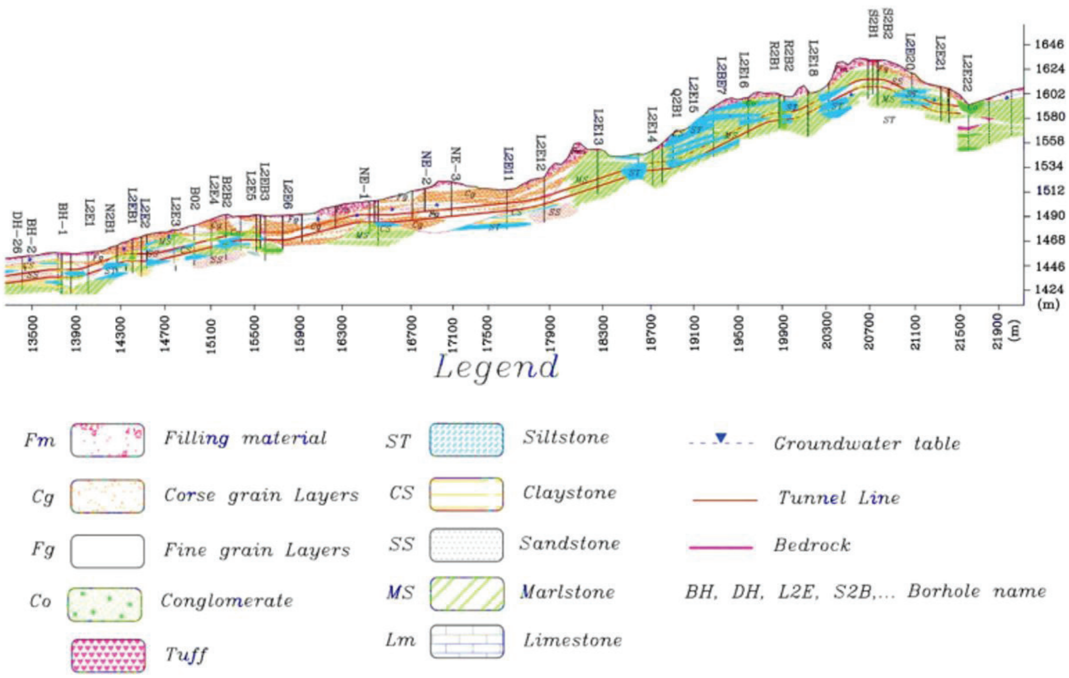

Figure 3. Geotechnical section of the western part of tunnel route line 2 of Tabriz's metro (Mohammadi et al., 2016).

Pliocene age fish and Sahand pyroclastic units of Pliocene to Early Quaternary age. The central part of the city is also located on alluvial sediments.

Based on the geological and groundwater data obtained from boreholes of the western part of tunnel route line 2 of Tabriz's metro, Figure 3 shows the boreholes and soil layers' location. Geologically, this part of the tunnel comprises sedimentary rocks consisting of marls, claystone, siltstone, and sandstone, which are underlain by surface alluvium with a thickness of 5-15 m. In this part, the water table varies between 6 and 30 m, and the consistency of the alluvium is classified as hard and very hard (Mohammadi et al. 2016).

As the former Yaghmaei-Sabegh & Hassani (2020) have pointed out, the most intensification occurs in soft soil layers, which Vs30 is usually less than 175. Therefore, it is expected that in areas with denser alluvial layers, the maximum intensification of peak ground acceleration will be observed.

4.3 The North Tabriz Fault

As mentioned earlier, the North Tabriz Fault was the target fault in this study. The daily mild motion and shaking of the ground occur in Tabriz. The placement of Alborz and Zagros Mountain ranges and Tabriz, located at the intersection of these two mountains, in the Alpine belt, is the reason for the large and destructive earthquakes in these areas. The belt originates from the middle of the Atlantic and crossing the Mediterranean Sea, north of Turkey, Iran, India, China, and the Philippine Islands and merges to another belt that revolves around the Pacific Ocean. Evidence shows that this fault is about 150 km long and its rupture can be very hazardous due to its location within the Tabriz metropolitan area. As referred before, the North Tabriz Fault is the longest active one with a significant portion within the urban area. According to the constructions done on North Tabriz Fault, this fault is called the most dangerous fault of the Iranian plateau. Other faults in the Iranian plateau either have a far distance that reduces their impact on the study area or do not have the power to create maximum acceleration and magnitude as the North Tabriz fault. Therefore, the North Tabriz Fault is considered as the main fault.

The length, wide, and the dip of the fault are 150 km, 12 km, 87 degrees, respectively, and its seismicity depth is estimated about 10 to 20 km based on the recorded micro-seismic data which are classified as surface earthquakes (Ambraseys & Melville, 1982; Wells & Coppersmith, 1994).

4.4 Input parameters

Table 2 presents the key input parameters for simulating the artificial seismogram for Tabriz's north fault by the stochastic finite-fault method using the EXSIM program.

4.5 Validation of input parameters

To validate and control the opted parameters' correction, a comparison was made between an initial modeling and the scaling relationships that indicated the maximum ground-motion parameters as a function of magnitude and distance. For this purpose, it was included four scaling relationships were developed by Sinaiean et al. (2007), Boore & Atkinson (2008), Campbell & Bozorgnia (2008), and Boore et al.

Table 2. The Input Parameters for Simulation.

Input Parameters of EXSIM	Value
Fault orientation (strike)	310°
Fault orientation (dip)	87°
Fault depth to upper edge (km)	5
Sub-fault dimensions (km)	2×2
Moment magnitude	7.5
Stress drop (bar)	60
Geometric spreading	$\frac{1}{R}$, $R \leq 85$ km $\frac{1}{R^{0.5}}$, $85<R<120$ km $\frac{1}{R^{0.5}}$, $R \geq 120$ km
Quality (Q) factor (f)	$95 f^{0.8}$
Distance-dependent duration	$T_0 + 0.1R$
Kappa coefficient	0.03
Pulsing area	50%
Windowing function	Saragoni-Hart
Shear-wave velocity (km/s)	3.3
Rupture velocity	$0.8 \times$ Shear wave velocity
Density (gr/cm^3)	2.8
Damping	5%
Starting rupture element	Random
Slip distribution	Random

The values of the software input parameters were extracted from previous studies (e.g., Wells & Coppersmith, 1994; Kanamori & Anderson, 1975; Anderson & Hough, 1984; Farahbod & Alahyarkhani, 2003; Hoseinpour & Zaré, 2009; Motazedian, 2006; Sinaiean, 2006).

(2014). Good agreement with Iran's earthquakes was the reason for their selection (Shoja-Taheri et al., 2010). Figure 4 displays a comparison among the obtained results of these four relationships with the initial ESXIM12 model.

The data depict the peak accelerating values of the initial modeling, along with the mentioned scaling relationships. As shown, there is a good agreement among the results of the initial model and scaling relationships, which shows that the selected input parameters for modeling the North Tabriz Fault have been selected correctly. As pointed in the presented results, the prediction equation presented by Sinaiean et al. (2007) predicts a maximum acceleration greater than the other equations near the fault, and the other results of the prediction equations are in complete agreement. However, the equation of Campbell & Bozorgnia (2008) with distance from the fault predicted a smaller maximum acceleration prediction.

The similarity of most of the predicted equations is in the input parameters, magnitude (M), fault length (R), soil shear wave velocity (V_{s30}), and distance from the fault (Z), which are used in all relations for validation. The original model was the same. This shows the importance and high impact of these parameters in the output of the presented results, which should be paid special attention to the correct selection of these parameters. However, some researchers, such as Boore et al. (2014), consider other parameters in the proposed method, such as the focal mechanism and the type of fault.

5. Modeling of the North Tabriz Fault

5.1 Zonation of peak acceleration in Tabriz boundary

After selecting the appropriate modeling parameters, the simulation was conducted based on the mentioned parameters on the seismic bedrock surface. Figure 5 depicts the points of the simulation of strong ground motion. The Peak Ground Acceleration (PGA) is calculated from the answer summing to obtain the results of the accelerogram and plot them based on acceleration and distance. A sample of the produced accelerogram is displayed in Figure 6. As well as, Figure 7 shows a map of the chirp lines for the simulated maximum horizontal acceleration.

As depicted, the peak horizontal acceleration produced by Tabriz's northern fault reaches 0.83g in the northern part of the city. In contrast, the peak acceleration in the southern part decreases to 0.48g. The obtained prediction results are in

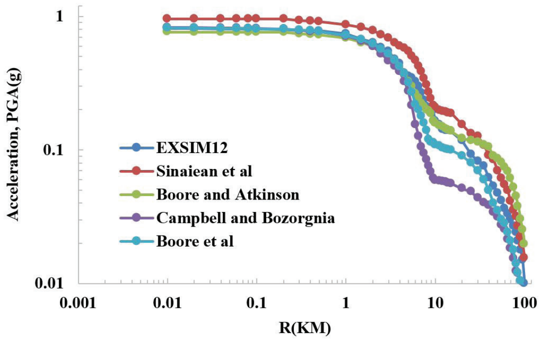

Figure 4. A comparison of PGA among the results of the empirical scaling relationship and initial EXSIM12 model.

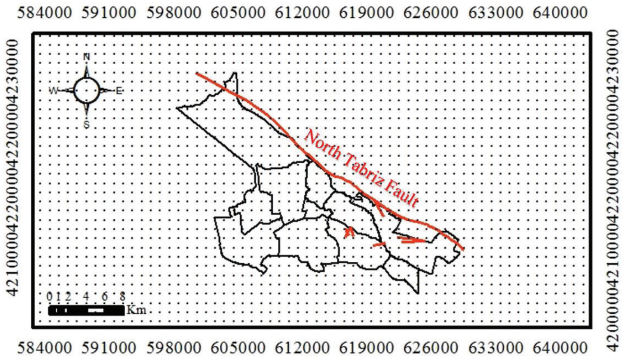

Figure 5. The points of artificially produced accelerograms.

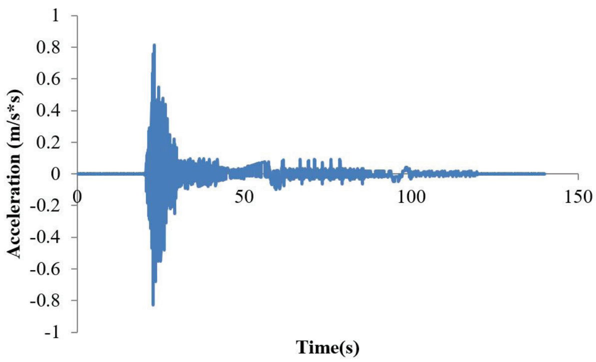

Figure 6. A sample of simulated accelerograms.

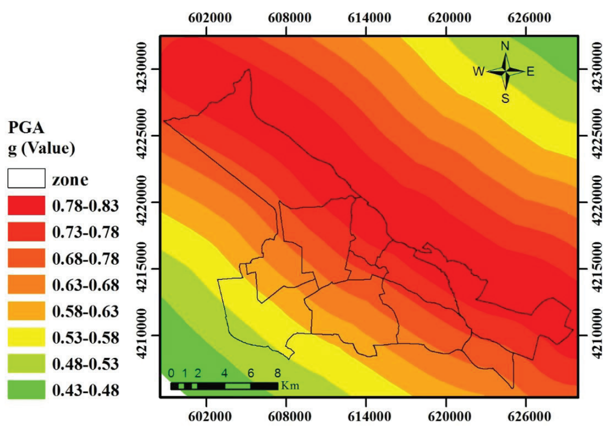

Figure 7. The chill lines map simulated for maximum horizontal acceleration.

good agreement with the results of Karimzadeh et al. (2014), who have obtained the peak ground acceleration due to the activation of the North Tabriz Fault by 0.3 to 0.8g using the Probabilistic Seismic Hazard Analysis (PSHA). Furthermore, the massive losses and destructions are estimated in Tabriz because of the direct rupture hazard in the city, the fault in the urban area on Tabriz, and the effects of a near-field fault the earthquake. In settlements such as Baghmisheh, Roshdieh, Eram, and Valiamr, at the northern part of Tabriz and near-field fault, there is a high potential for a landslide the marl-clay deposits. Given that Tabriz Airport is located in the near-field fault, earthquakes can cause serious destruction, leading to the disruption of assistance at the time of the possible earthquake.

In general, after an earthquake occurs inside the earth and the earth's energy is released, the energy released from its place of release, called the epicenter, propagates in the direction of vibration in all directions and carries the earthquake energy. These waves are very similar to the waves created by a rock falling into a pond's calm water. Just as a rock blow causes water waves to move, an earthquake creates seismic waves that propagate through the ground. The released energy is rapidly dispersed as it moves away from the epicenter, and due to the passage of rock and soil layers, it attenuates and decreases in intensity. That is the main reason for the maximum reduction of earthquake acceleration when moving away from the fault, known as the epicenter of an earthquake. The southern and southeastern parts of the area are more damped due to semi-dense conglomerate layers, but the southwestern and western parts of the area, due to the presence of young alluvial layers, maybe intensified in those areas, which are discussed in the next section.

5.2 Seismic peak acceleration at the surface

After obtaining the seismic zonation of the target area, 432 geotechnical and geophysical downhole data from different points of the urban area of Tabriz were gathered to assess the effect of soil stratification on the earthquake specification in terms of peak acceleration and frequency content. As shown in Figure 8, data from all points of the target area are used to have good distribution.

DEEPSOIL software was used to determine the peak ground acceleration at the surface and imply the amplification of the soil stratification effect. Accordingly, by having the seismic frequency in different points of the area, the gathered geotechnical characteristics (e.g., the soil layer thickness, specific gravity, the shear wave velocity of the soil layer, and attenuation in different layers) were utilized as the input variables for the software. Finally, the magnitude and effect of seismic frequency traveling from soil layers were determined in different samples. After collecting and presenting the results within the target area, seismic zonation after amplification on the ground surface using ArcMap software is depicted in Figure 9.

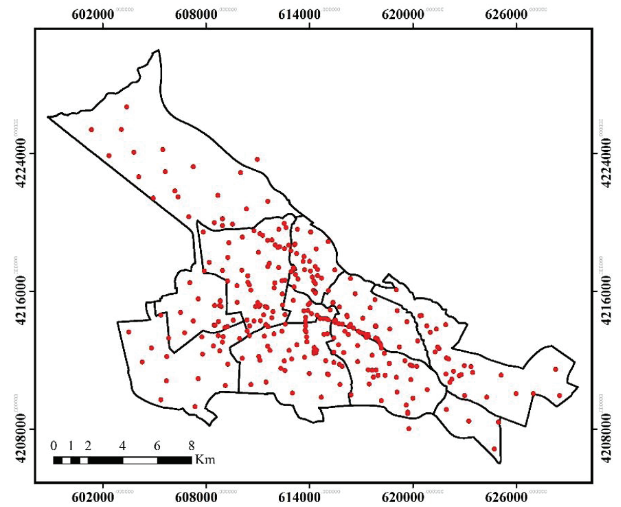

Figure 8. Distribution of collected data for seismic amplification.

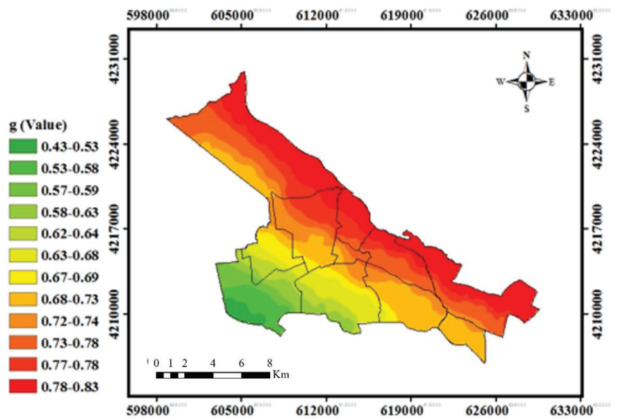

Figure 9. The seismic zonation of Tabriz surface after including soil layer and amplification factor.

The results show that in the north, east, and southeast of Tabriz, due to the low thickness of loose sedimentary deposits, the magnification of acceleration values is minimal. In contrast, the magnification of acceleration values in the western part of Tabriz has the highest rate due to the high thickness of sedimentary deposits. A comparison of acceleration maps calculated on the seismic bedrock and at the ground level shows the highest magnification areas, consistent with the magnification results performed by Amiranlou (2016).

Significant parameters in transmitting earthquake acceleration from bedrock to the ground surface are depth of subsurface, specific gravity, the hardness of subsoil, shear wave velocity in soil layers, soil layer damping, and shear wave hardness and velocity in bedrock. The most influential parameters are the shear wave velocities in the soil and bedrock layers, which change more the results are subject to further change.

6. Discussion

The current research evaluated Tabriz's urban area's seismic conditions and its location on the north of Tabriz's active fault. It was more attempted to determine the North Tabriz Fault's peak acceleration and provide the correct seismic zonation for the target area. For this purpose, the study applied a stochastic finite-fault method and EXSIM12 software. First, the initial model was verified, followed by examining this method's suitability for the target area by comparing its results with artificial accelerograms through the mentioned empirical relationships. The study then further evaluated the modeling parameters for the North Tabriz Fault that presented in Table 2. More efforts were made by comprehensively reviewing the references provided to select them correctly, which have a significant impact on the simulation results and showed how the modeling results could be sensitive to the input parameters like the effect of distance from the fault on the peak acceleration results and the influence of the presence of alluvial layers on the rate of peak intensification of seismic acceleration at the ground. Therefore, it is recommended to be extremely careful about selecting parameters and their compatibility with the selected model. Finally, by calculating the peak horizontal acceleration caused by the active North Tabriz Fault, it was observed that this value could increase up to 0.83 g in the northern part of Tabriz that occasionally lies on the fault. Still, in the southern part of the city, which is far from the fault, it decreased to 0.48 g. Considering the North of Tabriz's active fault, as well as the geotechnical conditions and landslide possibility and shaking at the due time of the earthquake, based on studies conducted by Karimzadeh et al. (2014) on the type and quality of structures and the effect of earthquakes on them, the buildings that have been constructed along the North Tabriz fault will be destroyed, and the buildings with a short distance will be very high destruction. Therefore, stopping the construction in the northern parts and continuing the settlement to the city's southern regions are inevitable.

In terms of assessing the resilience of vital uses of Tabriz city against earthquakes, the situation of the eastern, southeastern, and western regions of the study area is favorable. The western half of the northern and northwestern regions, especially the city center, which is the city's old texture and has high population density, have an unfavorable condition. Therefore, considering the improvement and renovation and observing the necessary regulations and standards, investment is recommended to make the existing vital uses more resilient and transfer and relocate essential services to other areas for Tabriz's central region (Mohammad Raza et al., 2018).

Based on the results related to the seismic zonation after implying the soil layer effects on the depth up to the bedrock and amplification, most of the site effect's consequences were observed in the central and center-west part of Tabriz city. A comparison of acceleration maps calculated on the seismic bedrock and at the ground level shows the highest magnification areas, consistent with the magnification results performed by Amiranlou (2016). Such outcomes were due to the existence of the alluvial layers of the current age (i.e., west and southwest boundary) and the young alluviums (along the Goorichay River) and the presence of low resistant and density soil layers (Rustaei & Sari Sarraf, 2006). Eventually, these layers' effect on seismic acceleration intensity by amplification reached 15-20% in some points in the provided map.

7. Conclusion

The study further evaluated the modeling parameters for the North Tabriz Fault and showed how the results of the modeling could be sensitive to the input parameters. Therefore, it is recommended to be extremely careful about the selection of parameters and their compatibility with the selected model.

Peak ground surface acceleration caused by the active North Tabriz Fault was observed. This value could increase up to 0.83g in the northern part of Tabriz, which occasionally lies in the fault. Considering the active fault in the North of Tabriz, as well as the geotechnical conditions and landslides possibility especially in the North East of the study area (Baghmisheh town) and shaking at the due time of an earthquake, stopping the construct in the northern parts and extending the settlement construction to the southern parts of the city is inevitable.

Based on the results related to the seismic zonation after implying the soil layer effects on the depth up to the bedrock and amplification, most of the site effect's consequences were observed in the central and center-west part of Tabriz. Such outcomes were due to the existence of the alluvial layers of the current age and the young alluviums and the existence of low resistant and density soil layers. Eventually, these layers' effect on seismic acceleration intensity by amplification reached 15-20% in some points in the provided map.

Declaration of interest

The authors certify that there is no actual or potential conflict of interest in relation of this article.

Author's contributions

Armin Sahebkaram Alamdari: conceptualization, methodology, validation. Rasoul Jani: data curation, writing - original draft preparation. Fariba Behrouz Sarand: investigation, validation. Rouzbeh Dabiri: supervision. Rouzbeh Dabiri: writing - reviewing and editing.

References

Ambraseys, N.N., & Melville, C.P. (1982). *History of Persian earthquakes*. Cambridge: Cambridge University Press.

Amiranlou, H. (2016). *Seismic geotechnical microzonation of Tabriz from the perspective of construction effects based on simulated earthquakes* [PhD thesis]. Islamic Azad University of North Tehran.

Amiranlou, H., Pourkermani, M., Dabiri, R., Qoreshi, M., & Bouzari, S. (2016). The stochastic finite-fault modeling based on a dynamic corner frequency simulating of strong ground motion for earthquake scenario of North Tabriz Fault. *Open Journal of Earthquake Research*, 5(2), 114-121.

Anderson, J., & Hough, S. (1984). A model for the shape of the Fourier amplitude spectrum of acceleration at high frequencies. *Bulletin of the Seismological Society of America*, 74, 1969-1993.

Ansari, A., Noorzad, A., & Zafarani, H. (2009). Clustering analysis of the seismic catalog of Iran. *Computers & Geosciences*, 35(3), 475-486. http://dx.doi.org/10.1016/j.cageo.2008.01.010.

Atesh, E., & Uyanık, O. (2019). Ground and structural interaction using geophysical methods. *Süleyman Demirel University Journal of Natural and Applied Sciences*, 23, 46-60.

Atkinson, G., & Assatourians, K. (2015). Implementation and validation of EXSIM (A Stochastic Finite-Fault Ground-Motion Simulation Algorithm) on the SCEC broadband platform. *Seismological Research Letters*, 86(1), 48-60.

Atkinson, G., Goda, K., & Assatourians, K. (2011). Comparison of nonlinear structural responses for accelerograms simulated from the stochastic finite-fault approach versus the hybrid broadband approach. *Bulletin of the Seismological Society of America*, 101(6), 2967-2980.

Atkinson, G.M., & Silva, W. (1997). An empirical study of earthquake source spectra for California earthquakes. *Bulletin of the Seismological Society of America*, 87, 97-113.

Berberian, M., & Yeats, R.S. (1999). Patterns of historical earthquake rupture in the Iranian Plateau. *Bulletin of the Seismological Society of America*, 89(1), 120-139.

Berberian, M. (1976). *Contribution to the Seismotectonics of Iran (Part II)* (Report, No. 29). Tehran, Iran: Geological Survey of Iran.

Beresnev, I., & Atkinson, G. (1998). FINSIM: a FORTRAN program for simulating stochastic acceleration time histories from finite faults. *Seismological Research Letters*, 69(1), 27-32.

Boore, D.M., & Atkinson, G.M. (2008). Ground-motion-prediction equations for the average horizontal component of PGA, PGV, and 5%-damped PSA at spectral periods between 0.01s and 10 s. *Earthquake Spectra*, 24(1), 99-138.

Boore, D.M. (1983). Stochastic simulation of high-frequency ground motions based on seismological models of the radiated spectra. *Bulletin of the Seismological Society of America*, 73, 1865-1894.

Boore, D.M. (2003). Prediction of ground motion using the stochastic method. *Pure and Applied Geophysics*, 160(3), 635-676.

Boore, D.M. (2005). *SMSIM – FORTRAN programs for simulating ground motions from earthquakes: version 2.3. A revision of OFR 96-80-A: a modified version of*

OFR 00- 509.59. Retrieved in January 20, 2020, from http://daveboore.com/software_online.html

Boore, D.M. (2009). Comparing stochastic point- and finite-source ground-motion simulations: SMSIM and EXSIM. *Bulletin of the Seismological Society of America*, 99(6), 3202-3216.

Boore, D.M., Stewart, J.P., Seyhan, E., & Atkinson, G.M. (2014). NGA-West2 equations for predicting PGA, PGV, and 5% damped PSA for shallow crustal earthquakes. *Earthquake Spectra*, 30(3), 1057-1085.

Bour, M., & Cara, M. (1997). Test of a simple empirical Green's function method on moderate-sized earthquakes. *Bulletin of the Seismological Society of America*, 87, 668-683.

Brune, J.N. (1970). Tectonic stress and the spectra of seismic shear waves from earthquakes. *Journal of Geophysical Research*, 75(26), 4997-5009.

Campbell, K.W., & Bozorgnia, Y. (2008). NGAground motionmodel for the geometric mean horizontal component of PGA, PGV, PGD and 5%-damped linear elastic response spectra for periods ranging from 0.01 to 10 s. *Earthquake Spectra*, 24(1), 139-171.

Drennov, A.F., Dzhurik, V.I., Serebrennikov, S.P., Bryzhak, E.V., & Drennova, N.N. (2013). Acceleration response spectra for the earthquakes of the southwestern flank of the Baikal Rift Zone. *Russian Geology and Geophysics*, 54(2), 223-230.

Eker, A.M., Akgun, H., & Kockar, M.K. (2012). Local site characterization and seismic zonation study by utilizing active and passive surface wave methods: a case study for the northern side of Ankara, Turkey. *Engineering Geology*, 151, 64-81.

Farahani, J. (2015). The cause of dual earthquakes in the East Azarbaijan and the seismicity of the region. In *2nd International Conference on Geotechnical and Urban Seismic Engineering*, City Tabriz. [In persian].

Farahbod, A.M., & Alahyarkhani, M. (2003). Attenuation and propagation characteristics of seismic waves in Iran. In *4th International Conference on Seismology and Earthquake Engineering*, City Tehran.

Groholski, D.R., Hashash, Y.M.A., & Matasovic, N. (2014). Learning of pore pressure response and dynamic soil behavior from downhole array measurements. *Civil and Environmental Engineering*, 61-62, 40-56.

Hamzehloo, H., Alikhanzadeh, A., Rahmani, M., & Ansari, A. (2012). Seismic hazard maps of Iran. In *The 04th World Conference on Earthquake Engineering*, Lisbon.

Hartzell, S. (1978). Earthquake aftershocks as Green's functions. *Geophysical Research Letters*, 5(1), 1-14.

Hashash, Y.M.A., Grohalski, D.R., & Philips, C.A. (2010). Recent advances in non-linear site response analysis. In *5th International Conference on Recent Advances in Geotechnical Earthquake Engineering and Soil Dynamics*, San Diego, California.

Hashash, Y.M.A., Musgrove, M.I., Harmon, J.A., Groholski, D.R., Phillips, C.A., & Park, D. (2016). *DEEPSOIL 6.1: user manual.* Urbana.

Hisada, Y., & Bielak, J. (2003). A theoretical method for computing near fault ground motion in a layered half-spaces considering static offset due a surface faulting, with a physical interpretation of fling step and rupture directivity. *Bulletin of the Seismological Society of America*, 93(3), 1154-1168.

Hoseinpour, N., & Zaré, M. (2009). Seismic hazard assessment of Tabriz, a city in the northwest of Iran. *Journal of the Earth*, 4(2), 21-35.

Irikura, K., & Kamae, K. (1994). Estimation of strong ground motion in broad-frequency band based on a seismic source scaling model and an empirical Green's function technique. *Annali di Geofisica*, 37, 1721-1743.

Irikura, K. (1983). Semi-empirical estimation of strong ground motions during large earthquakes. *Bulletin of the Disaster Prevention Research Institute*, 33, 63-104.

Irikura, K. (1992). The construction of large earthquake by a superposition of small events. *Proceedings of the Tenth World Conference on Earthquake Engineering*, 10, 727-730.

Jackson, J.A., Haines, J., & Holt, W. (1995). The accommodation of Arabia-Eurasia plate convergence in Iran. *Journal of Geophysical Research*, 11, 4114-4109. http://dx.doi.org/10.1029/95JB01294.

Kanamori, H., & Anderson, D.L. (1975). Theoretical basis of some empirical relations in seismology. *Bulletin of the Seismological Society of America*, 65, 1073-1095.

Karimiparidari, S., Zaré, M., & Memarian, H. (2011). New seismotectonic zoning map of Iran. In *6th International Conference on Seismology and Earthquake Engineering*, City Tehran.

Karimzadeh, S., Miyajima, M., Hassanzadeh, R., Amiraslanzadeh, R., & Kamel, B. (2014). A GIS-based seismic hazard, building vulnerability and human loss assessment for the earthquake scenario in Tabriz. *Soil Dynamics and Earthquake Engineering*, 66, 263-280.

Karimzadeh, S., Ozsarac, V., Askan, A., & Erberik, M.A. (2019). Use of simulated ground motions for the evaluation of energy response of simple structural systems. *Soil Dynamics and Earthquake Engineering*, 123, 525-542.

Khoshnevis, N., Taborda, R., Azizzadeh-Roodpish, S., & Cramer, C.H. (2017). Seismic hazard estimation of northern Iran using smoothed seismicity. *Journal of Seismology*, 21(4), 941-964.

Manafi, M. (2012). Seismic potential of Tabriz city and surrounding areas. In *National Symposium on Pathology and Programming of Earthquake Effects*, Tabriz, Iran. [In persian].

Masson, F., Djamour, Y., Van Gorp, S., Chery, J., Tatar, M., Tavakoli, F., Nankali, H., & Vernant, P. (2006). Extension in NW Iran driven by the motion of the South Caspian

Basin. *Earth and Planetary Science Letters*, 252(1-2), 180-188.
Mirzaei, N. (1997). *Seismic Zoning of Iran* [Ph.D. Dissertation]. Institute of Geophysics, State Seismological Bureau.
Mirzaei, N., Gao, M., & Chen, Y.T. (1998). Seismic source regionalization for seismic zoning of Iran: major seismotectonic provinces. *Journal of Earthquake Prediction Research*, 9, 354-394.
Mohammadi, D.S., Firuzi, M., & Asghari Kaljahi, E. (2016). Geological-geotechnical risk in the use of EPB-TBM, case study: tabriz Metro, Iran. *Bulletin of Engineering Geology and the Environment*, 75(4), 1571-1583. http://dx.doi.org/10.1007/s10064-015-0797-7.
Mojarab, M., Memarian, H., Zaré, M., Hossein-Morshedy, A., & Pishahang, M.H. (2013). Modeling of the seismotectonic Provinces of Iran using the self-organizing map algorithm. *Computers & Geosciences*, 59, 41-51.
Motazedian, D., & Atkinson, G. (2005). Stochastic finite-fault model based on dynamic corner frequency. *Bulletin of the Seismological Society of America*, 95(3), 995-1010.
Motazedian, D. (2006). Region-specific key seismic parameters for earthquakes in Northern Iran. *Bulletin of the Seismological Society of America*, 96(4A), 1383-1395.
Nogol-Sadat, M.A.A. (1994). *Seismotectonic map of Iran, Teritise on the Geology of Iran. 0001110111 Scale Tehran, Iran.* Iran.
Nowroozi, A.A. (1996). Seismotectonic provinces of Iran. *Bulletin of the Seismological Society of America*, 55, 139-195.
Park, D., & Hashash, Y.M.A. (2005). Evaluation of seismic site factors in the Mississippi Embayment. II. Probabilistic seismic hazard analysis with nonlinear site effects. *Soil Dynamics and Earthquake Engineering*, 25(2), 145-156. http://dx.doi.org/10.1016/j.soildyn.2004.10.003.
Pitilakis, K., Gazepis, C., & Anastasiadis, A. (2004). Design response spectra and soil classification for seismic code provisions. In *Proceedings of 13th World Conference on Earthquake Engineering* (Paper No. 2904). Vancouver, Canada.
Mohammad Raza, P. M., Hanyeh, Y. S., & H. Dalir Karim, H. (2018). Evaluation of resilience of vital uses of Tabriz metropolis against natural earthquake risk. *Geographical Research in Urban Planning*, 6(1), 55-74. [In persian].
Rodríguez-Marek, A., Bray, J.D., & Abrahamson, N.A. (2001). An empirical geotechnical seismic site response procedure. *Earthquake Spectra*, 17(1), 65-87.
Rustaei, S., & Sari Sarraf, B. (2006). Zoning of environmental hazards affecting the physical development of Tabriz. *Journal of Land*, 10, 126-110. [In persian].
Samaei, M., Miyajima, M., & Yazdani, A. (2014). Prediction of strong ground motion using stochastic finite fault method: a case study of Niavaran Fault, Tehran. *Geodynamics Research International Bulletin*, 2(4), 13-23.
Scandella, L., Lai, C.G., Spallarossa, D., & Corigliano, M. (2011). Ground shaking scenarios at the town of Vicoforte, Italy. *Soil Dynamics and Earthquake Engineering*, 31(5-6), 757-772.
Schneider, J.F., Silva, W.J., & Stark, C. (1993). Ground motion model for the 1989 M 6.9 Loma Prieta earthquake including effects of source, path, and site. *Earthquake Spectra*, 9(2), 251-287.
Shoja-Taheri, J. (1984). Acceleration of the 1978 Tabas (Iran) Earthquake: The Generalized Records of Correlation between the Strong Motion Parameters in Different Frequency Bands. In *Regional Assembly of IASPEI*, Heyderabad, India [Oral presentation].
Shoja-Taheri, J., Naserieh, S., & Hadi, G. (2010). A test of the applicability of NGA models to the strong ground-motion data in the Iranian plateau. *Journal of Earthquake Engineering*, 14(2), 278-292.
Shreyasvi, C., Venkataramana, K., & Chopra, S. (2019). Local site effect incorporation in probabilistic seismic hazard analysis: a case study from southern peninsular India, an intraplate region. *Soil Dynamics and Earthquake Engineering*, 123, 381-398.
Siahkali Moradi, A., Hatsfeld, D., & Pal, A. (2008). Research crust velocity structure and mechanism faulting in Tabriz Strike Slip Region. *Journal of Geology Science*, (70).
Sinaiean, F. (2006). *A study of the strong ground motions in Iran* [Ph.D. thesis]. International Institute of Earthquake Engineering and Seismology.
Sinaiean, F., Zaré, M., & Fukushima, Y. (2007). A study on the empirical PGA attenuation relationships in Iran. In *Proceedings of the 5th International Conference on Seismology and Earthquake Engineering*, Tehran.
Tavakoli, B. (1996). *Major seismotectonic Provinces of Iran*. Tehran, Iran: International Institute of Earthquake Engineering and Seismology (IIEES). [In Persian].
Uyanık, O. (2015). Predetermination of earthquake heavy damage areas and importance of macro and micro zoning for urban planning. *Süleyman Demirel University Journal of Natural and Applied Sciences*, 19(2), 24-38.
Uyanık, O., Ekinci, B., & Uyanık, N.A. (2013). Liquefaction analysis from seismic velocities and determination of lagoon limits Kumluca/Antalya example. *Journal of Applied Geophysics*, 95, 90-103.
Uyanık, O., Türker, E., & İsmailov, T. (2006). Sığ Sismik Mikro-Bölgeleme ve Burdur/Türkiye Örneği. *Ekologiya ve Su Teserrüfatı, Elmi-Texniki ve istehsalat Jurnalı*, 1, 9-15.
Verdugo, R., Ochoa-Cornejo, F., Gonzalez, J., & Valladares, G. (2019). Site effect and site classification in areas with large earthquakes. *Soil Dynamics and Earthquake Engineering*, 126, 105071. http://dx.doi.org/10.1016/j.soildyn.2018.02.002.
Wang, Z., Su, J., Liu, C., & Cai, X. (2015). New insights into the generation of the 2013 Lushan Earthquake (M_s 7.0), China. *Journal of Geophysical Research. Solid Earth*, 120(5), 3507-3526.
Wells, D.L., & Coppersmith, K.J. (1994). New empirical relationships among magnitude, rupture length, rupture

width, rupture area, and surface displacement. *Bulletin of the Seismological Society of America*, 84(4), 974-1002.

Yaghmaei-Sabegh, S., & Hassani, B. (2020). Investigation of the relation between Vs30 and site characteristics of Iran based on horizontal-to-vertical spectral ratios. *Soil Dynamics and Earthquake Engineering*, 128, 105899.

Yaghmaei-Sabegh, S., & Motallebzade, R. (2012). An effective procedure for seismic hazard analysis including nonlinear soil response. *Natural Hazards*, 64(2), 1731-1752.

Yazdani, A., & Kowsari, M. (2013). Earthquake ground-motion prediction equations for northern Iran. *Natural Hazards*, 69(3), 1877-1894.

Zaré, M., & Memarian, H. (2000). *Simulation of earthquakes intensity in Iran, research report of Iranian Red Crescent*. Tehran, Iran. 41 p. [In Persian].

Zaré, M. (2000). Investigation of tectonic seismology and slope vector analysis in Lake District of Urmia. In *International Institute of Seismology and Earthquake Engineering*, Tehran. [In Persian].

Zaré, M. (2001). The risk of earthquakes and construction in the north of Tabriz fault zone and fault zone of earthquake faults in Iran. In *International Institute of Seismology and Earthquake Engineering*, Tehran. [In Persian].

Zaré, M., Bard, P.Y., & Ghafory-Ashtiany, M. (1999). Site characterizations for the Iranian strong motion network. *Soil Dynamics and Earthquake Engineering*, 18(2), 101-123.

Zaré, M., Karimi-Paridari, S., & MonaLisa, (2009). An investigation on Balakot, Muzaffarabad (Pakistan) earthquake, 8 Oct. 2005, Mw 7.6; geological aspects and intensity distribution. *Journal of Seismology*, 13(3), 327-337.

Zonno, G., Basili, R., Meroni, F., Musacchio, G., Mai, P.M., Valensise, G., & Boschi, E. (2012). High-frequency maximum observable shaking map of Italy from fault sources. *Bulletin of Earthquake Engineering*, 10(4), 1075-1107.

Soils and Rocks

An International Journal of Geotechnical and Geoenvironmental Engineering

ISSN 1980-9743
ISSN-e 2675-5475

Prediction of maximum dry unit weight and optimum moisture content for coarse-grained lateritic soils

Charles M. O. Nwaiwu[1], Ethelbert O. Mezie[1#]

Article

Keywords
Compaction
Compactive effort
Lateritic soils
Fines content-sand content ratio
Maximum dry unit weight
Optimum moisture content

Abstract

Laboratory compaction of soils is an important aspect in the selection of materials for earthwork construction. Owing to time constraints and concern for depleting resources, it becomes imperative that empirical relationships would be developed to predict compaction parameters, maximum dry unit weight (MDUW) and optimum moisture content (OMC) from easily measured index properties. The aim of this note is to develop empirical relationships between MDUW /OMC and logarithm of compaction energy (E)/fines content: sand content ratio (FC/S_dC) for some lateritic soils. Index property tests were carried out on twenty (20) lateritic soils to classify them and obtain the FC/S_dC. The soils were compacted at three compaction energies; British Standard Light (BSL), West African Standard (WAS) and British Standard Heavy (BSH). Two models were developed from relationships based on slopes and intercepts derived from MDUW/OMC versus log E plots; one model employs 'FC/S_dC' and one compactive effort (BSL) while the other model employs only 'FC/S_dC'. The models were validated for robustness with soils used in the development of the models and six (6) other soils not used to develop the models. For the prediction of BSH, the model employing FC/S_dC and one compactive effort showed typical errors of ±0.63 kN/m^3 and ±0.76% for MDUW and OMC respectively. The model employing only FC/S_dC showed typical errors of ±0.4 kN/m^3 and ±0.83% for MDUW and OMC respectively. The typical errors are within allowed variations for projects and standards for MDUW and OMC, thus the models are quite robust.

1. Introduction

The continual depletion of valuable earth resources due to structural developments have been of much concern in the quest for sustainability, thus, the importance of soil compaction cannot be overemphasized. The world population is increasing every day and there is constant need of more infrastructures such as roads, runways, dams, buildings, jetties, railways etc. All these structures are built on soils which sometimes do not have adequate bearing capacity to resist the loads coming on them. In Nigeria, the common soils used for construction work which are laterite are sometimes found unsuitable in its natural state for intended use. Thus, there is the need for soil improvement of which compaction is among the commonest and the cheapest.

Laterites are described as highly weathered and altered residual soils formed by insitu weathering and decomposition of parent rocks under tropical and subtropical climatic conditions (Aginam et al., 2014). The increasing use of this soil is linked to its availability, cheapness and amenability to compaction. Compaction of lateritic soils like other soils, increases the bearing capacity of the soils. It also decreases the amount of undesirable settlement of structures constructed over such soils and increases the stability of slopes of embankments (Ratnam & Prasad, 2019). The strength of foundations largely depend on compaction control which is based on finding the maximum dry unit weight (MDUW) corresponding to an optimum moisture content (OMC) at a given compaction energy.

Laboratory compaction is usually done in Nigeria with British Standard Light (BSL) (equivalent of standard Proctor method), West African Standard (WAS), and British Standard Heavy (BSH) (equivalent of modified Proctor method). These methods are laborious, time-consuming and material-consuming (Jayan & Sankar, 2015). The shortcomings outlined above together with proof by some earlier authors Ring et al. (1962), Ramiah et al. (1970), Benson et al. (1998) and most recently Anjita et al. (2017) that soil type, its grain size distribution, index properties, and specific gravity influence the MDUW and OMC of soils led researchers to develop empirical relationships between MDUW/OMC and index properties of soils. Such index properties as liquid limit (LL), plastic limit (PL), plasticity index (PI), fines content (FC), sand content (S_dC) etc. have previously been used.

[#]Corresponding author. E-mail address: eo.mezie@unizik.edu.ng
[1]Nnamdi Azikiwe University, Department of Civil Engineering, Awka, Anambra State, Nigeria.

Submitted on July 14, 2020; Final Acceptance on December 30, 2020; Discussion open until May 31, 2021.

DOI: https://doi.org/10.28927/SR.2021.054120

The empirical relationships developed were often based on soft computational methods such as regression analysis (Tenpe & Kaur, 2015) as in the works of Benson et al. (1998), Parkoh (2016) and Oyelakin et al. (2016). Due to the fact that many factors affect compaction parameters as opined by Ardakani & Kordnaeij (2017), most empirical relationships developed from statistical methods such as regression analysis may contain some deviation. However, this opinion seems not well substantiated. Ardakani & Kordnaeij (2017) among other authors employed the use of artificial neural network and genetic algorithm to develop similar relationships to predict MDUW and OMC. Chenari et al. (2015) employed evolutionary polynomial regression method to develop models to predict MDUW and OMC while Gansonré et al. (2019) recently developed a method of predicting insitu dry unit weight from penetrometer tests in calibration chamber. These are novel achievements in this field, however the interest of this technical note is to examine how fines content-sand content ratio (FC/S_dC) affect the compaction properties of soil and the empirical relationship to be developed would be based on regression analysis. The importance of this research is derived from the fact that no literature consulted have been found to carry out similar research and to have used lateritic soil for such. Besides this, previous particle size analysis carried out in most lateritic soils available in Nigeria showed that they have significant FC and S_dC and in most cases negligible gravel content (GC). Since the level of FC have been found to affect important properties of soil including soil composition, particle friction, compaction, moisture, and type of soil (Hveem, 2000; Ayodele et al., 2009), the authors wish to examine how the numerical properties of MDUW/OMC can be affected based on the ratio of fines content to sand content (FC/S_dC) present in the soil.

2. Materials and methods

2.1 Materials

Twenty (20) lateritic soils drawn from different sources were used in the research. The samples were collected from different parts of Anambra state of Nigeria. Anambra is a state located in the southern part of Nigeria. The state is bordered to the North by Kogi state, to the East by Enugu state, to the west by Delta state and to the South by Imo and Rivers states. The state is notable in Nigeria for its trading activities. It is host to the largest market in West Africa which is Onitsha main market. Figure 1 showed the map of Nigeria showing the location of Anambra state while Figure 2 showed full map of Anambra state with geographical coordinates.

The climatic classification of Anambra state based on Koppen Geiger classification is *Aw* which is a symbol used to denote tropical savannah climate with dry winter characteristics. The annual average temperature is 27.0 °C. The rainfall is around 1828 mm per year with much rainfall in summer than in winter (Climate-Data.org, 2020). The collected samples labeled 1 to 20 (including the sources) are shown in Table 1. The samples were packaged in polythene bags after collection to avoid moisture loss. They were transferred to

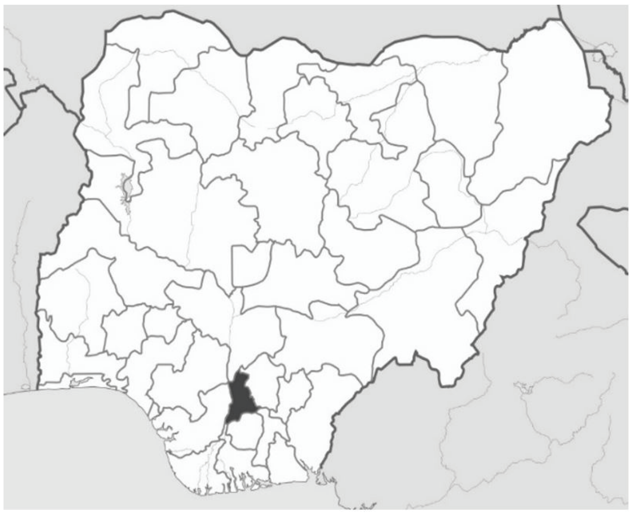

Figure 1. Anambra state in Nigeria (online Wikipedia content).

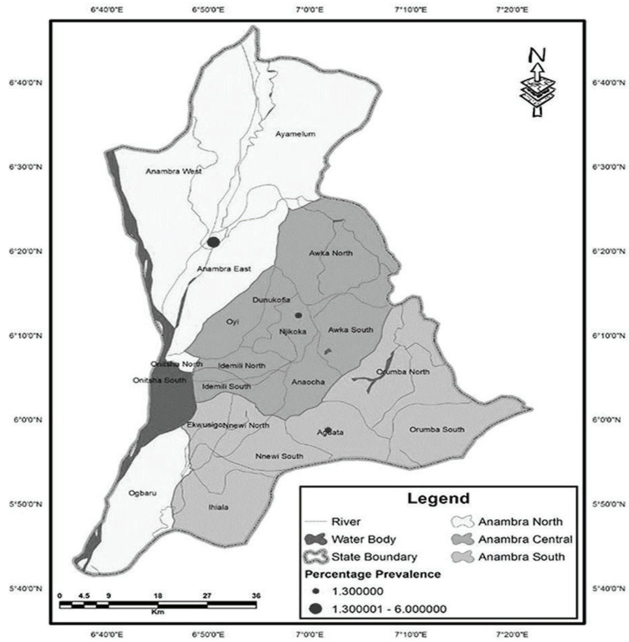

Figure 2. Map of Anambra State showing the geographical coordinates (Ndukwe et al., 2019).

Table 1. Sources of samples used in the work.

Samples	1 to 4	5 to 13	14 to 20
Sources	Mbamalu (2016)	Ozor (2017)	Anjorin (2016)

civil engineering laboratory of Nnamdi Azikiwe University, Awka for laboratory tests.

2.1.1 Sample preparation

Prior to compaction tests on the soils, the samples were first air-dried and clods were broken down. The whole gradation of each soil was used in the compaction tests because the soils do not have sizes greater than 4.75 mm.

2.2 Methods

The index properties of the soils were determined in accordance with BS (1990a). Three compactive efforts British Standard Light (BSL) BS (1990b), West African Standard (WAS), and British Standard Heavy (BSH) BS (1990b) corresponding to 605.90 kNm/m^3, 1009.82 kNm/m^3 and 2726.19 kNm/m^3 compaction energies respectively were used to obtain the compaction characteristics of the soils. Each compaction utilized the BS mould which has a volume of 1000 cm^3. The BSL compaction involves a 2.5 kg rammer falling through a height of 304.8 mm onto three (3) layers of soil in the BS mould, each layer receiving 27 blows of the rammer. The WAS compaction involves the use of 4.5 kg rammer falling through a height of 457 mm onto five (5) layers of soil, with each layer receiving 10 blows of the rammer (Osinubi & Nwaiwu, 2006). In the case of BSH compaction, the 4.5 kg rammer was made to fall through a height of 457 mm onto five (5) layers of soil, each layer receiving 27 blows of the rammer.

3. Results and discussion

3.1 Index and compaction characteristics of the soils

Table 2 showed the index and compaction characteristics of the twenty (20) lateritic soils used to develop the models. The soils fall into different classes according USCS. Samples 1 to 4 fall under (*SC*) which represented clayey sands. Samples 5 to 13 were classified as inorganic clay of low to medium plasticity *(CI* or *CL)* except sample 11 which was an inorganic silt of medium compressibility *(MI)*. Sample 14 was silty sand while the other remaining samples (15 to 20) were all clayey sands *(SC)*. These classes were typical of the constituents of laterite. The percentage fines for all the soil samples were less than 50% which is typical of most lateritic soils found in South-Eastern part of Nigeria. Figures 3 and 4 show the graphical distribution (bar chart) of MDUW and OMC respectively for the samples.

3.2 Linear relationships between MDUW/OMC and Log E

Figures 5 and 6 show the linear relationships between MDUW/OMC and log E. The slope and intercept obtained from the linear relationships were described using Figures 7 and 8, respectively. It was observed from the Figures 7 and 8 that when the slope became maximum, the intercept became minimum and vice versa. The R-squared values obtained from the relationship in Figures 5 and 6 were all significant with values ranging from 0.7424 to 0.9987 for MDUW (Average of 0.9325) and 0.7632 to 1 for OMC (Average of 0.9405). The equations used to describe the relationship were of the form shown in (1) and (2).

$$\gamma_{dmax} = m \log E + c \tag{1}$$

where γ_{dmax} is maximum dry unit weight; *m* is slope; E is compactive effort; *c* is intercept

$$W_{opt.} = n \log E + d \tag{2}$$

where w_{opt} is optimum moisture content; *n* is slope; E is compactive effort; *d* is intercept.

Table 2. Index and compaction characteristics of soils used to develop models.

SAMPLE	SG	PARTICLE SIZE DISTRIBUTION, %				ATTERBERG LIMITS, %			COMPACTION CHARACTERISTICS					
									British Standard Light (BSL)		West African Standard (WAS)		British Standard Heavy (BSH)	
		Fines Content (FC)	Sand Content (S_dC)	FC/SC	Gravel Content (GC)	Liquid Limit (LL)	Plastic Limit (PL)	Plasticity Index (PI)	MDUW, kN/m^3	OMC, %	MDUW, kN/m^3	OMC, %	MDUW, kN/m^3	OMC, %
1	2.45	38.11	61.17	0.623	0.72	39.5	21.32	18.18	17.46	13.5	17.85	13.5	19.03	13.2
2	2.51	37.45	62.33	0.6	0.22	35.2	24.6	10.6	18.73	13	18.79	12.5	19.23	12
3	2.61	40.7	59.15	0.688	0.15	36.3	27.3	15.97	17.76	15	18.1	14.5	18.54	14
4	2.6	38.18	60.77	0.628	1.045	36.6	23.7	14.15	18.83	12.2	19.23	12	19.52	9
5	2.69	39.82	60.18	0.661	0.11	31	17.8	13.2	17.6	14.4	18.6	13.5	20	12.8
6	2.58	36.03	63.97	0.563	0.14	35.5	23.2	12.3	17.82	13.8	18.72	12.5	21.05	11.5
7	2.62	32.12	67.88	0.473	0.05	34.5	22.2	12.3	18.55	11.6	19.53	11.5	20	10.8
8	2.64	22.04	77.96	0.282	0.12	27.7	15.7	12	18.32	11.8	19.8	11	20.52	9.3
9	2.62	40.46	59.34	0.681	0	36	23.1	12.9	17.78	15.8	18.87	13	19.89	11.5
10	2.66	42.43	57.57	0.737	3.2	37.8	20.1	17.7	16.95	16.5	17.7	15.8	20.2	14.4
11	2.62	40.03	59.97	0.667	3.01	47	30.5	16.5	16.8	17.5	17.95	17	18.6	14
12	2.68	25.04	74.96	0.334	8.88	35.5	18	17.5	18.6	11.2	20.1	10.7	21.05	8.5
13	2.68	31.25	68.75	0.454	0.65	35.5	17.5	18	17.17	13.3	19.38	12.5	20.2	11.5
14	2.48	35.93	63.93	0.562	0.14	51.3	32.55	18.75	18.07	13.8	18.8	12.3	20.46	11.2
15	2.55	19.79	80.21	0.246	0	28	15.98	12.02	19	12.8	18.97	10.4	20.1	8.4
16	2.51	30.09	69.87	0.43	0.04	40.5	19.49	21.01	19.28	12.4	20.03	11.5	20.2	9.5
17	2.59	35.87	64.05	0.563	0.08	24.4	13.37	11.03	18.85	12.4	19.3	11.2	19.65	9.4
18	2.49	25.28	74.72	0.338	0	20.9	8.58	12.32	19.45	11.8	19.71	9.8	20.31	9
19	2.46	27.76	65.56	0.423	6.68	23.6	13.21	10.39	18.84	12.4	19.18	11.5	19.95	8.8
20	2.42	27.75	72.25	0.384	0	22.25	15.78	6.47	19.39	12	19.76	10.1	20.21	9.6

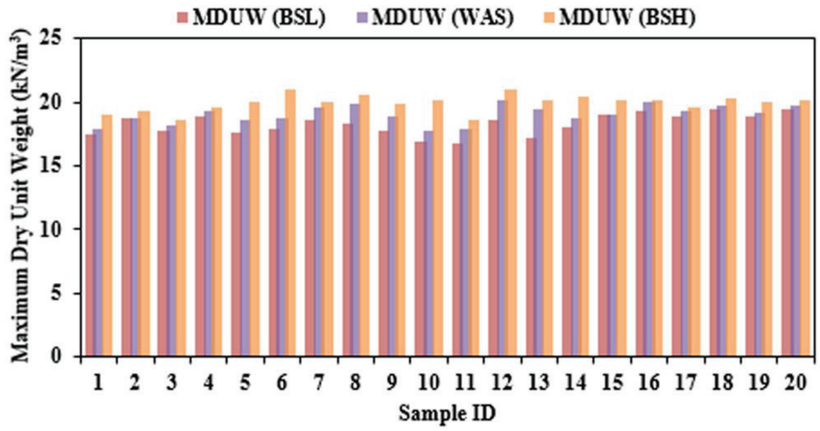

Figure 3. Distribution of maximum dry unit weight of the soils.

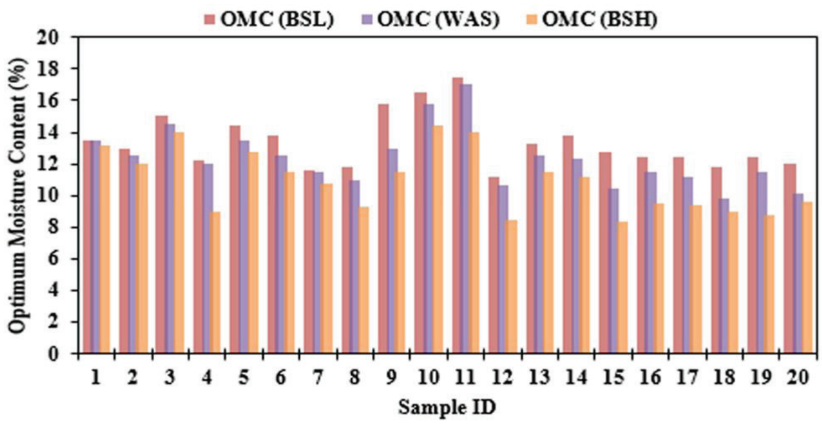

Figure 4. Distribution of optimum moisture content of the soils.

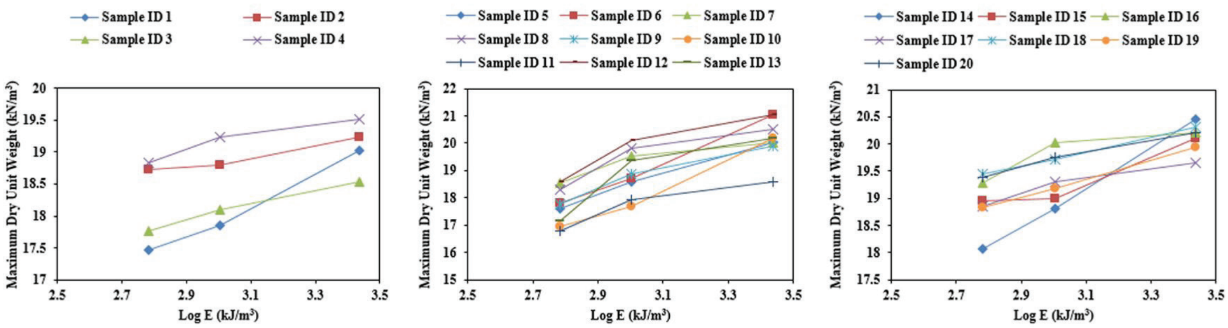

Figure 5. Linear relationship between maximum dry unit weight (MDUW) and log E.

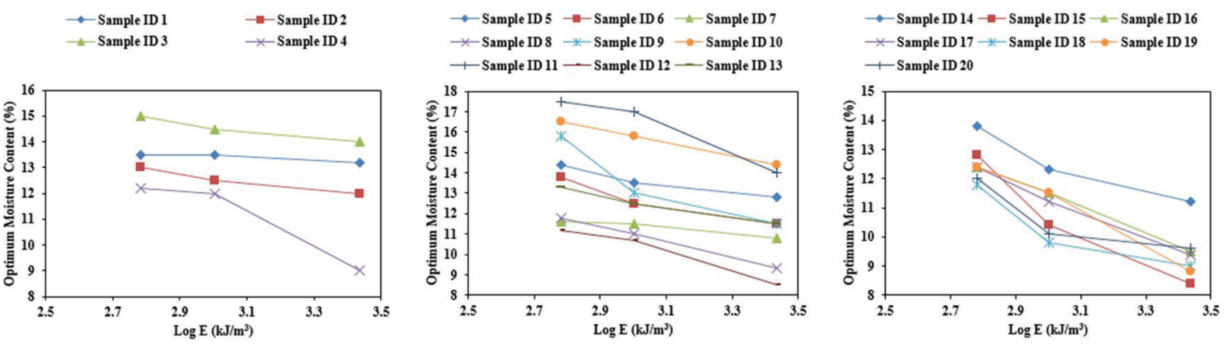

Figure 6. Linear relationship between optimum moisture content (OMC) and log E.

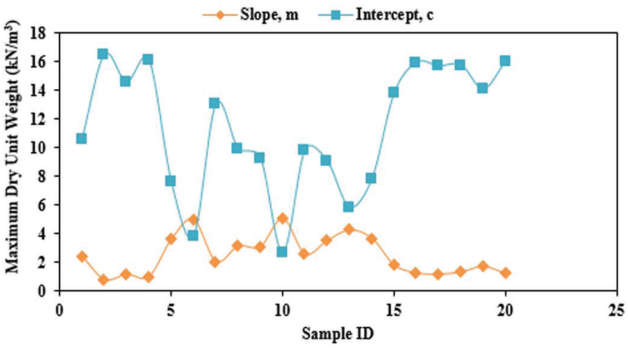

Figure 7. Graph of slope/intercept versus sample ID for MDUW.

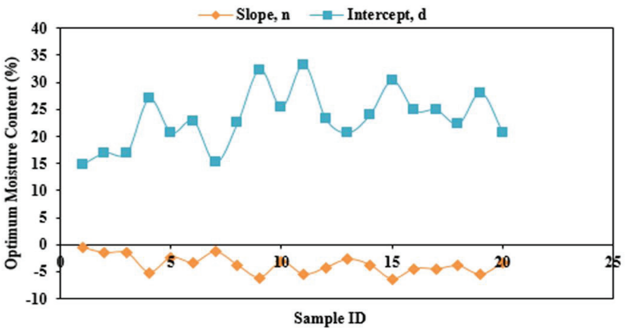

Figure 8. Graph of slope/intercept versus sample ID for OMC.

3.3 Relationship between MDUW/OMC versus Log E linear parameters and 'FC/S_dC'

Researches have shown that significant relationship exist between MDUW/OMC and index parameters such as LL, plastic limit (PL), plasticity index (PI), FC, and S_dC (Hassan et al., 2020) but to the authors' knowledge as noted elsewhere, no work found have sought to know the kind of relationship that exist between MDUW/OMC and 'FC/S_dC'. Benson et al. (1998) showed that stronger linear relationships exist between MDUW/OMC and log E which is also evident in the soils used (Figures 5 and 6).

In order to develop equations in which 'FC/S_dC' would be a function of slopes (m and n) and intercepts (c and d), the authors' sought to establish the relationship between 'm', 'c', 'n', 'd' and 'FC/S_dC', a ratio which can be obtained from easily measured quantities of FC and S_dC. The aim was to obtain a linear equation for 'm', 'c', 'n', and 'd'. The Equations 3 to 6 below were obtained from linear regression between 'm', 'c', 'n', 'd' parameters respectively with 'FC/S_dC' values for all soils where 'm', 'c', 'n', and 'd' represent independent parameters while 'FC/S_dC' represent dependent parameter. The combinations used would be too big to be outlined in the paper. The following equations were obtained from the regression analysis to describe the relationship between 'm', 'n', 'c', 'd' and 'FC/S_dC'

$$m = 1.73\left(FC / S_dC\right) + 1.60 \quad (3)$$

$$c = 15.83 - 8.58\left(FC / S_dC\right) \quad (4)$$

$$n = 3.07\left(FC / S_dC\right) - 5.26 \quad (5)$$

$$d = 23.59 - 0.39\left(FC / S_dC\right) \quad (6)$$

3.4 Application of equations

The Equations 3, 4, 5 and 6 developed above can be applied in two ways. First, it can be applied to determine compaction characteristics when only the 'FC/S_dC' is known. The MDUW/OMC for a given soil at a given compactive effort can be determined as follows:

$$\gamma_{d\,\max} = \left[1.73\left(FC / S_{dC}\right) + 1.6\right]\log E + 15.83 - 8.58\left(FC / S_dC\right) \quad (7)$$

$$w_{opt.} = \left[3.07\left(FC / S_dC\right) - 5.26\right]\log E + 23.59 - 0.39\left(FC / S_dC\right) \quad (8)$$

Alternatively, they can also be applied to determine MDUW/OMC for another compactive effort (E_u) when one compactive effort (E_k) and its corresponding MDUW/OMC ($\gamma_{dmax,k}$/$w_{opt,k}$) are known respectively. The following equations can be applied in this case.

$$\gamma_{d\,\max,u} = \gamma_{d\,\max,k} + \left[1.73\left(FC / S_dC\right) + 1.6\right]\log\left(E_u / E_k\right) \quad (9)$$

$$w_{opt,u} = w_{opt,k} + \left[3.07\left(FC / S_dC\right) - 5.26\right]\log\left(E_u / E_k\right) \quad (10)$$

Equations 9 and 10 would definitely have a wide application than (7) and (8) because it can be applied over other compactive efforts. It would be more precisely applied with respect to compactive efforts used to develop the models.

3.5 Validation of equations

The equations were validated for robustness using two Checks known as Checks A and B. Check A was done with data used in the development of the models while Check B was done with data that was not used in the development of the models. In Check A, one compactive effort (BSL) and 'FC/S_dC' were used to predict the MDUW for compactive efforts, WAS and BSH. Then, the 'FC/S_dC' only was used to predict the MDUW for same compactive efforts, WAS and BSH. The summary of predicted values for WAS only are shown in Table 3. Root mean square error (RMSE) was also provided in this Table to show the overall prediction accuracy. For Check A, the RMSE values range from 0.025 to 0.376 for MDUW and 0.005 to 0.469 for OMC for prediction using BSL and FC/S_dC. There is not significant margin between the range produced using this model and the model employing only FC/S_dC for WAS (Table 3). Generally, the lower the RMSE, the better the prediction accuracy. Similar precision were obtained when the values of BSH were predicted. It is expected that these predictions would give a good fit because the data were used to develop the models.

3.6 Discussion of results

The results were discussed based on the prediction outcome of MDUW/OMC and predicted errors from the two Checks carried out as shown in Tables 3 and 5. Figures 9-16

Table 3. Summary of results for Check A (WAS).

Sample ID	m, c, n, d calculated from 'FC/SC'				BSL and 'FC/S_dC'				FC/S_dC' only			
					predicted for WAS		Root Mean Square Error (RMSE)		predicted for WAS		Root Mean Square Error (RMSE)	
	m	c	n	d	MDUW	OMC	MDUW	OMC	MDUW	OMC	MDUW	OMC
1	2.678	10.485	-3.347	23.347	18.054	12.758	0.046	0.037	18.529	13.291	0.152	0.047
2	2.638	10.682	-3.418	23.356	19.315	12.242	0.117	0.058	18.607	13.088	0.041	0.131
3	2.790	9.927	-3.148	23.322	18.378	14.302	0.062	0.044	18.309	13.866	0.047	0.142
4	2.686	10.442	-3.332	23.345	19.425	11.461	0.044	0.121	18.512	13.336	0.161	0.299
5	2.744	10.159	-3.231	23.332	18.208	13.684	0.088	0.041	18.400	13.627	0.045	0.028
6	2.574	10.999	-3.532	23.370	18.391	13.017	0.074	0.116	18.732	12.762	0.003	0.059
7	2.418	11.772	-3.808	23.406	19.086	10.756	0.099	0.166	19.036	11.967	0.110	0.104
8	2.088	13.410	-4.394	23.480	18.783	10.826	0.227	0.039	19.682	10.280	0.026	0.161
9	2.778	9.987	-3.169	23.324	18.396	15.097	0.106	0.469	18.333	13.804	0.120	0.180
10	2.875	9.507	-2.997	23.303	17.587	15.836	0.025	0.008	18.143	14.298	0.099	0.336
11	2.754	10.107	-3.212	23.330	17.410	16.788	0.121	0.047	18.380	13.680	0.096	0.742
12	2.178	12.964	-4.235	23.460	19.083	10.261	0.227	0.098	19.506	10.739	0.133	0.009
13	2.385	11.935	-3.866	23.413	17.699	12.443	0.376	0.013	19.100	11.799	0.063	0.157
14	2.572	11.008	-3.535	23.371	18.640	13.017	0.036	0.160	18.735	12.753	0.015	0.101
15	2.026	13.719	-4.505	23.494	19.399	11.801	0.089	0.313	19.804	9.962	0.180	0.098
16	2.344	12.141	-3.940	23.422	19.800	11.527	0.051	0.006	19.182	11.587	0.190	0.019
17	2.574	10.999	-3.532	23.370	19.421	11.617	0.027	0.093	18.732	12.762	0.127	0.349
18	2.185	12.930	-4.222	23.458	19.934	10.864	0.050	0.238	19.493	10.774	0.049	0.218
19	2.332	12.201	-3.961	23.425	19.357	11.522	0.040	0.005	19.205	11.525	0.006	0.006
20	2.264	12.535	-4.081	23.440	19.892	11.095	0.030	0.222	19.337	11.181	0.095	0.242

In Check B, Six (6) different samples (Table 4) were used to validate the models. These soils fall under classes, clayey sands, *SC*, inorganic clay of low compressibility, *CI* and inorganic silt of medium compressibility, *MI* respectively based on USCS. Just as in Check A, RMSE values fall within close range and all values are low. The prediction outcome for WAS only was shown here (Table 5).

Table 4. Index properties of soil used to validate method.

Sample No	Measured MDUW (kN/m^3)			Measured OMC (%)			Fines Content (FC) %	Sand Content (SC) %	FC/SC (%)
	BSL	WAS	BSH	BSL	WAS	BSH			
S1	18.7	19.92	20.2	12.9	11.6	10	25.36	74.64	0.34
S2	18.25	20.4	20.52	10.2	9	8.5	26.05	73.95	0.352
S3	18.52	19.88	20.02	12.4	11.5	9.3	31.08	68.92	0.451
S4	18.72	20	20.07	11	10.8	9.2	29.37	70.63	0.416
S5	17.72	19.45	19.78	13.2	11.6	12	35	65.35	0.536
S6	18.09	19.8	20.06	12.5	10.7	10.5	29.65	70.35	0.421

Table 5. Summary of results for Check B (WAS).

Sample No.	m, c, n, d calculated from 'FC/SC'				BSL and 'FC/SC'				FC/SC' only			
					predicted for WAS		Root Mean Square Error (RMSE)		predicted for WAS		Root Mean Square Error (RMSE)	
	m	c	n	d	MDUW (kN/m^3)	OMC (%)	MDUW (kN/m^3)	OMC (%)	MDUW (kN/m^3)	OMC (%)	MDUW (kN/m^3)	OMC (%)
1	2.188	12.913	-4.216	23.457	19.185	11.965	0.164	0.082	19.486	10.792	0.097	0.181
2	2.209	12.810	-4.179	23.453	18.740	9.274	0.371	0.061	19.446	10.898	0.213	0.424
3	2.380	11.960	-3.875	23.414	19.048	11.541	0.186	0.009	19.111	11.772	0.172	0.061
4	2.320	12.261	-3.983	23.428	19.234	10.117	0.171	0.153	19.229	11.463	0.172	0.148
5	2.527	11.231	-3.614	23.381	18.280	12.399	0.262	0.179	18.823	12.523	0.140	0.206
6	2.328	12.218	-3.968	23.426	18.606	11.621	0.267	0.206	19.212	11.507	0.131	0.180

showed the comparison of measured and predicted values for MDUW/OMC using line of equality plots based on Table 3. The measured and predicted values are quite close to the line of equality which shows that there was not much wide difference between measured values and predicted values especially for OMC. The R-squared values obtained by line of best fit fall within 0.528 and 0.591 for MDUW with one exception and 0.653 and 0.842 for OMC.

The following were considered for discussion; the maximum error, minimum error, average error (mean error/ measure of bias) and the standard deviation (measure of precision) obtained from the prediction outcomes. These are shown in sections 3.6.1 and 3.6.2.

3.6.1 Check A

3.6.1.1 Prediction outcome for West African Standard (WAS)

When 'FC/S$_d$C' and a compactive effort are known, the maximum error for MDUW was 1.68 kN/m^3, the minimum error was -0.53 kN/m^3, the mean error or bias was 0.21 kN/m^3 and the standard deviation was 0.55 kN/m^3. For the OMC, the maximum error was 0.74%, the minimum error was -2.10%, the mean error was -0.21% while the standard deviation was 0.74%. From these results it can be seen that the variation that uses 'FC/S$_d$C' and one compactive effort is nearly unbiased and show minimal variability. When

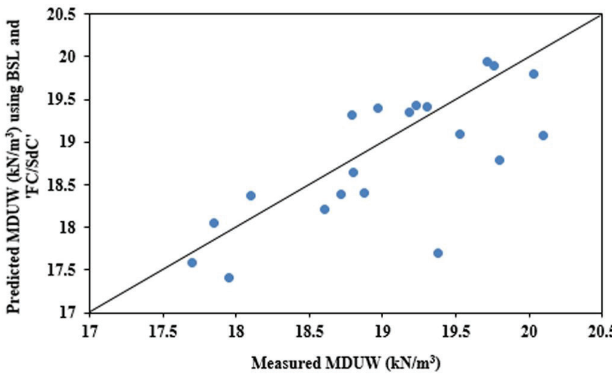

Figure 9. Relationship between measured values and predicted values of MDUW for WAS using BSL and 'FC/S$_d$C'.

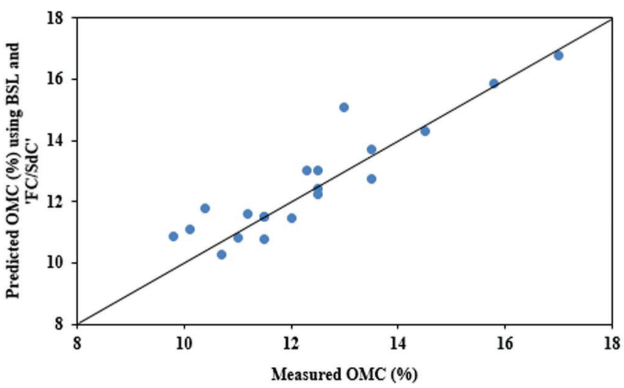

Figure 10. Relationship between measured values and predicted values of OMC for WAS using BSL and 'FC/S$_d$C'.

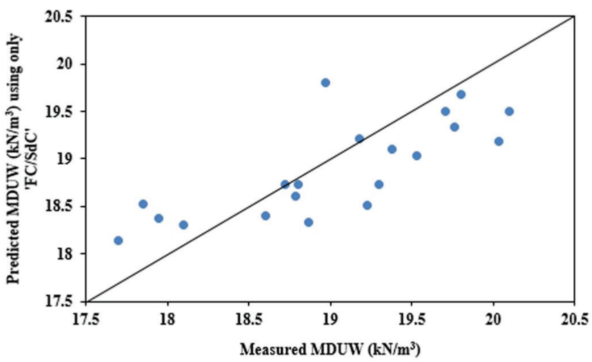

Figure 11. Relationship between measured values and predicted values of MDUW for WAS using only 'FC/S$_d$C'.

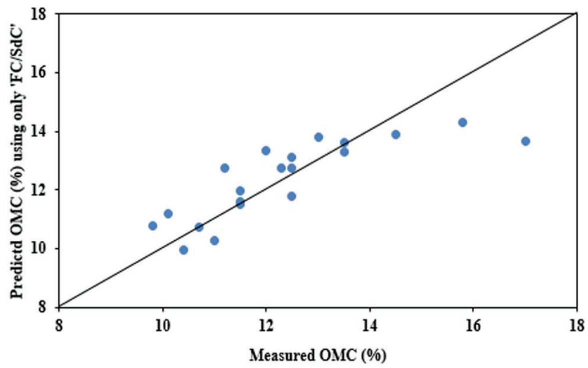

Figure 12. Relationship between measured values and predicted values of OMC for WAS using only 'FC/S$_d$C'.

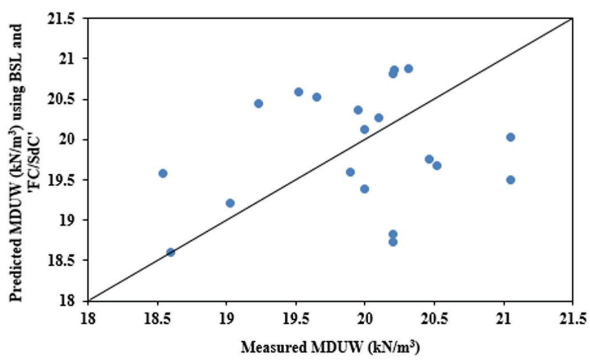

Figure 13. Relationship between measured values and predicted values of MDUW for BSH using BSL and 'FC/S$_d$C'.

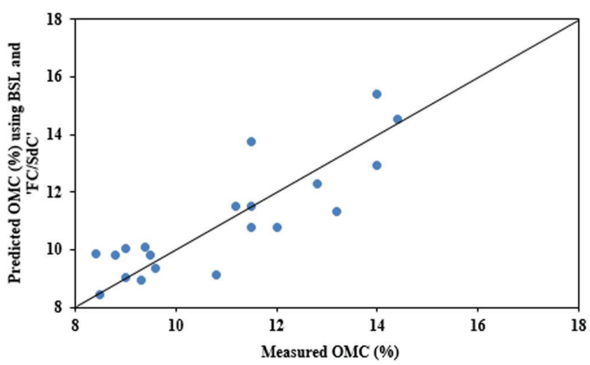

Figure 14. Relationship between measured values and predicted values of OMC for BSH using BSL and 'FC/S$_d$C'.

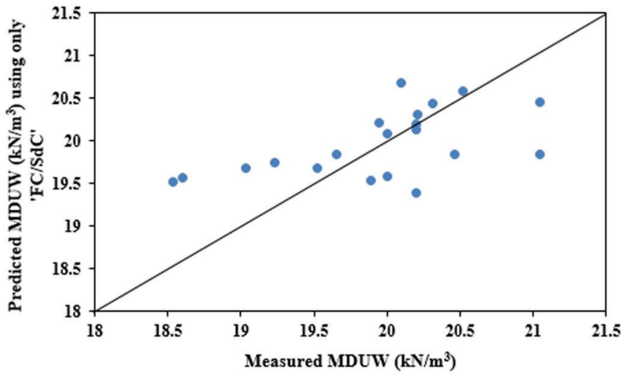

Figure 15. Relationship between measured values and predicted values of MDUW for BSH using only 'FC/S_dC'.

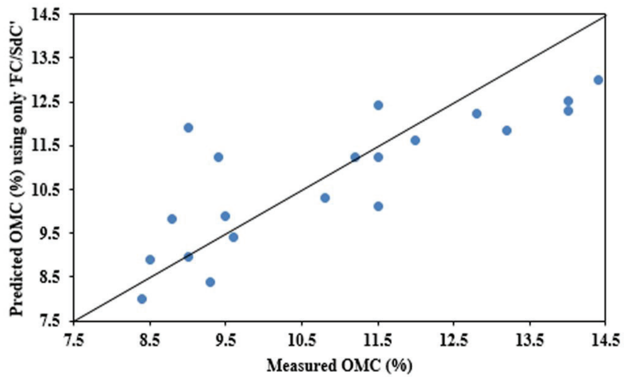

Figure 16. Relationship between measured values and predicted values of OMC for BSH using only 'FC/S_dC'.

only 'FC/S_dC' was used in the prediction, similar bias was also observed with almost the same range of standard deviation, the maximum error for MDUW was 0.85 kN/m^3, the minimum error was -0.80 kN/m^3, the mean error was 0.13 kN/m^3 while the standard deviation was 0.46 kN/m^3. For the OMC, the maximum error was 3.32%, the minimum error was -1.56%, the mean error was -0.01% while the standard deviation was 1.09%. The maximum error represents the maximum difference between predicted values and corresponding measured values while the minimum error represents the minimum difference between predicted values and corresponding measured values. The standard deviation shows how far the predicted values are from the mean. For MDUW, the standard deviation show low variation since it is less than 1 but for OMC, the variation is slightly high. The error values (maximum, mean and minimum) are in accordance with the most used compaction control values, that is, it is within the allowed variation, in projects or standards, for MDUW and for OMC. Similar prediction outcome was obtained for BSH.

3.6.2 Check B

3.6.2.1 Prediction outcome for West African Standard (WAS)

When using 'FC/S_dC' and BSL, the maximum error for MDUW was 1.66 kN/m^3, the minimum error was -0.74 kN/m^3, the mean error was 1.06 kN/m^3 while the standard deviation was 0.36 kN/m^3. For the OMC, the maximum error was 0.68%, the minimum error was -0.92%, the mean error was -0.29% while the standard deviation was 0.58%. Using only 'FC/S_dC' variation, the maximum error for MDUW was 0.95 kN/m^3, the minimum error was 0.43 kN/m^3, the mean error was 0.69 kN/m^3 while the standard deviation was 0.18 kN/m^3. For the OMC, the maximum error was 0.81%, the minimum error was -1.90%, the mean error was -0.63% while the standard deviation was 0.89%. The definition of maximum error, minimum error and standard deviation as shown in section 3.6.1 also applies here. The standard deviation for both MDUW and OMC are less than 1 which generally depicts low variation. However, MDUW was more distinct in this category. The error values (maximum, mean and minimum) are in accordance with the most used compaction control values, that is, it is within the allowed variation, in projects or standards, for MDUW and for OMC. Just as in Check A, the prediction outcome for BSH was also good with negligible differences.

4. Conclusion

Twenty (20) lateritic soils collected from different borrow pits in different parts of Anambra state in Nigeria were subjected to laboratory compaction tests using three common laboratory compaction methods namely: BSL, WAS and BSH. Linear regression was used to establish the relationships between MDUW/OMC, log E and 'FC/S_dC'. The equations obtained in these relationships were used to develop two models, one model based on one compactive effort and 'FC/S_dC' and the other model based on 'FC/S_dC' only. The models were used to predict MDUW/OMC when log E and 'FC/S_dC' were known for the twenty (20) soils used to develop the models. Six (6) other lateritic soils that were not used in the development of the models were used to validate the models. Owing to the variations in error values obtained which are within values mostly used in compaction controls, it would be accepted that the models are quite unbiased and robust. The models quite agree with similar work done by (Benson et al., 1998) using liquid limit for some clayey soils. For the model employing 'FC/S_dC' and one compactive effort for the prediction of BSH, standard (typical) errors of ±0.63 kN/m^3 and ±0.76% were observed for MDUW and OMC respectively while for the prediction of WAS, standard errors of ±0.39 kN/m^3 and ±0.52% were observed. This is quite precise and this model is preferred because it has wider application. For the model employing only 'FC/S_dC', standard errors of ±0.4 kN/m^3 and ±0.83% were observed for MDUW and OMC respectively for the prediction of BSH while the standard errors of ±0.33 kN/m^3 and ±0.77% for MDUW and OMC respectively were observed for the prediction of WAS. The note further shows how the fines content and sand content of soils influence their compaction behaviour. Even though these models are quite robust, it is recommended that the method should be checked against at least one series of compaction curve to ensure the result is acceptable for soils being used. The method should be limited to lateritic soils with 0.246 ≤ 'FC/S_dC' ≤ 0.737 and laterites with fines content less than 50%.

Acknowledgements

The authors wish to acknowledge the staff of geotechnics laboratory of Nnamdi Azikiwe University, Awka for their assistance in carrying out the laboratory tests.

Declaration of interest

There is no conflict of interest associated with the work.

Author's contributions

Charles M. O. Nwaiwu: Conceptualization and methodology. Ethelbert O. Mezie: Writing-reviewing and editing.

References

Aginam, C.H., Nwakaire, C., & Nwajuaku, A.I. (2014). Engineering properties of lateritic soils from Anambra central senatorial zone, Nigeria. *International Journal of Soft Computing and Engineering*, 4(6), 1-6.

Anjita, N.A., Christy, A.G., & Krishnankutty, S.V. (2017). Prediction of maximum dry density using Genetic Algorithm. International. *Journal of Engineering Research and Technology*, 6(3), 550-552.

Anjorin, J.R. (2016). *Compaction and compressibility behavior of some lateritic soils* [Unpublished master's thesis]. Nnamdi Azikiwe University.

Ardakani, A., & Kordnaeij, A. (2017). Soil compaction parameters prediction using *GMDH*-type neural network and genetic algorithm. *European Journal of Environmental and Civil Engineering*, 23(4), 449-462. http://dx.doi.org/10.1080/19648189.2017.1304269.

Ayodele, A.L., Falade, F.A., & Ogedengbe, M.O. (2009). Effects of fines content on some Engineering properties of Laterite soils in Ile-Ife. *Nigerian Journal of Engineering Research*, 14(1), 10-20.

Benson, C.H., Blotz, L.R., & Boutwell, G.P. (1998). Estimating optimum water content and maximum dry unit weight for compacted clays. *Journal of Geotechnical and Geoenvironmental Engineering*, 124(9), 907-912. http://dx.doi.org/10.1061/(ASCE)1090-0241(1998)124:9(907).

BS 1377-2. (1990a). *Methods of test for soils for civil engineering purposes: classification tests.* British Standards Institution, London.

BS 1377-4. (1990b). *Methods of test for soils for civil engineering purposes: compaction related tests.* British Standards Institution, London.

Chenari, R.J., Tizpa, P., Rad, M.R.G., Machado, S.L., & Fard, M.K. (2015). The use of index parameters to predict soil geotechnical properties. *Arabian Journal of Geosciences*, 8(7), 4907-4919. http://dx.doi.org/10.1007/s12517-014-1538-0.

Climate-Data.org. (2020). *Climatic data of Anambra state*. Retrieved in July 24, 2020, from https://en.climate-data.org/africa/nigeria/anambra

Gansonré, Y., Breul, P., Bacconnet, C., Benz, M., & Gourvès, R. (2019). Prediction of in-situ dry unit weight considering chamber boundary effects on lateritic soils using Panda penetrometer. *International Journal of Geotechnical Engineering*, 1-7. http://dx.doi.org/10.1080/19386362.2019.1698211.

Hassan, W., Ahmad, M., Farooq, A., Ajwad, A., Ali, H.Q., & Ilyas, Y. (2020). Correlation of maximum laboratory dry density and optimum moisture content of soil with soil parameters. *NCF-IEFR Journal of Engineering and Scientific Research*, 5, 1-6.

Hveem, F.N. (2000). Importance of clay in applied soil mechanics. *Clay and Clay Technology Bulletin*, 169, 191-195.

Jayan, J., & Sankar, N. (2015). Prediction of compaction parameters of soils using artificial neural network. *Asian Journal of Engineering and Technology*, 3(4), 369-375.

Mbamalu, F.C. (2016). *Compaction and strength of quarry dust-soil mixtures* [Unpublished master's thesis]. Nnamdi Azikiwe University.

Ndukwe, Y.E., Obiezue, R.N.N., Aguzie, I.O.N., Anunobi, J.T., & Okafor, F.C. (2019). Mapping of urinary schistosomiasis in Anambra State, Nigeria. *Annals of Global Health*, 85(1), 52. http://dx.doi.org/10.5334/aogh.2393.

Osinubi, K.J., & Nwaiwu, C.M.O. (2006). Compaction delay effects on properties of lime-treated soils. *Journal of Materials in Civil Engineering*, 18(2), 250-258.

Oyelakin, M.A., Mbamalu, C.F., Amolegbe, A.A., & Bakare, S.B. (2016). Empirical prediction of compaction parameters of soil of south-Eastern Nigeria based on linear relationship between liquid limit and compaction curve. *International Conference of Science, Engineering & Environmental Technology*, 1(9), 63-69.

Ozor, E.C. (2017). *Compaction behavior of coarse-grained lateritic soils* [Unpublished bachelor's thesis]. Nnamdi Azikiwe University.

Parkoh, E.A. (2016). *Prediction of compaction characteristics of lateritic soils in Ghana* [Unpublished master's thesis]. Near East University.

Ramiah, B., Viswanath, V., & Krishnamurthy, H. (1970). Interrealtionship of compaction and index properties. In *Proceedings of the 2nd South East Asian Conference on Soil Engineering* (pp. 577-587), Rotterdam, the Netherlands.

Ratnam, U.V., & Prasad, K.N. (2019). Prediction of compaction and compressibility characteristics of compacted soils. *International Journal of Applied Engineering Research*, 14(3), 621-632.

Ring, G., Sallberg, J., & Collins, W. (1962). Correlation of compaction and classification test data. *Highway Research Board Bulletin*, 325, 55-75.

Tenpe, A., & Kaur, S. (2015). Artificial neural network modeling for predicting compaction parameters based on index properties of soil. *International Journal of Scientific Research*, 4(7), 1198-1202.

List of symbols

γ_{dmax} Maximum Dry Unit Weight
w_{opt} Optimum Moisture Content
$\gamma_{dmax,u}$ Maximum Dry Unit Weight for unknown compactive effort
$\gamma_{dmax,k}$ Maximum Dry Unit Weight for known compactive effort
$w_{opt,u}$ Optimum Moisture Content for unknown compactive effort
$w_{opt,k}$ Optimum Moisture Content for known compactive effort
E Compactive effort
E_u Unknown compactive effort
E_k Known compactive effort
m Slope of maximum dry unit weight versus log of compactive effort
n Slope of optimum moisture content versus log of compactive effort
c Intercept of maximum dry unit weight versus log of compactive effort
d Intercept of optimum moisture content versus log of compactive effort
MDUW Maximum Dry Unit Weight
OMC Optimum Moisture Content
FC/S_dC Fines content-Sand content ratio
BSL British Standard Light
WAS West African Standard
BSH British Standard Heavy
LL Liquid Limit
PL Plastic Limit
PI Plasticity Index
S_dC Sand Content
GC Gravel Content
FC Fines Content
SG Specific Gravity
SC Clayey Sands
CI Inorganic clay of medium compressibility
CL Inorganic clay of low compressibility
MI Inorganic silt of medium compressibility
RMSE Root Mean Square Error

Soils and Rocks

An International Journal of Geotechnical and Geoenvironmental Engineering

www.soilsandrocks.com

ISSN 1980-9743
ISSN-e 2675-5475

Soil-water characteristic curve and permeability coefficient prediction model for unsaturated loess considering freeze-thaw and dry-wet

Yaling Chou[1#], Lijie Wang[1]

Article

Keywords
Unsaturated loess
Soil-water characteristic curve
Filter paper method
Permeability coefficient function
Freeze-thaw cycle
Dry-wet action

Abstract

The SWCC has played an important role in studying the physical-mechanical behavior and hydraulic property of unsaturated soils. Laboratory experiments of SWCC were performed on unsaturated loess based on filter paper method considering freeze-thaw cycle, coupling of freeze-thaw cycle and dry-wet action. The main results indicate that: (1) With the increase of freeze-thaw cycle or freeze-thaw and dry-wet coupling, the matric suction was logarithmically decreasing and the dry-wet path affected matric suction significantly. There were obvious hysteresis loops between the two SWCC curves of different dry-wet paths, which increased with the increase of water content. (2) The Gardner Model was more appropriate to describe the SWCC, and through measured SWCC from Gardner Model and Childs & Collis-George Model, the prediction model of unsaturated loess permeability coefficient was gained, which had an exponential relationship with matric suction and a power function relationship with volumetric water content, respectively. (3) The vertical distribution model of permeability coefficient under one-dimensional steady state flow was established. The vertical permeability coefficient gradually decreased from groundwater table to ground surface, it decreased first then increased and gradually stabilized with the increase of freeze-thaw cycle at the same depth of soil.

1. Introduction

The soil water characteristic curves (SWCCs) describe the relationship between soil water content (or saturation) and soil water potential (or suction), which is the basis to explain a variety of processes in unsaturated soils, ranging from transport phenomena to mechanical behaviors (Liu et al., 2012). Loess is widely distributed in northwestern China, and mainly concentrated in arid and semi-arid areas, belonging to unsaturated soil and seasonally frozen region. Therefore, the complex climatic environments including repeated freezing and thawing, evaporation and rainfall have a significant influence on the mechanical behavior of shallow unsaturated loess. And the physical and mechanical properties of shallow unsaturated loess have always been changing dynamically due to the disturbance of external climate. Especially, the roadbed, slope engineering, airport, water conservancy and other engineering projects are mostly in the shallow unsaturated zone, and are extensively exposed to the air. That is to say, most geotechnical projects are built in the unsaturated zone, which is located near the ground surface area forming the connection between weather systems above and saturated ground below, and interacts with the surrounding environment.

In the aspect of theoretical research, the scholars at home and abroad have made rich researches on SWCC,and a lot of useful conclusions were drawn (Bishop et al., 1960; Fredlund et al., 1994; Fredlund and Rahardjo, 1997). The SWCC reflecting the engineering mechanical properties and hydraulic property of unsaturated soil indicates the relationship between the matric suction and the volumetric water content of unsaturated soil, and is one of the constitutive relations explaining the mechanical properties of unsaturated soil. It is also of great significance for predicting and analyzing the hydraulic properties, shear strength and deformation characteristic of unsaturated soils, and is of important practical value for analyzing engineering problems such as slope stability evaluation and foundation deformation calculation (Chen, 1999; Wang et al., 2003; Xiong et al., 2005; Li et al., 2007; Lu and Cheng, 2007; Bai et al., 2011). Fredlund et al. (1994) established the permeability function of unsaturated soil by the SWCC. Vanapalli et al. (1996) and Fredlund et al. (1996) both studied the relationship between the SWCC and unsaturated soil strength. Sillers et al. (2001) systematically analyzed and evaluated various fitting models of SWCC. Liu et al. (2011) carried out a series of

[#]Correspondence author. E-mail address: chouyaling@lzb.ac.cn
[1]Lanzhou University of Technology, Key Laboratory of Disaster Prevention and Mitigation in Civil Engineering, Lanzhou, China.

Submitted on October 13, 2020; Final Acceptance on December 30, 2020; Discussions open until May 31, 2021.

DOI: https://doi.org/10.28927/SR.2021.058320

experiments by means of GCTS-type SWCC device for SWCC of remolded unsaturated loess specimen at different bulk densities under dry-wet cycle, and developed the concept named “degree of hysteresis” to study the SWCC hysteresis behavior of unsaturated loess. Zhao and Wang (2012) measured the SWCC of loess by Ku-pF apparatus and pressure plate extractors, as well as suggested the air entry value and residual water content. Also, the effects of dry density and dry-wet cycles on the SWCC of loess were analyzed through both experimental data and microstructure. Zhao et al. (2015) studied the effects of vertical stress and dry-wet cycles on SWCC of compacted unsaturated loess by using unsaturated soil oedometer. Liu and Ye (2015) studied the SWCC of unsaturated red clay by pressure plate instrument considering different influencing factors. Yang et al. (2016) used Tempe Membrane Gauge and Multifunctional SWCC Test Instrument to study the influences of drying-wetting cycle on SWCC of unsaturated clay considering consolidation pressure and compactness. Zhang et al. (2016) analyzed the effects of compactness and dry-wet cycles on the SWCC of silt soil in Eastern Henan, China. As far as permeability coefficient of unsaturated soil was concerned, Lian (2010; Lian et al., 2010) conducted penetration experiment of loess in Yangling Region of Shaanxi Province (in China) under the freeze-thaw cycles and confirmed that the freeze-thaw cycle had certain influence on the permeability and pore ratio of loess. Xiao et al. (2014) researched the effect of freeze-thaw on the permeability of loess. Liu et al. (2015) explored the SWCC under dry-wet cycles and predicted permeability coefficient of unsaturated loess.

In summary, most of the existing researches have focused on the effects of many impact factors such as water content, dry density, consolidation pressure, compactness and dry-wet cycles on SWCC. However, it is rarely noticed that the freeze-thaw action, coupling of freeze-thaw and dry-wet considering dry-wet path have effect on the matric suction of unsaturated loess. And the related research results on how the freeze-thaw cycle influences vertical distribution of unsaturated soil permeability coefficient have not been consulted. In view of the above analysis, this research has systematically studied how the freeze-thaw cycle, coupling of freeze-thaw and dry-wet action considering dry-wet path influence the matric suction and SWCC of unsaturated loess through laboratory experiments. At the same time, the Gardner Model, the Fredlund & Xing Model and the Van Genuchten Model were used to fit the SWCC under different experimental conditions, respectively. The applicability of each model was evaluated, and the Gardner Model was found to be more appropriate to describe the SWCC under the given experimental conditions. As a result, according to measured SWCC from Gardner Model, the relationship between the unsaturated soil permeability coefficient and the matric suction or volumetric water content was established by using Childs & Collis-George Model. Using this relationship, the vertical distribution model of unsaturated soil permeability coefficient with the one-dimensional steady state flow under different freeze-thaw cycles was obtained. The research results may play a significant role in the investigation on SWCC and permeability coefficient prediction model for unsaturated loess considering freeze-thaw cycle or coupling of freeze-thaw and dry-wet action.

2. Experimental method

The soil samples used in the experiment are remolded loess. The loess is taken from a foundation pit engineering in the Qilihe District of Lanzhou City in China, and the soil is obtained from 5.0m to 6.0m under the ground surface. Representative soil is taken through quarter diagonal sampling method, and the grain composition of the soil obtained by the screening test is shown in Table 1.

The basic physical parameters of the loess used in the experiment are: liquid limit 25.8%, plastic limit 16.7%, plasticity index 9.1, maximum dry density 1.82g/cm^3, optimum moisture content 15.6%, specific gravity of soil particles 2.72, saturated permeability coefficient 2.5×10^{-6} m/s. All the unsaturated remolded loess samples are obtained by manual compaction test, and soil material is passed through a 0.5mm standard sieve. The soil samples are prepared with water content of 10%, 12%, 14%, 16%, 18% and 20%, respectively. In order to make the water migrate evenly, the soil material is put into a sealed bag and sealed for 24 hours after mixing the soil evenly. The measured water content of soil samples are 9.75%, 11.45%, 13.60%, 15.85%, 17.57% and 19.33%, respectively. Dry density of all the prepared remolded samples is set as 1.60g/cm^3, and the error is controlled within 0.05 g/cm^3. The size of the soil samples is 2cm in height and 6cm in diameter.

This paper studies the effect of freeze-thaw action, coupling of freeze-thaw and dry-wet on SWCC of the unsaturated soil. Therefore, this research adopts an adjustable temperature refrigerator to simulate freeze-thaw cycle. In the test, the number of freeze-thaw cycles are set as 0, 1, 3, 5, 7 and 10 times, respectively. The prepared samples sealed with plastic wrap are put into the refrigerator and frozen for 12 hours (the temperature in the refrigerator is set as -17°C). After freezing, the samples are removed from the refrigerator and thawed at room temperature (17°C~20°C) for 12 hours to complete a whole freeze-thaw cycle. During

Table 1. Grain composition

Loess Soil	Particle size distribution (%)					
	>2mm	2~1mm	1~0.5mm	0.5~0.25mm	0.25~0.075mm	<0.075mm
Percent	9.5	4.8	10.7	11.4	31.9	31.7

the freezing-thawing process, the samples are in a closed state and no water is supplied from outside. In order to achieve the wetting and drying cycle, the natural air drying is used for dehydration and the titrated water injection is used for moisture absorption. There are two types of dry-wet paths. One of the dry-wet paths is first absorption and then desorption, which is named drying followed by wetting path. And another dry-wet path is first desorption and then absorption, which is called wetting followed by drying path. And the coupling times of freeze-thaw and dry-wet are set as 1, 2, 3 and 4 times respectively.

Under the above experimental conditions, the matric suction is measured by the filter paper method, which can be used to measure a large range of matric suction in the laboratory conveniently. According to the different contact degree between the filter paper and the soil, the filter paper method can be divided into direct contact method and non-contact method. The total suction of the soil is tested based on the non-contact method, and the direct contact method is used to measure matric suction. Herein, the contact method is adopted. The specific test steps are as follows. First, the filter papers are put into the oven and baked for 2 hours under temperature of 105°C, and then 3 pieces of baked filter paper are taken out with a tweezer. One filter paper is the measuring filter paper (diameter: 55mm), protected by the other two filter papers (diameter: 70mm). The measuring filter paper, weighed before and after each test by using an electronic balance (precision: 0.0001), is placed in the middle of the two protective filter papers, and the 3 pieces of filter paper are squeezed between two soil samples. The samples for measuring matric suction are sealed with adhesive tape and are placed in a sealed box for 7 days because the water between soil and filter paper will reach an equilibrium state after 7 days according to the related theory of unsaturated soil mechanics (Lu & Likos, 2012).

The Whatman's No.42 ash-free quantitative filter paper is adopted, and Equation 1 and Equation 2 give the calibration curves between water content and matric suction of filter paper under equilibrium state, respectively:

$$\log s = 2.909 - 0.0229 w_f, w_f \geq 47\% \quad (1)$$

$$\log s = 4.945 - 0.0673 w_f, w_f < 47\% \quad (2)$$

where, s is matric suction (kPa); w_f is equilibrium water content of filter paper (%).

3. Experimental results and discussion

3.1 Effect of freeze-thaw cycle on matric suction

Freeze-thaw cycle, one of the typical weathering processes, has remarkable influence on the physical-mechanical behavior and hydraulic property of unsaturated soils. When the initial dry density of remolded unsaturated loess is 1.60 g/cm³, the variation of the matric suction and its corresponding regression equation of soil samples with different water contents under freezing and thawing cycle are shown in Figure 1 and Table 2, respectively. Through the analysis of the experimental data, what can be seen from Figure 1 is that as the number of freeze-thaw cycle increases, the matric suction decreases gradually and tends to stabilize. As regards the soil samples with different water contents, the change of matric suction is the largest when freeze-thaw occurs once, and the variation amplitude of matric suction gradually decreases with the number of freeze-thaw cycle continuing to increase. After 7 freeze-thaw cycles, the matric suction basically tends to be stable. This happens mainly because the freeze-thaw action causes the ice crystals in the pores to expand, which makes the arrangement and connection of soil particles be changed and the initial soil structure be destroyed, and results in pores development and fissures formation. The fissures are generated among the soil particles, which leads to the adhesion of soil particles decreases and the water film among the soil particles disintegrates, so the matric suction in the soil decreases. As the number of freeze-thaw cycle continues to increase, the original structure is gradually damaged and a new relatively stable structure is slowly formed. Therefore, after 7 freeze-thaw cycles, the effect of freeze-thaw on the matric suction tends to be stable. It can be seen from Table 2 that the changing process of matric suction with the number

Table 2. Regression equation of matric suction and freeze-thaw cycles

Water content (%)	Regression equation	R^2
9.75	y=209.313-49.119ln(x+0.037)	0.9747
11.45	y=54.364-4.426ln(x+0.003)	0.9196
13.60	y=43.728-4.333ln(x+0.181)	0.9062
15.85	y=35.791-4.394ln(x+0.109)	0.8710
17.57	y=17.834-1.832ln(x+0.007)	0.9141
19.33	y=8.351-3.222ln(x+0.082)	0.8599

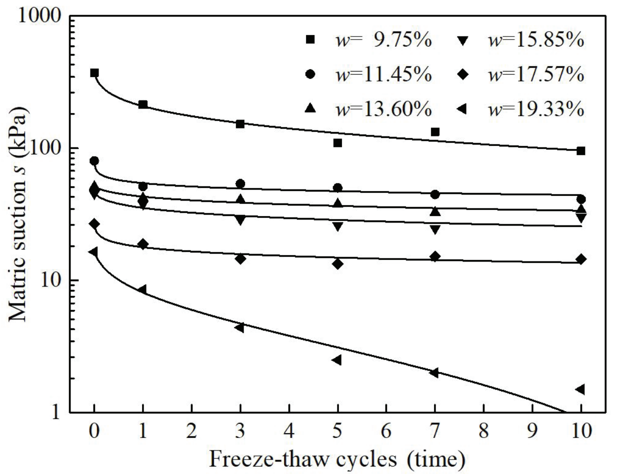

Figure 1. The relation between matric suction and freeze-thaw cycles.

of freeze-thaw cycles follows logarithmic curve and the correlation coefficient reaches significant level.

3.2 Effect of coupling of freeze-thaw and dry-wet on matric suction

In northwestern China, the climate experiences dry-wet alternation and freeze-thaw cycle repeatedly, and this has a significant influence on the mechanical behavior of shallow unsaturated soil. According to the previous research results, various dry-wet paths have obvious effect on the matric suction of unsaturated soil. Under the same water content, the matric suction under drying followed by wetting path would be greater than that under wetting followed by drying, which indicates that different dry-wet paths lead to different strengths of unsaturated soil. The variation of the matric suction and its corresponding regression equation of soil samples under coupling of freeze-thaw and dry-wet considering different dry-wet paths are shown in Figure 2 and Table 3, respectively.

It can be seen from Figure 2 that when studying the effect of the coupling of freeze-thaw and dry-wet on the matric suction, different dry-wet action paths similarly have a certain influence on the matric suction of the unsaturated remolded loess. In general, for the soil samples with the same water content, the matric suction under the path of drying followed by wetting is slightly larger than that under the path of wetting followed by drying. When the coupling of freeze-thaw and dry-wet is once, the change of matric suction is the largest, and the variation amplitude becomes smaller and tends to stabilize with the increase of coupling number. This conclusion is consistent with the research results of the literature (Qi et al., 2005), which pointed the first freeze-thaw cycle had the greatest influence on soil properties and there was little effect on soil after 3-5 freeze-thaw cycles. And the matric suction changing with the coupling of freeze-thaw and dry-wet cycle follows logarithmic curve and the correlation coefficient reaches a significant level (Table 3).

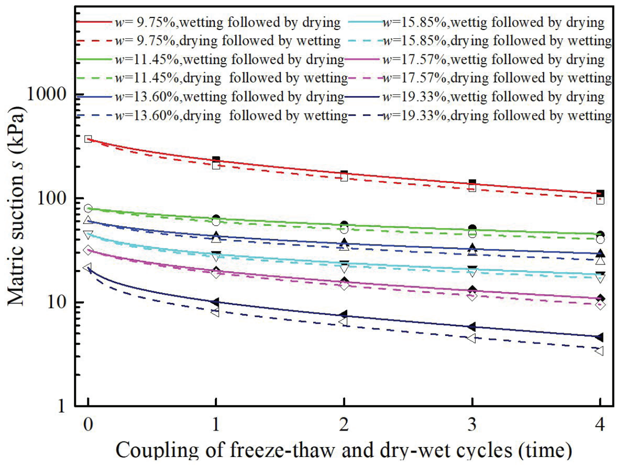

Figure 2. The relation between matric suction and coupling of freeze-thaw and dry-wet.

3.3 SWCC curve fitting

3.3.1 SWCC fitting model

In order to attain unsaturated soil permeability coefficient model from limited experimental data or predict the permeability coefficient equation from conventional constitutive equations especially SWCC model, researchers have developed many mathematical models. Three kinds of SWCC models, including Gardner equation, Fredlund & Xing equation and Van Genuchten equation, commonly used in geotechnical engineering are introduced to predict the permeability coefficient equation.

1. Gardner equation

$$\theta_w = \theta_r + \frac{\theta_s - \theta_r}{1 + \left(\frac{\psi}{a}\right)^b} \tag{3}$$

where, θ_w is volumetric water content (%); θ_s and θ_r are the saturated and residual volumetric water content (%), respectively; ψ is the matric suction (kPa) ; *a* is a parameter related to the air entry value (kPa) ; *b* is a parameter related to the soil dehydration rate when the matric suction is larger than the air entry value.

Table 3. Regression equation of matric suction and freeze-thaw/dry-wet cycles

Dry-wet path	Water content (%)	Regression equation	R^2
wetting followed by drying	9.75	y=222.557-86.674ln(x+0.179)	0.9083
	11.45	y=65.194-16.705ln(x+0.412)	0.9013
	13.60	y=43.056-12.144ln(x+0.238)	0.9228
	15.85	y=28.246-7.881ln(x+0.110)	0.9059
	17.57	y=20.747-7.787ln(x+0.242)	0.9157
	19.33	y=8.336-3.397ln(x+0.021)	0.9012
drying followed by wetting	9.75	y=258.952-101.156ln(x+0.328)	0.9089
	11.45	y=73.638-18.295ln(x+0.709)	0.8981
	13.60	y=46.268-11.554ln(x+0.292)	0.9267
	15.85	y=30.039-8.056ln(x+0.145)	0.9159
	17.57	y=21.905-7.577ln(x+0.271)	0.9078
	19.33	y=10.343-4.043ln(x+0.063)	0.9095

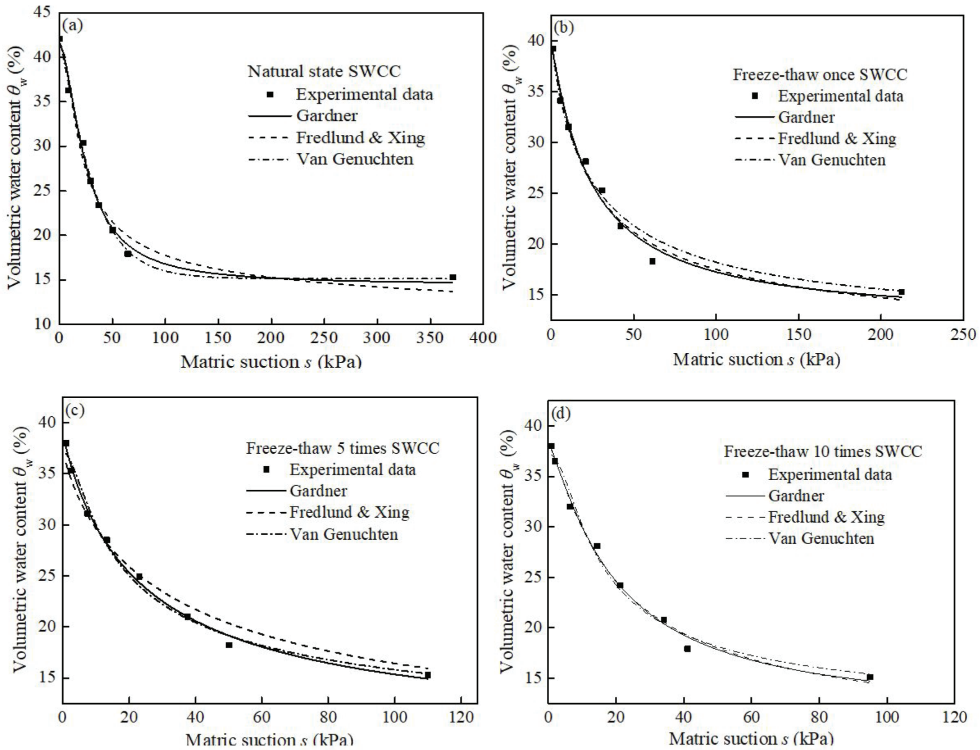

Figure 3. Function fitting for SWCC of different freeze-thaw cycles: (a) Natural state; (b) Freeze-thaw once; (c) Freeze-thaw 5 times; (d) Freeze-thaw 10 times.

2. Fredlund & Xing equation

$$\theta_w = \frac{\theta_s}{\left\{\ln\left[e+\left(\frac{\psi}{a}\right)^b\right]\right\}^c} \tag{4}$$

where, c is a parameter related to residual water content; e=2.71828, and the other letters represent the same meanings as Formula 3.

3. Van Genuchten equation

$$\theta_w = \theta_r + \frac{\theta_s - \theta_r}{\left[1+(a\cdot\psi)^b\right]^c} \tag{5}$$

where, the letters represent the same meanings as Formula 3 and Formula 4, respectively.

3.3.2 SWCC model fitting under freeze-thaw action

The Gardner Model, the Fredlund & Xing Model and the Van Genuchten Model are used to fit the measured matric suction under different freeze-thaw cycles, respectively. The experimental data and fitting curve are shown in Figure 3. The fitting parameters of each model equation under different freeze-thaw cycles are shown in Table 4, respectively. Due to space constraints, the experimental results of freeze-thaw for 0, 1, 5, and 10 times are only highlighted because there are generally similar rules under other freeze-thaw cycles. In general, the fitting effect of the Gardner Model is the best. The Van Genuchten Model has the second fitting effect, and the Fredlund & Xing Model has a slightly worse fitting effect.

3.3.3 SWCC function fitting under coupling of freeze-thaw and dry-wet cycle

In the same way, these three typical theoretical models including Gardner Model, Fredlund & Xing Model and Van Genuchten Model are used to fit the experimental data under coupling of freeze-thaw cycle and dry-wet alternation considering dry-wet paths, respectively. The fitting results are shown in Figure 4 and the fitting parameters of each model equation are shown in Table 5, respectively. Similarly, in order to save space, the experimental results of freeze-thaw and dry-wet coupling for 1, 4 times are listed in Table 5. Through comparative analysis, the fitting effect of the Gardner Model is the best. The Van Genuchten Model has the second fitting effect, and the Fredlund & Xing Model has a slightly worse fitting effect, too.

3.4 Prediction of unsaturated permeability coefficient

According to the above fitting rules of SWCC under different experimental conditions, it is concluded that the experimental data are fitted by using Gardner Model, which has the best fitting effect. Therefore, the experimental SWCC is obtained in line with the Gardner Model fitting. The permeability coefficient of unsaturated soil is not constant, and it is a function of matric suction. With the use of permeability

Table 4. The fitting values of parameters

Engineering conditions	Model types	*a*	*b*	*c*	θ_r	θ_s	R^2
Natural state	Gardner	25.062	1.700		14.442	41.416	0.9329
	Fredlund & Xing	10.852	2.035	0.562		41.576	0.9101
	Van Genuchten	0.005	1.240	10.215	15.127	41.772	0.9404
Freeze-thaw once	Gardner	24.345	1.080		12.389	39.585	0.9300
	Fredlund & Xing	9.656	1.149	0.781		39.688	0.9255
	Van Genuchten	0.034	0.826	1.120	11.518	40.836	0.9101
Freeze-thaw 5 times	Gardner	24.202	0.9189		8.888	39.140	0.9422
	Fredlund & Xing	16.379	0.844	1.199		37.488	0.9085
	Van Genuchten	0.146	1.834	0.238	6.183	37.195	0.9276
Freeze-thaw 10 times	Gardner	19.596	1.210		11.231	38.338	0.9391
	Fredlund & Xing	9.443	1.266	0.867		38.348	0.9373
	Van Genuchten	0.129	2.182	0.295	9.999	37.191	0.9219

Table 5. The fitting values of parameters

Dry-wet path	Engineering conditions	Model types	*a*	*b*	*c*	θ_r	θ_s	R^2
Absorption before desorption	Coupling once	Gardner	22.641	1.087		12.671	39.770	0.9330
		Fredlund & Xing	5.167	0.823	0.813		41.034	0.8864
		Van Genuchten	0.004	0.893	7.234	14.673	40.134	0.9152
	Coupling 4 times	Gardner	17.512	0.919		10.362	39.126	0.9365
		Fredlund & Xing	5.937	1.001	0.882		38.981	0.9263
		Van Genuchten	0.082	1.200	0.677	9.145	36.598	0.8791
Desorption before absorption	Coupling once	Gardner	22.421	1.297		13.290	40.189	0.9380
		Fredlund & Xing	9.550	1.143	0.814		40.869	0.9282
		Van Genuchten	0.049	0.961	0.831	11.803	41.698	0.8695
	Coupling 4 times	Gardner	14.567	1.137		11.795	40.353	0.9416
		Fredlund & Xing	6.194	1.026	0.995		41.051	0.9275
		Van Genuchten	22.421	1.297		13.290	40.189	0.9380

coefficient on Childs & Collis-George Model, the relationship between permeability coefficient and matric suction is built on the experimental SWCC. The SWCC is divided into *m* equal parts along the volumetric water-content axis, and the unsaturated permeability coefficient $k(\theta)_i$ is calculated by using the matric suction of each equal part's midpoint according to the following formula.

$$k(\theta)_i = \frac{k_s}{k_{sc}} A_d \sum_{j=i}^{m} \left[(2j+1-2i)(u_a-u_w)_j^{-2} \right] \tag{6}$$

$$i = 1, 2, \cdots, m$$

where, $k(\theta)_i$ is permeability coefficient determined by volumetric water content $(\theta)_i$ corresponding to the midpoint of *i*-th segment (m/s); k_s is the measured saturated permeability coefficient (m/s), and it is 2.5×10^{-6} m/s; k_{sc} is the calculated saturated permeability coefficient (m/s); A_d is the adjustment constant ($m \cdot s^{-1} \cdot kPa^2$); *i* is segment number; *j* is a number from *i* to *m*; *m* is the total number of segments from the saturated volumetric water content θ_s to the lowest volumetric water content θ_L on the soil-water characteristic curve (That is, *m*=20); $(u_a-u_w)_j$ is matric suction value corresponding to the midpoint of the *j*-th segement (kPa); And A_d is obtained by Formula 7.

$$A_d = \frac{T_s^2 \rho_w g}{2\mu_w} \frac{\theta_s^p}{N^2} \tag{7}$$

where, T_s is the surface tension of water (kN/m); ρ_w is the density of water (kg/m³); g is the acceleration of gravity (m/s²); μ_w is the absolute viscosity of water (N·s/m²); θ_s is the saturated volumetric water content (%); p is the constant considering the interaction between pores of different sizes, set as 2.0 (Green & Corey); *N* is the total number of segments between saturated volumetric water content and zero volumetric water content (θ_w=0), $N = m\left[\theta_s / (\theta_s - \theta_L)\right], m \le N$.

And k_{sc} in Formula 6 is obtained from Formula 8.

$$k_{sc} = A_d \sum_{j=i}^{m} \left[(2j+1-2i)(u_a-u_w)_j^{-2} \right] \tag{8}$$

$$i = 0, 1, 2, \cdots m$$

where, $(u_a-u_w)_j$ is the matric suction value corresponding to the midpoint of the *j*-th segement (kPa); the other letters represent the same meanings as Formula 6 and Formula 7, respectively.

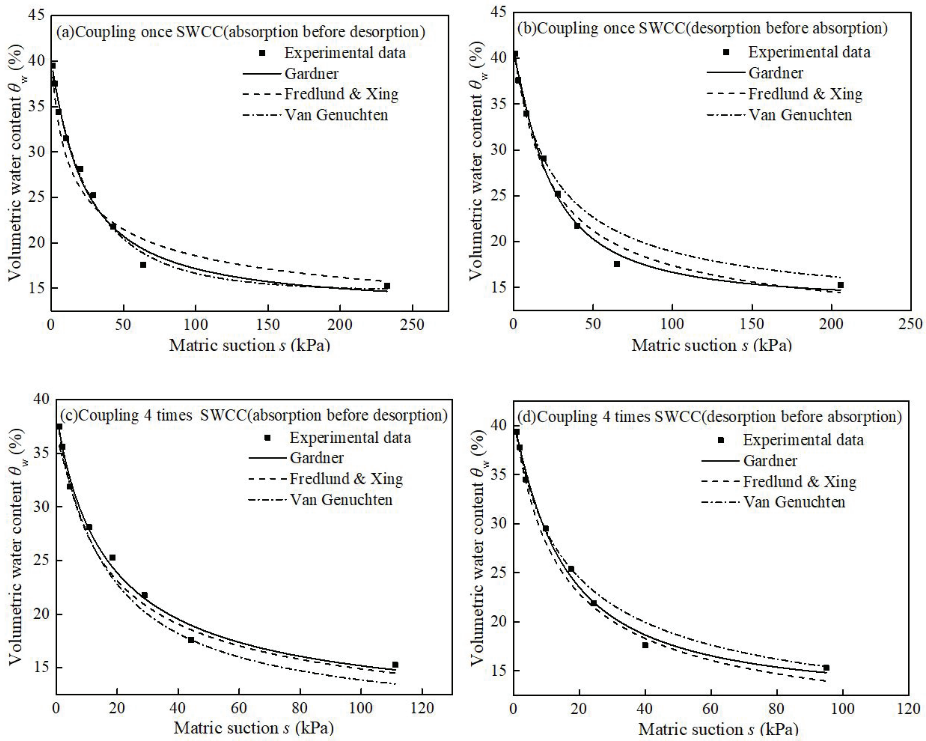

Figure 4. Function fitting for SWCC of different coupling of freeze-thaw and dry-wet: (a) Coupling once and absorption before desorption; (b) Coupling once and desorption before absorption; (c) Coupling 4 times and absorption before desorption; (d) Coupling 4 times and desorption before absorption.

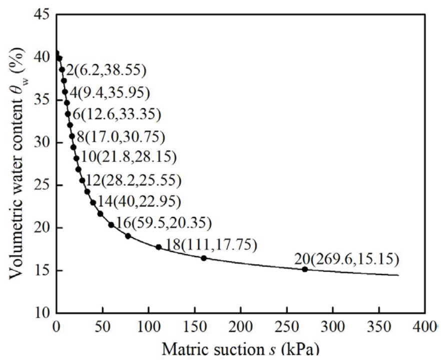

Figure 5. The predicting method of permeability coefficients based on soil-water characteristic curve.

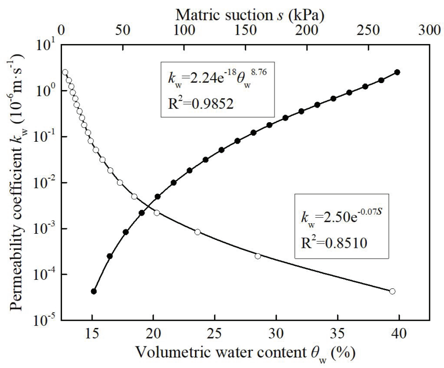

Figure 6. The permeability coefficient function.

The SWCC fitted based on the Gardner Model according to the experiment data is shown in Figure 5. When the experimental temperature is 20°C, the surface tension of water is that $T = 7\ 28 \times 10^{-}\ kN/m$; absolute viscosity of water is that $\mu_w = 100.5 \times 10^{-5} N \cdot s \cdot m^{-2}$; and the minimum volumetric water content on the SWCC obtained from the experiment is that $\theta_L = 14.5\%$; by calculating, $N = 32$, $A_d = 4.14 \times 10^{-2} m \cdot s^{-1} \cdot kPa^2$, $k_{sc} = 3.31 \times 10^{-2} m \cdot s^{-1}$, $k_s / k_{sc} = 7.55 \times 10^{-5}$, respectively, which are used to calculate all unsaturated permeability coefficient subsequently. The permeability coefficients calculated by the matric suction at the midpoint of each equal part are shown in Table 6.

Based on the above analysis, the changes of permeability coefficient with matric suction and volumetric water content are given in Figure 6, respectively. It can be seen that the relationship between the permeability coefficient and the matric suction can be expressed by an exponential function, and the permeability coefficient decreases sharply with the matric suction increases. And the relationship between the permeability coefficient and the volumetric water content can be expressed in the form of a power function formula.

The regression equations between the unsaturated permeability coefficient and the matric suction as well as the volumetric water content are expressed by Formula 9 and Formula 10, respectively.

$$k_w = \left(2.50 \times 10^{-6}\right) e^{-0.07s} \quad (9)$$

Table 6. The calculated permeability coefficients under different matric suctions

Interval i	Volumetric water contents $(\theta)_i$ (%)	Matric suctions u_a-u_w (kPa)	Permeability coefficients $k(\theta)_i$ (m/s)
1	39.85	3.2	2.500×10^{-6}
2	38.55	6.2	1.669×10^{-6}
3	37.25	8.3	1.224×10^{-6}
4	35.95	9.4	9.063×10^{-7}
5	34.65	11.5	6.690×10^{-7}
6	33.35	12.6	4.906×10^{-7}
7	32.05	14.9	3.532×10^{-7}
8	30.75	17.0	2.543×10^{-7}
9	29.45	18.7	1.779×10^{-7}
10	28.15	21.8	1.213×10^{-7}
11	26.85	24.0	8.017×10^{-8}
12	25.55	28.2	5.107×10^{-8}
13	24.25	33.6	3.132×10^{-8}
14	22.95	40	1.827×10^{-8}
15	21.65	47.8	9.946×10^{-9}
16	20.35	59.5	4.942×10^{-9}
17	19.05	77.8	2.189×10^{-9}
18	17.75	111	8.350×10^{-10}
19	16.45	160	2.511×10^{-10}
20	15.15	269.6	4.300×10^{-11}

where, k_w is the unsaturated permeability coefficient ($m \cdot s^{-1}$); s is the matric suction (kPa).

$$k_w = \left(2.24 \times 10^{-6}\right) e^{-18} \theta_w^{8.76} \tag{10}$$

where, k_w is the unsaturated permeability coefficient ($m \cdot s^{-1}$); θ_w is the volumetric water content (%).

3.5 Vertical distribution model of permeability coefficient of one-dimensional steady flow unsaturated soil

Due to the vertical joints and pore development of loess, the permeability coefficient of loess is anisotropic and the vertical permeability coefficient is significantly larger than the horizontal permeability coefficient. Therefore, for the construction of the loess engineering, it is of great significance to study the vertical permeability coefficient of unsaturated loess. It is known that the vertical unsaturated flow can be expressed by Darcy's Law under steady state. The water flow flowing downward is set as negative sign and flowing upward is set as positive sign, and the specific discharge expression in the vertical direction is by Formula 11.

$$q = -k_w \left[\frac{d\left(u_w - u_a\right)}{\gamma_w dy} + 1 \right] \tag{11}$$

where, q is specific discharge ($m \cdot s^{-1}$); γ_w is the bulk density of water (kN / m^3); y is the position from water table in vertical direction (m); the other letters represent the same meanings as above, respectively.

The water table is set as $y = 0$, and y above the water table is positive. By boundary condition that when $y = 0$, the matric suction is 0, and the distribution model of the matric suction along the direction y is derived from the Formula 9 and Formula 11 as follows:

$$0.07s = -\ln\left[\left(1 + \frac{q}{2.50 \times 10^{-6}}\right) e^{-0.07\gamma_w \cdot y} - \frac{q}{2.50 \times 10^{-6}}\right] \tag{12}$$

where, the letters represent the same meanings as above, respectively.

By substituting Equation 12 into Equation 9, the expression of one-dimensional steady state unsaturated permeability coefficient distributed vertically in the natural engineering condition is derived as Formula 13.

$$\begin{aligned} k_y &= \left(2.50 \times 10^{-6}\right) e^{\ln\left[\left(1 + \frac{q}{2.50 \times 10^{-6}}\right) e^{-0.07\gamma_w \cdot y} - \frac{q}{2.50 \times 10^{-6}}\right]} \\ &= \left(2.50 \times 10^{-6}\right) \left[\left(1 + \frac{q}{2.50 \times 10^{-6}}\right) e^{-0.07\gamma_w \cdot y} - \frac{q}{2.50 \times 10^{-6}}\right] \end{aligned} \tag{13}$$

where, k_y is vertical permeability coefficient ($m \cdot s^{-1}$); the other letters represent the same meanings as above, respectively.

Similarly, the expression of one-dimensional steady state unsaturated permeability coefficient distributed vertically under the experimental condition of one freeze-thaw cycle is derived as Formula 14.

$$k_y = \left(1.69 \times 10^{-6}\right) \left[\left(1 + \frac{q}{1.69 \times 10^{-6}}\right) e^{-0.1\gamma_w \cdot y} - \frac{q}{1.69 \times 10^{-6}}\right] \tag{14}$$

where, the letters represent the same meanings as above, respectively.

The expression of one-dimensional steady state unsaturated permeability coefficient distributed vertically under the experimental condition of 10 freeze-thaw cycles is derived as Formula 15.

$$k_y = \left(3.24\times 10^{-6}\right)\left[\left(1+\frac{q}{3.24\times 10^{-6}}\right)e^{-0.03\gamma_w \cdot y} - \frac{q}{3.24\times 10^{-6}}\right] \quad (15)$$

where, the letters represent the same meanings as above, respectively.

By using the vertical distribution models of unsaturated permeability coefficient under the above different experimental conditions to calculate and analyze, the results are shown in Figure 7. The calculating soil layer is homogeneous soil layer with a thickness of 10m, water table $y = 0m$, the earth's surface $y = 10m$, specific discharge $q = -3.14\times 10^{-8}\, m\cdot s^{-1}$.

As can be seen from Figure 7, the permeability coefficients distributed vertically of unsaturated loess under different freeze-thaw cycles have the same trend as that in the natural condition. That is, the permeability coefficient from the water table to the ground surface shows a decreasing trend. After undergoing the freeze-thaw action, the vertical permeability coefficient of the soil has been reduced by 1 or 2 orders of magnitude. The vertical permeability coefficient at the same depth of soil layer shows the law of decreasing first, then increasing and tending to be stable with the number of freeze-thaw increasing. Mainly because the loess has the features of vertical joint developing, large pores, loose structure and weak cementation, when the water in the soil freezes to form the ice crystals and the soil volume expands, there is enough pore space among the particles caused by frost heave and the soil structure will be strongly damaged. At the same time, the ice crystals formed during the freezing process have a pressure effect on the soil particles, which makes the particles to compact with each other, so the void ratio decreases and accordingly the permeability coefficient increases. For unsaturated soil, the pore water exists as adsorbed water films on the soil particles, so a smaller void ratio results in a greater permeability coefficient under the same matric suction. With the continuous increase of the number of freeze-thaw, the effect of freeze-thaw action on soil particles and structures becomes weakened and the void ratio tends to be stable, which makes the permeability coefficient tend to be stable.

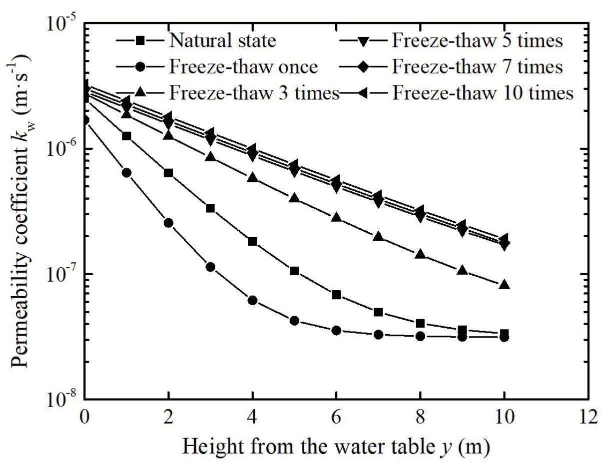

Figure 7. The calculation of vertical permeability coefficient under different conditions.

4. Conclusions

As the typical weathering processes, freeze-thaw action and dry-wet alternation both have significant impacts on the structure of soil, thus changing its physical and mechanical properties. In this study, based on filter paper method, the SWCC on unsaturated loess considering freeze-thaw cycle, coupling of freeze-thaw cycle and dry-wet action was carried out, and some valuable conclusions were drawn according to the experimental data.

4. The first freeze-thaw cycle has the greatest influence on matric suction. As the number of freeze-thaw cycle increases, the matric suction decreases gradually and basically tends to be stable after 7 freeze-thaw cycles. Under the same water content, the matric suction with the number of freeze-thaw cycles follows logarithmic curve;
5. The first coupling of freeze-thaw and dry-wet action has the greatest influence on matric suction. With the increase of coupling times, the matric suction of unsaturated loess was logarithmically decreasing, and the dry-wet path affected matric suction significantly. For the soil samples with the same water content, the matric suction under the path of drying followed by wetting is slightly larger than that under the path of wetting followed by drying;
6. For Gardner Model, Fredlund & Xing Model and Van Genuchten Model, the Gardner Model is more appropriate to describe the SWCC under given experimental conditions, so according to measured SWCC from Gardner Model and by using Childs & Collis-George Model, the prediction model of unsaturated loess permeability coefficient is gained, and the permeability coefficient has an exponential relationship with matric suction and a power function relationship with volumetric water content, respectively;
7. The vertical permeability coefficient of unsaturated loess decreases from groundwater level to surface under different freeze-thaw cycles. At the same depth of soil, it decreases and then increase and gradually stabilize with the increase of freeze-thaw cycles.

Acknowledgements

This research project was funded by the National Natural Science Foundation of China (Grant No. 51769013, 41971093) and Basic Research Innovation Group of Gansu (20JR5RA478).

Declaration of interest

The authors declare that there are no conflicts of interest regarding the publication of this paper.

Author's contributions

Yaling Chou: idea, conceptualization, methodology, validation, writing - reviewing and editing, language. Lijie Wang: experiment, data curation, writing - original draft preparation, investigation, modeling, validation.

References

Bai, F.Q., Liu, S.H., & Yuan, J. (2011). Measurement of SWCC of Nanyang expansive soil using the filter paper method. *Chinese Journal of Geotechnical Engineering*, 33(6), 928-933.

Bishop, A.W., Alpan, I., Blight, G.E., & Donald, I.B. (1960). Factors controlling the strength of partly saturated cohesive soils. In *Proceedings of the A.S.C.E. Conference on the Shear Strength of Cohesive Soils* (pp. 503-532). New York: ASCE.

Chen, Z.H. (1999). Deformation, strength, yield and moisture change of a remolded unsaturated loess. *Chinese Journal of Geotechnical Engineering*, 21(1), 82-90. http://dx.doi.org/10.3321/j.issn:1000-4548.1999.01.018.

Fredlund, D.G., Xing, A.Q., & Huang, S.Y. (1994). Predicting the permeability function for unsaturated soils using the soil-water characteristic curve. *Canadian Geotechnical Journal*, 31(4), 533-546. http://dx.doi.org/10.1139/t94-062.

Fredlund, D.G., & Rahardjo, H. (1997). *Soil mechanics for unsaturated soils*. Beijing: China Architecture and Building Press,.

Fredlund, D.G., Xing, A.Q., Fredlund, M.D., & Barbour, S.L. (1996). The relationship of the unsaturated soil shear strength to the soil-water characteristic curve. *Canadian Geotechnical Journal*, 33(3), 440-448. http://dx.doi.org/10.1139/t96-065.

Li, Z.Q., Li, T., Hu, R.L., Li, X., & Li, Z.J. (2007). Methods for testing and predicting of SWCC in unsaturated soil mechanics. *Journal of Engineering Geology*, 15(5), 700-707. http://dx.doi.org/10.3969/j.issn.1004-9665.2007.05.020.

Lian, J.B. (2010). *Study on the variation of physical properties of loess under freezing-thawing cycles*. Northwest A & F University, Yangling, shaanxi, China.

Lian, J.B., Zhang, A.J., Guo, M.X., & Dong, X.H. (2010). Influence of iterative freezing-thawing on void ratio and permeability coefficient of loess. *Yangtze River*, 41(12), 55-58.

Liu, F.Y., Zhang, Z., Zhou, D., Zhao, X.G., & Zhu, L. (2011). Effects of initial density and drying-wetting cycle on soil water characteristic curve of unsaturated loess. *Rock and Soil Mechanics*, 33(S2), 132-136+142. https://doi.org/10.16285/j.rsm.2011.s2.086.

Liu, P.F., Yin, Y.P., Li, B., & Sun, Y.B. (2015). The tests of soil-water characteristic curve and permeability coefficient prediction of the wetting-drying cycles for unsaturated loess. *The Chinese Journal of Geological Hazard and Control*, 26(4), 125-129. http://dx.doi.org/10.16031/j.cnki.issn.1003-8035.2015.04.22.

Liu, X.W., & Ye, Y.X. (2015). Experimental study of the soil-water characteristic curve of unsaturated laterite under different affecting factors. *Hydrogeology & Engineering Geology*, 59(2), 97-104. http://dx.doi.org/10.16030/j.cnki.issn.1000-3665.2015.02.15.

Liu, Z., Zhang, B., Yu, X., & Tao, J.L. (2012). A new method for soil water characteristic curve measurement based on similarities between soil freezing and drying. *Geotechnical Testing Journal*, 35(1), 2-10. http://dx.doi.org/10.1520/GTJ103653.

Lu, J., & Cheng, B. (2007). Research on soil-water characteristic curve of unsaturated loess. *Chinese Journal of Geotechnical Engineering*, 29(10), 1591-1592. http://dx.doi.org/10.3321/j.issn:1000-4548.2007.10.027.

Lu, N., & Likos, W.J. (2012). *Unsaturated soil mechanics*. Beijing: China Higher Education Press.

Qi, J.L., Cheng, G.D., & Vermeer, P.A. (2005). State-of-the-art of influence of freeze-thaw on engineering properties of soils. *Diqiu Kexue Jinzhan*, 20(8), 887-894. http://dx.doi.org/10.3321/j.issn:1001-8166.2005.08.010.

Sillers, W.S., Fredlund, D.G., & Zakerzadeh, N. (2001). Mathematical attributes of some soil-water characteristic curve models. *Geotechnical and Geological Engineering*, 19(3), 243-283. http://dx.doi.org/10.1007/978-94-015-9775-3_3.

Vanapalli, S.K., Fredlund, D.G., & Pufahl, D.E. (1996). The relationship between the soil-water characteristic curve and unsaturated shear strength of a compacted glacial till. *Geotechnical Testing Journal*, 19(3), 259-268. http://dx.doi.org/10.1520/gtj10351j.

Wang, Z., Yang, J.X., Kuang, J.J., An, J.Y., & Luo, Y.D. (2003). Application of filter paper method in field measurement of matric suction. *Chinese Journal of Geotechnical Engineering*, 25(4), 405-408. http://dx.doi.org/10.3321/j.issn:1000-4548.2003.04.004.

Xiao, D.H., Feng, W.J., Zhang, Z., Ming, J., & Wang, Q. (2014). Research on the Lanzhou loess's permeabilities changing with freezing-thawing cycles. *Journal of Glaciology and Geocryology*, 36(5), 1192-1198. http://dx.doi.org/10.7522/j.issn.1000-0240.2014.0142.

Xiong, C.R., Liu, B.C., & Zhang, J.S. (2005). Relation of matric suction with moisture state and density state of remolded cohesive soil. *Chinese Journal of Rock Mechanics and Engineering*, 24(2), 321-327. http://dx.doi.org/10.3321/j.issn:1000-6915.2005.02.023.

Yang, Y., Chen, Y., Li, P., & Tang, J.X. (2016). Influence of compaction and drying-wetting cycle with loading on soil-water characteristic curve. *Water Resources and Power*, 34(3), 128-131.

Zhang, T., Yue, J.C., & Zhang, J.R. (2016). Influence of compaction degree and drying-wetting cycle on the soil water characteristic curve of Yudong silt. *Journal* *of Zhengzhou University*, 37(6), 53-57. http://dx.doi.org/10.13705/j.issn.1671-6833.2016.03.027.

Zhao, T.Y., & Wang, J.F. (2012). Soil-water characteristic curve for unsaturated loess soil considering density and wetting-drying cycle effects. *Journal of Central South University*, 57(6), 2445-2453.

Zhao, W.B., Xu, J., Cheng, Q., & Lu, Y.H. (2015). Influences of vertical stress and drying-wetting cycles on soil-water characteristic curve of loess. *Kexue Jishu Yu Gongcheng*, 15(36), 189-193. http://dx.doi.org/10.3969/j.issn.1671-1815.2015.36.034.

Soils and Rocks

An International Journal of Geotechnical and Geoenvironmental Engineering

www.soilsandrocks.com

ISSN 1980-9743
ISSN-e 2675-5475

Validation of a 3D numerical model for piled raft systems founded in soft soils undergoing regional subsidence

Andrea J. Alarcón Posse[1#], Juan F. Rodríguez Rebolledo[1], Julián A. Buriticá García[1], Bernardo Caicedo Hormaza[2], Edgar Rodríguez-Rincón[3]

Article

Keywords
Numerical analysis
Piled raft
Centrifuge modeling
Hardening soil model
Regional subsidence
Small scale

Abstract

In this paper a 3D numerical model using a software based on the Finite Element Method (FEM), was developed and validated using the results obtained in a geotechnical centrifuge model of a piled raft system founded in soft soils undergoing regional subsidence. The piled raft configuration had nine piles distributed in the center of the raft. The kaolin parameters were obtained, calibrated, and validated for the Hardening Soil Model (HSM), based on laboratory triaxial and oedometer test results. Also, a single pile load test was carried out in the centrifuge to get the resistance parameters used in the FEM. The developed numerical model reproduced satisfactorily soil and foundation consolidation displacements due, not only by the structural service load but also by the pore pressure drawdown. For load distribution on piles and raft, the model reproduces with good agreement the foundation behavior only for the structural service load, for pore pressure drawdown some adjustments on the embedded piles elements shaft and base resistance had to be done. The developed model allowed to identify the most sensitive parameters for this type of simulation, to define the types and stages of analysis that had the best fit for the physical model, and to obtain additional results to those measured in the physical model, e.g., the axial load distribution developed along the piles and therefore the magnitude of the negative skin friction, that is an important load that should be considered for the structural safety review of piled foundations subjected to this complex conditions.

1. Introduction

On many occasions, commercial software based on numerical models are used indiscriminately for the analysis of complex problems without a real understanding of the problem. Also, by ignoring the influence that different geotechnical parameters have on the simulation results. The cases of instrumented structures and/or physical models in laboratory allow obtaining results closer to reality and with a clearer understanding of the phenomenon. However, these results may be limited by the number of case studies, model dimensions, number of variables, time of assembly and execution, type and quantity of instruments and problems related to the installation of the instruments and during monitoring. Regarding the numerical models, they can be calibrated and validated through the results produced by the physical tests and, at the same time, be used to obtain additional results. This calibration and validation process is complex since it must consider the selection of the constitutive model, the adjustment of the parameters, the definition of the initial stress states and pore pressure, and the definition of the analysis stages. The result of this process allows developing a better understanding of the sensitivity of the different parameters and a more realistic analysis methodology.

In this paper, the case of a piled raft system used on soft soils undergoing regional subsidence was studied. According to Alnuaim et al. (2018), a piled raft is a composite structure with three components: subsoil, raft, and piles. The structural components interact with each other and with the surrounding soil (pile-soil, raft-soil, and pile-raft) to bear vertical, horizontal, and moment loads coming from the superstructure. Luo et al. (2018) refer to this system as an effective foundation due to its efficiency in reducing settlements and improving bearing capacity.

Many papers have been presented to understand the behavior of piled raft systems using different ways of approaching (field test, laboratory test, and numerical modeling). The use of numerical modeling has increased considerably, and it has been used as a tool that allows simulating the behavior of complex structures in real projects. Some models have been

[#]Corresponding author. E-mail address: julianaalarcon2@hotmail.com
[1]Universidade de Brasília, Brasilia, DF, Brasil.
[2]Universidad de los Andes, Bogotá, Colombia.
[3]Universidad Nacional de Colombia, Bogotá, Colombia.

Submitted on July 6, 2020; Final Acceptance on January 20, 2021; Discussion open until May 31, 2021.

DOI: https://doi.org/10.28927/SR.2021.053620

developed using different software and constitutive models mainly to evaluate how the pile spacing, load sharing, pile length, and diameter affect the settlement of the foundation (Cui et al., 2010b; Lee et al., 2010; El-Mossallamy, 2008; Roy & Chattopadhyay, 2011; Cho et al., 2012; van Tran et al., 2012b; Rodríguez-Rebolledo et al., 2015; Watcharasawe et al., 2015; Banerjee et al., 2016; Sinha & Hanna, 2017; Zhang & Liu, 2017; Alnuaim et al., 2017; Khanmohammadi & Fakharian, 2018; Luo et al., 2018; Mali & Singh, 2018). Although some of those works consider consolidation analyses, few studies have really focus on simulating the subsidence process in a more precise way using more accurate constitutive models that represent the soil behavior, which can lead to a closer analysis of the system's behavior.

Geotechnical centrifuge modeling is an advanced physical modeling technique that provides data for investigating mechanisms of deformation and failure and for validating analytical and numerical methods (Ng, 2014). Some authors have presented centrifuge tests that evaluate the influence of regional subsidence in a different type of constructions (Sun et al., 2008; Cui et al., 2010a; Cheng et al., 2011; Tang et al., 2012; Wang et al., 2013; Zhang et al., 2017a, b). On the other hand, various researches have been done using piled raft system on centrifuge like Thaher & Jessberger (1991), Horikoshi & Randolph (1996), Bajad & Sahu (2008), Goh & Zhang (2017), among others. van Tran et al. (2012a), Rodríguez-Rincón (2016) and Rodríguez-Rincón et al. (2020), focused specifically on the behavior of the piled raft under the effects of regional subsidence, assessing not only settlements but also load distribution.

The aim of this work is to develop and validate a three dimensional (3D) numerical model based on the Finite Element Method (FEM, Plaxis 3D) capable of simulating the complex behavior of a piled raft system founded in soft soils undergoing regional subsidence. For this purpose, the results obtained by Rodríguez-Rincón (2016) of a geotechnical centrifuge model were used. This model allows to identify the most sensitive parameters for this type of simulation, to define the types and stages of analysis that had the best fit to the physical model, and to obtain additional results to those measured in the physical model, e.g., the axial load distribution developed along the piles and therefore the magnitude of positive and negative skin fractions and point load. According to Auvinet & Rodríguez-Rebolledo (2017), the effect of the negative skin friction developed on piles shafts should be considered for the structural safety review and for the estimation of the long-term displacements of piled foundations.

Being one of the most complete constitutive models of Plaxis, the Hardening Soil Model (HSM) was chosen to simulate the soil behavior. To complete the data needed for the numerical simulation, new laboratory tests, and a load test in a single pile in the centrifuge were performed. The parameters obtained for the HSM were calibrated through numerical modeling of the tests using the *SoilTest* module of Plaxis software. Based on the evaluation and calibration of these parameters, a geotechnical model profile to represent the centrifuge experimental test is proposed. The calibration by displacements and by loads distribution of the 3D numerical model by comparison with the centrifuge test results is presented and discussed. Finally, the axial loads developed along the center, border and corner piles, for the different stages of the problem, are presented and interpreted.

2. Materials and methods

2.1 Case study - centrifuge model

The case study is based on a centrifuge model developed by Rodríguez-Rincón (2016); Rodríguez-Rincón et al. (2020) at the Geotechnical Models Laboratory of the Universidad de Los Andes, Bogota, Colombia. The model is focused on the evaluation of the behavior of piled raft systems in soft soils along the consolidation process generated both by the structural load and by the pore-pressures drawdown. The decrease of the pore pressure value was associated with the subsidence process induced by the extraction of water from deep permeable layers (Figure 1).

The soil profile used was composed of three layers of a mixture of kaolin with water content at 1.5 times the liquid limit, divided by two sand layers that work as a filter and a bottom layer as drainage. This profile is intended to represent a soft clay soil typical of the city of Bogotá. To physically model a piled raft foundation, a 70 g centrifugal acceleration was adopted due to the capacity of the modeling box (boundary conditions), the size of elements sections after scaled and

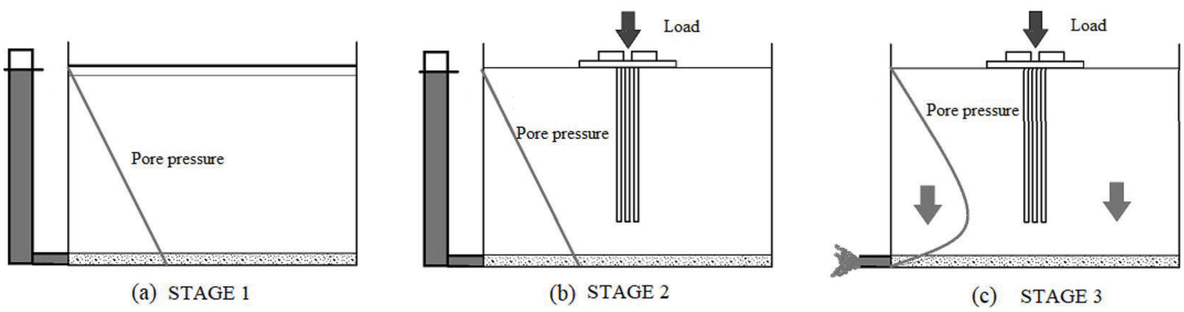

Figure 1. Representation of pore pressure conditions at testing stages. Adapted from Rodríguez-Rincón (2016).

the size and capacity of the available instrumentation. The configuration of the piled raft is a model with nine piles distributed in the center of the raft, with a pile spacing of two diameters. Table 1 summarizes the dimensions and parameters of the piled raft elements.

The test setup that was employed to evaluate the performance of the piled raft is shown in Figure 2. The instrumentation used were composed of three linear variable differential transducers (LVDT) on the soil and three on the raft, four piezometers and a load cell. Four piles were also instrumented with miniature load cells to measure the load transmitted to the top piles. Important results were obtained regarding the piled raft behavior and were used for the present paper.

2.2 Hardening Soil Model (HSM)

The research was conducted by using Plaxis 3D software, which is widely used for geotechnical analysis. As mentioned by Rodríguez-Rebolledo et al. (2019), soil constitutive models have advanced significantly from basic models that idealize the soil as a linear elastic medium or a perfectly plastic linear elastic medium. The HSM is an isotropic hardening double surface plasticity model that gives more accurate displacements patterns for conditions at working load (Schanz et al., 1999). This model considers both theories of the non-linear elasticity and the plasticity, representing a significant advance in comparison with the basic linear elastic models (LE) and the elastic-perfectly plastic model of Mohr-Coulomb (MC). This model is available in the Plaxis software and was implemented by the program initially as an extension of the MC model (Nordal, 1999). Although the results obtained with this model are closer to "reality", it requires a greater number of input parameters that demand more experimental tests. The HSM basic characteristics are given by:

- Total strains are calculated using a stress-dependent stiffness according to a power law (input parameter *m*);
- Shear hardening: plastic straining is due to primary deviatoric loading (input parameter E_{50}^{ref});
- Compression hardening: plastic straining is due to primary compression (input parameter E_{oed}^{ref});
- Failure according to MC criterion (input parameters *c'* and φ›);
- Stiffness defined by loading and unloading/reloading conditions (input parameters E_{ur}^{ref} and ν_{ur});
- Non-associated flow rule assumed for shear hardening (input parameter ψ);
- Associated flow rule assumed for compression hardening.

Table 1. Elements dimensions of the piled raft for models with a scale factor of 70g.

Element	Parameter	Model
Raft	Material	Aluminum
	Thickness	13 mm
	Young's modulus	70000 MPa
	Width	200 mm
	Length	200 mm
Piles	Material	Aluminum
	Diameter	9 mm
	Young's modulus	70000 MPa
	Length	320 mm

2.3 Parameters determination from laboratory tests

With the aim of numerically reproduce the behavior of a pile raft foundation system and to take into account the need to determine the mechanical parameters of the HSM,

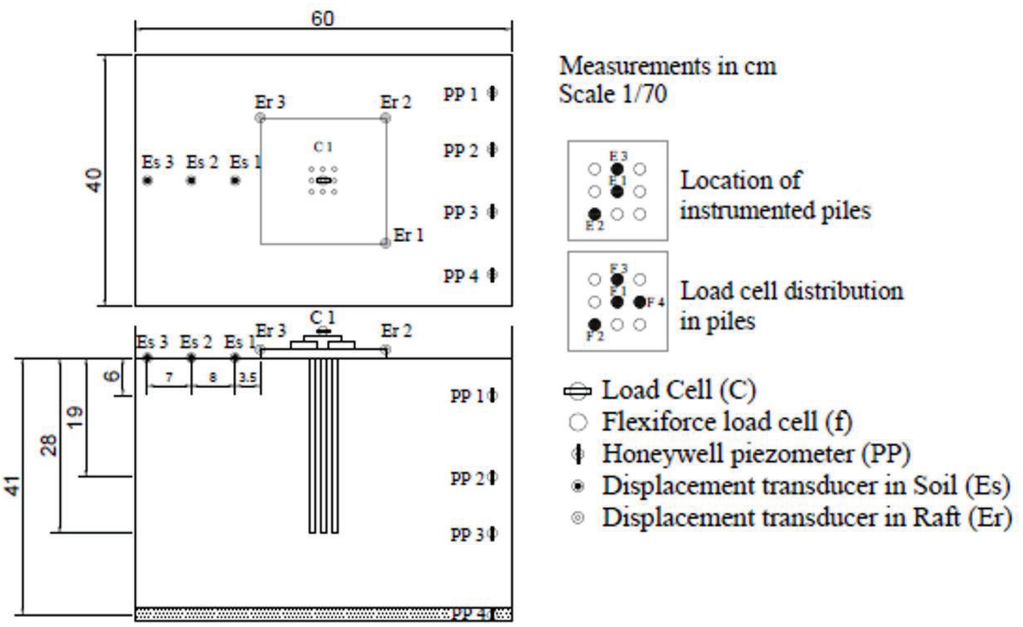

Figure 2. Distribution of the instrumentation on the centrifuge model M3. Adapted after Rodríguez-Rincón (2016).

it was necessary to carry out tests on a kaolin soil mixture whose profile represented the one proposed by Rodríguez-Rincón (2016). In this way, it was possible to experimentally determine the behavior of the soil in a different stress state, as well as the value of the axial pile resistance. The procedure described by Rodríguez-Rincón et al. (2020) was used for the fabrication of the soil mixture in the experiments. The results of the oedometer, triaxial tests, and the pile load test in the centrifuge are presented next.

a) Oedometer tests data

The oedometer tests were conducted on three samples at different layers of the fabricated soil labeled M1, M2 and M3. Table 2 shows the calculated values of the reference oedometer modulus (E_{oed}^{ref}, $E_{ur,\,oed}^{ref}$) and the parameter that defines the dependency level of the strains on the stress state (*m*). The methodology to calculate the parameters was the one suggested by Surarak et al. (2012) and Rodríguez-Rebolledo et al. (2019). The results are plotted in Figure 3.

b) Triaxial tests data

Three isotropically drained consolidated triaxial tests (CID) were conducted at the three distinct layers of the experiment M1 to M3. The confining pressures σ_3 used for the M1 and M2 samples were 100, 200, 300 kPa, and for the M3, σ'_3 was equal to 200, 300, and 500 kPa. The friction angle (φ') obtained were 25°, 22°, and 18°; whereas the cohesion (*c*') was 21, 40 and 1 kPa, respectively. The reference modulus at 50% of strength (E_{50}^{ref}) and power *m* determined from the CID tests using double log scale plots are given in Figure 4. These values are summarized in Table 3 and were also obtained following the methodology described by Surarak et al. (2012) and Rodríguez-Rebolledo et al. (2019).

2.4 Calibration of parameters

To calibrate the soil parameters listed in Tables 2 and 3, the CID triaxial and oedometer tests were modeled in Plaxis using the *SoilTest* tool. This tool is a quick and convenient procedure to simulate basic soil lab tests based on a single point algorithm, i.e., without the need to create a complete finite element model (Brinkgreve et al., 2018). It works with the inputted soil parameters obtained from a site investigation to compare with the behavior as defined by the soil model chosen (HSM in this case).

In order to obtain suitable parameters to give the best fit results, the input parameters were adjusted, as presented in Figures 5, 6 and 7, for layers M1, M2 and M3, respectively. The results from the three layers reveal good agreements among all the stress-strain and stress path behavior for different confining pressure values (σ'_3 = 100, 200, and 300 kPa). Although the M3 layer results (Figure 7) calculated were not as successful as those of the M1 (Figure 5) and

Table 2. Parameters calculated from oedometer tests.

Layer	E_{ur}^{ref} (kPa)	*m*	E_{oed}^{ref}(kPa)	*m*
M1	4,976	1.13	830	0.99
M2	6,164	1.08	1,347	0.82
M3	7,707	0.91	2,214	0.5

Table 3. Parameters calculated from triaxial tests.

Layer	E_{50}^{ref} (kPa)	*m*	ϕ' (°)	*c*' (kPa)
M1	1,413	0.8	25	21
M2	2,044	0.5	22	40
M3	843	1	18	1

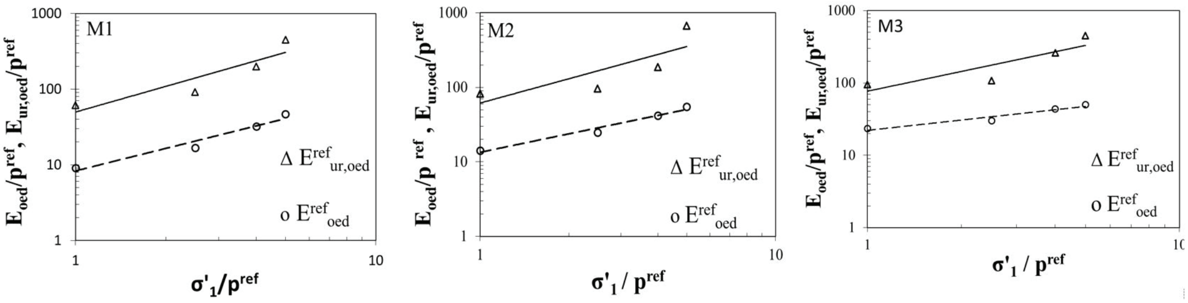

Figure 3. Oedometer Modulus *versus* consolidation pressure calculated from one-dimensional consolidation tests.

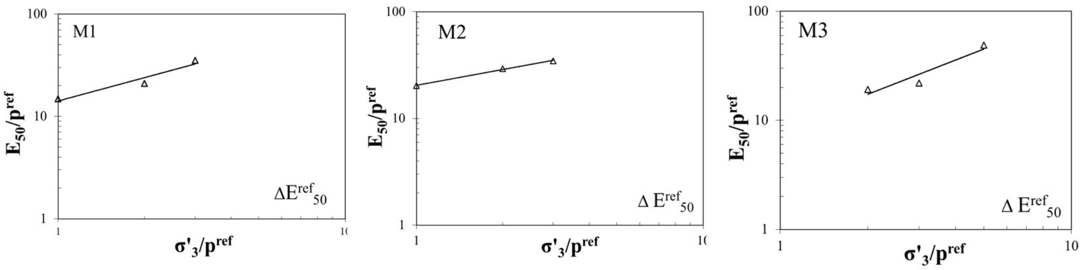

Figure 4. Variation in E_{50} with confining pressure.

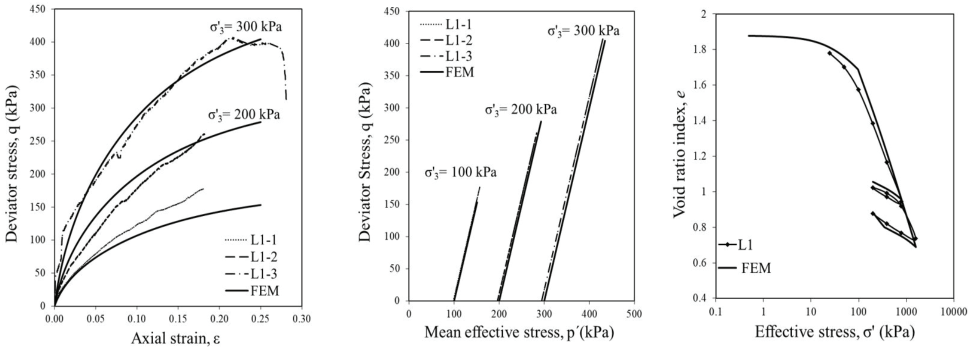

Figure 5. CID triaxial and oedometer test results and their FEM simulations with HSM for layer M1.

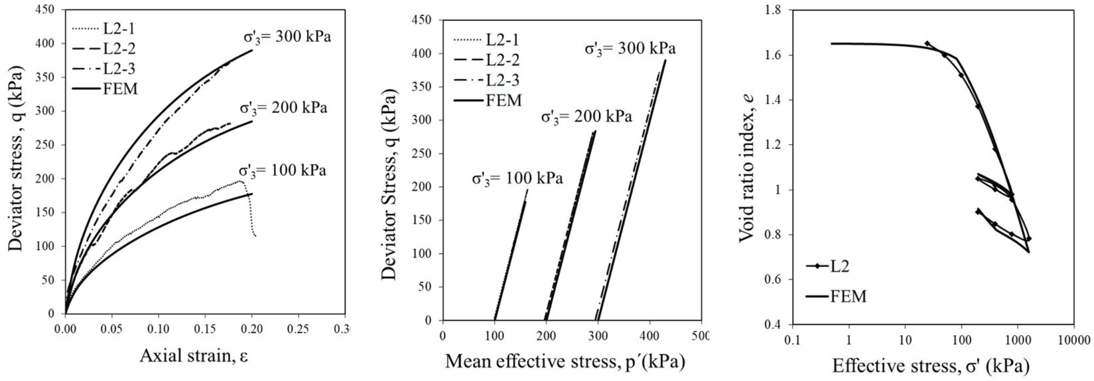

Figure 6. CID triaxial and oedometer test results and their FEM simulations with HSM for layer M2.

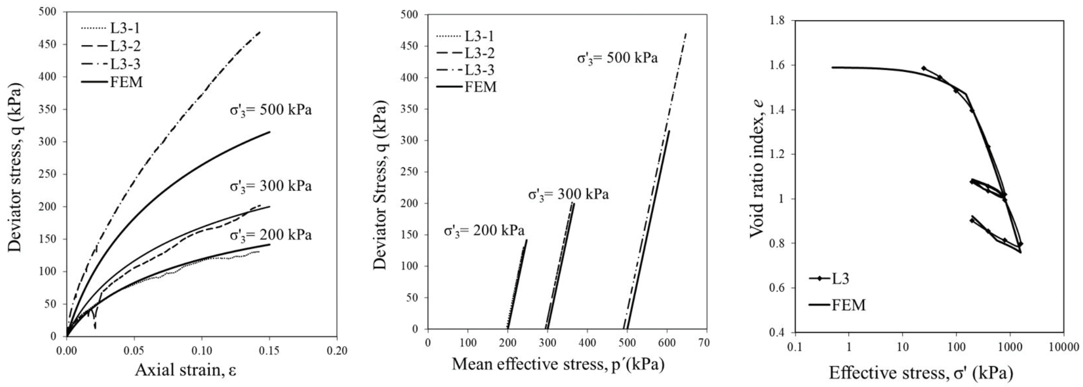

Figure 7. CID triaxial and oedometer test results and their FEM simulations with HSM for layer M3.

M2 (Figure 6) layer, since they were underestimated for the confining pressure of 500 kPa, nevertheless, it can be stated that the HSM predictions agree reasonably well with the triaxial test results.

As the stress state has a significant variation throughout the depth, for the numerical simulation, the soil profile was divided into several layers using the over consolidation ratio (OCR) values as a criterion. Besides being an indicator of the stress state, the OCR is one of the input parameters of the HSM. Also, the ground-water table was considered at 3.5m of depth as originally proposed by Rodríguez-Rincón (2016). Since in the process of fabrication and lowering of the water level a stiff layer was formed on the surface, the parameters adopted for this layer were the ones calibrated for a stiff clay by Surarak et al. (2012). The geotechnical parameters for the different soil layers obtained for the numerical simulations are presented in Table 4.

2.5 Long term bearing capacity estimation

Having the load measured on the top of the piles from the centrifuge, it was considered fundamental to calibrate the model not only with the displacements but also with the load distribution, so to have a more accurate model. In consequence, a pile load test on an isolated pile was carried out in the centrifuge to better establish the long-term parameters for the numerical model.

Table 4. Geotechnical parameters for the soil profile.

Layer		z	γ	σ'$_0$	σ	σ$_P$	c'	ϕ	k$_0$	k_0^{nc}	E_{50}^{ref}	E_{ur}^{ref}	E_{oed}^{ref}	m	ν	k	OCR
		m	kN/m^3	kPa	kPa	kPa	kPa	°			MPa	MPa	MPa			m/h	
M1	L-1	0 - 3.5	18.67	10	28	170	11.5	28	1.24	0.53	9.5	30	12	1	0.2	8x10^{-6}	6.07
	L-2	3.5 - 6	16.68	30	75	170	21	25	1.2	0.58	1.41	10	1	1	0.2	8x10^{-6}	5.66
	L-3	6 - 9	16.68	50	125	191	21	25	0.97	0.58	1.41	10	1	1	0.2	8x10^{-6}	3.39
M2	L-4	9 - 19	17.03	81	200	223	20	22	0.92	0.62	2.4	15	1.55	1	0.2	8x10^{-6}	2.77
M3	L-5	19-23	17.03	141	342	342	20	17	0.74	0.71	2.5	16	1.58	0.8	0.2	8x10^{-6}	1.27
	L-6	23-28	17.03	176	425	382	20	17	0.69	0.71	2.5	16	1.58	0.8	0.2	8x10^{-6}	1.01

L-1: Crust, over consolidated high plasticity clay subject to wetting and drying cycles; L-2 to L-6: Soft clay formation, from over to normally consolidated high plasticity saturated clay.

Table 5. Parameters of the pile.

Parameter	Value	Unit
Axial skin resistance	11.38	kN/m
Base resistance	205	kN

The test was performed in a cylindrical container with an inner diameter of 30 cm and 60 cm in height, and a model scale of 1/70 was used with a centrifugal acceleration of 70*g*. The instrumented pile was made of an aluminum bar with a 6 mm diameter and Young's modulus of 70 GPa. The outer diameter of this pile was 10 mm with 400 mm of length. The applied axial load was monitored by a central load cell, and four extra lateral units were used to measure the axial load transfer along the pile shaft during the tests. Also, a linear variable differential transducer (LVDT) was employed to track the pile displacement during test (Figure 8).

The installation of the model pile was carried out at l*g* with a compression rate of about 0.5 mm/s. This model was tested in two stages: first, without loading the pile till stabilization of the readings so to guarantee the adherence of the pile shaft with the soil; and second, with the subsequent development of the load test. In general, each load increment was held until the cells had reached their steady state condition before another load increment was further applied. After stopping the centrifuge, vane tests were conducted at different depths to check on the undrained shear strength.

The load and displacement data are shown in Figure 9. Test results are expressed in the prototype scale unless stated otherwise. The maximum applied load was 539 kN. Table 5 presents the input parameters that were needed for the model, in terms of pile shaft and base resistance for long term behavior. It was observed that the pile-soil adherence

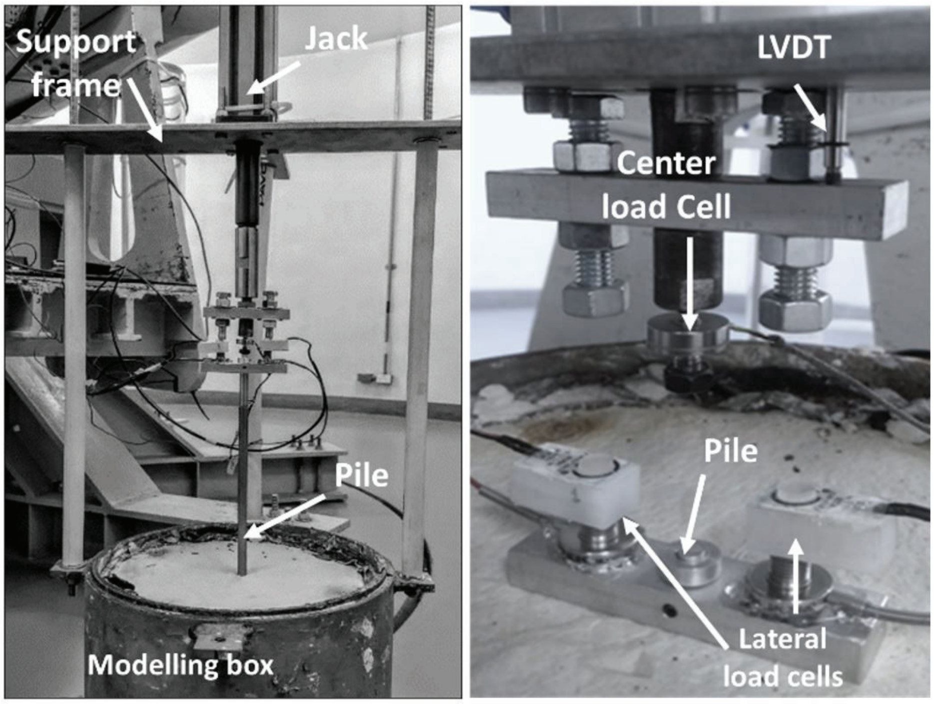

Figure 8. Centrifuge model assembly and instrumentation.

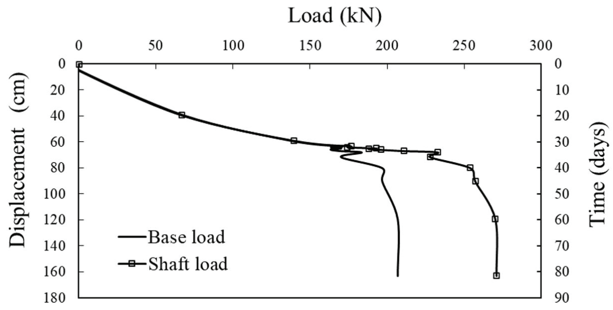

Figure 9. Displacement and time *versus* load curves.

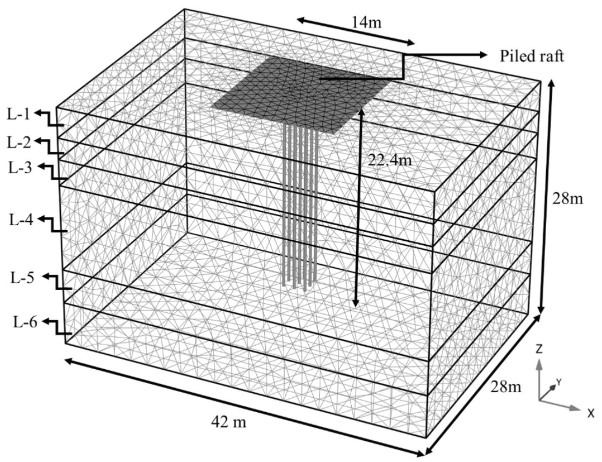

Figure 10. Geometry and mesh of the proposed 3D FEM model.

Table 6. Parameters of the structural elements

Element	Parameter	Value
Plate (Raft)	Unit weight	25 kN/m^3
	Thickness	1.147 m
	Young's modulus	35 GPa
	Width	14 m
	Length	14 m
Embedded beams (Piles)	Unit weight	25 kN/m^3
	Diameter	0.63 m
	Young's modulus	30 GPa
	Length	22.4 m
	Axial skin resistance	11.38 kN/m
	Base resistance	205 kN

is low, which has consequently generated a significant displacement of the pile.

2.6 Proposed model

To model the structural components, such as concrete piles and raft, a linear elastic constitutive model was assumed. Regarding the element type used for the design of the piled raft foundation, a plate element for the raft and embedded beams for the piles, were assumed. Plates are structural objects used to model structures in the ground with a significant flexural rigidity that does not allow plastification, only linear elastic behavior. As for an embedded beam element, it is defined as a structural object with special interface elements providing the interaction between the beam and the surrounding soil. The interaction involves a skin friction as well as a base resistance, which is determined by the relative displacement between soil and pile. This element type was chosen instead of the volume elements since with them it is possible to generate a mesh with fewer finite elements, thus decreasing the analysis time (Oliveira, 2018).

The geometry of the piled raft and the boundary conditions of the soil body are presented in Figure 10. Their properties are listed in Table 6. The horizontal movements in the four boundaries were fixed as well as the vertical displacement at the lower frontier. Regarding the water boundary conditions, it shall be noticed that the water flow exit was restricted in the lower edge in all phases before pore pressure drawdown.

2.7 Stages of analysis

A graphic representation of the stages of the centrifuge test performed and the conditions of each of them are presented in Figure 11, where time intervals are also specified. The numerical model was analyzed in terms of effective stresses, with drained parameters and initial drained conditions. According to Rodríguez-Rebolledo (2011), this type of analysis is applied to obtain stresses, strains, and displacements before, during, and after the consolidation process, which is the purpose in the present work.

To represent the centrifuge test, the considered calculation phases are described below:

- *Initial Phase*: at this stage, the initial stress of the soil is generated. This stress state is usually characterized by an initial vertical effective stress. In Plaxis, initial stresses may be generated by using the K_0 procedure that is a special calculation method to define these stresses, considering the loading history of the soil (Brinkgreve et al., 2018) (Plaxis, 2018);
- *Phase 1, construction and loading:* in this phase it was simulated the construction of the piled raft and the application of the load along the foundation surface, in accordance with the experimental test. A consolidation calculation was used to analyze the development of pore pressure as a function of time. As it is possible to apply load in this analysis, a value of 38.25 kPa was applied in 5000 hours corresponding to the interval time from t_C-t_E of the centrifuge test, Figure 11;
- *Phase 2, consolidation:* in this phase, the same analysis was used as in the previous one to represent the interval time from t_E-t_F (Figure 11) in which the load has reached its maximum value. The load was maintained for more 8,914 hours;
- *Phases 3 to 6, pore water pressure drawdown:* these phases correspond to the Stage 3 previously explained in Figure 11 in which a drawdown of pore pressure

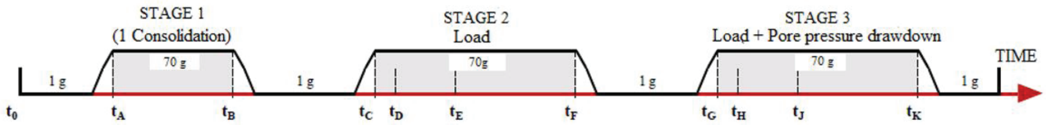

Time	Description	Activity	Conditions	Stage
t_0	Start of modeling			
		Soil fabrication – Installation of instruments		
t_A	Reach scale model	Consolidation in the centrifuge	Without load W/o drawdown pore pressure	Stage 1
t_B	Stop			
		Installation of models and additional instruments		
t_C	Reach scale model	Consolidation with load	With load W/o drawdown pore pressure	Stage 2
t_D	Start loading			
t_E	Maximum load maintained			
t_F	Stop			
		Valve opening for drawdown pore pressure		
t_G	Reach scale model	Consolidation with load and drawdown pore pressure	With load With drawdown pore pressure	Stage 3
t_H	Start loading			
t_J	Maximum load maintained			
t_K	Stop			

Figure 11. Description of the test carried out in the centrifuge and the pore pressure condition in the three stages. Adapted from Rodríguez-Rincón (2016).

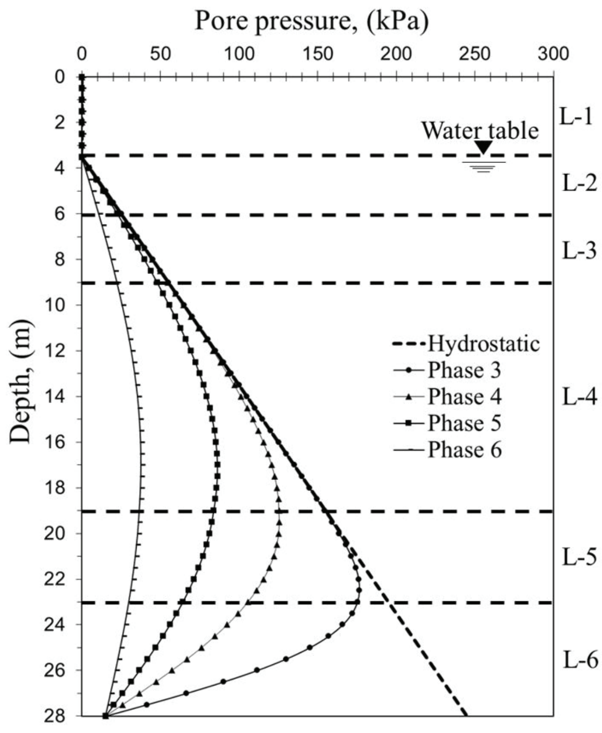

Figure 12. Pore water pressure conditions.

Table 7. Description of the phases that simulated the drawdown pore pressure.

Phase	Consolidation degree (%)	Time (hr)
3	20	606,8
4	40	1736
5	60	2868
6	88	7787

is generated, Figure 12. Table 7 summarizes each of these phases, that correspond to a particular degree of consolidation to be reached in a certain period.

In the last stage of the centrifuge test, drawdown phase, the soil was brought to an 88% degree of consolidation. This stage was divided in four parts in the numerical model, where pore pressures were sequentially imposed to reach 20, 40, 60 and 88% of degree of consolidation. The piezometer data obtained in the centrifuge test was measured very close to the filter layers, so it could not be used as an initial input in the numerical simulation to model the exact decrease of pore pressure. Consequently, the isochrones presented in Figure 12 were established by using the finite difference method.

3 Results and discussions

3.1 Calibration by displacements

The displacement-time curve for the piled raft foundation, under vertical loading and pore pressure drawdown, obtained from the centrifuge test is presented along with the results obtained from FEM. Figure 13 shows the displacements measured at a point over the soil near the raft (*Es1*) with respect to time. In the first stage of the test, the results in the prototype are reasonably close to those from the centrifuge. Regarding the drawdown pore pressure phase, the results move away slightly, although the tendency is similar.

The displacements on the foundation system in the model were measured in three corners on top of the raft, labeled as Er_1, Er_2 and Er_3. The results are plotted in Figure 14. The experimental centrifuged results measured in the three corners of the raft were slightly different, and this can be due to a possible uneven load application, that probably caused an unequal load distribution among the system's components. When comparing the model and FEM results, it is observed that the two paths are reasonably close. Hence, with close results presented for soil and foundation, and a quite accurate representation of the phenomenon, therefore is possible to consider that the numerical model is calibrated by displacements for the centrifuge tests carried out in the laboratory.

FEM displacement results obtained from phase 2 (consolidation with load) and the final phase 6 (consolidation with load and decrease of pore pressure) are presented in Figures 15 and 16, respectively. The subsidence due to drawdown can be seen in Figure 16, where the settlements were considerably larger than in the previous phase (Figure 15). In phase 2 the maximum settlements reached up to 6 cm in the raft region, and plastification points are observed at the tip of the piles. At the end of phase 6 the maximum settlement was approximately 50 cm, which is 8 times the one obtained in phase 2. These comparative results do evidence

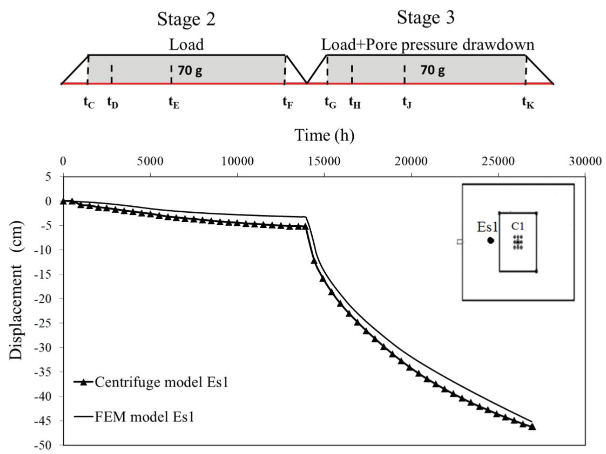

Figure 13. Displacements *versus* time curves obtained at point Es1 by centrifuge and FEM models.

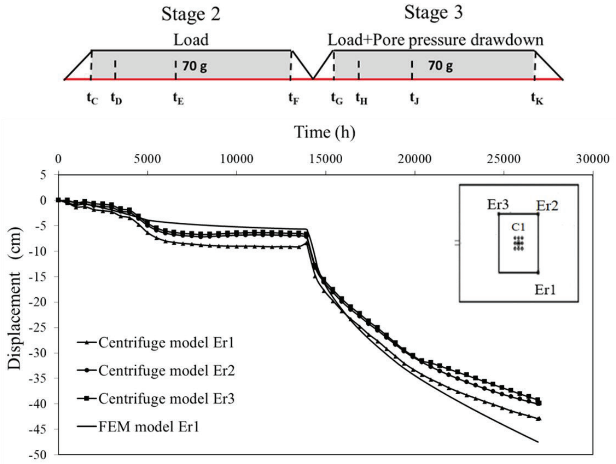

Figure 14. Displacements *versus* time curves obtained at raft corner points Er1, Er2 and Er3 by centrifuge and FEM models.

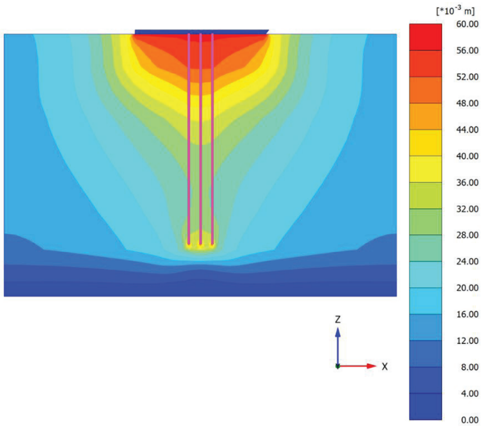

Figure 15. Vertical section at the center of the FEM model showing the total vertical displacements obtained at the end of Phase 2.

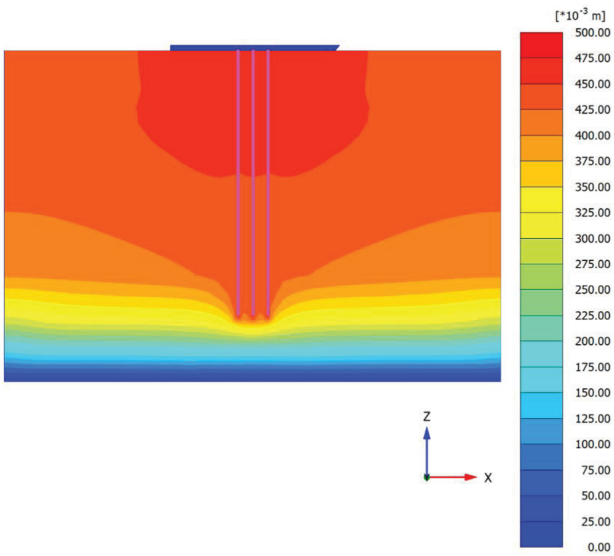

Figure 16. Vertical section at the center of the FEM model showing the total vertical displacements obtained at the end of Phase 6.

Table 8. Comparison between the centrifuge and FEM load values measured at the top of the piles for each stage of the test.

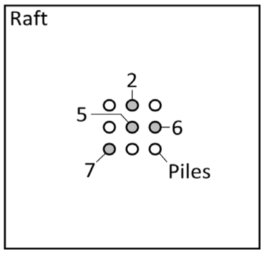

Element	Stage 2			Stage 3		
	Load		Dif. %	Load		Dif. %
	Centrifuge	FEM		Centrifuge	FEM	
Pile 2	196 kN	226 kN	+15	347 kN	156 kN	-122
Pile 5	173 kN	228 kN	+32	393 kN	222 kN	-77
Pile 6	164 kN	227 kN	+38	463 kN	172 kN	-169
Pile 7	215 kN	241 kN	+12	352 kN	158 kN	-122
All piles	1,753 kN	2,098 kN	+20	3,421 kN	707 kN	-384
	13%	16%	+23	26%	5%	-420
Raft	87%	84%	-3	74%	95%	+28

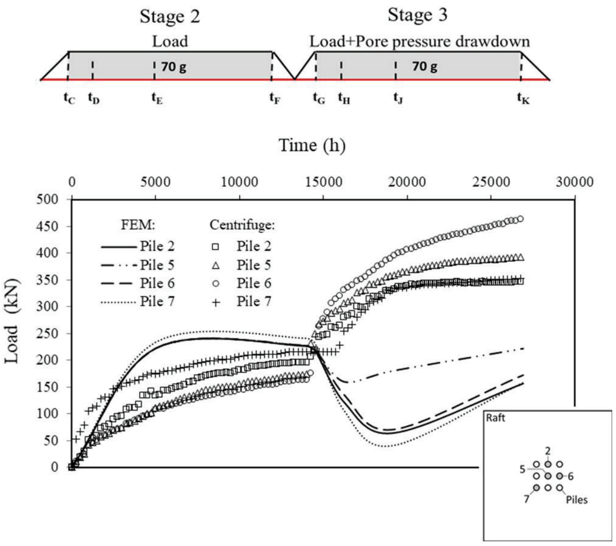

Figure 17. Load *versus* time curves obtained at the top of the instrumented piles 2, 5, 6 and 7 by centrifuge and FEM models.

the distinct phenomena and resulting engineering behavior that take place on a typical system founded in this type of environment, where loading and subsequent drawdown of pore water pressure can happen.

3.2 Calibration by load distribution

The load-time curves for each instrumented pile, under vertical loading and pore pressure drawdown, obtained from the centrifuge test are presented along with the results obtained from FEM. Figure 17 shows the load measure at the top of piles 2, 5, 6 and 7 with respect to time. In the first stage of the test, the results in the prototype are reasonably close to those from the centrifuge. Regarding the drawdown pore pressure phase, the values obtained with the FEM are considerably lower than those obtained experimentally. Table 8 shows a comparison of the results obtained with both models at the end of each stage. For stage 2 differences between FEM and centrifuge models from 12 to 38% were obtained, while for stage 3 from -77 to -169%. Centrifuge model shows that from stage 2 to 3 load transmitted by piles increases (from 13% to 26%) while load transmitted by raft decreases (from 87 to 74%). As explained by Rodríguez-Rincón et al. (2018) this is because, in stage 3, when pore pressure drawdown occurs, the soil continues to settle, a movement that is not accompanied by the raft, generating an apparent emersion process, and hence, a reduction of contact between the soil and the raft. This phenomenon is not developing in the FEM model because the considered skin resistance of the piles is not enough to allow the generation of the negative skin friction necessary for this.

The pore pressure drawdown generated in stage 3 produces an increment in effective stresses throughout the compressible soil, leading to an increase in shear resistance. The FEM results show that the embedded pile element does not consider the increase of the shear resistance parameters related to skin friction that happen when the soil is subjected to a consolidation process. To overcome this problem, the input parameters for this element, in stage 3, were further adjusted to properly “match” the centrifuge data in a sort of back-analysis. This analysis was made running the model increasing the base and axial skin resistance gradually until satisfactory match the data measured.

Figure 18 shows the load measure at the top of piles 2, 5, 6 and 7 with respect to time after adjustment of base and skin resistance of embedded piles elements. It is possible to observe a behavior more like that of the experimental model, mainly in the magnitude of the load obtained at the end of the stage. The differences between models during pore pressure drawdown are mainly due to the type of drainage considered in each one. In the model of the centrifuge this is developed in a more “efficient” way because it occurs through three draining layers, obtaining a stabilization of most of the loads for a time of approximately 20,000 hours. For the numerical model, the drainage was simulated in a more “realistic” way considering only a draining layer down to the compressible stratum, observing its stabilization only until the end of the consolidation process.

Table 9 shows a comparison of the results obtained with both models at the end of each stage, after being adjusted. It is possible to observe that now, for stage 3, the numerical model is simulating the same behavior as the experimental one, presenting variations in the piles loads from -4 to 21%.

Table 9. Comparison between the centrifuge and FEM load values measured at the top of the piles for stage 3, after adjustment.

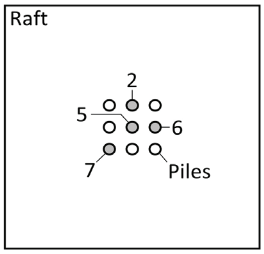

Element	Stage 2			Stage 3		
	Load		Dif. %	Load		Dif. %
	Centrifuge	FEM		Centrifuge	FEM	
Pile 2	196 kN	226 kN	+15	347 kN	382 kN	+10
Pile 5	173 kN	228 kN	+32	393 kN	477 kN	+21
Pile 6	164 kN	227 kN	+38	463 kN	430 kN	-7
Pile 7	215 kN	241 kN	+12	352 kN	298 kN	-15
All piles	1,753 kN	2,098 kN	+20	3,421 kN	3,293 kN	-4
	13%	16%	+23	26%	25%	-4
Raft	87%	84%	-3	74%	76%	+3

This was only possible by increasing the base and axial skin resistance of the embedded piles elements, during stage 3, in about 3.5 times, this research demonstrates the limitation in the use of this type of elements for the simulation of this kind of problems. To avoid this problem, two solutions are proposed:

1) determine the long-term base and skin resistance of the embedded piles using previously a simple 2D FEM model (axisymmetric), through the simulation of a load test of a single pile in a medium previously subjected to pore pressures drawdown.
2) use of volume elements for problems with a relatively small number of piles, the use of this type of elements can lead to exceptionally large finite element meshes and therefore high or even irrational computational costs (time and memory).

3.3 Obtaining the axial load along the pile

Having the model calibrated, it was possible to obtain the variation of axial loads with depth for center, border and corner piles (Figure 19), which allows to properly access the negative skin friction that can be eventually generated.

For phase 2 (Figure 19a), due to the high rigidity of the raft and to the proximity between piles, the load transmitted to the three elements is practically the same, slightly higher (+13 kN) for the corner one. For phase 6 (pore pressure drawdown) the model evidences the development of negative skin friction in the three piles (Figure 19b), being higher in the corner and lower in the center one. As excess pore pressure dissipates, the neutral level of the piles stabilizes at a depth between 15 to 16 m. These results agree with those reported by Auvinet & Rodríguez-Rebolledo (2017), they also demonstrate that the depth of such level depends significantly on the initial pile load conditions. The differences between piles in the magnitude of the axial loads is related to the corresponding influence area, e.g., the influence area of the corner pile is considerably larger than other piles leading to higher values of negative skin friction. Also, Lee (1993) stated that negative friction at an individual pile in the group is smaller than in an isolated pile due to the interaction effects.

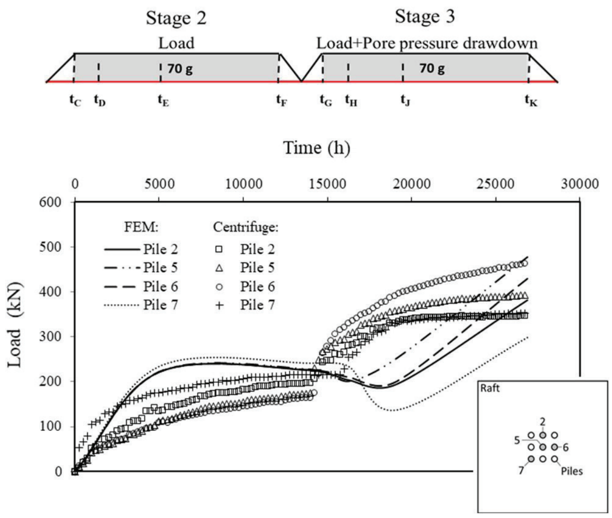

Figure 18. Load *versus* time curves obtained at the top of the instrumented piles 2, 5, 6 and 7 by centrifuge and FEM models, after adjustment.

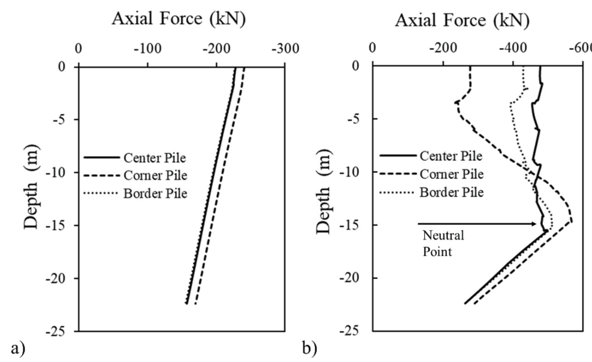

Figure 19. Axial forces developed along the piles with different positions in the piled raft (border, corner and center), for: (a) Phase 2; and (b) Phase 6.

The obtained results show the importance of considering the negative skin friction on the pile design, the maximum axial load transmitted by the piles due to the structural service load is approximately 240 kN, whereas, when porewater pressure drawdown develops, the axial load increases to 560 kN, 2.3 times higher.

4. Conclusions

In this work a 3D numerical model based on the Finite Element Method (FEM) capable of simulating the complex behavior of a piled raft system founded in soft soils undergoing regional subsidence was developed and validated by the results obtained by a geotechnical centrifuge model. This model allowed to identify the most sensitive parameters for this type of simulation, to define the types and stages of analysis that had the best fit to the physical model, and to obtain additional results to those measured in the physical model as the magnitude of the developed negative skin fraction.

For the simulation of the soft soil behavior (kaolin) an advanced isotropic hardening double surface plasticity model (Hardening Soil Model, HSM) implemented in Plaxis software were used. The parameters for the HSM were obtained from oedometer and drained consolidated triaxial tests using the methodology proposed by Surarak et al. (2012) and Rodríguez-Rebolledo et al. (2019). The obtained parameters were satisfactorily calibrated and adjusted using the Soil Test tool from the Plaxis software.

Pile shaft and base resistance for long term behavior were obtained from a pile load test carried out in a centrifuge model, as they were also needed as input parameters for the chosen numerical model.

The developed numerical model reproduced satisfactorily soil and foundation consolidation displacements due, not only by the structural service load but also by the pore pressure drawdown (regional subsidence). For service load the maximum settlements reached up to 6 cm in the raft region. At the end of pore pressure drawdown, the maximum settlement was approximately 50 cm (8 times bigger). These comparative results do evidence the distinct phenomena and resulting engineering behavior that take place on a typical system founded in this type of environment.

For load distribution on piles and raft, the model reproduces with good agreement the foundation behavior only for the structural service load, for pore pressure drawdown some adjustments on the shaft and base resistance of the embedded piles elements had to be done.

For service loads differences between FEM and centrifuge models from 12 to 38% were obtained, while for pore pressure drawdown from -77 to -169%. Centrifuge model shows that from one stage to the other the load transmitted by piles increases (from 13% to 26%) while load transmitted by raft decreases (from 87 to 74%). As explained by Rodríguez-Rincón et al. (2018) this is because, when pore pressure drawdown occurs, the soil continues to settle, a movement that is not accompanied by the raft, generating an apparent emersion process, and hence, a reduction of contact between the soil and the raft. This phenomenon was not developing in the FEM model because the considered skin resistance of the piles was not enough to allow the generation of the negative skin friction necessary for this. The generated pore pressure drawdown produces an increment in effective stresses throughout the compressible soil, leading to an increase in shear resistance. The FEM results show that the embedded pile element does not consider the increase of the shear resistance parameters related to skin friction that happen when the soil is subjected to a consolidation process. To approximately match the models results (variations in the piles loads from -4 to 21%), it was necessary to adjust the base and axial skin resistance of the embedded piles elements in about 3.5 times, demonstrating the limitation in the use of this type of elements for the simulation of this kind of problems. To avoid this problem, two solutions were proposed:

1) determine the long-term base and skin resistance of the embedded piles using previously a simple 2D FEM model (axisymmetric), through the simulation of a load test of a single pile in a medium previously subjected to pore pressures drawdown;
2) use of volume elements for problems with a relatively small number of piles, the use of this type of elements can lead to exceptionally large finite element meshes and therefore high or even irrational computational costs (time and memory).

The model evidences the development of negative skin friction in the center, border and corner piles, being higher in the corner and lower in the center one. As excess pore pressure dissipates, the neutral level of the piles stabilizes at a depth between 15 to 16 m. These results agree with those reported by Auvinet & Rodríguez-Rebolledo (2017), they also demonstrate that the depth of such level depends significantly on the initial pile load conditions. The differences between piles in the magnitude of the axial loads is related to the corresponding influence area, e.g., the influence area of the corner pile is considerably larger than other piles leading to higher values of negative skin friction.

It is finally concluded that a simulation model for piled raft foundation systems founded on consolidation soft strata, via loading or porewater pressure drawdown, is feasible with a quite reasonable approximation of the field behavior/site conditions. This will be extremely useful for future design scenarios via parametric analysis of this same system, thus aiming to optimize the performance of this type of foundation structure when undergoing a regional subsidence phenomenon.

Acknowledgements

The research of the first author is possible through a scholarship provided by the Brazilian sponsorship organization named Conselho Nacional de Desenvolvimento Científico e Tecnológico - Brazil (CNPq), which is most appreciated. The authors also want to acknowledge the Universidad de Los Andes - Colombia for their support for the development of the centrifuge modeling, and Prof. Renato P. Cunha of the University of Brasília for the critical comments, and diligent support provided throughout the development of the numerical stage of this research.

Declaration of interest

The Authors declares that there is no conflict of interest that could inappropriately bias the work presented.

Author's contributions

Andrea J. Alarcón Posse: conceptualization, methodology, investigation, validation, writing - original draft. Juan F. Rodríguez Rebolledo: supervision, conceptualization, methodology. Julián A. Buriticá García: investigation. Bernardo Caicedo Hormaza: resources. Edgar Rodríguez-Rincón: resources.

References

Alnuaim, A.M., El Naggar, H., & El Naggar, M.H. (2017). Evaluation of piled raft performance using a verified 3D nonlinear numerical model. *Geotechnical and Geological Engineering*, 35(4), 1831-1845. http://dx.doi.org/10.1007/s10706-017-0212-1.

Alnuaim, A.M., El Naggar, M.H., & El Naggar, H. (2018). Performance of micropiled rafts in clay: numerical investigation. *Computers and Geotechnics*, 99, 42-54. http://dx.doi.org/10.1016/j.compgeo.2018.02.020.

Auvinet, G., & Rodriguez-Rebolledo, J. (2017). Criteria for the design of friction piles subjected to negative skin friction and transient loads. *Ingeniería, Investigación y Tecnología*, 18, 279-292. http://dx.doi.org/10.22201/fi.25940732e.2017.18n3.025.

Bajad, S.P., & Sahu, R.B. (2008). An experimental study on the behaviour of vertically loaded piled raft on soft clay. In *Proceedings of the 12th International Conference of International Association for Computer Methods and Advances in Geomechanics*, Goa, India.

Banerjee, S., Joy, M., & Sarkar, D. (2016). Parametric study and centrifuge-test verification for amplification and bending moment of clay-pile system subject to earthquakes. *Geotechnical and Geological Engineering*, 34(6), 1899-1908. http://dx.doi.org/10.1007/s10706-016-9999-4.

Brinkgreve, R. B. J., Kumarswamy, S. & Swolfs, W. M. (2018). *Reference manual and material models manual PLAXIS.* The Netherlands.

Cheng, S., Zhang, G., Zheng, R.H., & Sun, Z.Y. (2011). Centrifuge modeling of response of bridge due to exploiting groundwater. *Yantu Lixue*, 32(6), 1781-1786.

Cho, J., Lee, J.H., Jeong, S., & Lee, J. (2012). The settlement behavior of piled raft in clay soils. *Ocean Engineering*, 53, 153-163. http://dx.doi.org/10.1016/j.oceaneng.2012.06.003.

Cui, C., Luan, M., & Li, M. (2010a). A study on time-effects of piled raft system by using computational methods. In *Proceedings of the GeoShanghai International Conference 2010* (pp. 42-51), Shanghai, China.

Cui, Z.-D., Tang, Y.-Q., & Yan, X.-X. (2010b). Centrifuge modeling of land subsidence caused by the high-rise building group in the soft soil area. *Environmental Earth Sciences*, 59(8), 1819-1826. http://dx.doi.org/10.1007/s12665-009-0163-9.

El-Mossallamy, Y. (2008). Modeling the behaviour of piled raft applying Plaxis 3D Foundation Version 2. *Plaxis Bulletin*, (23), 1-4.

Goh, S.H., & Zhang, L. (2017). Estimation of peak acceleration and bending moment for pile-raft systems embedded in soft clay subjected to far-field seismic excitation. *Journal of Geotechnical and Geoenvironmental Engineering*, 143(11), 04017082. http://dx.doi.org/10.1061/(ASCE)GT.1943-5606.0001779.

Horikoshi, K., & Randolph, M.F. (1996). Centrifuge modelling of piled raft foundations on clay. *Geotechnique*, 46(4), 741-752. http://dx.doi.org/10.1680/geot.1996.46.4.741.

Khanmohammadi, M., & Fakharian, K. (2018). Evaluation of performance of piled-raft foundations on soft clay: a case study. *Geomechanics and Engineering*, 14(1), 43-50. http://dx.doi.org/10.12989/gae.2018.14.1.043.

Lee, C.Y. (1993). Pile groups under negative skin friction. *Journal of Geotechnical Engineering*, 119(10), 1587-1600.

Lee, J., Kim, Y., & Jeong, S. (2010). Three-dimensional analysis of bearing behavior of piled raft on soft clay. *Computers and Geotechnics*, 37(1-2), 103-114. http://dx.doi.org/10.1016/j.compgeo.2009.07.009.

Luo, R., Yang, M., & Li, W. (2018). Normalized settlement of piled raft in homogeneous clay. *Computers and Geotechnics*, 103, 165-178. http://dx.doi.org/10.1016/j.compgeo.2018.07.023.

Mali, S., & Singh, B. (2018). Behavior of large piled-raft foundation on clay soil. *Ocean Engineering*, 149, 205-216. http://dx.doi.org/10.1016/j.oceaneng.2017.12.029.

Ng, C.W.W. (2014). The state-of-the-art centrifuge modelling of geotechnical problems at HKUST. *Journal of Zhejiang University. Science A*, 15(1), 1-21. http://dx.doi.org/10.1631/jzus.A1300217.

Nordal, S. (1999). Present of PLAXIS. In R.B.J. Brinkgreve (Ed.), *Beyond 2000 in Computational Geotechnics: ten years of PLAXIS International* (pp. 45-54). London: Routledge.

Oliveira, B. (2018). *Avaliação do atrito negativo em grupos de estacas assentes em solos moles* [Master's dissertation]. Universidade de Brasília.

Rodríguez Rebolledo, J.F., Auvinet-Guichard, G.Y., & Martínez-Carvajal, H.E. (2015). Settlement analysis of friction piles in consolidating soft soils. *Dyna*, 82(192), 211-220. http://dx.doi.org/10.15446/dyna.v82n192.47752.

Rodríguez-Rebolledo, J.F. (2011). *Modeling behavior of piles and inclusions under regional consolidation in the lake area of Mexico City* (244 p.). Mexico: National Autonomous University of Mexico. (In Spanish).

Rodríguez-Rebolledo, J.F., León, R.F.P., & Camapum de Carvalho, J. (2019). Obtaining the mechanical parameters for the hardening soil model of tropical soils in the city of Brasília. *Soils and Rocks*, 42(1), 61-74. http://dx.doi.org/10.28927/SR.421061.

Rodríguez-Rincón, E. (2016). *Experimental analysis of piled raft systems in consolidating soft soils* (261 p.). Brasília: Universidade de Brasília. (In Portuguese).

Rodríguez-Rincón, E., Cunha, R.P., & Caicedo Hormaza, B. (2020). Analysis of settlements in piled raft systems founded in soft soil under consolidation process. *Canadian Geotechnical Journal*, 57(4), 537-548. http://dx.doi.org/10.1139/cgj-2018-0702.

Rodríguez-Rincón, E., Cunha, R.P., & Caicedo, B. (2018). Behaviour of piled raft foundation systems in soft soil with consolidation process. In *Proceedings 9th Int. Conf. on Physical Modelling in Geotechnics*, London.

Roy, S., & Chattopadhyay, B. C. (2011). Piled-Raft foundation behaviour on consolidating soft soil. In *Proceedings of the International Conference on Structural Engineering Construction and Management*, Kandy.

Schanz, T., Vermeer, P. A., & Bonnier, P. G. (1999). The hardening soil model: formulation and verification. In R.B.J. Brinkgreve (Ed.), *Beyond 2000 in Computational Geotechnics: ten years of PLAXIS International* (pp. 281-296). London: Routledge.

Sinha, A., & Hanna, A.M. (2017). 3D numerical model for piled raft foundation. *International Journal of Geomechanics*, 17(2), 04016055. http://dx.doi.org/10.1061/(ASCE)GM.1943-5622.0000674.

Sun, Z., Zhang, G., Zhang, J., Li, G., & Zheng, R. (2008). Centrifuge modeling of ground settlement due to groundwater pumping. *China Civil Engineering Journal*, 41(4), 67-72.

Surarak, C., Likitlersuang, S., Wanatowski, D., Balasubramaniam, A., Oh, E., & Guan, H. (2012). Stiffness and strength parameters for hardening soil model of soft and stiff Bangkok clays. *Soil and Foundation*, 52(4), 682-697. http://dx.doi.org/10.1016/j.sandf.2012.07.009.

Tang, Y.Q., Ren, X., Chen, B., Song, S., Wang, J.X., & Yang, P. (2012). Study on land subsidence under different plot ratios through centrifuge model test in soft-soil territory. *Environmental Earth Sciences*, 66(7), 1809-1816. http://dx.doi.org/10.1007/s12665-011-1406-0.

Thaher, M., & Jessberger, H. (1991). Investigation of the behaviour of pile-raft foundation by centrifuge modelling. In *Proceedings of the 10th European Conference on Soil Mechanics and Foundation Engineering* (Vol. 2, pp. 597-603), Firenze, Itália.

van Tran, T., Kimura, M., & Boonyatee, T. (2012b). 3D FE analysis of effect of ground subsidence and piled spacing on ultimate bearing capacity of piled raft and axial force of piles in piled raft. *Open Journal of Civil Engineering*, 2(4), 206-213. http://dx.doi.org/10.4236/ojce.2012.24027.

van Tran, T., Teramoto, S., Kimura, M., Boonyatee, T., & Vinh, L.B. (2012a). Effect of ground subsidence on load sharing and settlement of raft and piled raft foundations. *Stress*, 1(3), 120-127.

Wang, J., Huang, T., & Sui, D. (2013). A case study on stratified settlement and rebound characteristics due to Dewatering in Shanghai Subway Station. *The Scientific World Journal*, 2013, 213070. http://dx.doi.org/10.1155/2013/213070.

Watcharasawe, K., Kitiyodom, P., & Jongpradist, P. (2015). Numerical analyses of piled raft foundation in soft soil using 3D-FEM. *Geotechnical Engineering*, 46(1), 109-116.

Zhang, L., & Liu, H. (2017). Seismic response of clay-pile-raft-superstructure systems subjected to far-field ground motions. *Soil Dynamics and Earthquake Engineering*, 101, 209-224. http://dx.doi.org/10.1016/j.soildyn.2017.08.004.

Zhang, L., Goh, S.H., & Liu, H. (2017b). Seismic response of pile-raft-clay system subjected to a long-duration earthquake: centrifuge test and finite element analysis. *Soil Dynamics and Earthquake Engineering*, 92, 488-502. http://dx.doi.org/10.1016/j.soildyn.2016.10.018.

Zhang, L., Goh, S.H., & Yi, J. (2017a). A centrifuge study of the seismic response of pile-raft systems embedded in soft clay. *Geotechnique*, 67(6), 479-490. http://dx.doi.org/10.1680/jgeot.15.P.099.

List of symbols

α is an auxiliary parameter of the model
β auxiliary parameter of the model related to the reference tangent stiffness modulus for oedometric loading
γ_p plastic shear strain
φ' Internal friction angle
σ'_3 confining stress in the triaxial test
ψ dilatancy angle
c' Cohesion
ε axial strain
ε_1 vertical strain
ε_1^p plastic axial strain
ε_v^{pc} volumetric plastic strains in isotropic compression
ε_v^p plastic volumetric strain
E_i initial stiffness
E_{oed} axial stress-dependent stiffness modulus for primary oedometric loading
E_{50} is the confining stress-dependent stiffness modulus for the primary load
E_{ur} stress-dependent stiffness modulus for unloading and reloading stress
E_{50}^{ref} reference secant stiffness modulus for the drained triaxial test
E_{oed}^{ref} reference tangent stiffness modulus for oedometric loading
E_{ur}^{ref} reference stiffness modulus for unloading and reloading conditions
f^c cap compression hardening yield function
f_s shear hardening yield function
K_o^{nc} coefficient of earth pressure at rest (NC state)
K_o coefficient of earth pressure at rest
m Exponential power
OCR Over Consolidation Ratio
p is the isotropic stress
p_p is the pre-consolidation isotropic stress
p_{ref} Stress of reference
q deviatoric stress
q_a asymptote of the shear strength
q_f ultimate deviatoric stress at failure
$\tilde{q}$ is the special stress measurement for deviatoric stresses
R_f failure ratio
v_{ur} Unloading/reloading Poisson's Ratio

Soils and Rocks
An International Journal of Geotechnical and Geoenvironmental Engineering
www.soilsandrocks.com
ISSN 1980-9743
ISSN-e 2675-5475

Unconfined compression strength of an artificially cemented aeolian dune sand of Natal/Brazil

Tahyara Barbalho Fontoura[1,2#], Olavo Francisco dos Santos Junior[3], Ricardo Nascimento Flores Severo[4], Roberto Quental Coutinho[2], Paulo Leite de Souza Junior[5]

Article

Keywords
Unconfined compression
Cemented sand
Dune sand
Natal sand
Strength compression

Abstract

Soil behavior is influenced by the void ratio and bonds between grains. The aim of this study was to describe the strength behavior of an aeolian sand from the dunes of Natal, Brazil, artificially cemented in unconfined compression tests. The influence of cement content and moisture on molding and the validity of using the void/cement factor in estimating unconfined compression strength (UCS) were assessed. Tests were conducted with samples using three molding moisture contents (6, 9 and 12%), four cement contents (2.5, 5.0, 7.5 and 10%) and a void ratio of 0.6 (D_r = 95%). The results showed that unconfined compression strength rises with increase in cement content and decreasing in molding moisture. The void/cement factor proved to be a reliable parameter in predicting the behavior of sand from Natal for the dosage of soil cement.

1. Introduction

Mixing cemented agents with soil is a traditional soil enhancement technique that has been used for highway paving, foundations, retaining walls and to prevent liquefaction. In recent decades, a number of studies have been conducted to understand the behavior of cemented soil (in which the grains are held together by a chemical agent) (Saxena & Lastrico, 1978; Clough et al., 1979, 1981; Acar & El-Thair, 1986; Das et al., 1995; Schnaid et al., 2001; Haeri et al., 2005). Studies demonstrate that an increase in cement content causes a rise in strength and stiffness of the mixture.

Consoli et al. (2007) studied the influence of cement content, porosity and molding moisture on the compression strength of cemented soil and found that compression strength increases with cement content and exponentially as porosity declines, thereby obtaining a correlation between strength and the void-volumetric cement content ratio. Based on these findings, Consoli et al. (2007) proposed a rational method to determine the cement content and porosity necessary to obtain a given strength. According to Consoli et al. (2007), strength is a function of the η/C_{iv} ratio, with the volumetric cement content adjusted by an exponent x.

Several studies have assessed the validity of using the void/cement factor to estimate the strength of soil-cement mixtures. According to Cruz (2008), studies with sand from Osorio, Rio Grande do Sul state (RS) show that the void/cement factor is an effective and reliable parameter for predicting the behavior of the material according to the dosage of cemented soil in geotechnical projects. Similar results were obtained by Severo (2011) for lateritic soils from the Barreiras Formation on the coast of Rio Grande do Norte state (RN). What differed from one result to another was the value of the adjustment coefficient (x). Rios et al. (2013) showed that parameter x depends on the grain size and mineralogy of the soil.

Baldovino et al. (2018) studied the treatment of the Guabirotuba geological formation soil (Paraná Basin, Brazil) by lime addition for improve its usability in pavement construction, in protection of hillsides and slopes, or as shallow foundation support. It was observed that the q_t/q_u ratio is between 0.17 and 0.2 in relation to the curing time, and an exponential relation exists between them. Baldovino et al. (2020b) optimized and compared the behavior of soil-cement compacted blends against several molding and climate conditions under optimum compaction and non-optimum compaction parameters. The results show an increase in strength and durability properties of the blends when cement

#Corresponding author. E-mail address: tahyara.barbalho@ifrn.edu.br
[1]Instituto Federal de Educação, Ciência e Tecnologia do Rio Grande do Norte, Diretoria Acadêmica, São Paulo do Potengi, RN, Brasil.
[2]Universidade Federal de Pernambuco, Departamento de Engenharia Civil, Recife, PE, Brasil.
[3]Universidade Federal do Rio Grande do Norte, Departamento de Engenharia Civil, Natal, RN, Brasil.
[4]Instituto Federal de Educação, Ciência e Tecnologia do Rio Grande do Norte, Departamento de Construção Civil, Natal, RN, Brasil.
[5]Universidade Federal do Rio Grande do Norte, Natal, RN, Brasil.

Submitted on April 6, 2020; Final Acceptance on January 27, 2021; Discussion open until May 31, 2021.
DOI: https://doi.org/10.28927/SR.2021.049920

is added and reasonable dosages employing η/C_{iv} index to stabilize the soil were presented considering the strength and the durability parameters.

Baldovino et al. (2020a) evaluates the development of splitting tensile strength (q_t) and unconfined compressive strength (q_u) of two silty soils artificially cemented over 28 days. The results show an increase of the mechanical resistance with the increase of the cement content and with the decrease of the voids. A dosing equation for q_u and q_t of the soils studied and mixed with cement was developed using the η/C_{iv} ratio adjusted to an exponent 0,44 to make η/C_{iv} - q_u and η/C_{iv} - q_t variation rates compatible. The dosage equations obtained coefficients of determination above 94%.

Given this approach, the present study aimed to describe the strength behavior of a cemented sand and assess the influence of molding moisture content on the strength of the sand-cement mixture. This study used Aeolian sand sediments that form dunes, situated on the campus of the Federal University of Rio Grande do Norte (UFRN).

2. Materials and methods

2.1 Materials

The sand used here originated in dune sediments from the Dunes Park of Natal, a dune field on the coast of Natal, with an average width of 1.5 km and length of 9 km. Nearby is the Federal University of Rio Grande do Norte, where the samples were collected. This soil accounts for most of the subsoil of the city of Natal.

According to Jesus (2002), the geology of the area is essentially formed by materials of sedimentary origin, like the entire city of Natal. In Dunes Park it is possible to observe the outcrop of sediments from aeolian dunes field, study material of this work. These sediments are made up of quartzous sands, with grains sub-rounded to sub-angular, poorly selected, with a solid aspect.

The soil grain size distribution curve is presented in Figure 1 and the physical indices in Table 1. The soil is composed of approximately 72% medium sand and 4% fine grains. According to grain size analysis, this material can be classified (ASTM, 2006a) as a uniform, poorly graded medium-grained sand (SP).

High early-strength Portland cement (Type III) was used as cementing agent (ASTM, 2009). Portland cement was selected because it was used in previous studies (Consoli et al., 2007, 2012a, b; Cruz, 2008; Cruz & Consoli, 2010; Severo, 2011; Rios et al., 2013).

In geotechnics, the void ratio (e) is one of the most important parameters for expressing the engineering behavior of soils (Monkul, 2005). Çellek (2019) investigated the linear relationship between e_{max} and e_{min}. considering 3 types of clean marine sand. Figure 2 shows the line describing this relationship between e_{max} and e_{min}. Plotting on the chart the point referring to the sand of Natal dune, it is clear that it is consistent with the studies of Çelek (2019).

2.2 Experimental program and test methods

Unconfined compression tests were conducted for 3 molding moisture (6, 9 and 12%) and 4 cement contents (2.5%, 5.0%, 7.5% and 10.0%). The 0.6 void ratio used was near the minimum value.

The cement content values adopted are within the range reported in the literature. Consoli et al. (2007) used percentages between 1 and 7%; Cruz (2008) between 1 and 12%; Consoli et al. (2012a) between 3 and 9% and Severo (2011) between 2 and 5%. The moisture content values studied

Table 1. Physical indices for sand from Natal.

Specific gravity	2.62
Coefficient of Uniformity C_u	1.861
Coefficient of Curvature C_c	0.971
Effective Diameter, D_{10}	0.153
Mean Diameter, D_{50}	0.25
Minimum Void Ratio e_{min}	0.59
Maximum Void Ratio e_{max}	0.80

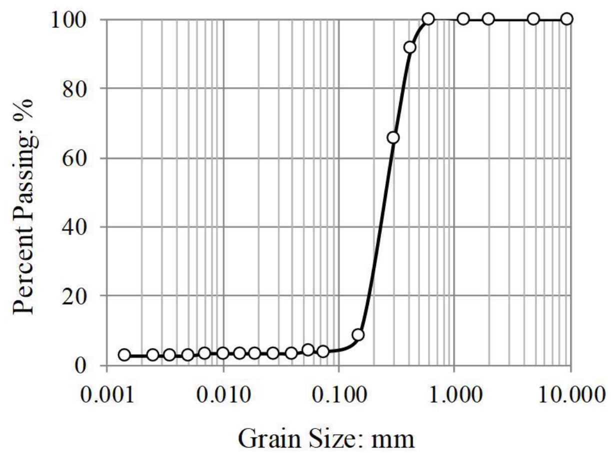

Figure 1. Grain size distribution curve.

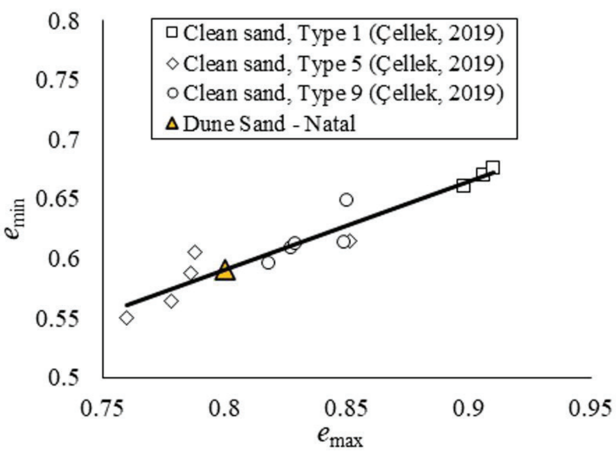

Figure 2. Relationship between e_{min} and e_{max} for marine sands (Çellek, 2019) and Natal Dune Sand.

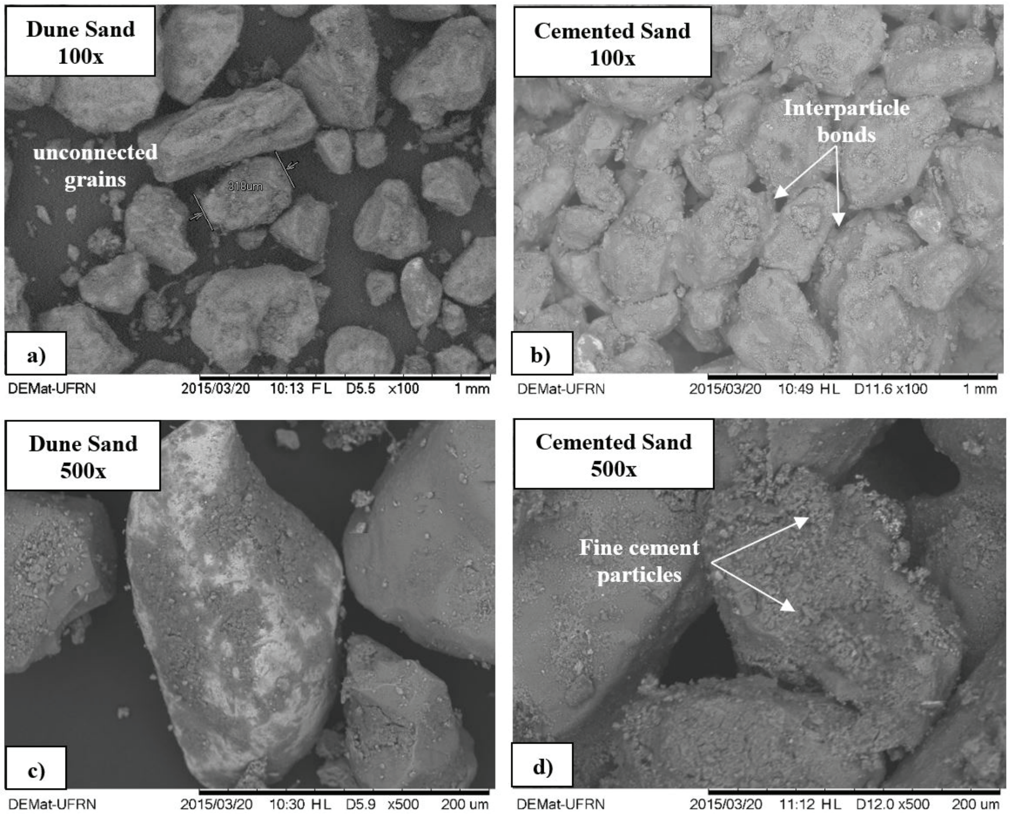

Figure 3. (a) Dune sand grains, - 100x magnification; (b) Cemented sand - 100x magnification; (c) Dune sand - 500x magnification grains; (d) cemented sand - 500x magnification.

were within the range used by Consoli et al. (2007), between 4 and 13.4%, and Consoli et al. (2012b), between 6 and 14%.

The cement and molding moisture used contributed to form interparticle bonds, making the soil structured by cementation. According to Prietto (2004), the structure provides the soil, when it is compared to the same material in the reconstituted (unstructured) state, with significantly superior strength and stiffness. This aspect is illustrated in Figure 3, where can be seen scanning electron microscopy (SEM) images of the dune sand sample and the cemented sand sample. As shown in Figure 3a and 3b, there is no interparticle bonds in the dune sand grains of Natal. When cement and water are added, as shown in Figure 3c and 3d, there is a connection between the grains of sand that are surrounded by fine cement particles.

2.2.1 Test specimen molding and curing

For all the tests, the samples were molded with a diameter of approximately 50 ± 1 mm and height of 100 ± 5 mm. The mixtures were prepared with the required amounts of sand, distilled water and cement, in order to reach the percentage of cement, moisture content and void ratio established for each sample. The soil-cement-water mixtures were compacted into a tripartite cylindrical mold. The samples were compacted into four layers, aimed at reaching the void ratio specified for each sample. Three test specimens were molded for each test condition.

After molding, the samples were cured for 30 days. During curing, the samples remained in conditions of high humidity in a humid box with a bottom covered with saturated sand to avoid premature evaporation of the water necessary for the hydration of the cement. The samples were cured for 30 days to ensure that the specimens reached the maximum possible strength.

2.2.2 Unconfined compression strength tests

The unconfined compression tests followed the procedures described in NBR 12025 (ABNT, 2012a), which is equivalent to ASTM D 2166-06 (ASTM, 2006b). For these tests, the strain rate applied in the tests was 1 mm/min.

After 30 days' curing, the test specimens were submerged in water for 4 hours before the test, in line with NBR 12025 (ABNT, 2012a). Just before the test, the test specimens were removed from the water and superficially dried with an absorbent fabric.

The eligibility criterion adopted for the unconfined compression strength test was that recommended by NBR 12253 (ABNT, 2012b). As such, the individual strengths of the three identical specimens could not be more than 10% different from their average. Thus, in the present study, in which 36 unconfined compression tests were performed, 30 tests that met the eligibility criterion will be presented.

3. Results and analyses

This section presents the results of the unconfined compression tests specified in the previous item. Figures 4 to 10 show the graphs obtained in the tests. The graphs show unconfined compression strength as a function of the cement content, molding moisture and void/cement ratio.

3.1 Effect of cement and molding moisture content

Figure 4 presents the results of the unconfined compression strength of the samples as a function of molding moisture content.

Unconfined compression strength increases with an increasing in cement content, for the three moisture contents analyzed. For the lowest cement content (2.5%), molding moisture content has little influence on unconfined compression strength. Thus, the higher the cement content, the greater the influence of molding moisture content. All the fitted curves exhibited similar shape, and all coefficients of determination (R^2) were above 0.97 (see the equations in Figure 4). This beneficial effect from an increase in cementation was reported by Consoli et al. (2009).

Figure 5 presents the results of the unconfined compression strength as a function of molding moisture content, for the samples with different cement content. An increase in strength with a decline in molding moisture content was observed. This graph also demonstrated the minor influence that molding moisture content exerts on samples with low cement content, compared to their counterparts with higher levels (7.5 and 10%). All the fitted curves exhibited coefficients of determination (R^2) above 0.87 (see the equations in Figure 5).

3.2 Effect of the water/cement ratio

The data illustrated in Figure 5 for cement contents of 2.5 to 10% were used to construct Figure 6, which shows unconfined compression strength as a function of the water/cement (w/C_i) ratio (defined as the weight of the water divided by the weight of the cement). A relationship can be established between these two factors, and compression strength rises with a decline in the w/C_i ratio. This relationship was reported by Horpibulsuk et al. (2003), in which the water/cement ratio was a useful parameter for analyzing the strength of materials, as occurs in concrete, where the amount of water once again reflects the amount of voids in mixture.

3.3 Effect of the void-cement ratio

Figure 7 presents unconfined compression strength as a function of the void/cement ratio, defined by the following equation:

$$\frac{V_v}{V_{ci}} = \frac{\textit{Void volume}}{\textit{Cement volume}} \tag{1}$$

The data exhibited in Figure 7 shows a correlation between this ratio and the unconfined compression strength (q_u) of the soil-cement mixture studied, whereby the larger the V_v/V_{ci}, the lower the sample strength, because the higher the void space. In addition, the larger this ratio, the smaller the effect of molding moisture content. This is probably because as the void volume becomes significantly greater

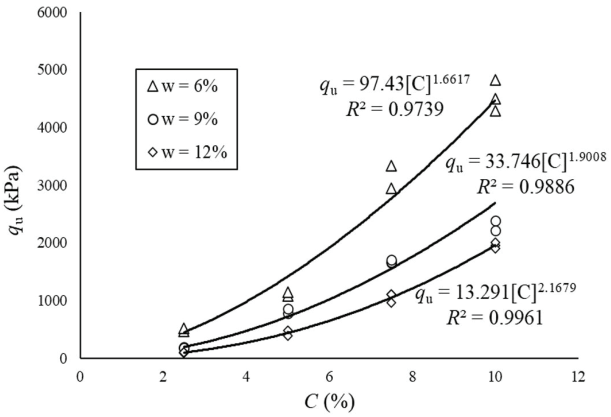

Figure 4. Variation in unconfined compression strength with cement content.

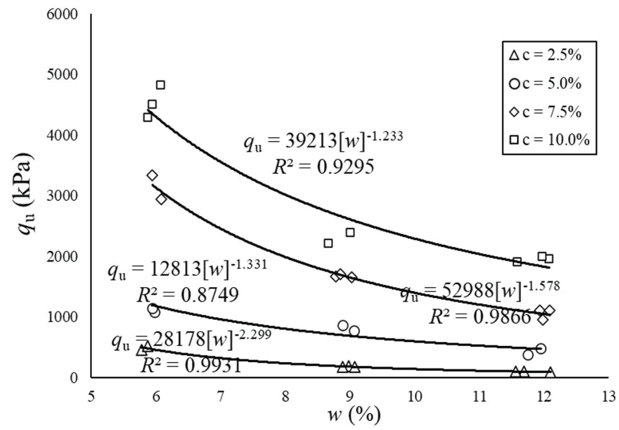

Figure 5. Effect of molding moisture content on unconfined compression strength.

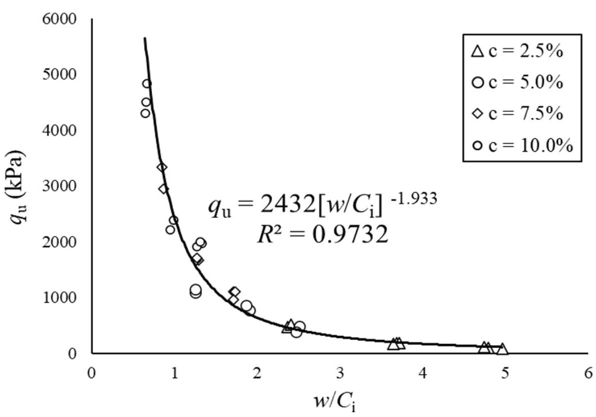

Figure 6. Variation in unconfined compression strength with the water/cement ratio.

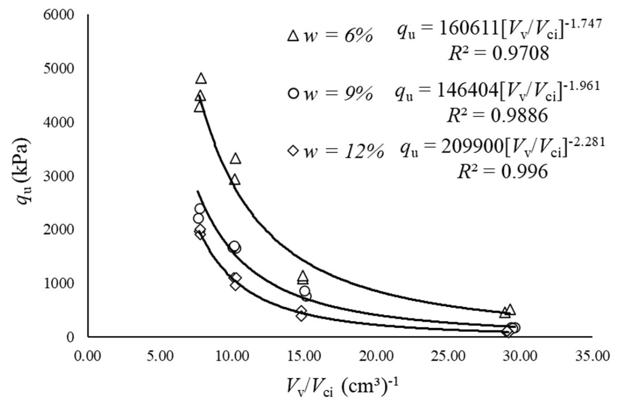

Figure 7. Variation in unconfined compression strength with the void volume/cement volume ratio.

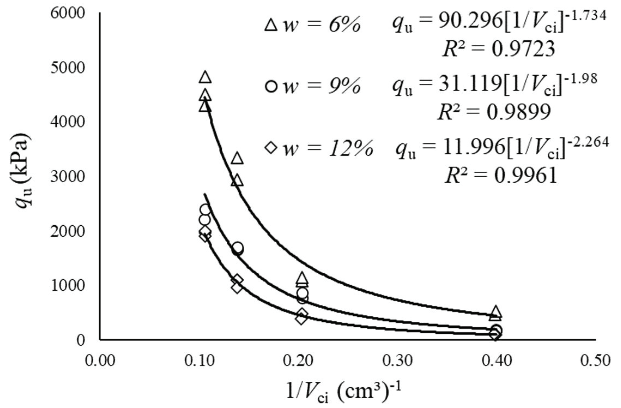

Figure 8. Relationship between inverse cement volume and unconfined compression strength

than the volume of cement becomes more difficult to form the bonds between the particles of cement, water and soil. This behavior was different from that reported by Consoli et al. (2009), who found no correlation between these parameters.

Figure 8 graphically presents the unconfined compression strength variation with an inverse cement volume for the moisture contents studied. The influence of V_v/V_{ci} and $1/V_{ci}$ ratios on strength was found to be very similar. This exponential growth of strength with a decline in the inverse ratio of cement volume was reported by Consoli et al. (2009).

Figure 9 shows unconfined compression strength as a function of the void/cement ratio, defined by the ratio (η/C_{iv}) between the porosity of the compacted mixture (η) and volumetric cement content (C_{iv}) for the three molding moisture contents used in the mixtures and different cement contents applied. Figure 9 shows the influence of the η/C_{iv} factor and moisture content on the unconfined compression strength of the artificially cemented sand. It can be concluded that the higher the void/cement ratio (η/C_{iv}), the lower the unconfined compression strength. Additionally, the lower the molding moisture content, the higher the strength, considering the molding moisture content between 6 and 12% studied here.

The void/cement factor, defined by the η/C_{iv} ratio, adjusted by an exponent ($\eta/(C_{iv})^{\xi}$), has proved to be adequate in assessing unconfined compression and triaxial shear strength for previously studied soils (Consoli et al., 2007). Figure 9 shows that the exponent to which the curve best fits was equal to 1. This fitted exponent (ξ) is bigger than that of the finer soil grains previously studied, and compatible with the fine sand content of the samples. Table 2 presents the exponent values (ξ) for some of the soils previously studied which corroborates the relationship between grain size and the cement void ratio.

Figure 10 shows the comparison of the unconfined compression strength versus void/cement ratio curves for the Natal Dune Sand and the Osório Sand (Consoli et al., 2011). According to Consoli et al. (2011), the exponent that adjusts the curve increases with the increase in the particle

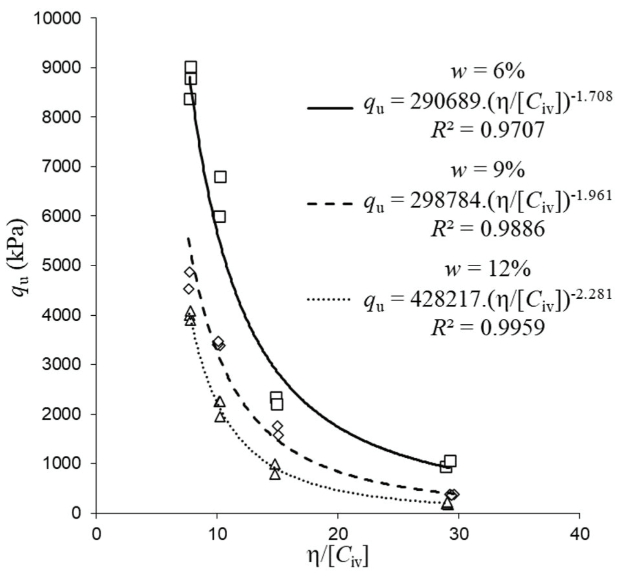

Figure 9. Variation in unconfined compression strength with the adjusted void/cement ratio.

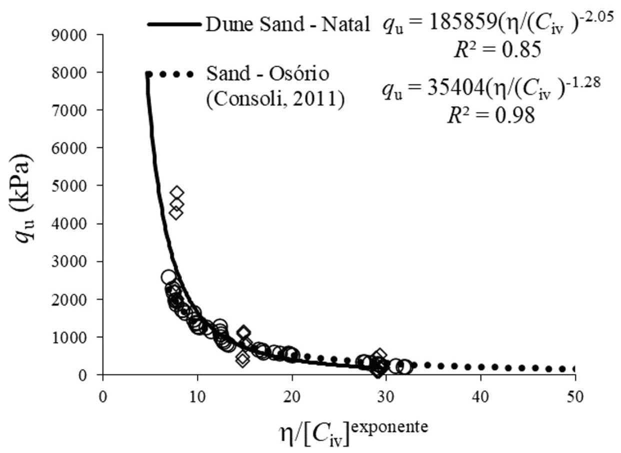

Figure 10. Variation in unconfined compression strength with the adjusted void/cement ratio for the Dune Natal Sand and Osório Sand (Consoli et al., 2011).

Table 2. Exponent values (ξ) of previously studied soils.

Type of soil (USCS)	Fine grains content (%)	Exponent value (ξ) $\eta/(C_{iv})^{\xi}$	Reference
Clayey sand (SC)- Porto Alegre, RS	41	0.28	Consoli et al. (2007)
Fine sand (SP) Osorio, RS	2	1.00	Consoli et al. (2011)
Clayey sand (SC) Ponta do Pirambu, RN	40	0.60	Severo (2011)
Silty sand (SM) Porto, Portugal	32	0.21	Rios et al. (2013)
Yellow and purple silt (MH) Guabirotuba Formation of Curitiba/Brazil	65-67	0.44	Baldovino et al. (2020a)
Aeolian Dune sand (SP) Natal, RN	4	1.00	The present study

size of the material. However, the same exponent was found for both sands and the curves almost intercept.

4. Final considerations

The behavior of the artificially cemented sand from the dunes of Natal depends on the void ratio, cement percentage and molding moisture content.

Unconfined compression strength increases with an increasing in the amount of cement and a decline in molding moisture content for all the samples studied. For the lowest cement content (2.5%), molding moisture content had little influence on unconfined compression strength. Thus, the higher the cement content, the greater the influence of molding moisture content, and the higher the inverse ratio of cement volume, the lower the strength of the samples. It was also found that the higher the inverse ratio of cement volume, the lower the effect of molding moisture content.

Analysis of the void/cement factor reveals that the higher the void/cement ratio (η/C_{iv}), the lower the unconfined compression strength. The fitted exponent of the q_u x η/C_{iv} curve for the sand of Natal is equal to 1. Thus, the void/cement ratio and the water/cement factor are good dosage parameters for mixtures cement- dune sands. Artificially cemented sand can be used below of shallow foundations for improvement the bearing capacity and as backfill in retaining wall, as pure dune sand is not good material for these applications. The results obtained in this work can be useful for the definition of the cement content and the compaction energy to be used to improve the Natal sand.

Acknowledgements

The authors are grateful to FAPERN (Research Support Foundation of Rio Grande do Norte State), CAPES (Coordination of Improvement of Higher Education Personnel) and CNPq (National Council for Scientific and Technological Development) for funding this study.

Declaration of interest

The authors declare the absence of conflicting interests.

Author's contributions

All authors contributed to the study conception and design. Material preparation, data collection and analysis were performed by Tahyara Barbalho Fontoura, Olavo Francisco dos Santos Junior, Ricardo Nascimento Flores Severo, Roberto Quental Coutinho and Paulo Leite de Souza Junior. The first draft of the manuscript was written by Tahyara Barbalho Fontoura and all authors commented on previous versions of the manuscript. All authors read and approved the final manuscript.

References

ABNT NBR 12025. (2012a). *Solo-cimento: ensaio de compressão simples de corpos-de-prova cilíndricos*. Associação Brasileira de Normas Técnicas, Rio de Janeiro.

ABNT NBR 12253. (2012b). *Solo-cimento: dosagem para emprego como camada de pavimento*. Associação Brasileira de Normas Técnicas, Rio de Janeiro.

Acar, Y.B., & El-Thair, E.A. (1986). Low strain dynamic properties of artificially cemented sand. *Journal of Geotechnical Engineering*, 112(11), 1001-1015. http://dx.doi.org/10.1061/(ASCE)0733-9410(1986)112:11(1001).

ASTM D2487-06. (2006a). *Standard practice for classification of soils for engineering purposes: unified soil classification system* (12 p.). ASTM International, West Conshohocken. https://doi.org/10.1520/D2487-06.

ASTM D2166-06. (2006b). *Standard test method for unconfined compressive strength of cohesive soil* (6 p). ASTM International, West Conshohocken.https://doi.org/10.1520/D2166-06.

ASTM C 150-09. (2009). *Standard specification for Portland cement* (10 p.). ASTM International, West Conshohocken. https://doi.org/10.1520/C0150_C0150M-09.

Baldovino, J.J.A., Izzo, R.L.S., Teixeira, W., & Pereira, M.D. (2020a). Variáveis que influenciam na resistência à tração e à compressão simples de dois solos sedimentares estabilizados com cimento. *Revista Matéria*, 25(2), e-12615. http://dx.doi.org/10.1590/s1517-707620200002.1015.

Baldovino, J.J.A., Izzo, R.L.S., & Rose, J.L. (2020b). Advances on dosages for cement stabilized rammed Guabirotuba silt depending on climate conditions. *Soils and Rocks*, 43(4), 631-645. http://dx.doi.org/10.28927/SR.434631.

Baldovino, J.J.A., Moreira, E.B., Teixeira, W., Izzo, R.L.S., & Rose, J.L. (2018). Effects of lime addition on geotechnical properties of sedimentary soil in Curitiba, Brazil. *Journal of Rock Mechanics and Geotechnical Engineering*, 10(1), 188-194. http://dx.doi.org/10.1016/j.jrmge.2017.10.001.

Çellek, S. (2019). The effect of shape on the linear relationship of maximum and minimum void ratios of various sand types. *Geotechnical and Geological Engineering*, 37(5), 3701-3713. http://dx.doi.org/10.1007/s10706-019-00862-9.

Clough, G.W., Kuck, W., & Kasali, G. (1979). Silicate-stabilized sands. *Journal of Geotechnical Engineering*, 105(1), 65-81. http://dx.doi.org/10.1016/0148-9062(79)91413-X.

Clough, G.W., Sitar, N., Bachus, R.C., & Shafii Rad, N. (1981). Cemented sands under static loading. *Journal of Geotechnical Engineering*, 107(6), 799-817. http://dx.doi.org/10.1016/0148-9062(81)90544-1.

Consoli, N.C., Foppa, D., Festugato, L., & Heineck, K.S. (2007). Key parameters for strength control of artificially cemented soils. *Journal of Geotechnical Engineering*, 133(2), 197-205. http://dx.doi.org/10.1061/(ASCE)1090-0241(2007)133:2(197).

Consoli, N.C., Viana da Fonseca, A., Cruz, R.C., & Heineck, K.S. (2009). Fundamental parameters for the stiffness and strength control of artificially cemented sand. *Journal of Geotechnical and Geoenvironmental Engineering*, 135(9), 1347-1353. http://dx.doi.org/10.1061/(ASCE)GT.1943-5606.0000008.

Consoli, N.C., Cruz, R.C., & Floss, M.F. (2011). Variables controlling strength of artificially cemented sand: influence of curing time. *Journal of Materials in Civil Engineering*, 23(5), 692-696. http://dx.doi.org/10.1061/(ASCE)MT.1943-5533.0000205.

Consoli, N.C., Stracke, F., Jung, J.G., & Korf, E.P. (2012a). A variação do teor de umidade de moldagem e a influência na resistência de uma areia artificialmente cimentada. In *XVI Anais do Congresso Brasileiro de Mecânica dos Solos e Engenharia Geotécnica* (Vol. 1, pp. 1-7), Porto de Galinhas.

Consoli, N.C., Fonseca, A.V., Silva, S.R., Cruz, R.C., & Fonini, A. (2012b). Parameters controlling stiffness and strength of artificially cemented soils. *Geotechnique*, 62(2), 177-183. http://dx.doi.org/10.1680/geot.8.P.084.

Cruz, R.C. (2008). *Influência de parâmetros fundamentais na rigidez, resistência e dilatância de uma areia artificialmente cimentada* [PhD Thesis]. Department of Civil Engineering, Federal University of Rio Grande do Sul. (In Portuguese).

Cruz, R.C., & Consoli, N.C. (2010). Metodologia de dosagem de um solo cimentado submetido à tração. In *Anais do XV Congresso Brasileiro de Mecânica dos Solos e Engenharia Geotécnica* (Vol. 1, pp. 1-4), Gramado.

Das, B.M., Yen, S.C., & Dass, R.N. (1995). Brazilian tensile strength test of lightly cemented samples. *Canadian Geotechnical Journal*, 32(1), 166-171. http://dx.doi.org/10.1139/t95-013.

Haeri, S.M., Hosseini, S.M., Toll, D.G., & Yasrebi, S.S. (2005). The Behaviour of an Artificially Cemented Sandy Gravel. *Geotechnical and Geological Engineering*, 23(5), 537-560. http://dx.doi.org/10.1007/s10706-004-5110-7.

Horpibulsuk, S., Miura, N., & Nagaraj, T.S. (2003). Assessment of strength development in cement-admixed high water content clays with Abram's Law as a basis. *Geotechnique*, 53(4), 439-444. http://dx.doi.org/10.1680/geot.2003.53.4.439.

Jesus, A.P. (2002). *Caracterização geológica, geomorfológica e geotécnica de um corpo de dunas na cidade de Natal-RN* [Master Thesis]. Department of Civil Engineering, Federal University of Rio Grande do Norte. (In Portuguese).

Monkul, M.M. (2005). *Influence of intergranular void ratio on the one dimensional compression* [PhD Thesis]. Dokuz Eylu¨l Unıversıty.

Prietto, P.D.M. (2004). *Resistência e Dilatância de Solos Cimentados: Uma abordagem Teórico-Experimental* [PhD Thesis]. Department of Civil Engineering, Federal University of Rio Grande do Sul. (In Portuguese).

Rios, S., Viana da Fonseca, A., Consoli, N.C., Floss, M., & Cristelo, N. (2013). Influence of grain size and mineralogy on the porosity/cement ratio. *Geotechnique*, 3(3), 130-136. http://dx.doi.org/10.1680/geolett.13.00003.

Saxena, S.K., & Lastrico, R.M. (1978). Static properties of lihtly cemented sand. *Journal of the Geotechnical Engineering Division*, 104(12), 1449-1465. http://dx.doi.org/10.1061/AJGEB6.0000728.

Schnaid, F., Prietto, P.D.M., & Consoli, N.C. (2001). Characterization of cemented sand in triaxial compression. *Journal of Geotechnical and Geoenvironmental Engineering*, 127(10), 857-868. http://dx.doi.org/10.1061/(ASCE)1090-0241(2001)127:10(857).

Severo, R.N.F. (2011). *Caracterização geotécnica da falésia da Ponta do Pirambu em Tibau do Sul – RN considerando a influência do comportamento dos solos nos estados indeformado e cimentado artificialmente* [PhD Thesis]. Department of Civil Engineering, Federal University of Pernambuco. (In Portuguese).

List of symbols

D_{50}: mean grain size
D_{10}: effective grain size
C: cement content
C_i: weight of the cement
C_u: uniformity coefficient
C_c: curvature coefficient
e_{min}: minimum void ratio
e_{max}: maximum void ratio
e: void ratio
q_u: unconfined compression strength
q_t: tensile strength
R_2: coefficient of determination
D_r: degree of compactness
η_{civ}: porosity of mixture
C_{iv}: volumetric cement content
V_v: void volume
V_{ci}: cement volume
w: moisture content
x: adjusted exponent

Soils and Rocks

An International Journal of Geotechnical and Geoenvironmental Engineering

www.soilsandrocks.com

ISSN 1980-9743
ISSN-e 2675-5475

Effects of underground circular void on strip footing laid on the edge of a cohesionless slope under eccentric loads

Tarek Mansouri[1], Rafik Boufarh[2#], Djamel Saadi[2]

Article

Keywords
Strip footing
Eccentric load
Slope
Underground void
Sand
Bearing capacity

Abstract

Owing to the comeback of small-scale models, this paper presents results of an experimental study based on the effect of underground circular voids on strip footing placed on the edge of a cohesionless slope and subjected to eccentric loads. The bearing capacity-settlement relationship of footing on the slope and impact of diverse variables are expressed using dimensionless parameters such as the top vertical distance of the void from the base of footing, horizontal space linking the void-footing centre, and load eccentricity. The results verified that the stability of strip footing is influenced by the underground void, as well as the critical depth between the soil and top layer of the void. The critical horizontal distance between the void and the centre was also affected by the underground void. Furthermore, the results also verified that the influence of the void appeared insignificant when it was positioned at a depth or eccentricity equal to twice the width of footing.

1. Introduction

The existence of an underground void on a foundation can cause serious engineering problems that destabilize it and expose its superstructure to severe damage, which could be very expensive and hazardous. The presence of underground voids negatively affects the ultimate bearing capacity of superficial foundations. Underground cavities that cross the subsoil can be generally categorized into two: artificial and natural. Artificial or man-made cavities result from urban installation, tunnelling, mining, and old conduits, including water and gas networks. Natural cavities are shaped by the dissolution of sedimentary rocks owing to the circulation of water (karst and natural gypsum), which forms cavities of widely varying sizes. In engineering practice, the existence of voids in the ground compromises the bearing capacity and structural integrity of foundations. These cavities indicate a very significant potential risk of collapse, especially in urban sectors where the stakes are high. Frequently, footings are positioned on a soil with voids that are either hidden before building or shaped after it. Extensive analytical and model studies have been carried out to investigate the behaviour of such soil. Several researchers have dealt with the impact of voids on the ultimate bearing capacity of foundations. Researchers such as (Atkinson & Potts, 1977; Badie & Wang, 1984; Baus & Wang, 1983; Wang & Badie, 1985) pioneered studies on voids and the load-carrying capacity of footing stability. They demonstrated how the presence of voids affects a certain critical region under the footing. The size of the critical region depends on numerous factors, such as: footing shape, soil property, void size, and void shape. Wang & Hsieh (1987) investigated the collapsed load of strip foundation on circular voids via the limit analysis theory, in which he reviewed several failure mechanisms. In 'Natural and artificial cavities as ground engineering hazards', Culshaw & Waltham (1987) briefly presented the different types of cavities, outlining the mode of creation and history of natural and artificial cavities, respectively. They proposed an outline process for tracing cavities and decreasing the risk of omission during site explorations. Then, via numerical analysis, Kiyosumi et al. (2007) determined that the failure zone emerged mainly from the adjacent footing-void and did not usually expand to other cavities. Additionally, this failure was less significant in soils without voids. A computational method was developed to approximately determine the yielding pressure of strip footing over numerous holes. Addressing the impact of voids on foundation stability, another research by Khalil & Khattab (2009) adopted a non-linear finite elements analysis method. The study verified that a significant zone exists under the footing 'radial shear and failure plane zone'. If a void is placed inside this zone, then the result will be critical. Settlement rate was observed for voids positioned in this zone below the foundation.

The experimental observation of Kiyosumi et al. (2011) demonstrated three sorts of failure modes for a single void, according to the void's size and position. Upper-bound calculations were presented to interpret the observed changes in bearing capacity. Mohamed (2012) carried out a numerical

#Corresponding author. E-mail address: rafik.boufarh@univ-tebessa.dz
[1]University of Batna 2, Faculty of Technology, Department of Civil Engineering, Research Laboratory in Hydraulic Applied LARHA, Batna, Algeria.
[2]Larbi Tebessi University, Faculty of Sciences and Technology, Department of Civil Engineering, Tebessa, Algeria.

Submitted on July 27, 2020; Final Acceptance on February 10, 2021; Discussion open until May 31, 2021.

DOI: https://doi.org/10.28927/SR.2021.055920

study based on the Plaxis software. The results obtained from this study confirmed that the stresses under the strip footing were augmented by 40% when the rock was encountered under the middle of the footing at a depth D of 0.5 m. Additionally, the stresses under the footing were altered when the buried rock was positioned away from the middle footing to the instability of the footing. Hussein (2014) presented results of finite element analysis for the stability of strip footing over circular continuous voids on sand. An equation was derived to define the relationship between the bearing capacity ratio and influencing feature. This equation provides a database for the design of continuous footing with an underground void at its centre. Lee et al. (2014) presented design charts estimating the undrained bearing capacity aspects as part of dimensionless factors connected to the vertical and horizontal cavity space from the footing, cavity size, and spacing between the two cavities, which contribute to soil rigidity and inconsistency. The ultimate bearing capacity is controlled by three different failures modes.

To explore the effect of inclination load on the bearing capacity of shallow continuous foundations situated on undrained clay soil with single and dual continuous cavities, small strain finite element analyses were performed by Lee et al. (2015). Additionally, they studied the influence of the position, form, and number of continuous voids. The results obtained are illustrated as normalized failure envelopes in the horizontal and vertical loading planes. Lavasan et al. (2016) numerically examined the bearing capacity and failure mechanism of a shallow strip foundation built above twin voids. The results obtained can be used to sketch the pattern of a footing on a cavity while the obtained failure mechanisms can be selected to improve analytical solutions. Moreover, it was inferred that a significant depth of the cavities and a critical space between them appear where the ultimate bearing capacity of the footing disappears. To study the impact of voids on the behaviour of strip footing under oblique load, Al-Jazaairry & Toma-Sabbagh (2017) applied the finite element analysis. They studied several footing cases, and in each case, an important depth appeared under which the existence of voids exposed the footing presented to minimum damage. When cavities were set up on this depth, the bearing capacity of the foundation varied according to the influence of many factors (position, size of the cavity, footing depth). The results obtained can be applied to create a shallow foundation laid on cavitied soil while the attained failure mechanisms can be utilized to develop numerical explanations to this sort of challenges. Zhou et al. (2018) examined the bearing capacity and failure mechanism of a perpendicular laden strip foundation on cohesive soil with square voids. The results indicate that the undrained bearing capacity with voids reacts to soil characteristics. The failure mechanism is linked to multiple soil properties, position of single voids, and straight space between two voids. Zhao et al. (2018) via the upper bound method carried out a study on the stability analysis of asymmetrical cavities. The results show that the stability numbers are augmented with an increase in the friction angle, but reduce with an increase in the horizontal distance and descriptor diameter values, with considerable asymmetrical failure mechanisms. The results also indicate that the major failure type for the soil near the cavity is the local shear failure. A clear bottom bulge fact is detected in the void at its small inner. Based on their results, Piro et al. (2018) noticed that a novel equivalent wave parameter was accurately defined to take into consideration the existence of the underground level and cavities in seismic soil-foundation-structure interactions. Then they suggested relationships between the most significant parameters controlling the interaction phenomena. Xiao et al. (2018a) examined the effects of voids on the bearing capacity of strip footing under the plane-strain state, where a reduction factor was delineated. The obtained results are illustrated in different design charts, and the critical failure mechanisms are represented. Xiao et al. (2018b) used finite element limit analysis to study the undrained bearing capacity of strip footing on voids in two-layered clays. Design charts and equations are presented to estimate the undrained bearing capacity factor Ns. The effect of the parameters on Ns has also been inspected, including the undrained shear stress ratio of the soil, thickness of the top layer, location, size, width, height, and spacing of the voids. Zhang et al. (2019) investigated the collapsed roof of deep circular voids in jointed rock masses via numerical analysis. The results are sketched in dimensionless stability diagrams and are compared with transformational findings conducted using the algorithm of an analytical upper bound solution. Then, based on the frictional Mohr-Coulomb model, and in accordance with the non-associated flow rule, Lee & Kim (2019) researched on the collapse of strip rigid foundations positioned on sandy soil with both single and dual continuous voids. The obtained results agree positively with existing theoretical and numerical solutions.

Throughout a series of laboratory-scale load tests, Jayamohan et al. (2019) investigated the impact of a subsoil cavity on the load-settlement behaviour of a strip foundation. The results show that the effect of cavities is significant when they reach a critical depth and eccentricity, after which the reinforced foundation bed develops the load-settlement behaviour of a soil with voids. Additionally, the existing subsoil cavities can lead to stress concentrations that trigger failure. Saadi et al. (2020) led an experimental inquiry on the impact of interference on the bearing capacity of dual adjoining foundations on a granular cavitied soil. The results revealed the influence of cavities and the interference of dual footings on the bearing capacity factor, as well as the efficiency factor. Then, the effects of the cavities vanished when the distance footings/cavities were greater than three.

The overall purpose of this study is to probe the impact of underground circular voids on the bearing-capacity behaviour of a shallow continuous footing located on the edge of a cohesionless slope (b/B=0) such as b is distance between foundation and the edge of a slope. To realise this objective, a strip pattern footing was experimented. Furthermore, a practical range of parameters were studied, such as the vertical distance of the top of void from the bottom of footing (H/B),

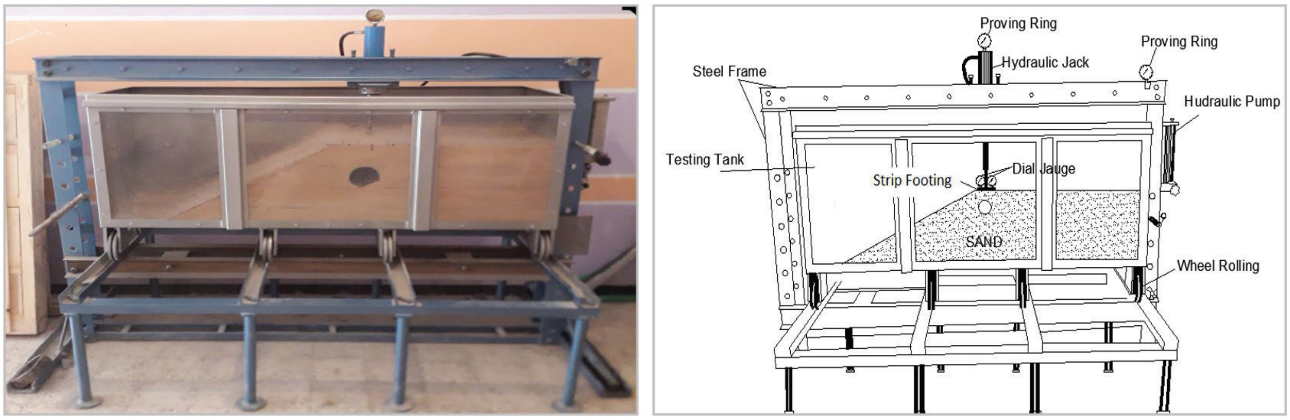

Figure 1. Experimental apparatus.

horizontal distance between cavities-footing centre (L/B), and various vertical load eccentricities (e/B).

2. Experimental apparatus

The experimental pattern tests were carried out in a tank with a dimension of 1.60 × 0.60 × 0.60 m. Figure 1 presents an illustration of the tank, which is made from steel with an entirely transparent plexiglass plate as the front part, and propped up with eight wheels rolling on straight steel support girders. The purpose of the rollers is to pull the box from under the loading mechanism in order to empty it and re-fill the soil into it.

These girders were strongly setup on horizontal steel pillars. The Plexiglass allowed the observation of the slope. It ensured the visibility of the sample throughout preparation. It also allowed the observation of sand particles' deformation throughout the testing. However, because the impact of sand pressure and the applied load could compromise the strength of the Plexiglass, it was strengthened with two steel columns. The tank box was solid enough to support the plane strain conditions by reducing the out of plane displacement. To guarantee its solidity and prevent deformation, a thick steel plate was used to manufacture the tank. The interior parts of the tank are coated and well-polished to reduce friction with the sand as much as possible. Based on the research conducted by Ueno et al. (1998), the boundary effects were taken into account, as shown in Figure 2.

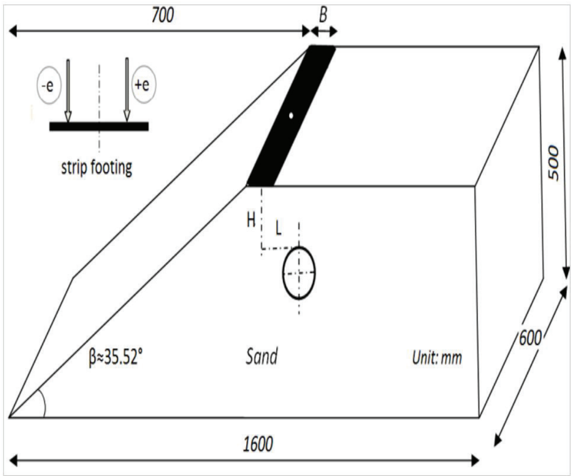

Figure 2. Geometry of the problem.

3. Footing

To implement the designed strip footing pattern, a thick steel plate consisting of a range of holes was utilized. Several holes were created on both sides (left and right) at a 10-mm distance from the centre hole of the footing to be used as foundation loading points, with the dimensions of 598 mm long, 100 mm wide (B), and 20 mm thick. Both ends of the testing footing were optimally lustred and lubricated to diminish frictional contact with the rigid box borders. Then, to ensure rugosity, a layer of sand paper was fixed to the footing base. To maintain plane strain conditions, the footing length and tank width were approximately the same values. Then, ball bearing was employed to allow an easy loading to the footing.

4. Soil proprieties

This research is based on an intermediate to coarse sand that was cleaned, dried and filtered according to sand particles size'. It was collected from the south-east region of Algeria. Particles' size distribution was established following dry sieving technique and the findings are presented in Figure 3. A particular gravity of 2.65 was determined by picnometer test. The maximum and the minimum dry densities of the sand were measured and the corresponding values of the minimum and the maximum void ratio were calculated. To assess the friction angle, a series of direct shear tests at a relative sand density of 60% were performed. The residual friction angle of the compacted sand was about 37°, which matches to densified sand. Additional parameters of the tested sand are illustrated in Table 1.

5. Cavity proprieties

The purpose of using PVC in this work is to ensure the presence of cavity void, the thickness of PVC used is

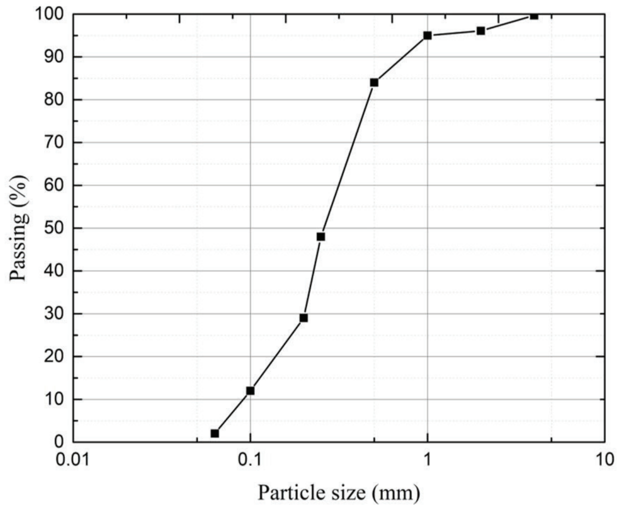

Figure 3. Grain size distribution curve of sand.

Table 1. Material properties of the sand used.

Property	Value
Specific gravity G_s	2.65
Uniformity coefficient C_u	3.19
Coefficient of curvature C_c	1.40
Maximum dry unit weight γ_d(max), kN/m^3	17.12
Minimum dry unit weight γ_d(min), kN/m^3	14.62
Peak friction angle φ ^{0}	37

Table 2. Properties of the PVC used.

Parameters	Value
Density (kN/m^3)	13.5-14.6
Tensile strength (MPa)	45
Elongation %	80
Elastic modulus (MPa)	3000

Table 3. Model tests program.

Strip footing (mm)	H/B	L/B	Eccentricities e (mm)
100x598	0.5	0,1,2,3	-30, -20, -10, 0, 10, 20, 30
	1	0,1,2,3	-30, -20, -10, 0, 10, 20, 30
	1.5	0,1,2,3	-30, -20, -10, 0, 10, 20, 30
	2	0,1,2,3	-30, -20, -10, 0, 10, 20, 30
	3	0,1,2,3	-30, -20, -10, 0, 10, 20, 30

02 mm, the exterior diameter is 110 mm and the length is 558 mm. In the design of the test model, the parameters of the PVC tube are shown in Table 2.

6. Testing process

A total of 140 load bearing experimental tests were conducted on the strip footing pattern situated in close proximity to the crest slope. To improve the validity of the experiment, every single test was carried out thrice using parameters such as vertical distance between the void and footing (H/B), load eccentricity (e/B), and the horizontal distance void-footing centre (L/B). Then, based on the process presented by El Sawwaf (2004), the experimental slope sand angle was equal to 35.52°. After that, via a manual rammer, the used sand was densified in each layer- 50 mm thick up to 500 mm height, at a relative density according to the designed testing program, the desired relative density was achieved after carrying out several preliminary experiments using different compacted energies and layers thick. During the compaction process, a void was positioned in our soil sample via a circular PVC with a diameter of 100 mm and length of 598 mm. The PVC was set down in the required position and sand compaction continued until the final bed was achieved. Tests were carried out for diverse locations of voids and varied parameters, as presented in Table 3. The sand sample was formed in line with the slope shape and framed on the plexiglass side. The formed surfaces were first levelled, then the model footing was positioned on sand, with a predetermined alignment, such that the load could be vertically transferred to the footing. To preserve typical conditions throughout the testing programme, the tank was poured out and refilled for each test.

7. Results and discussion

A total of 140 tests were conducted on the bearing capacity of stiff continuous footing situated on the slope of a soil with various void positions, a range of eccentric vertical loading ratios (e/B = 0, ± 0.1, ± 0.2, and ± 0.3), and constant footing space from slope crest (b/B = 0). The void positions moved horizontally (L/B) from the footing centre with alternating values between 0 and 3B, and also vertically from the soil surface (H/B) with alternating values between 0.5B and 3B, as presented in Table 1. A no-void reference test was also carried out.

To assess the validity and reliability of the small-scale laboratory test results, the bearing capacity was achieved by dividing the limit load on the area of footing. Ueno et al. (1998) tangent intersection method was used to set the bearing capacity results.

7.1 Effect of eccentricity

The influence of eccentric loading on bearing capacity is illustrated by the load-eccentricity curves (Figure 4**)** for different void locations and normalized slope/footing distances (b/B= 0).

It was established through the experimental results that the bearing capacity was considerably influenced by void presence and load eccentricities, here, the load diminished with an increase in the eccentricity ratio (±e/B). A significant increase in the bearing capacity value appeared when e/B = +0.1. Although this peculiarity can be explained in terms of load divergence from the crest's slope and the void centreline, at e/B = +0.2 and e/B = +0.3, a reversal of the footing was

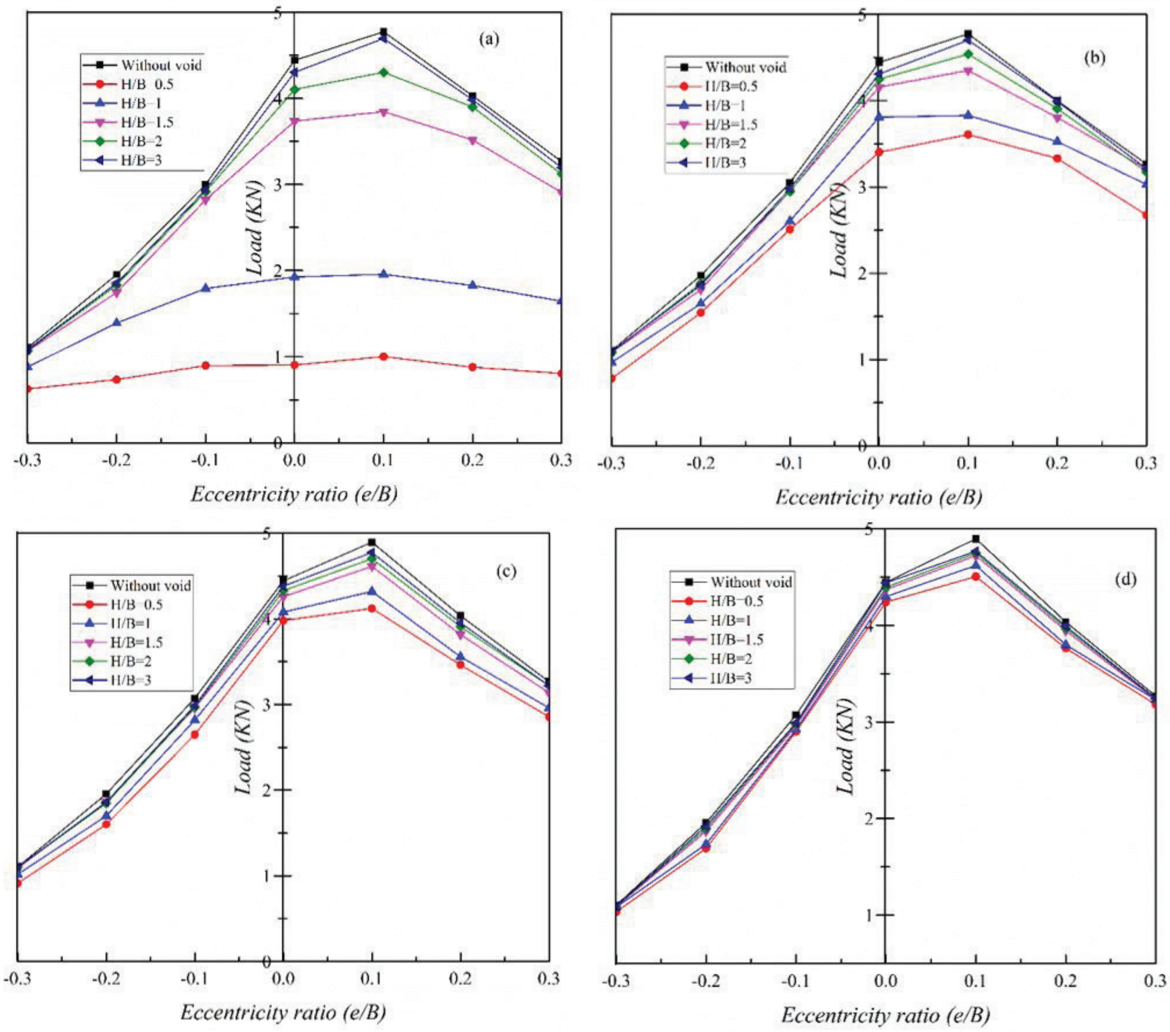

Figure 4. Load with variable eccentricities for void horizontal distance. (a) L/B=0; (b) L/B=1; (c) L/B=2; and (d) L/B=3.

observed, which occurred and gradually reduced the bearing capacity value.

Furthermore, the ultimate bearing capacity for a negative eccentric load is inferior to a positive one.

This signifies that the failure region under a positive eccentric loading is greater than that under a negative one. The gradual displacements shifted to the slope leaning, and a non-symmetrical failure mechanism was observed.

In contrast with the footing location, the passive region was imperfect, thus triggering a diminution in the bearing capacity.

7.2 The Effect of void's depth

Figure 5 shows the effect of embedment depth, from the foundation base to the void's crown, on the bearing pressure ratio of a strip foundation positioned on the edge of a sandy soil at different load eccentricities.

The obtained results were analysed in terms of a dimensionless parameter called bearing capacity ratio: $\boldsymbol{i_H} = q_v/q_{nv}$, where q_v represents the bearing capacity of the strip footing on the ground with a void while q_{nv} defines the ultimate bearing capacity for the same footing placed on the sand without void.

A significant instability between the soil and the nearby voids had been observed when the void distance H/B and L/B were equal to 0.5 and 0, respectively. Consequently, the soil collapsed with an 80% reduction in the bearing capacity value. This occurred because the small distance between the footing and void, including the soil mass underneath the footing was thin. Therefore, a low total shearing resistance was mobilized.

Then, an increase in the negative load eccentricity (direction of the slope) reduced the void embedding effect as we suspected. Moreover, the H/B effect was less influential for negative eccentricity than for positive eccentricity, this can be explained, that for negative eccentricity, the loading point moves away from the centre of the void and thus leads

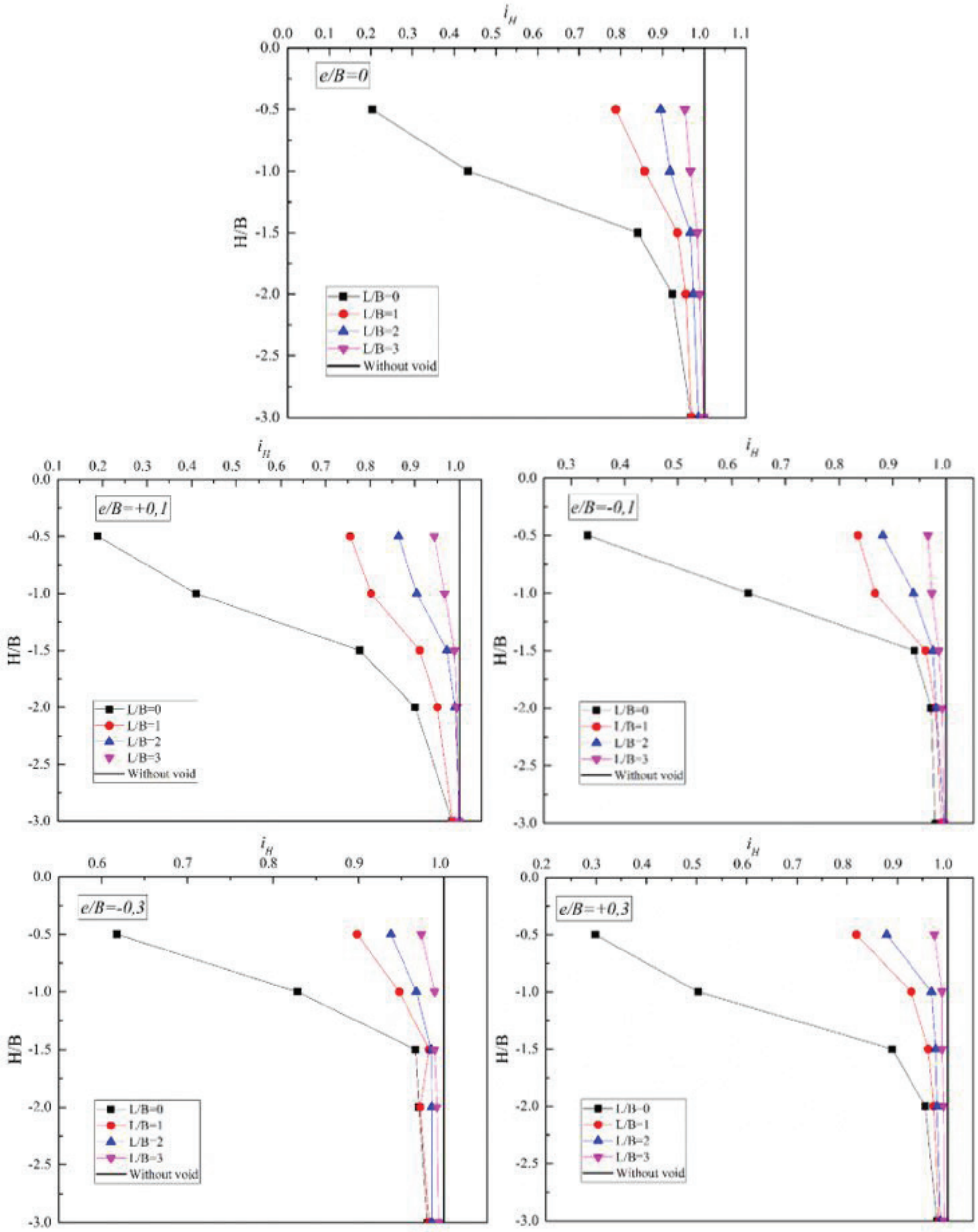

Figure 5. Effect of depth void with bearing capacity ratio.

to an increase in bearing capacity. Furthermore, in the cases at H/B=1 and H/B=1.5, notably, we observed the same impact for negative and positive load eccentricities but with less significant intensities.

As illustrated in Figure 5, irrespective of the eccentricity of the load and distance of the void from the centreline of the foundation, the bearing capacity ratio of the footing increases as the depth of the void's crown augments from a footing bottom, which reaches a maximum value at H/B = 2. This specific depth is called 'critical depth' and it was also determined by (Badie & Wang, 1984). Beyond this depth, the influence of the void on the bearing pressure ratio appeared to be the same as that of a footing without a void. Additionally, the values converged to the reference case. This behaviour occurs owing to the voids distant from the shear zone. Therefore, the failure mechanism formed was similar to that of the no-void. Finally, it was determined that when L/B = 3, the H/B effect is negligible.

7.3 The effect of void horizontal distance from foundation centreline

To probe the effect of the horizontal distance, several curves were plotted, as shown in Figures 6a, b, c, d. The results show that at L/B=2 and L/B=3, the effect of the void on the bearing capacity of a foundation under eccentric loads

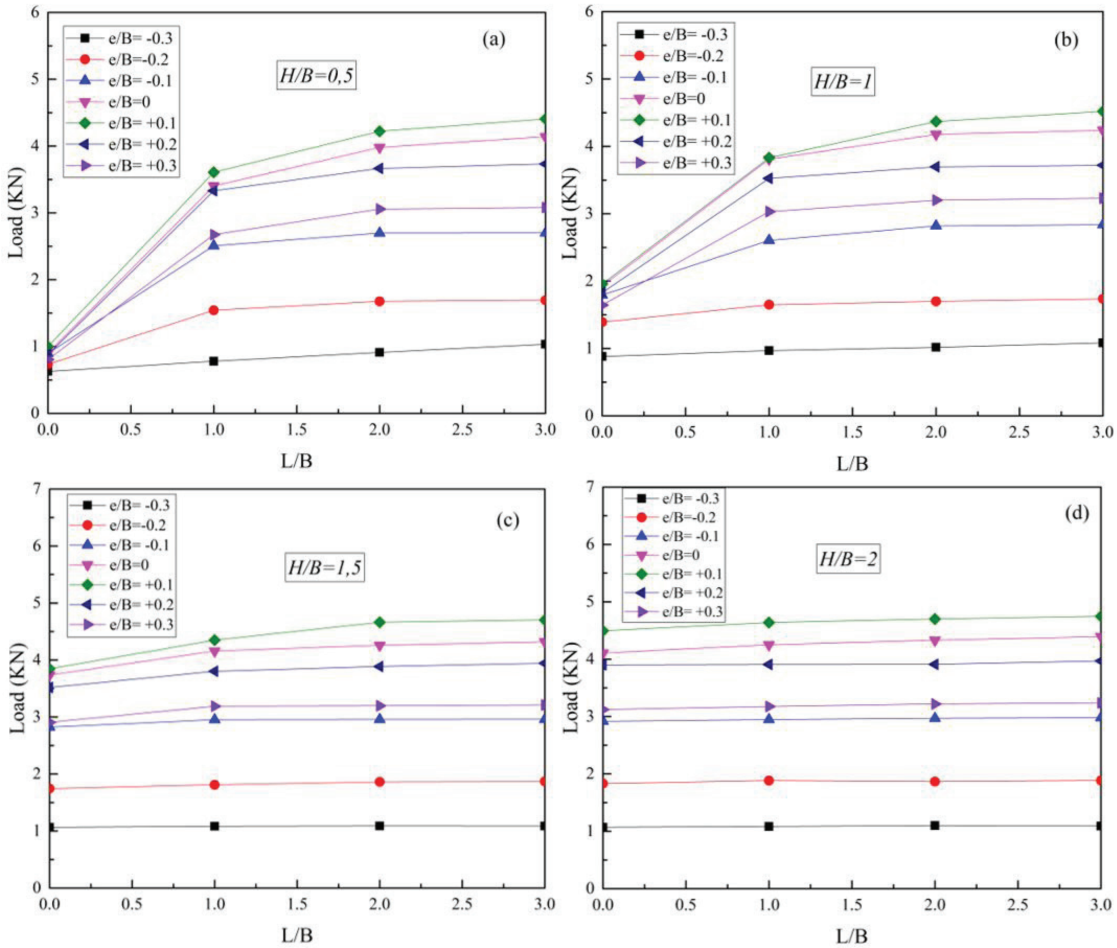

Figure 6. Effect of load with horizontal distance from foundation centreline. a) H/B=0.5; b) H/B=1; c) H/B=1.5 and d) H/B=2.

is annulled, and the behaviour of the footing is similar to that of a no-void foundation.

In Figure 6, it was set up such that for H/B = 0.5 and H/B = 1, the influence of the eccentricities on the bearing capacity was nearly negligible as the void moved closer to the base of the footing. For the other void depths, it can be observed that the curves converge towards the case without a void.

According to the test results presented in Figure 6, curves were designed at various void horizontal distances shifting from 0 to 3 B. Irrespective of the eccentricity of the applied load (e/B = -0.3, -0.2, -0.1, 0.0, +0.1, +0.2, +0.3), the void moves far away from the centreline footing, thus indicating a decrease in its influence. Moreover, its impact becomes insignificant when the void divergence equals twice the width of the footing. Beyond H/B = 2, the foundation behaves like a foundation without a void, as shown in Figure 6d.

A careful examination reveals that in the case of e/B = -0.3 and e/B= -0.2, the effect of the slope controls the behaviour of the foundation, whereas the effect of the horizontal distance is insignificant. Furthermore, owing to load eccentricity, the footing started to lose contact with the soil.

8. Conclusion

In this study, various performed laboratory tests were conducted to determine the impact of underground circular voids on the bearing-capacity behaviour of a shallow continuous footing located on the edge of a cohesionless slope (b/B=0). Based on the obtained results, the following findings and conclusions were made:

- The results prove that the bearing capacity is considerably influenced by the location of the void and load eccentricity;
- The ultimate bearing capacity for a positive eccentric load is greater than that of a negative one owing to the slope presence and underlying void;
- Because the soil mass underneath the footing is thin, the short distance between the footing and void leads to soil collapse along with a significant decrease in bearing capacity, thus mobilizing a low total shearing resistance is mobilized;
- The negative load eccentricity (direction of the slope) reduces the effect of void inclusion, whereas the effect of H/B is less significant on the negative eccentricity than on positive eccentricity;

- Irrespective of the eccentricity of the load and distance of the void from the centreline of the foundation, the bearing capacity of the footing increases as the depth of the void's crown augments till it reaches a maximum value at H/B = 2. Beyond this depth, the influence of the void on the bearing pressure appears to be the same as that of a footing without a void;
- In the case where the horizontal distance of the void from the foundation centreline equals three times the footing width, the effect of the void's depth is negligible;
- The impact of eccentricities on the bearing capacity is nearly negligible when the void moves closer to the base of the footing;
- The influence of the void is insignificant when the void is placed at a depth equivalent to 2 times the width of the footing;
- Regardless of the eccentricity of the applied load, the influence of the void gradually reduces as the void moves far away from the footing centreline, and its impact becomes more negligible when void divergence equals twice the width of the footing.

Declaration of interest

We have no conflicts of interest to disclose.

Author's contributions

Tarek Mansouri: methodology, investigation, data curation, writing - original draft preparation. Rafik Boufarh: conceptualization, supervision, validation. Djamel Saadi: data curation, writing - reviewing and editing.

References

Al-Jazaairry, A.A., & Toma-Sabbagh, T.M. (2017). Effect of cavities on the behaviour of strip footing subjected to inclined load. *International Journal of Civil, Environmental, Structural, Construction and Architectural Engineering*, 11(3), 292-298.

Atkinson, J.H., & Potts, D.M. (1977). Stability of a shallow circular tunnel in cohesionless soil. *Geotechnique*, 27(2), 203-215. http://dx.doi.org/10.1680/geot.1977.27.2.203.

Badie, A., & Wang, M.C. (1984). Stability of spread footing above void in clay. *Journal of Geotechnical Engineering*, 110(11), 1591-1605. http://dx.doi.org/10.1061/(ASCE)0733-9410(1984)110:11(1591).

Baus, R.L., & Wang, M.C. (1983). Bearing capacity of strip footing above void. *Journal of Geotechnical Engineering*, 109(1), 1-14. http://dx.doi.org/10.1061/(ASCE)0733-9410(1983)109:1(1).

Culshaw, M.G., & Waltham, A.C. (1987). Natural and artificial cavities as ground engineering hazards. *Quarterly Journal of Engineering Geology*, 20(2), 139-150. http://dx.doi.org/10.1144/GSL.QJEG.1987.020.02.04.

El Sawwaf, M.A. (2004). Strip footing behavior on pile and sheet pile-stabilized sand slope. *Alexandria Engineering Journal*, 43(1), 41-54. http://dx.doi.org/10.1061/(asce)1090-0241(2005)131:6(705).

Hussein, M.M.A. (2014). Stability of strip footing on sand bed with circular void. *Journal of Engineering Sciences*, 42(1), 1-17. http://dx.doi.org/10.21608/jesaun.2014.111011.

Jayamohan, J., Shajahan, T., & Sasikumar, A. (2019). Effect of underground void on the internal stress distribution in soil. In T. Thyagaraj (Ed.), *Ground improvement techniques and geosynthetics* (Lecture Notes in Civil Engineering, No. 14, pp. 45-56). Singapore: Springer. https://doi.org/10.1007/978-981-13-0559-7_6.

Khalil, A.A., & Khattab, S.A. (2009). Effect of cavity on Stress distribution and Settlement under Foundation. *AL-Rafdain Engineering Journal*, 17(6), 14-29. http://dx.doi.org/10.33899/rengj.2009.43621.

Kiyosumi, M., Kusakabe, O., & Ohuchi, M. (2011). Model Tests and analyses of bearing capacity of strip footing on stiff ground with voids. *Journal of Geotechnical and Geoenvironmental Engineering*, 137(4), 363-375. http://dx.doi.org/10.1061/(ASCE)GT.1943-5606.0000440.

Kiyosumi, M., Kusakabe, O., Ohuchi, M., & Le Peng, F. (2007). Yielding pressure of spread footing above multiple voids. *Journal of Geotechnical and Geoenvironmental Engineering*, 133(12), 1522-1531. http://dx.doi.org/10.1061/(ASCE)1090-0241(2007)133:12(1522).

Lavasan, A.A., Talsaz, A., Ghazavi, M., & Schanz, T. (2016). Behavior of shallow strip footing on twin voids. *Geotechnical and Geological Engineering*, 34(6), 1791-1805. http://dx.doi.org/10.1007/s10706-016-9989-6.

Lee, J.K., & Kim, J. (2019). Stability charts for sustainable infrastructure: collapse loads of footings on sandy soil with voids. *Sustainability*, 11(14), 3966. http://dx.doi.org/10.3390/su11143966.

Lee, J.K., Jeong, S., & Ko, J. (2014). Undrained stability of surface strip footings above voids. *Computers and Geotechnics*, 62, 128-135. http://dx.doi.org/10.1016/j.compgeo.2014.07.009.

Lee, J.K., Jeong, S., & Ko, J. (2015). Effect of load inclination on the undrained bearing capacity of surface spread footings above voids. *Computers and Geotechnics*, 66, 245-252. http://dx.doi.org/10.1016/j.compgeo.2015.02.003.

Mohamed, A.K. (2012). Numerical study for the behavior of strip footing on sand in the existence of a buried rock. *JES. Journal of Engineering Sciences*, 40(6), 1611-1624. http://dx.doi.org/10.21608/jesaun.2012.114532.

Piro, A., Silva, F., Di Santolo, A.S., Parisi, F., & Silvestri, F. (2018). Sensitivity analysis of seismic soil-foundation-structure interaction in masonry buildings founded on cavities. In *Proceedings of the 16th European Conference on Earthquake Engineering* (pp. 1-10), Thessaloniki.

Saadi, D., Abbeche, K., & Boufarh, R. (2020). Model experiments to assess effect of cavities on bearing capacity of two interfering superficial foundations resting on granular soil. *Studia Geotechnica et Mechanica*, 42(3), 222-231. http://dx.doi.org/10.2478/sgem-2019-0046.

Ueno, K., Miura, K., & Maeda, Y. (1998). Prediction of ultimate bearing capacity of surface footings with regard to size effects. *Soil and Foundation*, 38(3), 165-178. http://dx.doi.org/10.3208/sandf.38.3_165.

Wang, M.C., & Badie, A. (1985). Effect of underground void on foundation stability. *Journal of Geotechnical Engineering*, 111(8), 1008-1019. http://dx.doi.org/10.1061/(ASCE)0733-9410(1985)111:8(1008).

Wang, M.C., & Hsieh, C.W. (1987). Collapse load of strip footing above circular void. *Journal of Geotechnical Engineering*, 113(5), 511-515. http://dx.doi.org/10.1061/(ASCE)0733-9410(1987)113:5(511).

Xiao, Y., Zhao, M., & Zhao, H. (2018a). Undrained stability of strip footing above voids in two-layered clays by finite element limit analysis. *Computers and Geotechnics*, 97, 124-133. http://dx.doi.org/10.1016/j.compgeo.2018.01.005.

Xiao, Y., Zhao, M., Zhao, H., & Zhang, R. (2018b). Finite Element Limit Analysis of the Bearing Capacity of Strip Footing on a Rock Mass with Voids. *International Journal of Geomechanics*, 18(9), 04018108. http://dx.doi.org/10.1061/(ASCE)GM.1943-5622.0001262.

Zhang, R., Chen, G., Zou, J., Zhao, L., & Jiang, C. (2019). Study on roof collapse of deep circular cavities in jointed rock masses using adaptive finite element limit analysis. *Computers and Geotechnics*, 111, 42-55. http://dx.doi.org/10.1016/j.compgeo.2019.03.003.

Zhao, L., Huang, S., Zhang, R., & Zuo, S. (2018). Stability analysis of irregular cavities using upper bound finite element limit analysis method. *Computers and Geotechnics*, 103, 1-12. http://dx.doi.org/10.1016/j.compgeo.2018.06.018.

Zhou, H., Zheng, G., He, X., Xu, X., Zhang, T., & Yang, X. (2018). Bearing capacity of strip footings on c–φ soils with square voids. *Acta Geotechnica*, 13(3), 747-755. http://dx.doi.org/10.1007/s11440-018-0630-0.

List of symbols

(B): width of footing

(b): distance between foundation and the edge of a slope

(±e): positive, negative eccentric load

(H): top vertical distance of the void from the base of footing.

(L): horizontal distance between cavities-footing centre (L/B).

Ns: undrained bearing capacity factor.

(Gs): Specific gravity

(Cu): Uniformity coefficient

(Cc): Coefficient of curvature

(γd(max)): maximum dry unit weight

(γd(min)): minimum dry unit weight

(φ): Peak friction angle

(β): slope angle

PVC: (abbreviation coming from the English name (polyvinyl chloride)

(iH): dimensionless parameter called bearing capacity ratio

(qv): ultimate bearing capacity of the strip footing placed on the sand with a void

(qnv): ultimate bearing capacity of the strip footing placed on the sand without void.

Soils and Rocks
An International Journal of Geotechnical and Geoenvironmental Engineering
www.soilsandrocks.com
ISSN 1980-9743
ISSN-e 2675-5475

Analysis of the failure modes and development of landslides using the material point method

Daniela Toro Rojas[1#], Manoel Porfirio Cordão Neto[1], Marcio Muniz de Farias[1], Raydel Lorenzo Reinaldo[2]

Article

Keywords
Material point method
Landslides
Strength parameters
Deformability parameters

Abstract

Mass movements are frequent natural phenomena and especially dangerous due to increased population and irregular settlements in mountainous areas. Carrying out studies using methods that allow the numerical evaluation of their behavior is essential to mitigate and prevent these events' possible impacts. The traditional Limit Equilibrium and Finite Element methods fail to reproduce the problem from the beginning of the movement until the end of its development, so it is necessary to use new formulations. In this work the Material Point Method was selected to evaluate these movements in the stages of failure mode formation and development of landslide through an analysis of the soil shear strength and deformability parameters of a slope using the elastoplastic model with Mohr-Coulomb failure criterion. Maintaining a geometry and assuming soil mass behaves like a fluid, a single strength parameter and a single deformability parameter are analyzed to understand their influence before and after the failure.

1. Introduction

Landslides and mass movements are natural catastrophes that frequently occur in mountainous regions and urban areas, affecting the population and generating significant economic losses. In most cases, movements are caused when destabilizing forces exceed the resistance of the materials, by the alteration of the characteristics of the slope due to changes in the geometric factors (height, inclination), the materials conditioning factors or intrinsic factors (geology, hydrogeology and geotechnics) or by triggering factors (dynamic loads, variation in hydrogeological conditions, climatic factors, variations in geometry and reduction in resistance parameters). According to Skempton & Hutchinson (1969), mass movements develop in three stages: before the failure, the failure, and the landslides after it. Most research focuses on the study of the first two stages, i.e., the prevention of these movements by calculating the safety factor or the probability of failure.

Some authors have focused their studies on the development of methodologies that quantitatively and qualitatively evaluate the susceptibility to landslides (Park et al., 2013; Malet et al., 2009; Simoni et al., 2008; Kanungo et al., 2006). Others have focused on the study of deflagrating factors and triggering conditions, including their description, classification, and time of occurrence (Aristizábal et al., 2016; Borfecchia et al., 2016; Aghda & Bagheri, 2015). Giupponi et al. (2015), Li et al. (2010), Zêzere et al. (2008), and Uzielli et al. (2008) have estimated the loss degree of an element set exposed to the occurrence of a landslide, assessing the vulnerability or propensity to such loss. All these works come together in the common objective of calculating the probability and severity of a mass movement, that is, in the calculation of the risk from the product between the probability and the consequences of an event.

In order to improve the risk analysis and prevent mass movements, physical and mathematical models were developed to simulate the behavior of this type of phenomenon. Among the mathematical models, the Limit Equilibrium Method (LEM) is better known. It concentrates on the calculation of the safety factor using material resistance theories considering soil mass as a non-deformable rigid body. On the other hand, the Finite Element Method (FEM) has also been used as a more accurate tool for solving most problems in solid and soil mechanics (Nazem et al., 2006; Farias & Naylor, 1998). These methods concentrate only on the slope behavior before failure and at the beginning of instability, without considering the study of movement development, i.e., events after failure.

However, to model mass movements after failure with good precision, a numerical method is necessary to accompany the movement of the simulated body and to describe its behavior, i.e., a method capable of simulating large distortions and deformations. Currently, the FEM is

[#]Corresponding author. E-mail address: dtr1593@gmail.com
[1]Universidade de Brasília, Programa de Pós-graduação em Geotecnia, Brasília, DF, Brasil.
[2]Universidade Federal do Tocantins, Programa de Engenharia Civil, Palmas, TO, Brasil.

Submitted on September 22, 2020; Final Acceptance on February 18, 2021; Discussion open until May 31, 2021.

DOI: https://doi.org/10.28927/SR.2021.057820

the most used tool for the calculation of deformations in geotechnical problems; however, it is not possible to obtain reliable results on large deformation problems using this method with its traditional formulation due to excessive mesh distortions (Nazem & Sheng, 2005). To overcome this difficulty, other methods were proposed, such as the Discrete Element Method (DEM), Galerkin Element Free Method (EFMG), Smoothed Particle Hydrodynamics (SPH), Arbitrary Lagrangian-Eulerian Method (ALE), and the Material Point Method (MPM).

The MPM is a tool capable of solving problems of large deformations related to geotechnical engineering, where the material point is seen as a representative volume element. The MPM uses constitutive models based on the continuum mechanics, such as the elastoplastic models Mohr-Coulomb, Modified Cam-Clay, among others. In addition, the use of a background mesh allows the implementation of boundary conditions similar FEM, and compared to other mesh-free methods, MPM has computationally efficient features (Abe et al., 2013).

The MPM method has been used to model different geotechnical problems such as foundations (Lorenzo et al., 2013), anchors (Coetzee et al., 2005), problems of granular flows (Więckowski, 2003), fault deformations (Johansson & Konagai, 2007), analysis of soil flows propagation induced by earthquakes (Konagai et al., 2004) and geomembrane response to settlements (Zhou et al., 1999). Other authors have worked in mass movements, such as González Acosta et al. (2018), who studied the effect of a landslide colliding with a rigid wall, considering multiple initial conditions to identify the most critical case. Vardon et al. (2017) conducted several slope failure simulations that included the initiation and development of the movement to better quantify the risk and consequences of these events. Llano Serna et al. (2016) demonstrated the capabilities of the MPM to evaluate landslides and their behavior after failure, numerically validating the failure of the Tokai-Hokuriku highway in Japan and the Vajont landslide in Italy. Bhandari et al. (2016) adopted the MPM to simulate the progressive failure of a slope caused by an earthquake. Gabrieli & Ceccato (2016) simulated the impact of a dry granular flow on a rigid wall and compared their results with DEM, obtaining good approximations with both methods. Llano Serna et al. (2015) simulated the landslide of an urban slope to calculate velocity and energy variables to quantify the vulnerability of structures and people subjected to impact, and Mast et al. (2014) used the MPM to simulate gravity-driven slope failure to assess the interaction of these events with the built environment.

As in the mentioned studies, this work uses the MPM to evaluate mass movements, specifically in the stages of formation of the failure mode and development of the movement through an analysis of the soil shear strength and deformability parameters of a slope using the elastoplastic model with Mohr-Coulomb failure criterion. The results obtained in the failure are compared with the results calculated by LEM. Finally, the estimates of velocity and displacement are evaluated and compared with different values of Young's modulus and cohesion to understand, at a general level, their influence on the formation and development of a mass movement.

2. Materials and methods

As previously stated, the MPM developed by Sulsky et al. (1994, 1995) was used to perform the simulations. The MPM brings together ideas and procedures of the Particle in Cell Method (PIC) and FEM. Material bodies are discretized in a collection of particles not connected between them that transport a mass whose value is kept fixed to guarantee the mass conservation. Other parameters necessary to define the body's state, such as stress, density, and the history variables, are also assigned to the material points (Zabala & Alonso, 2011). The interaction between the particles is performed in the nodes of a stationary Eulerian computational mesh like those used in the FEM, which remains constant for the entire calculation eliminating the problem of distortion (Figure 1) This mesh is used to determine the governing equations' incremental solution by means of an Eulerian description (Al-Kafaji, 2013).

In this method, the equations of motion are solved in the background mesh that covers the entire domain of the problem. In each analysis step, the quantities transported by the material points are interpolated to the mesh nodes, using the functions associated with them as in the FEM. The boundary conditions are imposed on the mesh nodes, and the equations are solved incrementally in it. Then, the magnitudes of the variables in the material points are updated using the weighting of the nodes' results, using the same functions of form again. In the MPM, the mesh information is not required in the next steps of analysis, so it can be discarded (Zabala, 2010).

To evaluate the influence of the strength and deformability parameters on the formation of the failure mechanisms and on the development of a mass movement using the MPM, a slope was designed with the geometry presented in Figure 2 and

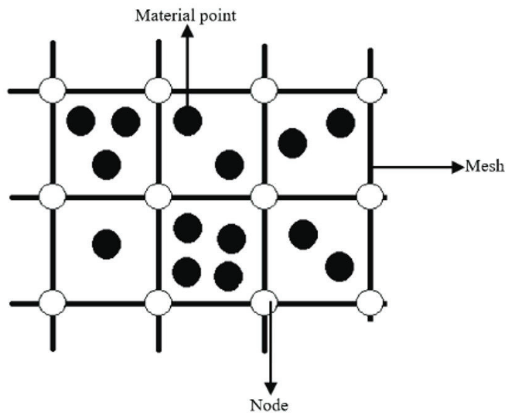

Figure 1. Discretization using the Material Point Method.

the properties of Table 1 (previously used in studies by Alelvan et al., 2020). As this method uses constitutive models based on the continuum mechanics, the elastoplastic model with Mohr-Coulomb failure criterion in the slope and the linear-elastic model in the foundation were used.

All analyses were performed with the ANURA3D® software, a 3D implementation of MPM, used to simulate the phenomenology involved in soil-water-structure interaction and large deformation problems. This tool was developed by Anura 3D Research Community: Soil and Rock Mechanics Research Group of Universitat Politècnica de Catalunya (UPC), GeoSystems (Geoengineering) Group of University of California Berkeley, Faculty of Civil Engineering and Geosciences of Delft University of Technology, Unit Geo-engineering and Deltares Software Center, Institute of Geotechnical Engineering and Construction Management of Technische Universität Hamburg-Harburg and Research Group Geotechnics of Università degli Studi di Padova (Anura3D, 2017). Some research related to mass movements was developed using Anura 3D®, such as Gabrieli & Ceccato (2016), Redaelli et al. (2017), and Ceccato & Simonini (2017).

Initially, it is necessary to evaluate the influence of the number of elements of the bottom mesh, and the number of material points in each cell, i.e. a sensitivity study of the discretization in the MPM should be performed. In this case, a series of analyses were carried out in which the slope instability due to its own weight is simulated, this being discretized with five types of meshes of different cell sizes, each one evaluated with one, four, and eight material points. The geometry used was the same as presented in Figure 2. The affix of each of the simulations (expressed by the MXMPY code where “M” is the mesh, “X” the reference to the size of the elements, “MP” the material points, and “Y” the quantity of them), the discretization used and the analysis time is presented in Table 2.

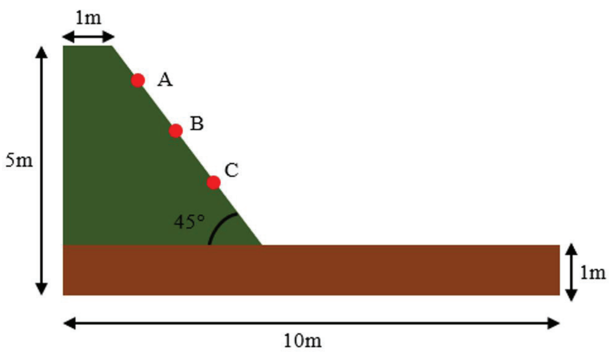

Figure 2. Slope geometry (A: crown, B: Center, C: Foot).

When the number of elements increases by decreasing the cell size, the analysis time rises significantly. n the other hand, the visual result is also influenced because as the cell size increases, the distance traveled by the unstable mass on the foundation decreases regardless of the number of material points. When the cell size is smaller, the distance reached by the mass is much greater, behaving practically the same with the three amounts of material points analyzed. Figure 3 shows the slope’s discretization and the final distance reached by the mass when the type of mesh changes.

Based on these results, the M5MP4 mesh was selected to perform the following simulations. Although this simulation’s analysis time was very long, the movement’s development was much more detailed. It should be noted that the mesh has a strong influence on the results, which is more important than the number of material points assigned.

2.1 Estimation of an initial failure surface

To estimate an initial failure surface, the slope of Figure 2 was analyzed with the LEM proposed by Morgenstern & Price (1965) using the GEOSLOPE software. The LEM is one of the most used to analyze the stability of a natural or artificial slope by calculating the safety factor. This method is based on statics principles, i.e., the static equilibrium of forces and moments without considering the soil mass’s displacements (Fredlund & Rahardo, 1993). With this method and the properties of Table 3, the calculated safety factor was 0.66, meaning the slope in the initial conditions was unstable. The cohesion was then increased to 1.8 kPa, the minimum value to guarantee the slope’s stability with a safety factor equal to 1 (Figure 4).

When running the MPM simulations, it was observed that the minimum cohesion value to keep the slope stable was 1.25 kPa. These results being different from those obtained with LEM due to the estimates of stresses and deformations in the material that this method does not consider (van Asch et al., 2007, quoting Bromhead, 1996).

Table 1. Material properties (adapted from Alelvan et al., 2020).

Material	Constitutive Model	Parameters	Value
Soil	Mohr-Coulomb	Density (kg/m^3)	2200
		Young’s Modulus (MPa)	30
		Poisson	0.33
		Friction angle (°)	30
		Cohesion (kPa)	0.1
Foundation	Linear Elastic	Density (kg/m^3)	2500
		Young’s Modulus (GPa)	4
		Poisson	0.33

Table 2. Identification, discretization, and analysis time.

ID	Size	Number of Elements	Number of Nodes	Material Points per Element	Time
M1MP1	1 (1m × 1m)	468	1053	1	30 min
M1MP4				4	
M1MP8				8	
M2MP1	2 (0.5m × 0.5m)	3744	6625	1	1 hour
M2MP4				4	
M2MP8				8	
M3MP1	3 (0.4m × 0.4m)	10098	16415	1	3 hours
M3MP4				4	
M3MP8				8	
M4MP1	4 (0.3m × 0.3m)	15480	24969	1	5 hours
M4MP4				4	
M4MP8				8	
M5MP1	5 (0.2m × 0.2m)	60450	90783	1	2 days
M5MP4				4	
M5MP8				8	

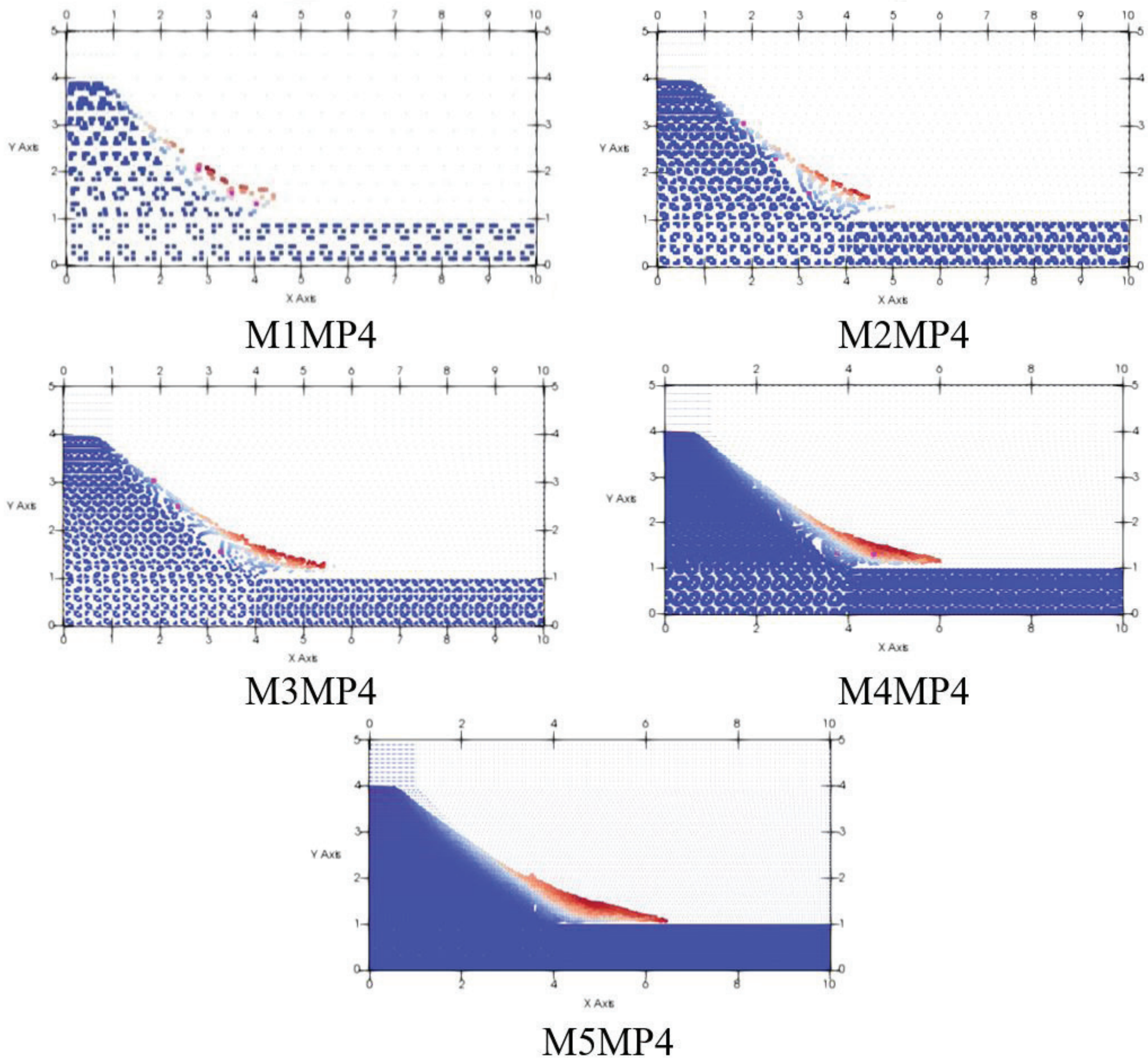

Figure 3. Discretization and displacement for five type of mesh with four material points.

Different situations were raised from these divergences to be analyzed with MPM through two stages: formation of the failure mode and development of the mass movement. The final properties of the materials for each case are presented in Table 4.

Each simulation was carried out in two stages: in the first one, the initial stress state was generated, and in the second, the failure was simulated due only to the effect of gravity.

3. Results

In all cases studied were selected three material points on the foot, center, and crown of the geometry as shown in Figure 2. For the ease of the reader, the results of the points located in the crown are presented, which exemplify the general behavior of each simulation.

3.1 Analysis of the failure mode

In this stage the first instants of the simulations are studied, where it is determined if the movement is progressive,

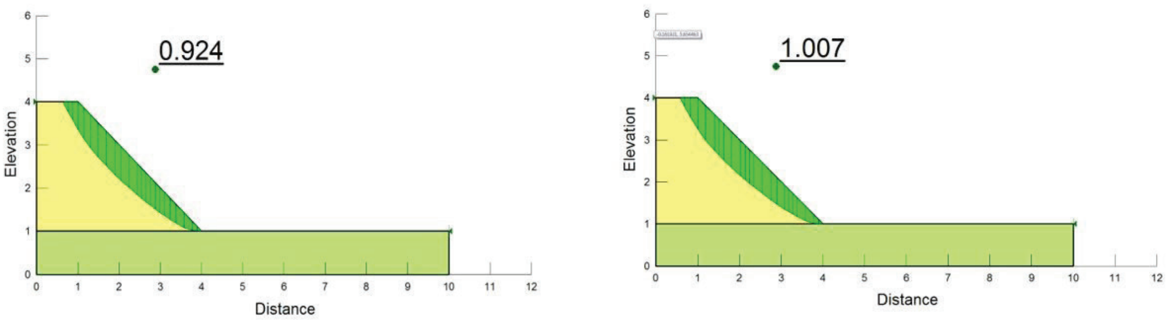

Cohesion 1.25 kPa

Cohesion 1.8 kPa

Figure 4. Safety factor with different cohesions.

Table 3. Material properties for Limit Equilibrium Method.

Material	Constitutive Model	Parameters	Value
Soil	Mohr-Coulomb	Specific Weight (kN/m^3)	22
		Friction (°)	30
		Cohesion (kPa)	0.1
			1.25
			1.5
			1.7
			1.8
Foundation		Specific Weight (kN/m^3)	25
		Friction (°)	30
		Cohesion (kPa)	40

Table 4. Material properties for the different stages.

Material	Parameters	Formation of the Failure mode	Development of mass movement
Soil	Density (kg/m^3)	2200	2200
	Young's Modulus (MPa)	30	30
		60	60
		150	150
		300	300
	Poisson	0.33	0.33
	Friction angle (°)	30	30
	Cohesion (kPa)	1.25	-
		1.5	0
		1.7	0.5
		1.8	1.0
Foundation	Density (kg/m^3)	2500	2500
	Young's Modulus (GPa)	4	4
	Poisson	0.33	0.33

that is, if a slide is going to occur or not. For this purpose, two types of analysis were performed: one varying the cohesion values and the other increasing Young's modulus values.

In Figure 5, it is possible to observe the small displacements of the material points for each simulation of the cases with different cohesion values. When cohesion decreases, the displacements' magnitude is increasingly greater and much more concentrated in the region close to the slope face, defining more precisely what will be the failure surface and the mass that will move after that failure. In this case, the boundary effect was considered as not influence the results. Figure 6 shows that with an increase in cohesion, displacements are smaller. As the slope approaches the failure, the displacements, and velocity increase, although they stabilize again after approximately 0.7 s.

The displacements and velocity recorded with the cohesion of 1.25 kPa to analyze the Young's modulus variation are shown in Figure 7. The magnitude of the displacements decreases when the module increases, i.e., when the material has a more rigid behavior, the particles' internal accommodation is reduced, bearing in mind that the slope is in the failure's imminence. Likewise, velocities are higher with low modulus.

3.2 Failure

To analyze the behavior of the slope at failure, accelerations before and after instability were calculated. Figure 8 illustrates the selected points' behavior on the sloped crown for different Young's modulus values and cohesion of 1.25 kPa (imminent failure). In this figure, it is possible to observe two successive increases of acceleration at the beginning of the analysis, followed by braking generated by the mass's accommodation that prevents other displacements. The movement then slows down and quickly returns to 0 m/s^2, just when the slope is stable again. It is also possible to observe that with the lowest modulus of 30 MPa the material point reaches the highest acceleration and takes longer to stop its movement compared to the other points; otherwise, it happens with the material point that represents the highest module of 300 MPa, which reaches a much lower acceleration and therefore stabilizes before the others.

Figure 9 shows the accelerations of the material points analyzed with a cohesion of 1.0 kPa. The initial behavior of these points resembles the cohesive action of 1.25 kPa. In this case, the processing time was longer. Only after 3s of analysis, it is possible to observe changes in the acceleration, which remains constant after reaching its first peak at the

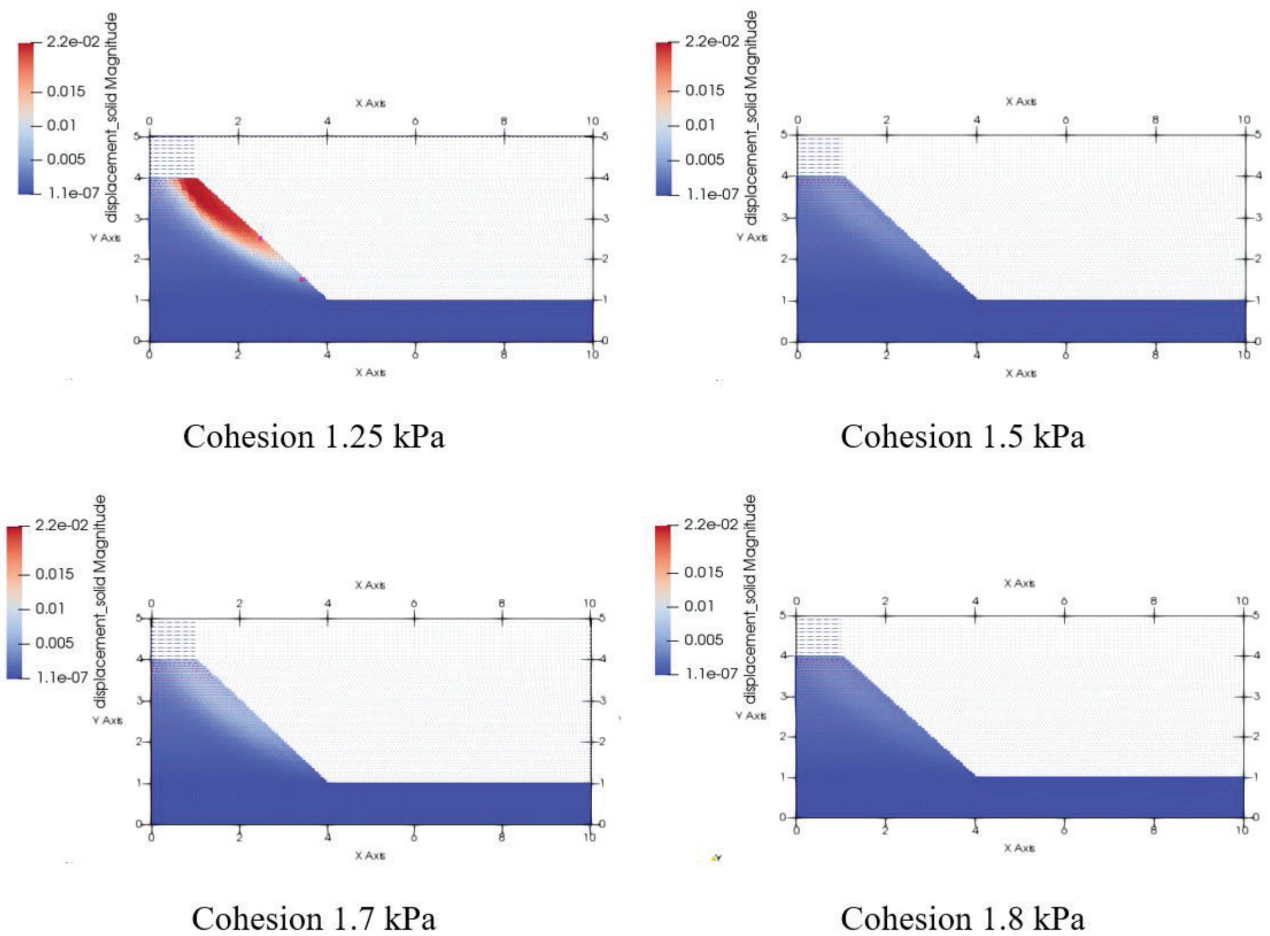

Figure 5. Displacement of PM.

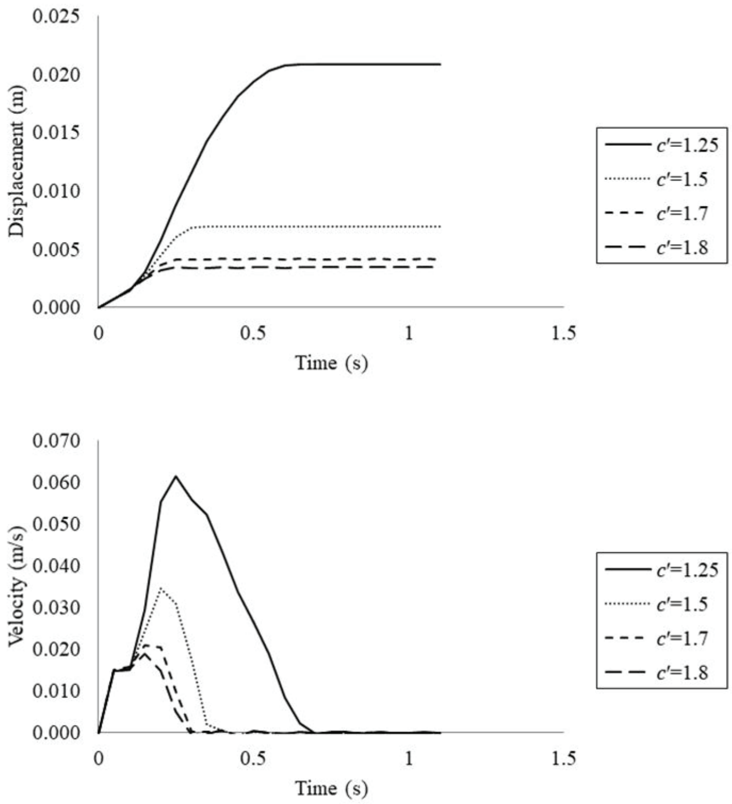

Figure 6. Displacement and velocity of points on the crown of the slope for different cohesions before failure.

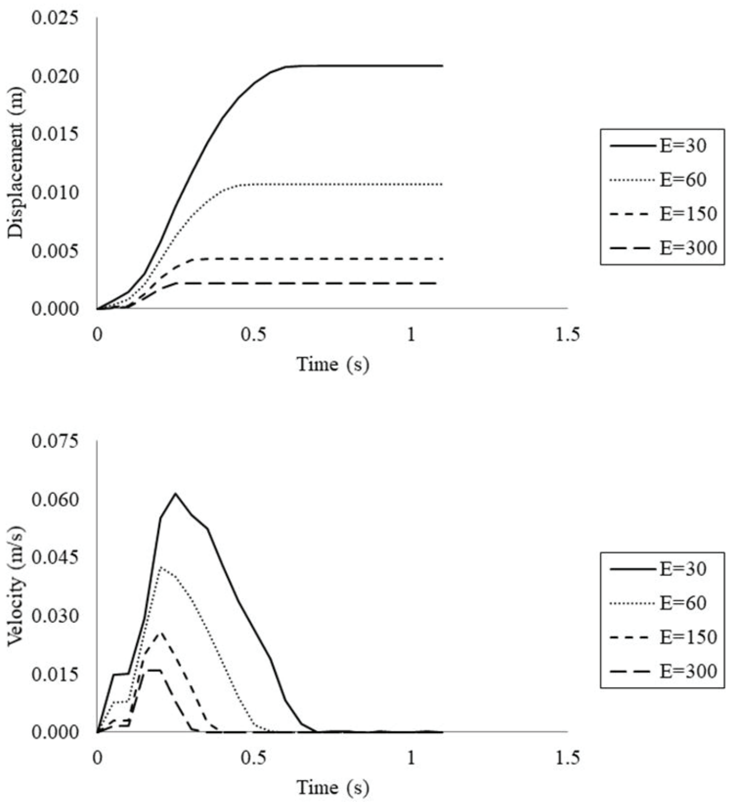

Figure 7. Displacement and velocity of points on the top of the slope for different modules before failure (Cohesion 1.25 kPa).

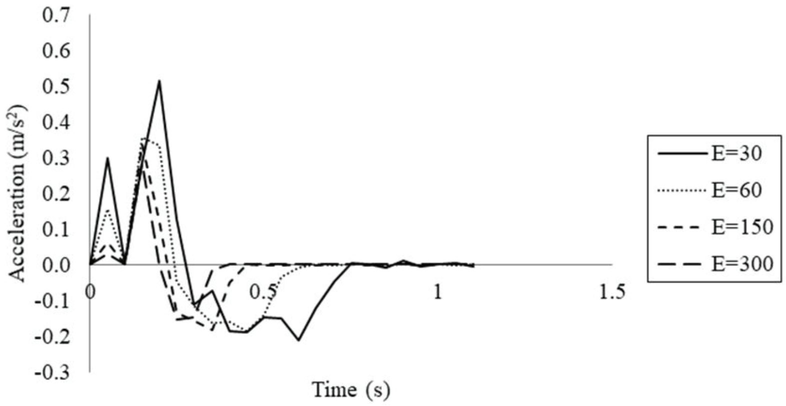

Figure 8. Acceleration of points at the top of the slope for different modules before failure (Cohesion 1.25 kPa).

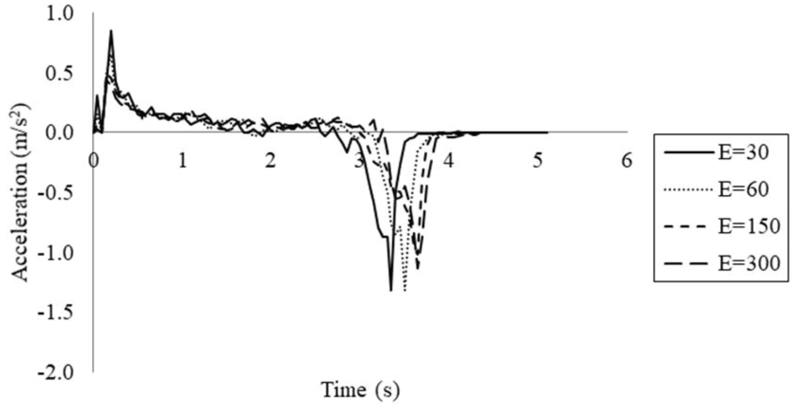

Figure 9. Acceleration of points at the crown of the slope for different modules after failure (Cohesion 1.0 kPa).

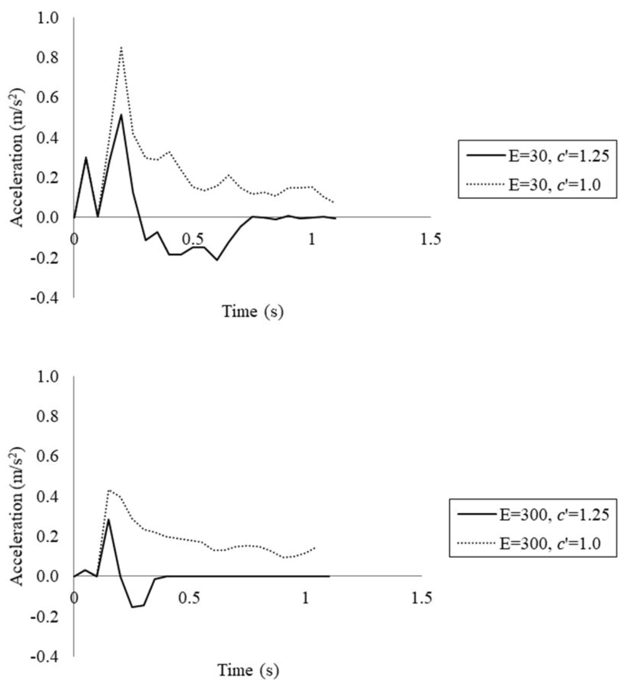

Figure 10. Acceleration of points at the crown of the slope for cohesions 1.0 kPa and 1.25 kPa.

beginning of the movement. The most critical decelerations occur in the time interval 3.0s-3.65s, being -1.31 m/s^2 the most significant magnitude reached by the material points of module 30 MPa and 60 MPa. After 4.25s, all points remain stable at an acceleration of 0 m/s^2.

The comparison of behavior with the two cohesions and the four modules simultaneously (0 s- 1.2 s) is presented in Figure 10. In all these graphs it is possible to observe the formation of the failure mechanism for slopes with cohesions equal to 1.0 kPa and the delay of this formation for slopes with the cohesion of 1.25 kPa, just when the acceleration is reduced. The increase or decrease in cohesion determines the number of points that are being plastified, this number being lower when cohesion is greater.

The difference in each case lies in the redistribution of stresses through strains that generate an acceleration reduction. For slopes with 1.25 kPa of cohesion, this distribution (where the points do not being plastified) is enough to produce a braking process that stops the sliding, unlike slopes with 1.0 kPa, where the points yielding and, therefore, the reduction of acceleration is not enough (still with positive magnitudes) to prevent movement.

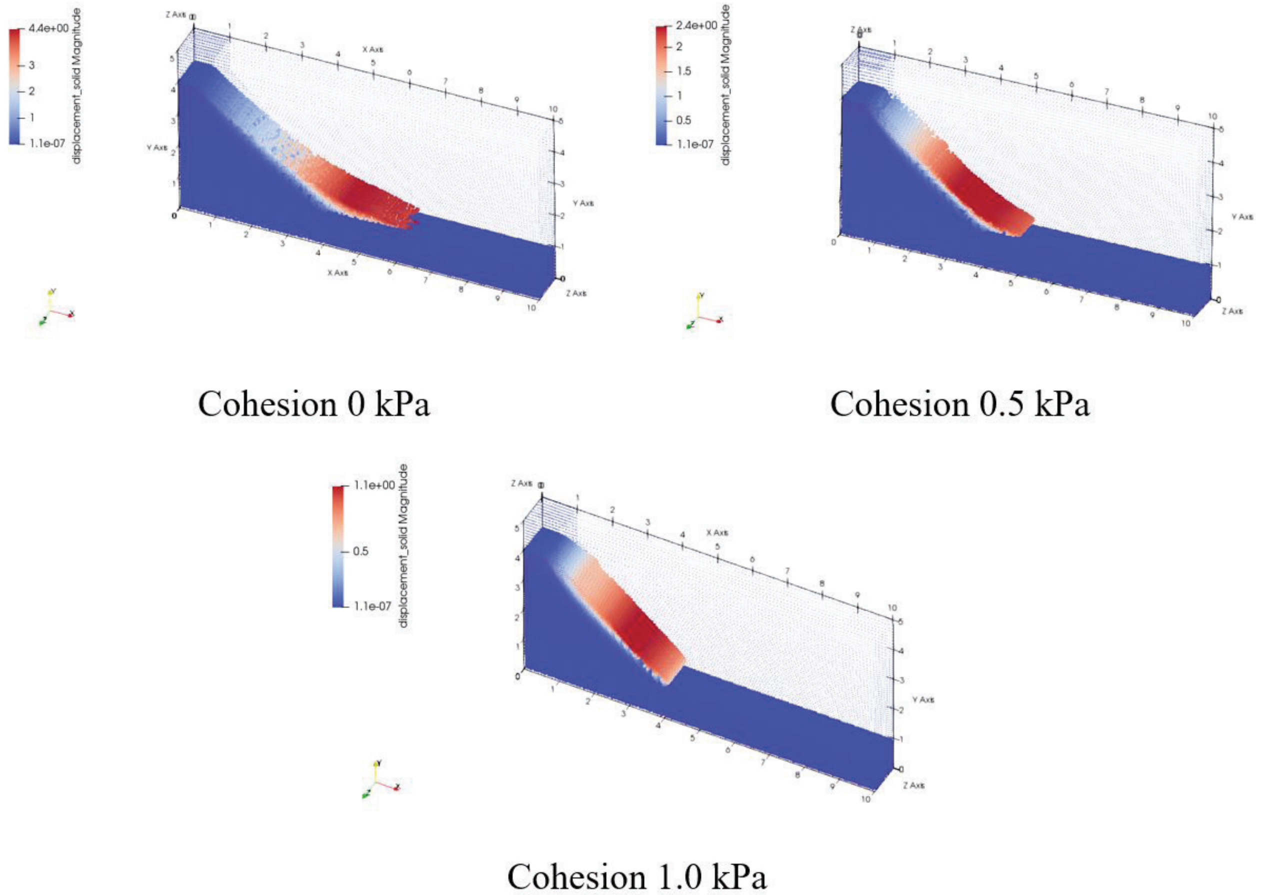

Figure 11. Displacement with Young's modulus 30, 60, 150, and 300 MPa.

In Figure 10, it is also possible to observe how the modulus is responsible for the increase or decrease of the acceleration in the formation of the failure mode: the greater the modulus, the lower the acceleration, both in the maximum peak reached and in its decrease until reaching the failure.

3.3 Development of the landslide

The Young's modulus does not influence the distance covered; otherwise, cohesion strongly influences it and is present in Figure 11. This mass reaches a greater distance when cohesion decreases and is barely displaced when cohesion is equal to 1.0 kPa, with sensitivity to cohesion being one of the essential characteristics of the cases studied.

Figure 12 compares the points on the sloped crown for cases with variation in cohesion after failure. In these analyses, there is no significant difference in the displacement and velocity results when Young's modulus increases, as the figure show for an example with E=30 MPa and E=300 MPa. In all cases, small increases in cohesion generate large decreases in the displacement magnitude. Likewise, this behavior is observed in the velocity of the three points, the greater the cohesion, the lower the velocities' magnitudes.

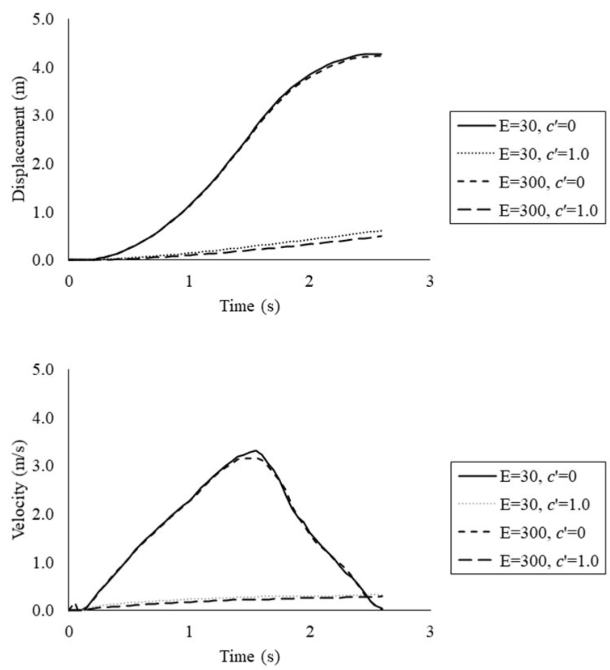

Figure 12. Displacement and velocity of points on the crown of the slope for different cohesions and modules after failure.

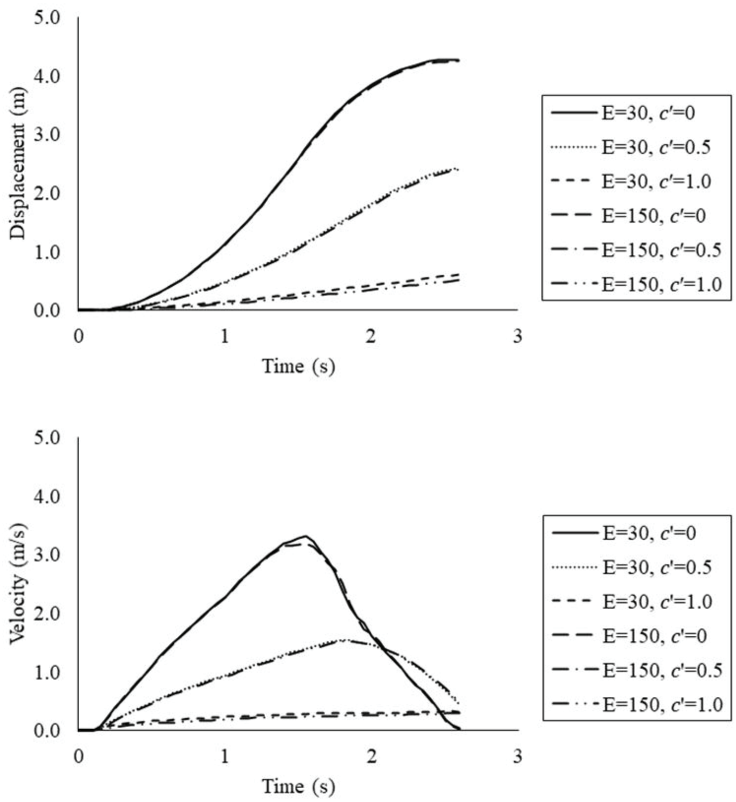

Figure 13. Displacement and velocity of points on the crown of the slope for different cohesions after failure.

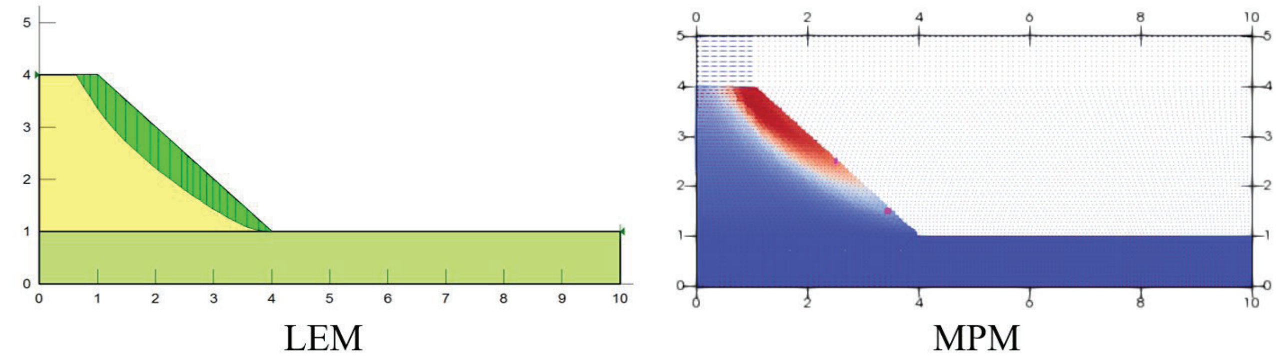

Figure 14. Types of failure.

Figure 13 shows that Young's modulus does not affect the magnitude of displacement either velocity. On the other hand, cohesion strongly influences the magnitude of displacement, velocity, and mass stabilization.

4. Conclusions

The material point method used in this investigation was efficient to analyze the three stages of a mass movement: before the failure, at failure, and the development of landslide. With this method, it was possible to evaluate the influence of strength and deformability parameters.

Despite its simplicity, the elastoplastic model with the Mohr-Coulomb failure criterion, allowed to identify the formation of the failure mode and the development of landslides by analyzing the influence of strength and deformability parameters. With this constitutive model, the behavior of the slope was evaluated using MPM and LEM methods. The results obtained with MPM are not congruent with the results obtained with LEM due to estimates of stress and strains in the material that this method does not consider. According to the MPM results, the slope would remain stable for a more extended time. Likewise, the unstable mass that would slide is overestimated by the LEM, which calculates a failure surface at the slope's foot and not in the body as approximated by the MPM and shown in Figure 14.

The analysis of the strength and deformability parameters showed that Young's modulus has no influence on the development of the movement and that only the strength parameters (cohesion) intervene in the landslide's behavior. After the failure, the soil mass flows and the shear strength properties are the only ones that influence the movements, being like the viscosity in a fluid.

The formation of the failure mode and the development of a mass movement is susceptible to variations in cohesion. Small increases in this property's values define the stability or instability of a slope (Figure 15).

It is possible to identify with the acceleration analysis if a property has, or not, importance in the formation of the failure mode and in the distance reached by the movement once this is developed. Therefore, the acceleration analysis is one of the most important in these results because it is the one that allows identifying entirely if the slope is stable or not. For example, the acceleration and deceleration mechanism is susceptible to small variations in cohesion since this property determines whether the points are being yielded (Figure 15).

Deformations on the slope before failure decrease as Young's modulus increases, as is expected in materials with high stiffness. On the other hand, once the slope slides, i.e., for

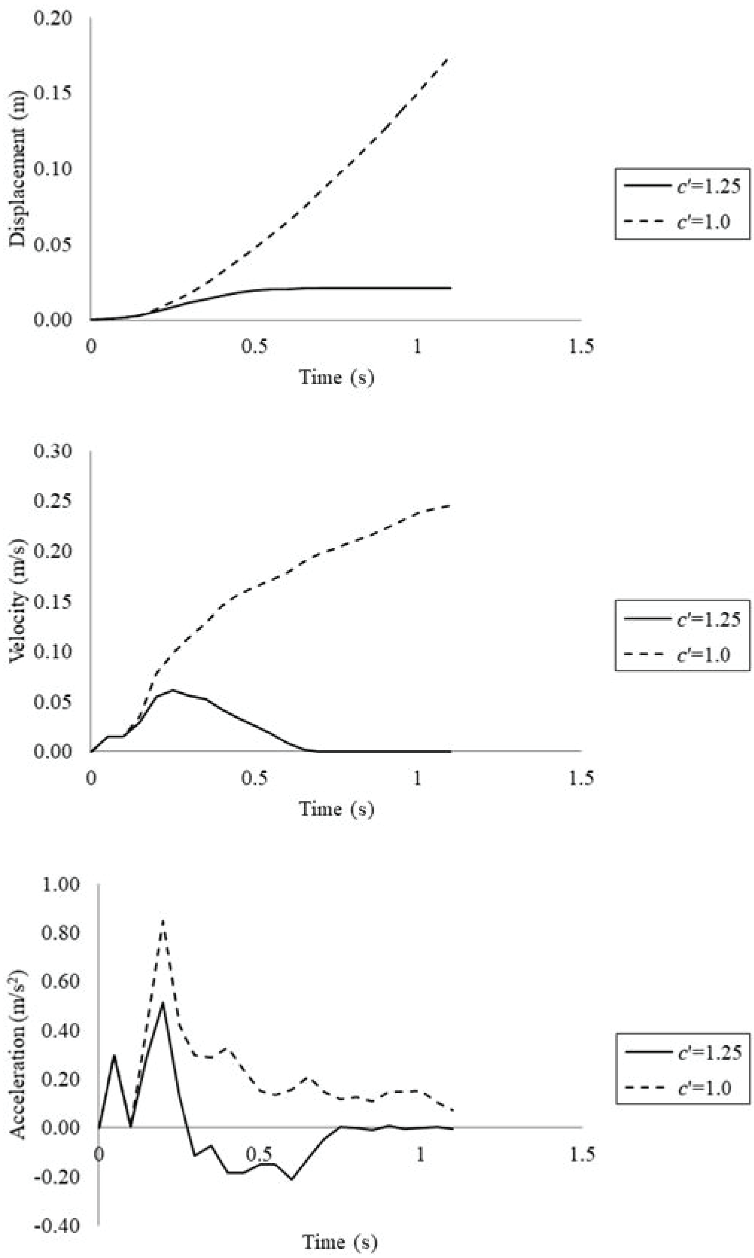

Figure 15. Formation of the failure mode for different cohesions and E=30MPa.

slopes with safety factors less than 1.0 the distance traveled and velocity are slightly influenced by Young's modulus, due to in a perfectly plastic elastic model, once the material is broken, the rigidity of the system tends to zero regardless of the modulus adopted. For this reason, after the break, the displacement and velocity results do not differ significantly from the module variations of up to 10 times the initial value.

The results obtained in this study are also being evaluated in other geometries with other types of materials (including those with different friction angles and higher cohesion values). They, therefore, will be part of future publications.

Acknowledgements

The authors would like to thank the Postgraduate Program in Geotechnic of the University of Brasilia and the National Council for Scientific and Technological Development ("CNPq" by Portuguese abbreviation) for the support of this research.

Declaration of interest

The authors declare that they have no conflict of interest. The research detailed in this report is original, has not been previously published, and is not currently being considered for publication elsewhere.

Author's contributions

Daniela Toro Rojas: conceptualization, methodology, writing - reviewing and editing. Manoel Porfirio Cordão Neto: conceptualization, methodology, validation. Marcio Muniz de Farias: validation, reviewing. Raydel Lorenzo Reynaldo: validation, reviewing.

References

Abe, K., Soga, K., & Bandara, S. (2013). Material point method for coupled hydromechanical problems. *Journal of Geotechnical and Geoenvironmental Engineering*, 140(3), 04013033. http://dx.doi.org/10.1061/(ASCE)GT.1943-5606.0001011.

Aghda, S.F., & Bagheri, V. (2015). Evaluation of earthquake-induced landslides hazard zonation methods: a case study of Sarein, Iran, earthquake (1997). *Arabian Journal of Geosciences*, 8(9), 7207-7227. http://dx.doi.org/10.1007/s12517-014-1658-6.

Alelvan, G.M., Toro-Rojas, D., Rossato, A.C., Lorenzo, R., & Cordão-Neto, M. (2020). MPM and ALE simulations of large deformations geotechnics instability problems. *Dyna*, 87(212), 226-235. http://dx.doi.org/10.15446/dyna.v87n212.80975.

Al-Kafaji, I. (2013). *Formulation of a dynamic material point method (MPM) for geomechanical problems* [Dissertation, Universität Stuttgart]. Online Publikationen der Universität Stuttgart. http://dx.doi.org/10.18419/opus-496

Anura3D. (2017). *Anura3D MPM software: tutorial manual*. Anura3D MPM Research Community.

Aristizábal, E., Vélez, J.I., Martínez, H.E., & Jaboyedoff, M. (2016). SHIA_Landslide: a distributed conceptual and physically based model to forecast the temporal and spatial occurrence of shallow landslides triggered by rainfall in tropical and mountainous basins. *Landslides*, 13(3), 497-517. http://dx.doi.org/10.1007/s10346-015-0580-7.

Bhandari, T., Hamad, F., Moormann, C., Sharma, K.G., & Westrich, B. (2016). Numerical modelling of seismic slope failure using MPM. *Computers and Geotechnics*, 75, 126-134. http://dx.doi.org/10.1016/j.compgeo.2016.01.017.

Borfecchia, F., De Canio, G., De Cecco, L., Giocoli, A., Grauso, S., La Porta, L., Martini, S., Pollino, M., Roselli, I., & Zini, A. (2016). Mapping the earthquake-induced landslide hazard around the main oil pipeline network of the Agri Valley (Basilicata, southern Italy) by means of two GIS-based modelling approaches. *Natural Hazards*, 81(2), 759-777. http://dx.doi.org/10.1007/s11069-015-2104-0.

Bromhead, E.N. (1996). Slope stability modeling: an overview. In: R. Dikau, D. Brunsden, L. Schrott & M.-L. Ibsen (Eds.), *Landslide recognition: identitication, movement and causes* (pp. 231-235). lnternational Association of Geomorphologists.

Ceccato, F., & Simonini, P. (2017). Numerical based design of protection systems against landslides. In *Conference on Numerical Methods in Geotechnics*, Hamburg, Germany.

Coetzee, C.J., Vermeer, P.A., & Basson, A.H. (2005). The modelling of anchors using the material point method. *International Journal for Numerical and Analytical Methods in Geomechanics*, 29(9), 879-895. http://dx.doi.org/10.1002/nag.439.

Farias, M.M., & Naylor, D.J. (1998). Safety analysis using finite elements. *Computers and Geotechnics*, 22(2), 165-181. http://dx.doi.org/10.1016/S0266-352X(98)00005-6.

Fredlund, D. G., & Rahardo, H. (1993). *Soil mechanics for unsaturated soils.* New York: Wiley.

Gabrieli, F., & Ceccato, F. (2016). Impact of dry granular flows on a rigid wall: discrete and continuum approach. In *VI Italian conference of researchers in Geotechnical Engineering*, Padova, Italia.

Giupponi, C., Mojtahed, V., Gain, A., Biscaro, C., & Balbi, S. (2015). Integrated risk assessment of water-related disasters. In P. Paron (Ed.), *Hydro-meteorological hazards, risks, and disasters*. Amsterdam: Elsevier.

González Acosta, L., Pantev, I., Vardon, P.J., & Hicks, M.A. (2018). The use of MPM to estimate the behaviour of rigid structures during landslides. In *Proceedings of the 9th European Conference on Numerical Methods in Geotechnical Engineering (NUMGE 2018)* (Vol. 1, No. 1), Porto, Portugal.

Johansson, J., & Konagai, K. (2007). Fault induced permanent ground deformations: experimental verification of wet and dry soil, numerical findings' relation to field observations of tunnel damage and implications for design. *Soil Dynamics and Earthquake Engineering*, 27(10), 938-956. http://dx.doi.org/10.1016/j.soildyn.2007.01.007.

Kanungo, D.P., Arora, M.K., Sarkar, S., & Gupta, R.P. (2006). A comparative study of conventional, ANN black box, fuzzy and combined neural and fuzzy weighting procedures for landslide susceptibility zonation in Darjeeling Himalayas.

Engineering Geology, 85(3-4), 347-366. http://dx.doi.org/10.1016/j.enggeo.2006.03.004.

Konagai, K., Johansson, J., & Itoh, H. (2004). Pseudo-three dimensional lagrangian particle finite difference method for modeling earthquake induced soil flows. In *Proceedings of the 13th World Conference on Earthquake Engineering* (No. 547), Vancouver.

Li, Z., Nadim, F., Huang, H., Uzielli, M., & Lacasse, S. (2010). Quantitative vulnerability estimation for scenario-based landslide hazards. *Landslides*, 7(2), 125-134. http://dx.doi.org/10.1007/s10346-009-0190-3.

Llano Serna, M.A., Muniz-de Farias, M., & Martínez-Carvajal, H.E. (2015). Numerical modeling of the High Green slip using the material point method. *Dyna*, 82(193), 150-159. http://dx.doi.org/10.15446/dyna.v82n194.48179.

Llano-Serna, M.A., Farias, M.M., & Pedroso, D.M. (2016). An assessment of the material point method for modelling large scale run-out processes in landslides. *Landslides*, 13(5), 1057-1066. http://dx.doi.org/10.1007/s10346-015-0664-4.

Lorenzo, R., Cunha, R.P., & Cordão-Neto, M.P. (2013). Material point method for geotechnical problems involving large deformation. In *PARTICLES III: Proceedings of the III International Conference on Particle-Based Methods: Fundamentals and Applications* (pp. 510-521), Stuttgart, Germany.

Malet, J.P., Thiery, Y., Hervàs, J., Günther, A., Puissant, A., & Grandjean, G. (2009). Landslide susceptibility mapping at 1: 1M scale over France: exploratory results with a heuristic model. In *Proceedings of the Landslide Process: from Geomorphologic Mapping to Dynamic Modelling* (pp. 315-320), Strasbourg, France.

Mast, C.M., Arduino, P., Miller, G.R., & Mackenzie-Helnwein, P. (2014). Avalanche and landslide simulation using the material point method: flow dynamics and force interaction with structures. *Computational Geosciences*, 18(5), 817-830. http://dx.doi.org/10.1007/s10596-014-9428-9.

Morgenstern, N.R., & Price, V.E. (1965). The analysis of the stability of general slip surfaces. *Geotechnique, London*, 15(1), 79-93. http://dx.doi.org/10.1680/geot.1965.15.1.79.

Nazem, M., & Sheng, D. (2005). Arbitrary lagrangian-eulerian method for consolidation problems in geomechanics. In *Proceedings of the International Conference on Computational Plasticity (COMPLAS)* (Vol. 8), Barcelona.

Nazem, M., Sheng, D., & Carter, J.P. (2006). Stress integration and mesh refinement for large deformation in geomechanics. *International Journal for Numerical Methods in Engineering*, 65(7), 1002-1027. http://dx.doi.org/10.1002/nme.1470.

Park, H.J., Lee, J.H., & Woo, I.K. (2013). Assessment of rainfall-induced shallow landslide susceptibility using a GIS-based probabilistic approach. *Engineering Geology*, 161, 1-15. http://dx.doi.org/10.1016/j.enggeo.2013.04.011.

Redaelli, I., Ceccato, F., Di Prisco, C., & Simonini, P. (2017). Solid-fluid transition in granular flows: MPM simulations with a new constitutive approach. *Procedia Engineering*, 175, 80-85. http://dx.doi.org/10.1016/j.proeng.2017.01.028.

Simoni, S., Zanotti, F., Bertoldi, G., & Rigon, R. (2008). Modelling the probability of occurrence of shallow landslides and channelized debris flows using GEOtop-FS. *Hydrological Processes: An International Journal*, 22(4), 532-545. http://dx.doi.org/10.1002/hyp.6886.

Skempton, A.W., & Hutchinson, J. (1969). Stability of natural slopes and embankment foundations. In *Proceedings of the Conference on Soil Mechanics & Foundation Engineering* (Vol. 7, pp. 3-35), Mexico.

Sulsky, D., Chen, Z., & Schreyer, H.L. (1994). A particle method for history-dependent materials. *Computer Methods in Applied Mechanics and Engineering*, 118(1-2), 179-196. http://dx.doi.org/10.1016/0045-7825(94)90112-0.

Sulsky, D., Zhou, S.J., & Schreyer, H.L. (1995). Application of a particle-in-cell method to solid mechanics. *Computer Physics Communications*, 87(1-2), 236-252. http://dx.doi.org/10.1016/0010-4655(94)00170-7.

Uzielli, M., Nadim, F., Lacasse, S., & Kaynia, A.M. (2008). A conceptual framework for quantitative estimation of physical vulnerability to landslides. *Engineering Geology*, 102(3-4), 251-256. http://dx.doi.org/10.1016/j.enggeo.2008.03.011.

van Asch, T.W., Malet, J.P., van Beek, L.P., & Amitrano, D. (2007). Techniques, issues and advances in numerical modelling of landslide hazard. *Bulletin de la Société Géologique de France*, 178(2), 65-88. http://dx.doi.org/10.2113/gssgfbull.178.2.65.

Vardon, P., Wang, B., & Hicks, M. (2017). Slope failure simulations with MPM. *Procedia Engineering*, 175, 258-264. http://dx.doi.org/10.1016/j.proeng.2017.01.021.

Więckowski, Z. (2003). Modelling of silo discharge and filling problems by the material point method. *Task Quarterly*, 4(4), 701-721.

Zabala, F. (2010). *Modeling of hydromechanical geotechnical problems using the material point method* [Doctoral thesis]. Polytechnic University of Catalonia. In Spanish. Retrieved in September 22, 2020, from http://hdl.handle.net/2117/93583

Zabala, F., & Alonso, E.E. (2011). Progressive failure of Aznalcóllar dam using the material point method. *Geotechnique*, 61(9), 795-808. http://dx.doi.org/10.1680/geot.9.P.134.

Zêzere, J.L., Garcia, R.A.C., Oliveira, S.C., & Reis, E. (2008). Probabilistic landslide risk analysis considering direct costs in the area north of Lisbon (Portugal). *Geomorphology*, 94(3-4), 467-495. http://dx.doi.org/10.1016/j.geomorph.2006.10.040.

Zhou, S., Stormont, J., & Chen, Z. (1999). Simulation of geomembrane response to settlement in landfills by using the material point method. *International Journal for Numerical and Analytical Methods in Geomechanics*, 23(15), 1977-1994. http://dx.doi.org/10.1002/(SICI)1096-9853(19991225)23:15<1977::AID-NAG45>3.0.CO;2-3.

Soils and Rocks
An International Journal of Geotechnical and Geoenvironmental Engineering
www.soilsandrocks.com
ISSN 1980-9743
ISSN-e 2675-5475

Analogy to the chaos theory applied to the study of rockfalls

Fernanda Valinho Ignacio[1#], Armando Prestes De Menezes Filho[1], Ana Cristina Castro Fontenla Sieira[1]

Article

Keywords
Mass movement
Rockfalls
Nonlinear systems
Chaos theory

Abstract

Chaos Theory is a mathematical theory devoted to study dynamic systems presenting very peculiar characteristics – sensitivity to initial conditions, positive or close to zero Lyapunov exponents, statistics governed by gaussian or non-gaussian distributions, among others - which make them, in the long run, unpredictable in time and space. This article aims at applying Chaos Theory to rockfall phenomenon. More precisely, the fall of unstable rock blocks was simulated through the RocFall 6.0 program by four preliminary case studies, having different rock slope geometry, different heights of the fall and blocks with different size and shapes. Moreover, the trajectories and reaches of gneissic rock blocks in a section of a phacoidal augen gneiss slope located in Morro do Cantagalo, in the city of Rio de Janeiro, were also simulated from the perspective of Chaos Theory. More precisely, the results suggest that the statistics of the number of fallen blocks at each end point of the trajectories located downstream of the respective slopes can be described by distributions derived from Chaos Theory. In addition, weakly or strongly chaotic behavior seems to be very specially associated with the concavity or convexity of the slopes.

1. Contextualization

Rio de Janeiro is inserted in an environment of rugged relief, with heterogeneous and discontinuous rock masses, and humid tropical climate, marked by manifestations of different types of mass movements. These phenomena, combined with the disorderly urban growth of cities and the absence of planning linked to infrastructure, lead to serious socioeconomic consequences (Menezes Filho, 1993; Ignacio, 2019).

Rockfalls have been considered an extremely important phenomenon due to its high sensitivity to the initial conditions of the unstable blocks, usually involving high kinetic energies and occurring abruptly, which turns out to be difficult to forecast. In order to prevent this type of movement, several rockfall prediction methods (Back analysis of events, *in situ* tests, laboratory tests, Fahrböschung principle, Minimum shadow angle and numerical methods, for example) have been developed and improved over the years. Based on observations and records of real cases, most of them aim at identifying its main characteristics, enabling to subsidize the selection and dimensioning of coexistence and mitigation measures (Evans & Hungr, 1993; Rocha, 2009; Gálvez, 2012; Vijayakumar et al., 2012; Spadari et al., 2012; Tavares, 2015).

However, a common characteristic of those methods is their very restricted application for global analysis of the movement, making the delimitation of potential areas to be eventually affected and parameter estimation seriously impaired. This is mainly due to the non-linearity found in the block falling process and, consequently, to the difficulty of understanding the movement mechanism and its particularities (Ignacio, 2019; Tavares, 2015).

The peculiarities of chaotic systems make them difficult to analyze, for the rockfall phenomena manifestly depend on the launching initial conditions and the impact points along the slope. In addition, several other parameters influence the final response, such as the geometric shape of the slope and the block, the dimensionality of the system and the restitution coefficient of the materials involved in the successive shocks. Such restrictions naturally lead to a probabilistic-statistical approach of investigation, in which the search for regularities in the phenomenon, in particular the final position of the blocks downstream of the slope and their associated probabilistic distributions, can bring a new understanding of the process of instability (Rocha, 2009; Freitas, 2013; Tavares, 2015).

The fall process and the successive shocks of the blocks against the slopes can be viewed as an exchange of information within the unstable system itself, thus changing its entropy over time. In this sense, it is known that the Boltzmann-Gibbs entropy is the one that most adequately describes the evolution of strongly chaotic dynamic systems, having distinctive characteristics, among others, short-range

[#]Corresponding author. E-mail address: fnignacio@gmail.com
[1]Universidade do Estado do Rio de Janeiro, Programa de Pós-Graduação em Engenharia Civil, Rio de Janeiro, RJ, Brasil.

Submitted on November 8, 2020; Final Acceptance on February 18, 2021; Discussion open until May 31, 2021.

DOI: https://doi.org/10.28927/SR.2021.059420

spatial and temporal correlations (or even absence of memory), ergodicity, markedly positive Lyapunov exponent, strong “mixing” in the phase space and compliance with the Central Limit Theorem. The probability distribution that maximizes this entropy is the Gaussian distribution (Equation 1 - where a, b and c are fitting parameters) (Beck & Schlögl, 1993; Tsallis, 1988, 2009).

Systems that present some of the above-mentioned characteristics are the following:

a. The classic Boltzmann gas, an idealized one where the particles move freely inside a stationary recipient, without interacting with one another – except for very brief collisions, where energy and momentum are exchanged with each other – is a paradigm of strongly chaotic system. It presents, for the velocity distribution of its particles, a Maxwell-Boltzmann (Gaussian) distribution (Sears, 1963);
b. Non–linear iterated maps are dynamical systems whose iterative processes are measured in discrete intervals (years, generations etc). One of these famous maps is the ‘logistic model of populational growth’, also known as ‘logistic map’. It shows Gaussian distributions in the regions characterized by positive Lyapunov exponent (i.é, strongly chaotic regions) (Peak & Frame, 1994);
c. Some strongly chaotic systems appear in certain classes of billiard problems. A billiard is a two-dimensional planar region in which a particle moves subjected to a constant velocity along a straight line trajectory between successive bounces from the boundary of the domain. In a special kind of billiard proposed by the Russian mathematician Yakov Sinai (called ‘Sinai billiards’), characterized by having convex domains (arcs of circles facing inwards to the interior domain), it is impossible to foresee the exact trajectories of nearby particles after the impact onto the boundaries. The origin of chaos is intuitively clear in this case, for the curvature of the boundary has a dispersing effect on two parallel trajectories, leading to a rapid separation of nearby trajectories after a few bounces. Furthermore, the velocity distribution of the particles turned out to be Gaussian (Sinai, 1970).

On the other hand, weakly chaotic systems - also called ‘complex systems’ - are described by ‘generalized non-additive entropies’, among which those proposed by Tsallis, such as S_q, S_δ and $S_{q,\delta}$. This time, dynamic systems are characterized by long-range spatial and temporal correlations (long-range memory), broken ergodicity, Lyapunov exponent close to zero, weak “mixing” in the phase space, some type of energy dissipation, and non-compliance to the Central Limit Theorem (Landsberg, 1999; Tsallis, 1988, 2009).

Systems that show some of the above-refered characteristics are the following:

a. Certain evolutionary dynamic systems spontaneously arrange themselves, after a long period of time, in a state of ‘self-organized criticality’, that is, a state of weak chaos characterized by the development of self-similar (fractal) spatial and temporal patterns. That is the case, for example, of the time evolution of elasto-plastic models of geologic materials analyzed under dynamic relaxation. Besides generating fractal fracture patterns, the equivalent plastic deformation time series show their respective Lyapunov exponents very close to zero (Menezes Filho, 2003);
b. Non-linear iterated maps at the primary edge of chaos show non-gaussian statistics, that is, Extended q-Exponentials with the exponent $\delta = 1$ in Equation 2 (Tsallis, 2009);
c. The ‘Stadium Billiard’, discovered by the Russian mathematician Leonid Bunimovich, is a two-dimensional planar billiard having concave domains (arcs of circle facing outward to the interior domain) linked by two parallel straight lines. This non-dispersing billiard shows, for certain particle orbits, a power law divergence of trajectories, with zero Lyapunov exponent (Bunimovich, 1979).

Therefore, weakly (strongly) chaotic systems show very specific characteristics: statistics governed by non-Gaussian (Gaussian) distributions, interacting (non-interacting or interacting for very brief moments) particles and a power-law (exponential) separation of trajectories, among others.

The reader will see further that, applied to the rockfall phenomena, those cited concepts lead to a very rich spectrum of questions: the identification of strong or weak chaotic phenomena through the probability distributions of the number of fallen blocks arrived at certain points downstream of the slope and their gaussianity or not, as well; the geometry of the rock slopes – concave or convex – and a possible analogy with Sinai and Bunimovich billiards; the rapid (exponential) or slow (power-law) divergence of trajectories in convex or concave slopes, due to their dispersing (diverging) or non-dispersing (converging) properties.

It should be pointed out that the application of generalized entropies to natural hazard phenomena – e.g. earthquakes - is quite recent. The researchers have been focusing on the statistics of foreshocks and aftershocks time signals, aiming at predicting these very intrincated phenomenon (Kalimeri et al., 2008; Papadimitriou et al., 2008; Eftaxias, 2010; Papadakis et al., 2015; Vallianatos, 2016).

However, the Authors of this paper are, to the best of their knowledge, unaware of any previous application of Chaos Theory and probability distributions derived from generalized entropies to the rockfall phenomenon in the technical literature.

The optimization of those parametric nonadditive entropies furnishes non-Gaussian probability distributions, among which the Extended q-Exponential distribution (Equation 2 - where *a*’, *b*’, *c*’, q and δ are fitting parameters, q is the entropic parameter and δ is an adjustment parameter) adopted in this research. It should be noted that the parameters *q* ($-\infty < q \leq 3$) and δ, when approaching unity, transform the above generalized distribution into Gaussian (Tsallis, 2009; Menezes Filho, 2003; Tsallis & Cirto, 2013).

$$p(x)_g = a\left[e^{\left[-\left(\frac{x-c}{b}\right)^2\right]}\right] \tag{1}$$

$$p(x)_{q,s} = a'\left[1-(1-q)\left(\frac{x'-c'}{b'}\right)^{\frac{2}{ä}}\right]^{\frac{1}{1-q}} = a'\, e_q^{-\left[\left(\frac{x-c'}{b'}\right)^2\right]^{\frac{1}{ä}}} \tag{2}$$

Here $e_q^{-x} \equiv [1-(1-q)\,x]^{\frac{1}{1-q}}$ $(q \in R)$ is the generalized exponential function, whose inverse is the generalized logarithmic function, defined by $\ln_q x \equiv \left(\frac{x^{1-q}-1}{1-q}\right)$ $(q \in R)$. The above probabilistic distributions derived from the optimization (maximization) of generalized entropic forms, make it possible to describe random-dependent phenomena, enabling to solve several practical problems in highly and weakly chaotic nonlinear systems, such as rockfalls along a slope.

Thus, the present article aims at contributing to a better understanding of the fall behavior, through an interdisciplinary analysis, associating Chaos Theory with the fall movement of rock blocks.

2. Materials and methods

To compose the study, four sections of gneissic (augen) rock slopes (C1, C2, C3 and C4) and the case of study were initially modeled with distinct concave and convex geometries, as shown in Figures 1, 2, 3, 4, and 5, respectively, in the RocFall 6.0 program. For each of these sections, typical blocks were modeled, having the same irregular geometric shape and different sizes, hereafter refered to as ‘Small Irregular Block’ (BIP), ‘Medium Irregular Block’ (BIM) and ‘Large Irregular Block’ (BIG).

For a given geometry of the slopes and the blocks, 100,000 simulations of the falls of these BIP, BIM and BIG blocks were performed in each of the proposed sections. A high number of simulations is mandatory in order to get robust statistics of the final block location points downstream of the slopes, since the number of blocks per each final position is the most relevant distribution for understanding the phenomenon.

In all cases, the Rigid Body Method was selected in the program, in which the unstable blocks were supposed not to be deformable. Moreover, use was made of Monte Carlo statistical-probabilistic sampling of the origin of launching points, generating results that are more realistic.

The histograms of the number of blocks per each final location points downstream of the slopes were adjusted to Gaussian and Extended q-Exponential distributions, according to their strongly or weakly chaotic behavior, derived, as refered, from the Boltzmann-Gibbs and the $S_{q,\delta}$ entropies, respectively. Afterwards, the process carried out in the preliminary study was also applied to the case of the Cantagalo Massif – RJ cut, in one of the sections mapped by GEO-RIO in 2009 during the field research work for the implementation of impact flexible barriers that took place in 2011.

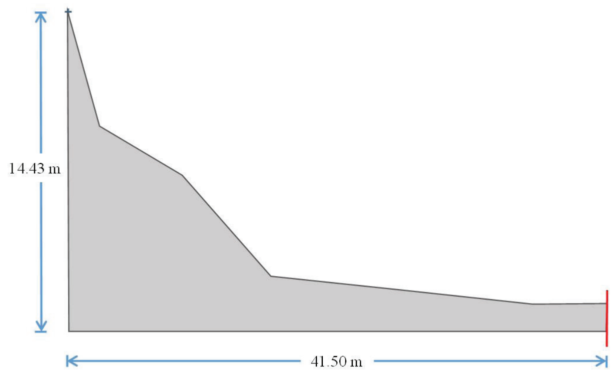

Figure 1. Case C1 geometry (not to scale).

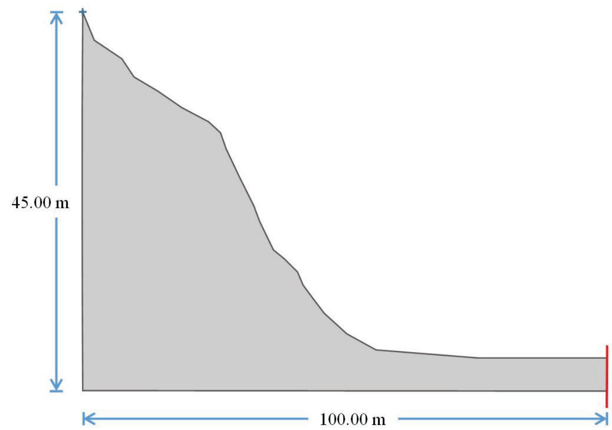

Figure 2. Case C2 geometry (not to scale).

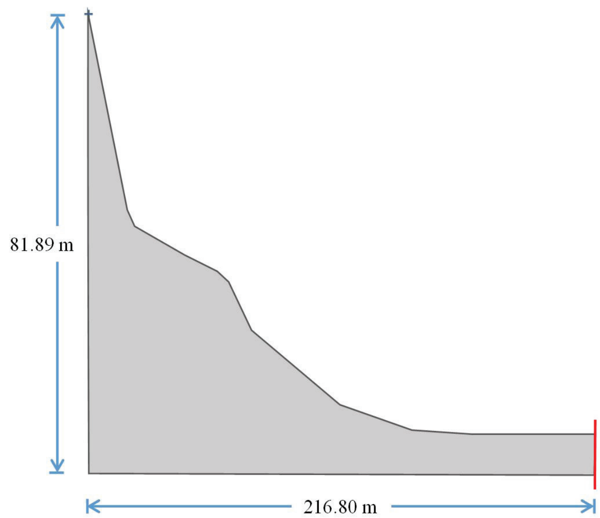

Figure 3. Case C3 geometry (not to scale).

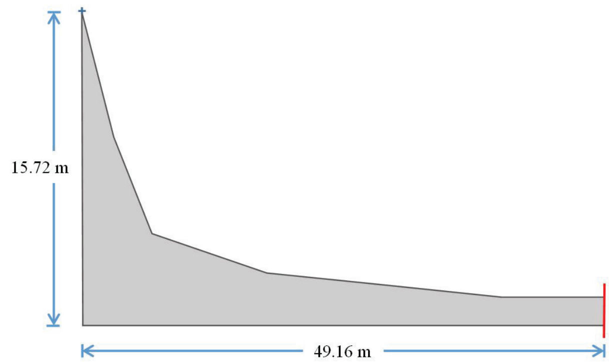

Figure 4. Case C4 geometry (not to scale).

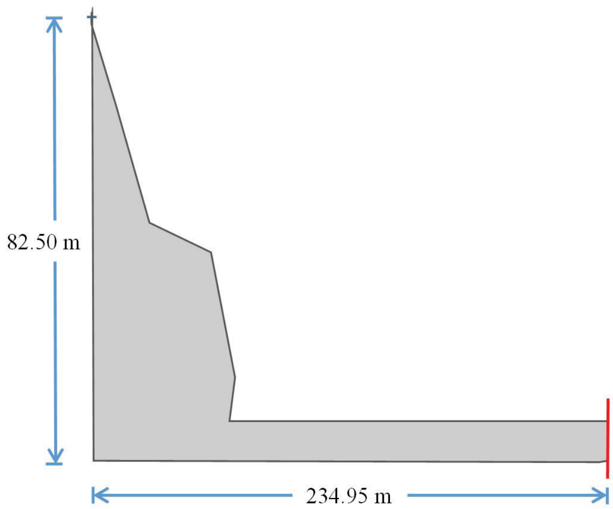

Figure 5. Case of study geometry (not to scale).

The geotechnical parameters of the phacoidal (augen) gneissic slopes and their respective rock blocks (normal and tangential restitution coefficients, dynamic or kinetic friction and rolling friction) were selected from Menezes Filho (1993), Rocha (2009) and Pelizoni (2014), as well as technical studies provided by GEO-RIO in 2009 at Cantagalo Massif. Table 1 shows the parameters required by the RocFall 6.0 program for the geotechnical modeling of the sections of the rock slopes.

The shape of the BIP, BIM and BIG rock blocks and the characteristics of each one of them are shown in Table 2. It should be noted that ‘approximated size’ refers to the edge of the larger size of the irregular block, whose area served as basis for calculating the mass of the blocks according to their specific weight.

All the geometries selected for the slope sections have an elongated base, perfectly articulated to their base level, therefore accommodating all trajectories developed by the fallen rock blocks. In addition, their lauching points are fixed to be the highest in all sections. It was also chosen to investigate the quality of the adherence of the probability distributions to the histogram points in the region of their tail. So, graphs with the vertical axis on a logarithmic decimal scale were made for each slope section and specific block size.

In addition, for each block size, the relation $Ln_q(P(x)/a')$ versus $((x\text{-}c')/b')^{(2/\delta)}$ was also plotted, in order to test the functional universality of the Extended q-Exponential - and its Gaussian counterpart - in describing the statistics of the unstable blocks per each of their final positions downstream of the slopes. Figure 6 shows the flowchart of the methodology adopted.

Table 1. RocFall 6.0 modeling parameters – C1, C2, C3, C4 and case study.

Rock material	Normal restitution coefficient	Tangential restitution coefficient	Dynamic friction	Rolling friction
Augen gneiss	0.35	0.85	0.5	0.15

Table 2. RocFall 6.0 modeling parameters – BIP, BIM and BIG

Block type	Representative format	Approx. size (m)	Mass (kg)	Specific weight (kN/m^3)
BIP		0.5	337.50	27.00
BIM	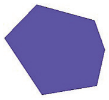	1.00	2,700.00	27.00
BIG		1.40	7,408.80	27.00

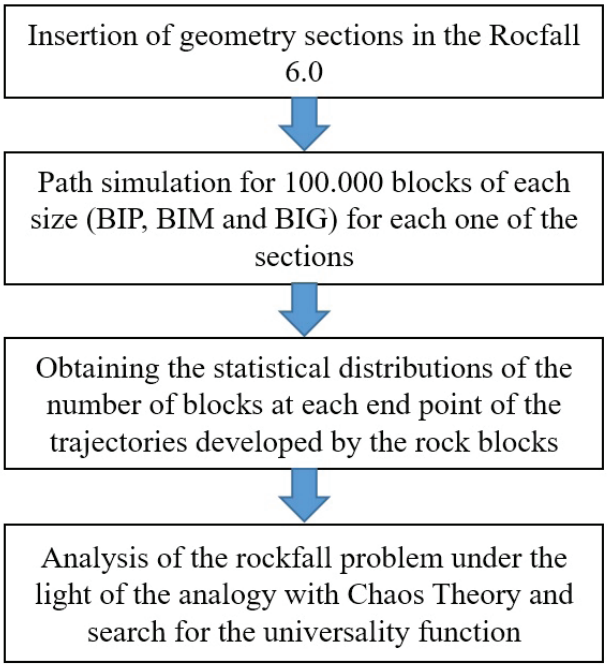

Figure 6. Flowchart of the methodology adopted.

3. Results

3.1 Preliminary study (Cases C1, C2, C3 and C4)

Figures 7, 8, 9, and 10 show the statistics of the number of fallen blocks per each final position downstream of the slopes C1, C2, C3 and C4, plotted in natural and semi-log scales (dot points). As previously explained in the text, the semi-log plot allows a better visualization of the tail of the distributions, a place of occurrence of rare events. Besides, it is also shown the fitting of Gaussian (blue continuous line) and Extended q-exponential (red continuous line) probability distributions. For the each case, the correlation coefficients (R) are also presented.

3.2 Case study

The C1, C2, C3 and C4 geometries previously presented made it possible to apply the same methodology to the case study of Cantagalo Massif – RJ, in which there is a real mapping of the slope, confering greater veracity to the data and analyzes found in the preliminary study.

The Cantagalo Massif is located in the Southern Zone of the City of Rio de Janeiro, specifically between the neighborhoods of Copacabana and Ipanema. On the face of the hill around Professor Gastão Bahiana Street, close to Barata Ribeiro Street and Mayor Sá Freire Alvim Tunnel, there is a rocky escarpment with approximately 175 meters high, in an area of approximately 8,000 m^2 composed mostly of phacoidal augen gneiss.

Due to the little vegetation that covers the escarpment, the face of the hill is constantly exposed to the action of physical and chemical weathering, mainly due to the thermal variation during the day - expansion and contraction of minerals with different thermal expansion coefficients. This has been leading to a gradual formation of (micro) fissures - fractures inside the rock volume, constantly growing over the years. For this reason, it is quite common to have, as a result, irregular blocks and thin, discontinuous and partially embedded chips along the entire escarpment, which may occasionally come off.

The inspections carried out by GEO-RIO identified that the rock mass has few fractures of tectonic origin, which could possibly detach more voluminous portions of the slope. These very superficial and low persistent fractures are mostly the result of thermal exfoliation isolating small to medium blocks.

Historically, the GEO-RIO database indicates that the geological accidents in the last 60 years on this slope refer to the detachment of small splinters and irregular blocks in the rock mass, with the capacity to cause damage from small

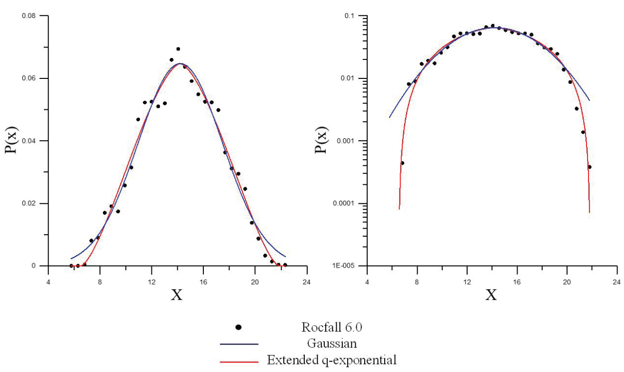

Figure 7. Case C1 – BIG (Gaussian R = 0.9843; Extended q-exponential R = 0.9883).

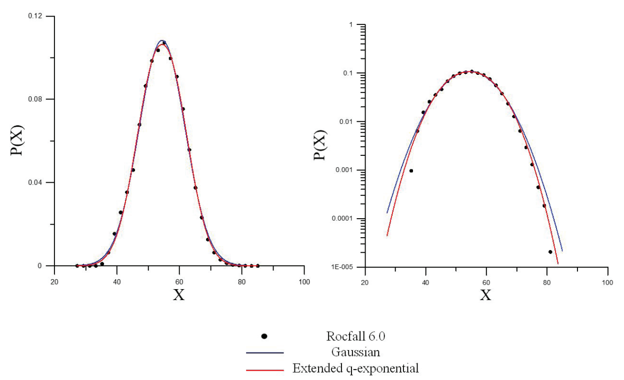

Figure 8. Case C2 – BIP (Gaussian R = 0.9988; Extended q-exponential R = 0.9991).

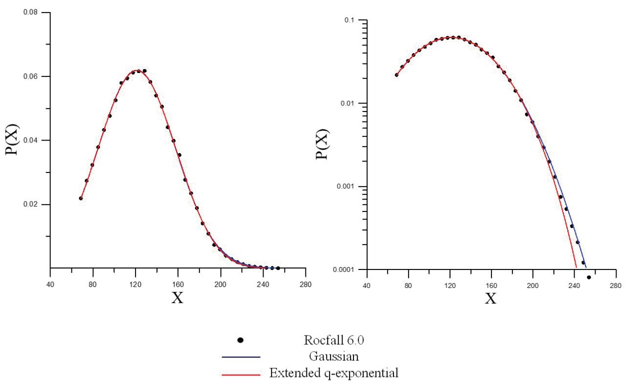

Figure 9. Case C3 – BIP (Gaussian R = 0,9994; Extended q-exponential R = 0.9995).

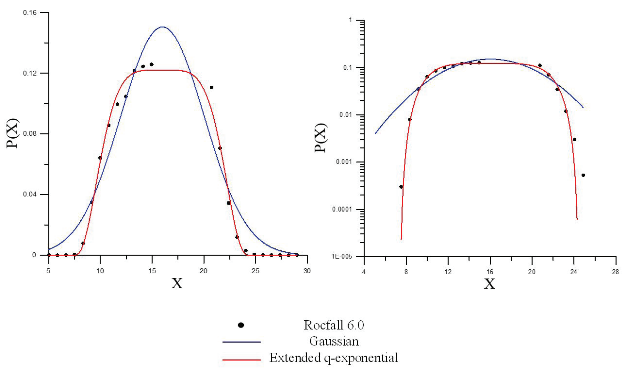

Figure 10. Case C4 – BIP (Gaussian R = 0.9599; Extended q-exponential R = 0.9954).

to medium size in the nearby buildings. Although the massif does not provide previous signs of movement, the existence of a situation of geological-geotechnical risk on the slope cannot be ruled out, as well as future interventions, mainly due to the proximity of local buildings to the southeastern slope of Cantagalo Massif.

Considering the geological-geotechnical risk, it appears that the possibility of the detachment of blocks is considerable and has been presented over the years, but so far without serious consequences. The profile was mapped by GEO-RIO in 2009 in order to study and enable the solution of coexistence of flexible barriers of impact on the site (GEO-RIO, 2009).

As in the preliminary study, Figure 11 shows Gaussian and Extended q-exponential probability distributions with the respective correlation coefficients (R) as an example for the case study.

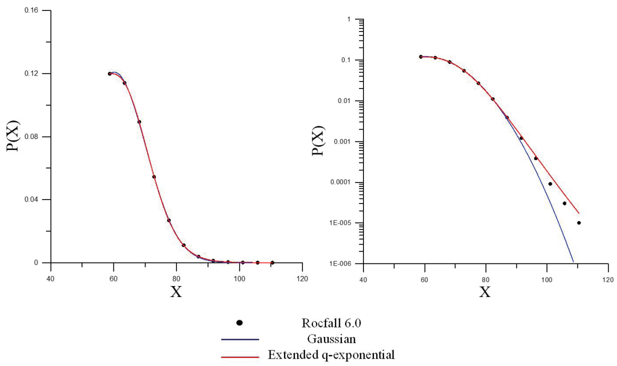

Figure 11. Case of study – BIM (Gaussian R = 0.9999; Extended q-Exponential R = 0.9999).

4. Discussions

The histograms of the number of unstable blocks located at each point downstream of the slopes show, after 100,000 simulations, consistent statistical data, sufficient to confirm the chaotic nature of the phenomenon in question. That is, the results suggest, as indicated in Table 3, that the Gaussian and the Extended q-exponential probability distributions, derived from the Boltzmann-Gibbs and $S_{q,\delta}$ entropies, respectively, describe strongly and weakly chaotic behavior.

Table 3. Compilation of the results obtained

Slope profile	Slope surface	Adjustment probability distribution	Chaotic behavior
Case C1	Concave	Extended q-Exponential	Weak
Case C2	Convex	Gaussian	Strong
Case C3	Convex	Gaussian	Strong
Case C4	Concave	Extended q-Exponential	Weak
Case study	Convex	Gaussian	Strong

Furthermore, in all slope profiles, it was possible to fit Extended q-exponential and Gaussian probability distributions to the experimental data of different block sizes (BIP, BIM and BIG) for the same slope material (phacoidal augen gneiss). So, it was initially found in each case that the size of the blocks (BIP, BIM and BIG) does not significantly influence the probability distributions obtained in the final analysis of the phenomenon. However, it is necessary to expand these studies, focusing on different block geometries, since, in the present research, the same geometry was used for all block sizes.

The experimental results clearly suggest that the slope profiles with markedly convex surfaces, such as C2, C3 and Case Study (Figures 2, 3, and 5) display a strongly chaotic behavior, having statistics characterized by Gaussian distributions (Figures 8, 9 and 11). It is intuitively clear that this may be due to the convex shape of the profiles involved, allowing the ejection of blocks in different trajectories, which promotes a wide dispersion along the slope, a very similar behavior encountered in Sinai billiard.

Therefore, it might be argued that the divergence between different block trajectories might follow an exponential law, typical of strongly chaotic phenomena. Accordingly, the two distributions provide very close results (Figures 8, 9 and 11), even in their tail regions, where both show strong adherence to experimental data.

On the other hand, the profiles of slopes with concave or globally concave surfaces, such as the C1 and C4 cases (Figures 1 and 4), present a weakly chaotic behavior. This time, the Extended q-exponential distribution provides much better results than the Gaussian one (Figures 7 and 10). Thus, it is a phenomenon ruled by non-Gaussian distributions, particularly in the region of the tails, which show strong adherence to experimental data. This seems to be mainly related to the concave shape of those profiles which, unlike the convex ones, tend to converge trajectories. In addition, the simulations show that the blocks remain in contact with the slope for a longer time, favoring the development of long-range memory due to the exchange of information within the system, while facilitating the dissipation of energy.

Through the previous analyzes, and with the data obtained in the preliminary study and in the case study, it is possible to elaborate the graph of the Figure 12, in which the argument $[(x\text{-}c')/b']^{2/\delta}$ and the generalized logarithmic function lnq $[p(x)/a']$ are plotted. More specifically, just as a common exponential function appears as a straight line, when plotted on a graph whose vertical axis is its inverse logarithmic function, in the same way a generalized exponential function will appear straight on a graph in which, on the vertical axis, is its generalized logarithmic inverse function.

Thus, in addition to providing a better visualization of the results obtained, it illustrates the tendency of the experimental data to collapse around the same and unique line (general equation: y = - 1.0346x + 0.0295; correlation coefficient $R = 0.9980$) (Figure 12), a clear manifestation of a

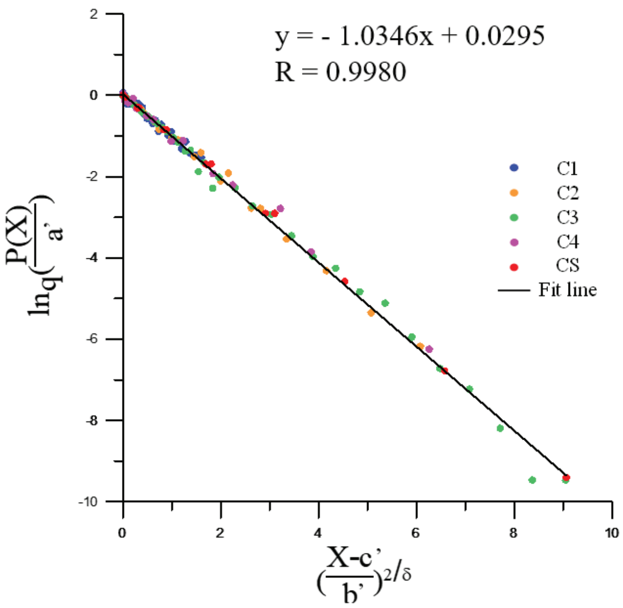

Figure 12. Functional universality graph.

type of functional universality that occurs in the phenomenon of rockfalls.

Therefore, the experimental results seem to suggest that, at least in the milestones and limitations involved in this research, regardless of the slope geometry, the height of the fall and the size of the block, the phenomenon's statistics seems to be adequately described by the Extended q-exponential distribution (and its Gaussian particular case).

5. Conclusions

The results obtained through numerical modeling showed that the profile of Cantagalo Massif (convex surface) provided probability distributions of trajectory-reach invariably Gaussian (or Extended q-exponentials in which q and δ tend to 1), whereas, in concave or globally concave profiles which gradually articulate with the base level, the Extended q-exponential probability distribution provides better results than the Gaussian one.

This suggests that convex slope profiles present a highly chaotic behavior, allowing the ejection of blocks in different trajectories and promoting a wide diffusion along the slope, in which the various trajectories might present an expressive (exponential) divergence between them.

On the other hand, the concave profiles show a weakly chaotic behavior, mainly related to the fact that in these profiles, unlike the convex ones, there is a tendency for the trajectories to converge. In addition, the blocks remain in contact with the slope for a longer time, which favors the development of a long-range memory due to the exchange of information within the system, while facilitating the dissipation of energy.

Furthermore, the results suggest that mass movements of rockfall type can be described by the Chaos Theory, in view of the unique functional universality found. More precisely, the Extended q-exponential probability distribution (and the Gaussian, for cases where q and δ tend to 1) is able to statistically describe the phenomenon, regardless of the geometric shape of the slopes, the height of the fall and the size of the blocks. This functional universality is typical of chaotic phenomena, which denote its great power of unification and systematization of acquired knowledge.

It is noteworthy that the correct definition of the probabilistic distributions that govern the phenomenon of rockfalls with respect to their trajectory and reach has a decisive influence on the establishment of safety zones for buildings and civil works around these potentially dangerous areas, enabling, therefore, for a better urban planning for the growth of cities, especially those established in mountaineous regions, as well as assisting current methods.

Acknowledgements

The authors thank CAPES for the financial assistance represented by the first author's scholarship, and Prof. Dr. Rogério Feijó (State University of Rio de Janeiro) for the transfer of data used in this research.

Declaration of interest

Absence of conflicting interests.

Author's contributions

Fernanda Valinho Ignacio: writing – original draft, investigation, formal analysis, visualization. Armando Prestes De Menezes Filho: conceptualization, methodology, supervision, writing – review & editing, validation. Ana Cristina Castro Fontenla Sieira: methodology, supervision, writing – review & editing, validation.

References

Beck, C., & Schlögl, F. (1993). *Thermodynamics of chaotic systems*. Cambridge University Press.

Bunimovich, L.A. (1979). On ergodic properties of nowhere dispersing billiards. *Communications in Mathematical Physics*, 65, 295-312. http://dx.doi.org/10.1007/BF01197884.

Eftaxias, K. (2010). Footprints of nonextensive tsallis statistics, selfaffinity and universality in the preparation of the L'Aquila Earthquake Hidden in a Pre-Seismic EM Emission. *Physica A*, 389(1), 133-140. http://dx.doi.org/10.1016/j.physa.2009.08.034.

Evans, S.G., & Hungr, O. (1993). The assessment of rockfall hazards at the base of talus slopes. *Canadian Geotechnical Journal*, 30(4), 620-636. http://dx.doi.org/10.1139/t93-054.

Freitas, A.S. (2013). *Numerical analysis of rockfall cases* [Master's dissertation, Federal University of Rio de Janeiro]. Federal University of Rio de Janeiro's repository (in Portuguese). Retrieved in November 9, 2020, from http://www.coc.ufrj.br/pt/dissertacoes-de-mestrado/378-msc-pt-2013/4212-andre -da-silva-freitas

Gálvez, J.H.F. (2012). *Geotechnical conditions and rockfall analysis of the RS71 / BR153 Highway, section 2* [Master's dissertation, Federal University of Rio Grande do Sul]. Federal University of Rio Grande do Sul's repositor (in Portuguese). Retrieved in November 9, 2020, from https://lume.ufrgs.br/han dle/10183/60724

GEO-RIO. (2009). *The characterization of the geological risk for the slope of professor gastão bahiana street* [Unpublished Diagnostic Report]. (in Portuguese).

Ignacio, F.V. (2019). *Application of chaos theory in the study of rock falls in Morro do Cantagalo, Rio de Janeiro – RJ* [Master's dissertation, State University of Rio de Janeiro]. State University of Rio de Janeiro's repositor (in Portuguese). Retrieved in November 9, 2020, from http://www.labbas.eng.uerj.br/p geciv/nova/ files/dissertacoes/170.pdf

Kalimeri, M., Papadimitriou, C., Balasis, G., & Eftaxias, K. (2008). Dynamical complexity detection in pre-seismic emissions using nonadditive tsallis entropy. *Physica A*, 387(5-6), 1161-1172. http://dx.doi.org/10.1016/j.physa.2007.10.053.

Landsberg, P. (1999). Entropies galore! *Brazilian Journal of Physics*, 29(1), 46-49. http://dx.doi.org/10.1590/S0103-97331999000100004.

Menezes Filho, A.P. (1993). *Geological-geotechnical aspects of a phacoidal gneiss alteration profile* [Unpublished master's dissertation]. Pontifical Catholic University of Rio de Janeiro (in Portuguese).

Menezes Filho, A.P. (2003). *Thermodynamic nonextensivity, discrete scale invariance and elastoplasticity: a study of a self-organized critical geomechanical numerical model* [Doctoral thesis, Pontifical Catholic University of Rio de Janeiro]. Pontifical Catholic University of Rio de Janeiro's repositor (in Portuguese). https://doi.org/10.17771/PUCRio.aca d.4249

Papadakis, G., Vallianatos, F., & Sammonds, P. (2015). A nonextensive statistical physics analysis of the 1995 Kobe, Japan Earthquake. *Pure and Applied Geophysics*, 172(7), 1923-1931. http://dx.doi.org/10.1007/s00024-014-0876-x.

Papadimitriou, C., Kalimeri, M., & Eftaxias, K. (2008). Nonextensivity and universality in the earthquake preparation process. *Physical Review*, E77(3):036101. https://doi.org/10.1103/P hysRevE.77.036101.

Peak, D., & Frame, M. (1994). *Chaos under control – the art and science of complexity*. W.H. Freeman and Company.

Pelizoni, A.B. (2014). *Analysis of debris flows in Região Serrana Fluminense* [Master's dissertation, Federal University of Rio de Janeiro]. Federal University of Rio de Janeiro's repository (in Portuguese). Retrieved in November 9, 2020, from http://www.coc.ufrj.br/pt/dissertacoes-de-mestrado/380-msc-pt-2014/4461-andrea-balbuzano-pelizoni

Rocha, J.S.A. (2009). *Numerical studies on rockfalls paths* [Master's dissertation, Federal University of Rio de Janeiro]. Federal University of Rio de Janeiro's repository (in Portuguese). Retrieved in November 9, 2020, from http://www.coc.ufrj.br/pt/ dissertacoes-de-mestrado/109-msc-pt-2009/1572-jose-simao-de-almeida-rocha

Sears, F.W. (1963). *An introduction to thermodynamics, the kinetic theory of gases, and statistical mechanics*. Addison-Wesley.

Sinai, Y.G. (1970). Dynamical systems with elastic reflections: ergodic properties of dispersing billiards. *Russian Mathematical Surveys*, 25(2), 141-192.

Spadari, M., Giacomini, A., Buzzi, O., Fityus, S., & Giani, G.P. (2012). In situ rockfall testing in New South Wales, Australia. *International Journal of Rock Mechanics and Mining Sciences*, 49, 84-93. http://dx.doi.org/10.1016/j.ijrmms.2011.11.013.

Tavares, L.M.M.S.C. (2015). *Parametric analysis in the study of rockfalls on Rocky slopes* [Master's dissertation, Porto University]. Porto University's repository (in Portuguese). Retrieved in November 9, 2020, from https://repositorio-abert o.up.pt/bitstream/10216/79774/2/36026.pdf

Tsallis, C. (1988). Possible generalization of boltzmann-gibbs statistics. *Journal of Statistical Physics*, 52, 479-487. http://dx.doi.org/10.1007/BF01016429.

Tsallis, C. (2009). *Introduction to nonextensive statistical mechanics – approaching a complex world*. Springer Press.

Tsallis, C., & Cirto, L.J.L. (2013). Black hole thermodynamical entropy. *European Physical Journal*, 73, 2487. http://dx.doi.org/10.1140/epjc/s10052-013-2487-6.

Vallianatos, F. (2016). Could complexity theory and statistical physics be used to support earthquake precursors recognition? In *Proceedings of the 35th General Assembly of the European Seismological Commission*. Trieste, Italy.

Vijayakumar, S., Yacoub, T., Ranjram, M., & Curran, J.H. (2012). Effect of rockfall shape on normal coefficient of restitution. In *Proceedings of the 46th US Rock Mechanics – Geomechanics Symposium*. Chicago, Illinois.

List of Symbols and Abbreviations

a Random variable a of the Gaussian probability distribution
a' Random variable a'of the Extended q-Exponential probability distribution
b Random variable b of the Gaussian probability distribution
b' Random variable b'of the Extended q-Exponential probability distribution
c Random variable c of the Gaussian probability distribution
c' Random variable c'of the Extended q-Exponential probability distribution
q Entropic parameter of the degree of non-additivity
R Correlation coefficient
S_q Tsallis' Generalized entropy
$S_{q,\delta}$ Generalization of Tsallis' Generalized Entropy
x Variable of probability distributions
y Fit line equation
δ Entropic adjustment parameter

Technical notes

Soils and Rocks

An International Journal of Geotechnical and Geoenvironmental Engineering

www.soilsandrocks.com

ISSN 1980-9743
ISSN-e 2675-5475

Analysis of different failure criteria to evaluate bauxite tailings mechanical behavior through numerical modelling

Giovani Jordi Bruschi[1#], Fernando Fante[1], Mariana Tonini de Araújo[1], Gustavo Dias Macedo[1], Cesar Alberto Ruver[1]

Technical Note

Keywords
Bauxite tailings
Mechanical behavior
Triaxial testing
Numerical simulation
ABAQUS

Abstract

In recent years several dam failures have been reported throughout the world, generating a social concern on mine tailings. Along these lines, it became essential to understand the mechanical behavior of these materials in order to refine current design technologies and prevent more tragedies. In this context, this research had two main goals: (i) to analyze bauxite tailings mechanical behavior through isotropically consolidated-undrained triaxial tests and consolidation tests; and (ii) to compare triaxial tests and numerical simulations results. Confining stresses of 75kPa, 150kPa, and 300kPa were applied in the triaxial tests. Numerical modelling was performed through ABAQUS software, in which three different failure criteria were analyzed, Mohr-Coulomb Model (MCM), Drucker-Prager Model (DPM), and Modified Cam-Clay Model (MCCM). Results indicated that all studied criteria showed satisfactory results, however, DPM was the best criterion to simulate bauxite tailings mechanical behavior and respective strength parameters.

1. Introduction

The mining industry generates large quantities of mine tailings daily. These materials are normally disposed of in hydraulic-fill tailing dams as slurries, and depending on their constituent minerals can negatively affect the environment if their deposition is deficient and/or incorrect (Schnaid et al., 2014). In the past decades, major incidents related to failures in mine tailing dams have been reported (Liu et al., 2015) and two recent and serious cases occurred in Brazil. The Mariana disaster, in 2015, resulted in the release of more than 50 million cubic meters of iron ore tailings, as well as in the death of 19 people (Gama et al., 2019). The Brumadinho disaster, in 2019, had more than 300 victims and 13 million cubic meters of mine tailings released (Furlan et al., 2020).

Safety assurance of mine tailing dams is a challenging task encountered in the mining process (Owen et al., 2020). The stability of these structures requires extensive geotechnical and geological investigation, such as water table configuration; aquifer boundaries; site characterization; and strength-stability analysis (Coulibaly et al., 2017). Besides, these parameters are normally associated with complex and expensive tests (e.g. SCPTu, VANE test). Numerical simulation, based on the Finite Element Method (FEM), can be presented as a relevant and low-cost alternative for predicting mine tailings strength parameters (Braga & Nogueira, 2019). The prediction of mine tailings mechanical behavior, without the need of expensive and time-demanding tests, is important in all engineering designs. In this context, ABAQUS is a software widely employed for finite element analysis in many engineering fields.

Concerning geotechnical engineering applications, Dai & Qin (2013) performed and evaluated natural clayey soil behavior using numerical simulation in ABAQUS and compared the fit between real and simulated results employing the Modified Cam-clay Model (MCCM), with simulation parameters acquired from an isotropic consolidation and triaxial tests. The model fitted well experimental e-ln p', u-ε_a, and q-ε_a curves. Grzyb et al. (2012) investigated the bearing capacity of a reinforced shallow foundation in ABAQUS, analyzing the impact of constitutive laws (Drucker-Prager and Modified Drucker-Prager with cap criteria). A small-scale laboratory model provided the simulation parameters. Results showed fair agreements among vertical force-displacement curves, measured and predicted; Drucker-Prager with cap criterion reproduced better the soil behavior. Liu & Chen (2017) implemented a strain-hardening Drucker-Prager model in ABAQUS through a subroutine, applying the numerical modeling to solve a tunnel excavation issue. Numerical results presented fair agreements with analytical ones in terms of mean effective stress, deviatoric stress, and plastic deviatoric strain. Other studies performed using ABAQUS were: (i) pipelines behavior simulation in unsaturated soils (Robert

[#]Corresponding author. E-mail address: giovani.bruschi@ufrgs.br
[1]Universidade Federal do Rio Grande do Sul, Departamento de Engenharia Civil, Programa de Pós-graduação em Engenharia Civil, Porto Alegre, RS, Brasil.
Submitted July 10, 2020; Final Acceptance on September 23, 2020; Discussion open until May 31, 2021.

DOI: https://doi.org/10.28927/SR.2021.053720

2017); (ii) soil-pipe interaction in dry and partially saturated sand (Jung et al. 2013); and (iii) slope stability analysis using extended Drucker-Prager yield criterion (Su and Li 2009).

However, previous works relating mine tailings and numerical analysis were performed in software other than ABAQUS. Braga & Nogueira (2019) studied a sandy tailing deposit from iron ore mining using the computational program ANLOG – Nonlinear Analysis of Geotechnical Works. Coulibaly et al. (2017) assessed the stability of a tailing dam through numerical analysis with SLOPE/W and SEEP/W. In a most recent study, Mahdi et al. (2020) numerically modeled a tailing dam containing residues of Alberta oil-sand industry in Canada by means of FLO-2D Software for two-dimensional flood or single-phase mud-flood simulation. Thus, there is a research gap related to the use of ABAQUS and tailing dams. To fill this gap, the present research sought to analyze the bauxite tailings strength behavior through isotropically consolidated-undrained triaxial testing and numerical simulation, the last performed in ABAQUS software. Three types of failure criteria were tested: Mohr-Coulomb, Drucker-Prager, and Modified Cam-Clay.

2. Experimental data

In order to obtain geomechanical parameters of the mining tailing samples, materials were collected from a bauxite mining industry in northern Brazil. Consolidated-Undrained (CIU) triaxial tests were conducted in undisturbed samples using three different confining stresses, 75kPa, 150kPa, and 300kPa. Table 1 presents the geomechanical information of each triaxial test. Terms “initial” and “final” refer to the sample’s starting and ending consolidation conditions, and term “at failure” refers to peak conditions defined by the Mohr-Coulomb failure criterion. Results of the CIU triaxial tests as well as their strength parameters are shown in Figure 1 and Figure 2, respectively. In Figure 1, the p’-q plan aids on the determination of the “*M*” parameter and the critical state friction angle “ϕ_{cs}’”, while the s’-t plan determines the peak friction angle “ϕ’”. Schnaid et al. (2014) obtained an “*M*” value of 1.4 and a “ϕ_{cs}” of 36° for bauxite tailings, similar to those obtained in this study.

Consolidation tests were also performed and followed ASTM D2435/D2435M-11 procedures (ASTM, 2020). Table 2 shows the parametrical information and Figure 3 shows consolidation tests graphical results.

Applying the geomechanical parameters acquired by means of experimental triaxial tests of bauxite tailing samples it was possible to perform the numerical simulations and compare computational results with experimental ones.

3. Method

The numerical analysis was based on the Finite Element Method (FEM) and performed through ABAQUS software. Three types of failure criteria were tested: Mohr-Coulomb Model (MCM), Drucker-Prager Model (DPM), and Modified Cam-Clay Model (MCCM). In ABAQUS software a 2.5 cm by 5 cm axisymmetric element was created, representing triaxial specimens with a 5 cm diameter and 10 cm height. In the model, Figure 4, the y-axis is applied to the roller to restrict horizontal movement, and the bottom horizontal surface is restricted in the vertical direction.

Table 1. Experimental triaxial data.

Parameter		σ'_3 = 75kPa	σ'_3 = 150kPa	σ'_3 = 300kPa
Initial	Height (mm)	101.0	101.2	100.5
	Diameter (mm)	48.57	50.56	49.55
	Moisture content (%)	28.4	37.0	32.3
	Dry density (N/m^3)	1.39e+4	1.28e+4	1.31e+4
	Saturation (%)	78.2	88.0	79.8
	Void ratio	1.06	1.23	1.18
Final	Moisture content (%)	35.9	40.1	36.7
	Dry density (N/m^3)	1.40e+4	1.32e+4	1.38e+4
	Cross sectional area (mm^2)	1839.0	1955.0	1832.0
	Saturation (%)	100.0	100.0	100.0
	Void ratio	1.05	1.17	1.07
	Back pressure (%)	399.0	399.0	398.9
Vertical effective consolidation stress (kPa)		74.92	153.6	300.6
Horizontal effective consolidation stress (kPa)		74.97	150.0	300.0
Vertical strain after consolidation (%)		-0.01505	-0.03742	-0.04021
Volumetric strain after consolidation (%)		0.8090	2.646	4.968
Shear strength (kPa)		58.66	92.77	117.8
Strain at failure (%)		1.58	1.85	2.32
Strain rate (%/min)		0.01247	0.01247	0.01247
Deviator stress at failure (kPa)		117.3	185.5	235.6
Effective minor principal stress at failure (kPa)		24.85	73.01	102.4
Effective major principal stress at failure (kPa)		142.2	258.5	338.0
B-Value		0.99	0.99	0.99

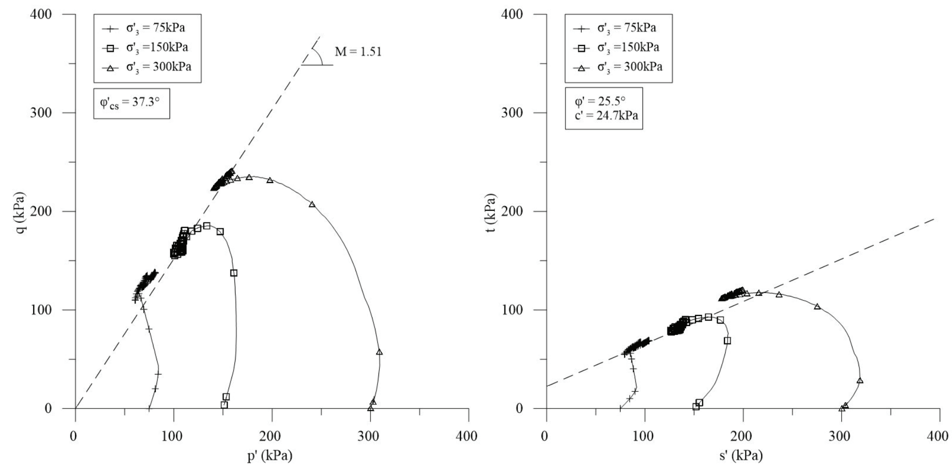

(a) (b)

Figure 1. Stress paths for the experimental triaxial data: (a) critical state parameters from p'- q plan; (b) peak parameters from s'- t plan.

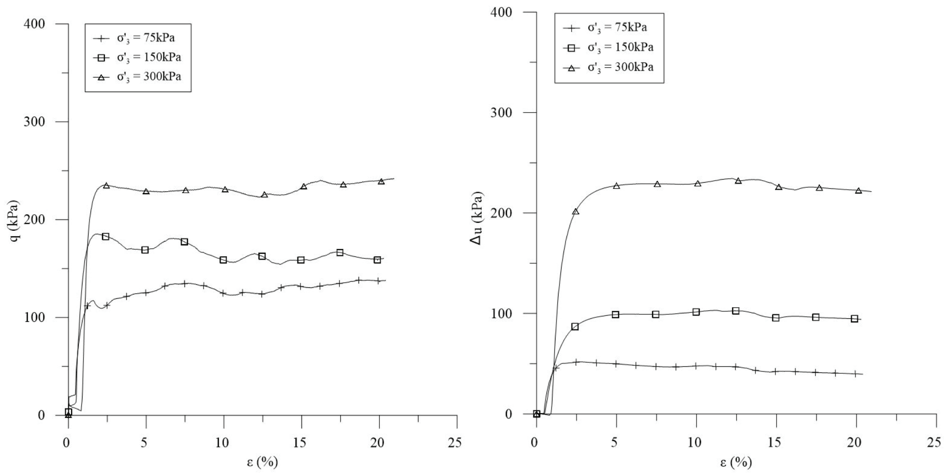

(a) (b)

Figure 2. Stress-strain curves (a) and pore-pressure variation (b) for the experimental triaxial data.

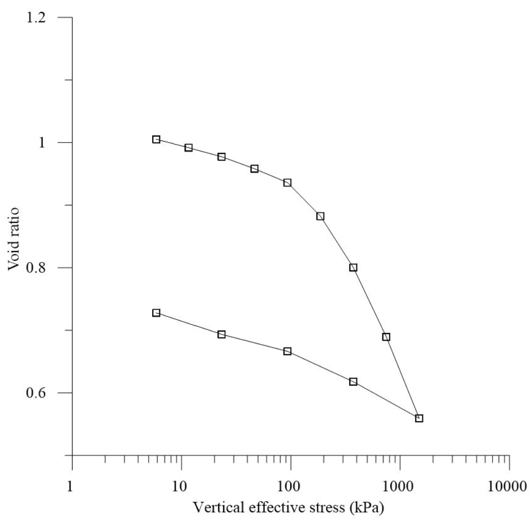

Figure 3. Isotropic consolidation test.

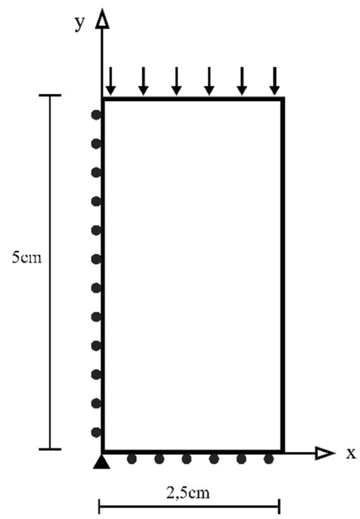

Figure 4. Numerical simulation section representation.

Table 2. Consolidation test data.

Type		Bauxite tailing
		Variegated clay
γ_n (kN/m^3)		17.3
W_i (%)		36.11
W_f (%)		31.65
e_0		1.02
C_c		0.36
C_r		0.06
C_e		0.08
Λ		0.83
σ'_{vm} (kPa)		195
$e_{\sigma'vm}$		0.87
K_{20} (cm/s)	50kPa	2.67e-7
	100kPa	9.23e-8
	200kPa	3.63e-8
	400kPa	1.76e-8

Table 3. General parameters.

Confining stress - σ'_3 (kPa)	Density - ρ (kg/m^3)	Permeability – k (m/s)	Specific weight of wetting liquid - γ_w (N/m^3)	Voids ratio – e_0
75				1.05
150	1.36e+3	1e-9	9.81e+3	1.17
300				1.07

Table 4. MCM parameters.

Elasticity		Plasticity		
Young modulus - E (kPa)	Poisson ratio - υ	Friction angle - ϕ' (°)	Dilation angle - Ψ (°)	Cohesion intercept - c' (kPa)
0.81e+3				
1.00e+3	0.3	25.5	0	24.7
1.02e+3				

The parameters inserted in the software were divided in general (i.e. used in all failure criteria) and specific, which were subdivided in elastic and plastic for each failure criterion. The general parameters were estimated from the experimental triaxial and consolidation tests shown in Section 2 and are presented in Table 3. The density parameter was obtained by the final dry densities average (Figure 1), and permeability is a typical value for bauxite tailings (Vick, 1990). Table 4, Table 5, and Table 6 present the specific parameters for the MCM, DPM, and MCCM respectively.

For MCM parameters (Table 4), the Young Modulus (E), the peak friction angle (ϕ'), and cohesion intercept (c') were all obtained through triaxial tests experimental results. Since studied triaxial tests were CIU no volumetric strain data was available for the calculation of the dilation angle (Ψ). Thus, a value of zero was utilized for this parameter. The Poisson ratio (υ), on the other hand, was retrieved from studies on bauxite tailings (Rout et al., 2013; Wu, 2014; Feng & Yang, 2018).

On the DPM parameters (Table 5), the Young Modulus (E) and the Poisson ratio (υ) were determined in the same way as the MCM parameters. The "β" and "d" model parameters were retrieved from the peak friction angle (ϕ') and cohesion intercept (c') of the experimental triaxial tests. The cap eccentricity (R), transition surface rad, and flow stress (K) are all theoretical parameters of the DPM.

The Poisson ratio (υ) of the MCCM was determined in accordance with the procedure applied to MCM and DPM. The Log Bulk modulus (κ) and the Bulk modulus (λ) were estimated through the experimental consolidation test. The stress ratio (M) and yield surface size ($p_{0'}/2$) were retrieved from the experimental triaxial tests. Lastly, the wet yield surf. size and flow stress rate are all theoretical parameters of the MCCM.

After the MCM, DPM, and MCCM criteria were numerically simulated, stress-strain curves were plotted and analyzed. Then, strength parameters for each model were determined. The next section explores results for all studied models.

Table 5. DPM parameters.

Elasticity		Plasticity				
Young modulus (kPa) - E	Poisson ratio - υ	β (°)	d (N/m^2)	Cap eccentricity - R	Transition surface rad	Flow stress - K
0.81e+3			90000			
1.00e+3	0.3	26.79	123000	0.35	0.03	1
1.02e+3			156174			

Table 6. MCCM parameters.

Elasticity		Plasticity				
Llog Bulk modulus - κ	Poisson ratio - υ	Log plas. Bulk modulus - λ	Stress ratio- M	Yield surf. Size (critical state) - $p_{0'}/2$ (N/m^2)	Wet yield surf. size	Flow stress rate
0.026	0.3	0.155	1.51	1.173e+5	1	1
				1.855e+5		
				2.356e+5		

4. Results and discussion

To allow verification and comparison, numerical results followed triaxial tests results representation, that is, stress-strain curves and pore-pressure variation as well as stress paths with strength parameters were drawn. Figures 5 to 7 express the stress-strain behavior and pore-pressure variation of studied failure criteria and experimental data, for each of the confining stresses, 75kPa, 150 kPa, and 300kPa. Stress paths for all models are shown in Figures 8 to 10 and strength parameters (i.e. friction angle and cohesion intercept) are presented in Table 7. It is important to note that both total and effective stress paths can be estimated through the numerical simulation, however, since experimental results were undrained tests only effective stress paths are shown in this research. Finally, results were analyzed considering (i) peak parameters – MCM and DPM; and (ii) critical state parameters – MCCM.

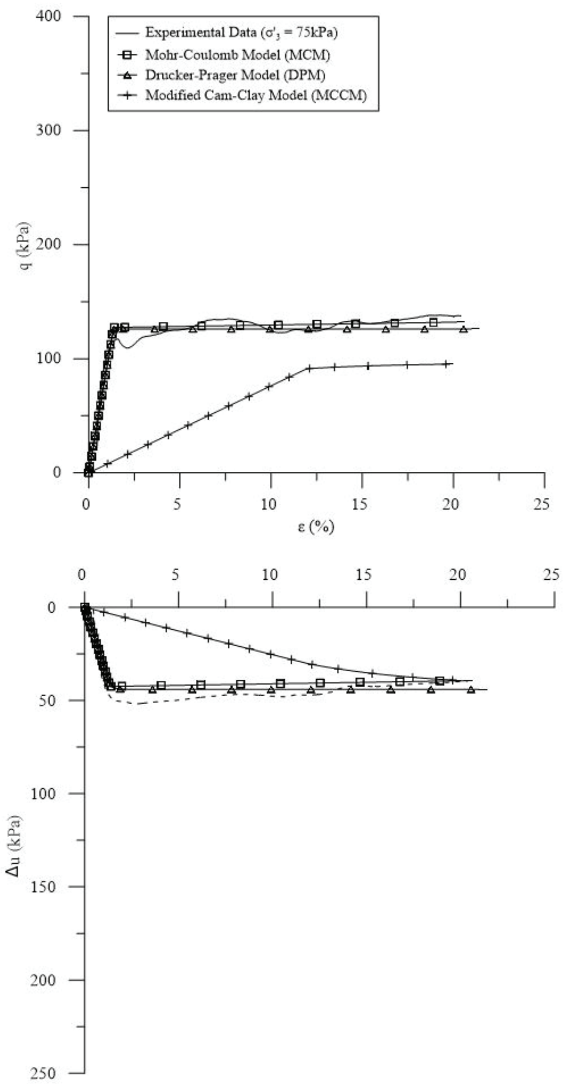

Figure 5. Simulation for 75kPa.

4.1. Peak parameters results

4.1.1. Stress-strain behavior and pore-pressure variation

It was possible to notice that in the confining stress of 75kPa the MCM accurately represented the stress-strain behavior of the bauxite tailing samples. However, on the confining stresses of 150kPa and 300kPa, the model exceeded the stress-strain of experimental results. For pore-pressure variation, MCM accurately represented the behavior on the 75kPa confining stress, and underestimated experimental results for 150kPa and 300kPa. This behavior is attributed to an elevated stress-state in conjunction with material's complexity, since this failure criterion was not created to represent materials that translate between sand and clay, such as bauxite tailings. Meanwhile, DPM accurately approached the behavior of bauxite tailings for all studied confining stresses. The model simulated stress-strain and pore-pressure variation reasonably well, presenting a small difference between numerical data and experimental results. According to Vermeer (1998), DPM presents approximate results for stiff clays with low friction angles, but not for sand, rock, or concrete.

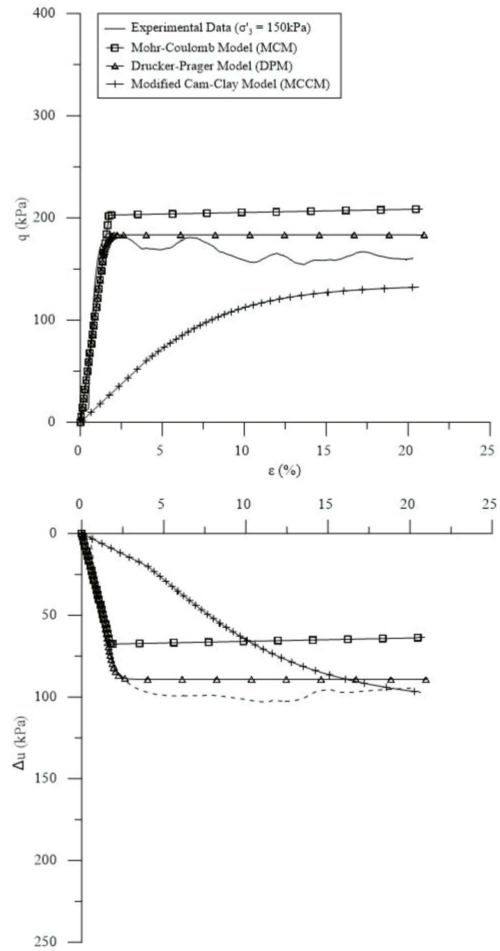

Figure 6. Simulation for 150kPa.

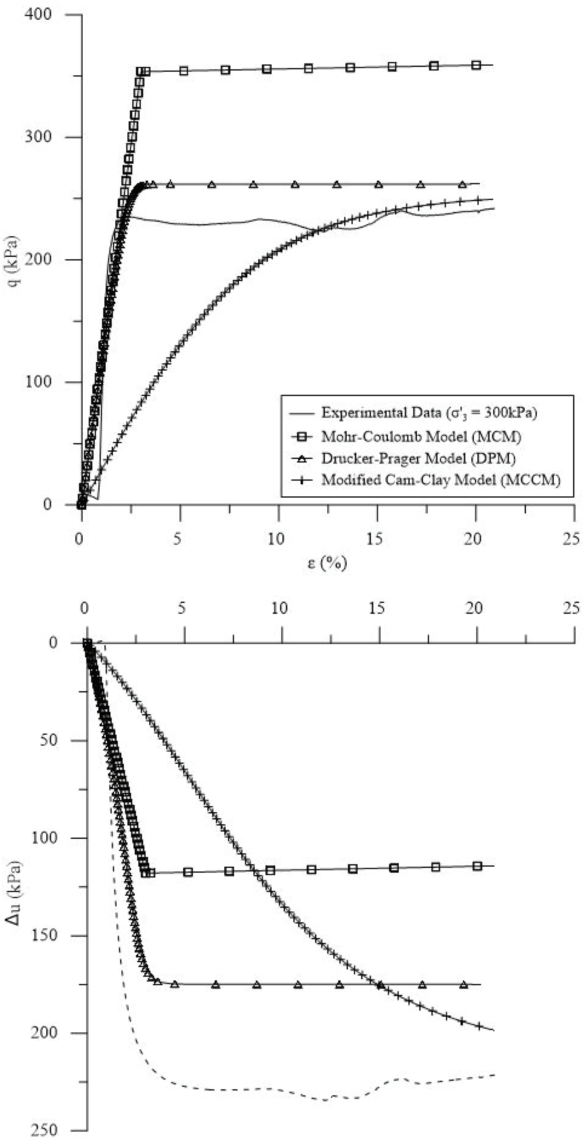

Figure 7. Simulation for 300kPa.

4.1.2. Stress paths and strength parameters

The DPM best represented stress paths and the failure envelope of bauxite tailings, presenting accurate strength parameters for all confining stresses. These results were expected, since the model was well adjusted in all numerical analyses. Although worse than DPM results, the MCM criteria presented a good estimation of the stress paths. Since strength parameters are part of the input data on the MCM, the peak friction angle and the cohesion intercept were equal to the experimental data.

4.2. Critical state parameters results

4.2.1. Stress-strain behavior and pore-pressure variation

For applied MCCM criteria, it was not possible to accurately simulate the pre-peak and peak stress-strain behavior, since the model is based on the Critical State Theory. When critical state is reached, approximately at ε=10%, the model represented fairly the material stress-strain behavior at a 300kPa confining stress. In turn, the criterion could not fully represent the stress-strain and pore-pressure variation for 75kPa and 150kPa stresses, since for these situations samples were on the overconsolidated state. In soils mechanics, the overconsolidation state or overconsolidation ratio (OCR) is the relation between the preconsolidation stress and the current soil effective stress. If OCR=1 the soil is normally

Table 7. FEM estimated strength parameters.

	Friction angle (°)	Cohesion intercept (kPa)
Experimental results (peak condition)	25.5	24.7
MCM	25.5	24.7
DPM	25.1	24.9
Experimental results (critical state condition)	37.3	0
MCCM	33.5	0

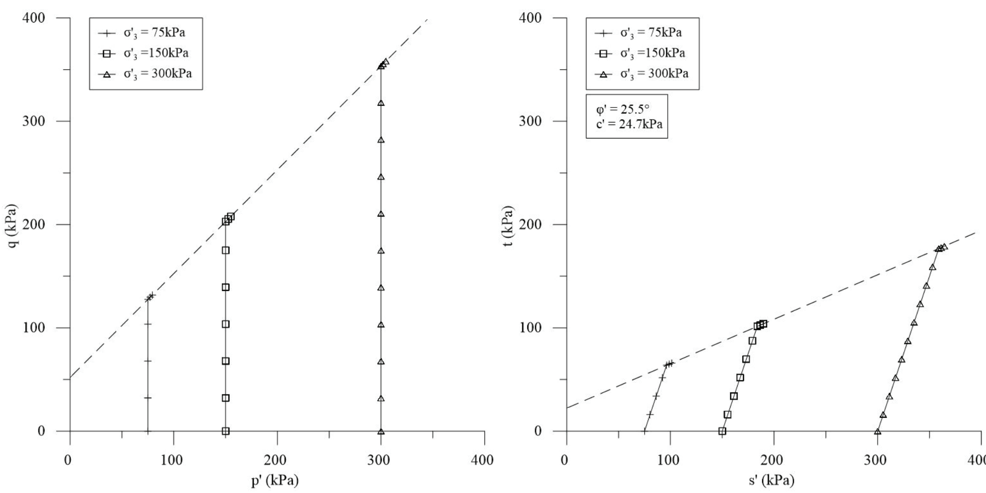

Figure 8. Stress paths MCM.

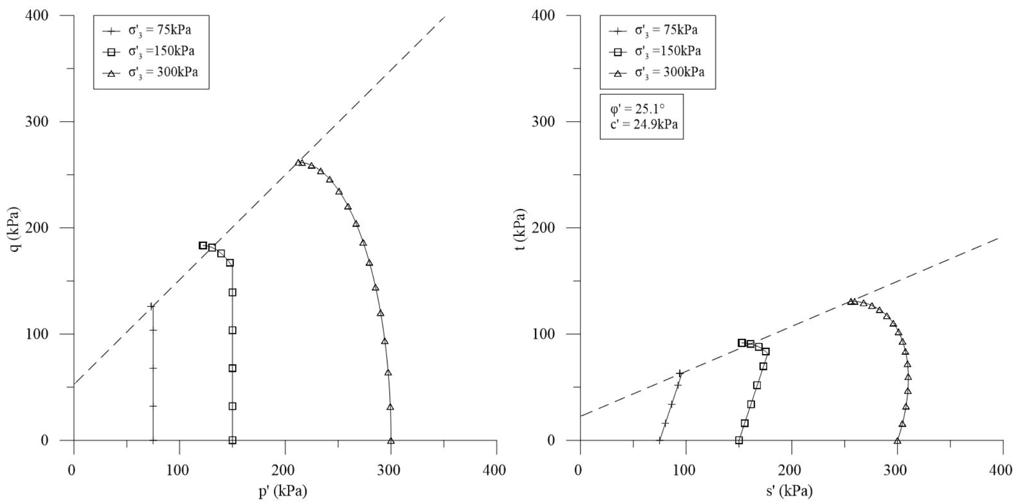

Figure 9. Stress paths DPM.

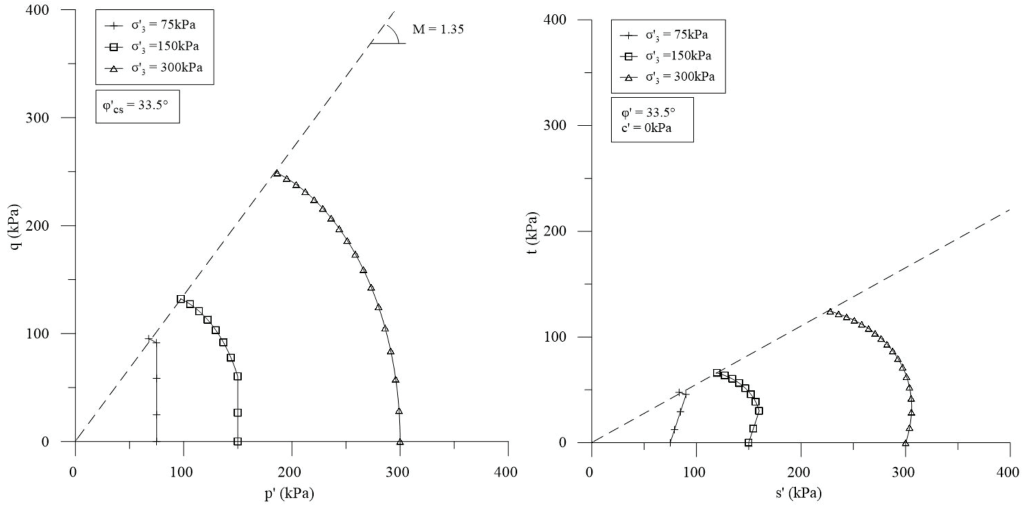

Figure 10. Stress paths MCCM.

consolidated (NC), if OCR>1 the soil is overconsolidated (OC) (Lambe & Whitman, 1979). The MCCM can simulate the mechanical behavior of normally consolidated materials satisfactorily, while it fails to predict the mechanical behavior of heavily overconsolidated soils (Fang & Daniels, 2006). One of the reasons lays on the fact that MCCM is unable to converge satisfactorily with materials that present negative variations in pore-pressure as well as softening behavior. Therefore, the model only showed good results for stresses of 300kPa (OCR=1). Likewise, the use of MCCM for simulating the mechanical behavior of overconsolidated soils can result in misleading stress-strain behavior.

4.2.2. Stress paths

In the critical state condition, the MCCM underestimated the stress paths due to samples overconsolidation. Thus, the use of this model to simulate the mechanical behavior of overconsolidated soils leads to lower strength parameters when compared to the actual strength of the materials.

5. Concluding remarks

This research presents bauxite mine tailings undrained shear strength and its mechanical behavior; then it makes a comparison between experimental and numerical triaxial tests results. The results showed that numerical simulation is a valid alternative for estimating strength parameters, as well as the mechanical behavior of bauxite tailings. The Mohr-Coulomb Model (MCM), Drucker-Prager Model (DPM), and Modified Cam-Clay Model (MCCM) were applied in the numerical analysis. Based on these experimental and theoretical results, several conclusions can be drawn and are summarized as follows:

- DPM presented the best results among all analyzed models (i.e. peak and critical parameters models), in terms of stress-strain behavior, pore pressure variation and peak strength parameters for the triaxial testing of the bauxite tailings;
- MCM served as a proper model to predict the bauxite tailings peak strength parameters. However, this

model overstated the stress-strain behavior and understated the pore pressure variation;

- MCCM bestowed satisfactory results, on the stress-strain behavior, exclusively for the normally consolidated sample (confining stress of 300kPa). This criterion failed to predict the mechanical behavior of the overconsolidated samples (confining stresses of 75kPa and 150kPa), resulting in lower strength parameters;
- Both total and effective stress paths can be estimated through numerical simulation using peak or critical state parameters, even though the experimental test was undrained;
- Results showed that numerical analysis through ABAQUS software is a valid low-cost alternative for estimating the strength parameters and the mechanical behavior of bauxite tailings. However, numerical simulation must be utilized cautiously due to the complexity and particularities of the analyzed failure criteria.

Declaration of interest

The authors certify that they have NO affiliations with or involvement in any organization or entity with any financial interest (such as honoraria; educational grants; participation in speakers' bureaus; membership, employment, consultancies, stock ownership, or other equity interest; and expert testimony or patent-licensing arrangements), or non-financial interest (such as personal or professional relationships, affiliations, knowledge or beliefs) in the subject matter or materials discussed in this manuscript.

Author's contributions

All authors contributed equally for the development of this research.

References

ASTM D2435/D2435M-11. (2020). *One-dimensional consolidation properties of soils using incremental loading*. ASTM International, West Conshohocken, PA. http://dx.doi.org/10.1520/D2435_D2435M-11R20.

Braga, A.L.C., & Nogueira, C de L. (2019). Coupled numerical simulation of a tailings deposit by fem. *Rev Esc Minas*, 72, 153-160. http://dx.doi.org/10.1590/0370-44672016720047.

Coulibaly, Y., Belem, T., & Cheng, L.Z. (2017). Numerical analysis and geophysical monitoring for stability assessment of the Northwest tailings dam at Westwood Mine. *International Journal of Mining Science and Technology*, 27, 701-710. http://dx.doi.org/10.1016/j.ijmst.2017.05.012.

Dai, Z.H., & Qin, Z.Z. (2013). Numerical and theoretical verification of modified cam-clay model and discussion on its problems. *Journal of Central South University*, 20, 3305-3313. http://dx.doi.org/10.1007/s11771-013-1854-7.

Fang, H.-Y., & Daniels, J.L. (2006). *Introductory geotechnical engineering: an environmental perspective*. CRC Press

Feng, Y., & Yang, C. (2018). Analysis on physical and mechanical properties of red mud materials and stockpile stability after dilatation. *Advances in Materials Science and Engineering*, 2018, http://dx.doi.org/10.1155/2018/8784232.

Furlan, J.P.R., dos Santos, L.D.R., Moretto, J.A.S., Ramos, M.S., Gallo, I.F.L., Alves, G.A.D., Paulelli, A.C., Rocha, C.C.S., Cesila, C.A., Gallimberti, M., Devóz, P.P., Barbosa Júnior, F., & Stehling, E.G. (2020). Occurrence and abundance of clinically relevant antimicrobial resistance genes in environmental samples after the Brumadinho dam disaster, Brazil. *The Science of the Total Environment*, 726, 138100. http://dx.doi.org/10.1016/j.scitotenv.2020.138100.

Gama, F.F., Paradella, W.R., Mura, J.C., & de Oliveira, C.G. (2019). Advanced DINSAR analysis on dam stability monitoring: a case study in the Germano mining complex (Mariana, Brazil) with SBAS and PSI techniques. *Remote Sens Appl Soc Environ*, 16, http://dx.doi.org/10.1016/j.rsase.2019.100267.

Grzyb, A., Dhaybi, M., & Pellet, F. (2012). Numerical modeling of a small scale shallow foundation reinforced by Soil-Mixing. In *Proceedings of the 2nd International Conference on Geotechnique, Construction Materials and Environment*. Kuala Lumpur – Malaysia. [CDRom].

Jung, J.K., O'Rourke, T.D., & Olson, N.A. (2013). Lateral soil-pipe interaction in dry and partially saturated sand. *Journal of Geotechnical and Geoenvironmental Engineering*, 139, 2028-2036. http://dx.doi.org/10.1061/(ASCE)GT.1943-5606.0000960.

Lambe, T.W., & Whitman, R.V. (1979). *Soil mechanics, SI version*. John Wiley & Sons, Inc.

Liu, K., & Chen, S.L. (2017). Finite element implementation of strain-hardening Drucker–Prager plasticity model with application to tunnel excavation. *Underground Space*, 2(3), 168-174. http://dx.doi.org/10.1016/j.undsp.2017.08.003.

Liu, R., Liu, J., Zhang, Z., Borthwick, A., & Zhang, K. (2015). Accidental water pollution risk analysis of mine tailings ponds in Guanting reservoir Watershed, Zhangjiakou city, China. *International Journal of Environmental Research and Public Health*, 12, 15269-15284. http://dx.doi.org/10.3390/ijerph121214983.

Mahdi, A., Shakibaeinia, A., & Dibike, Y.B. (2020). Numerical modelling of oil-sands tailings dam breach runout and overland flow. *The Science of the Total Environment*, 703, 134568. http://dx.doi.org/10.1016/j.scitotenv.2019.134568.

Owen, J.R., Kemp, D., Lèbre, É., Svobodova, K., & Pérez-Murillo, G. (2020). Catastrophic tailings dam failures and disaster risk disclosure. *International Journal of Disaster Risk Reduction*, 42, http://dx.doi.org/10.1016/j.ijdrr.2019.101361.

Robert, D.J. (2017). A modified mohr-coulomb model to simulate the behavior of pipelines in unsaturated soils.

Computers and Geotechnics, 91, 146-160. http://dx.doi.org/10.1016/j.compgeo.2017.07.004.
Rout, S.K., Sahoo, T., & Das, S.K. (2013). Design of tailing dam using red mud. *Central European Journal of Engineering*, 3, 316-328. http://dx.doi.org/10.2478/s13531-012-0056-7.
Schnaid, F., Nierwinski, H.P., Bedin, J., & Odebrecht, E. (2014). On the caracterization and classification of bauxite tailings. *Soil Rocks*, 37(2), 277-284.
Su, K., & Li, Y. (2009). Discussion of extended drucker-prager yield criterion in slope stability analysis. *Asia-Pacific Power Energy Eng Conf APPEEC*, 2, 2-5. http://dx.doi.org/10.1109/APPEEC.2009.4918285.
Vermeer, P.A. (1998). Non-associated plasticity for soils, concrete and rock. *Physics of Dry Granular Media*, 163-196.
Vick, S.G. (1990). *Planning, design, and analysis of tailings dams*. BiTech.
Wu, C.S. (2014). The drainage consolidation modeling of sand drain in red mud tailing and analysis on the change law of the pore water pressure. *Mathematical Problems in Engineering*, 2014, 876872. http://dx.doi.org/10.1155/2014/876872.

List of symbols

ASTM – American Society for Testing and Materials
CIU – Isotropically consolidated undrained
DPM – Drucker-Prager Model
FEM – Finite Element Method
MCCM – Cam-Clay Modified Model
MCM – Mohr-Coulomb Model
OCR – Over consolidation ratio
c' – cohesion intercept
Cc – coefficient of compression
Ce – coefficient of expansion
Cr – coefficient of recompression
d – MCM parameter for the cohesion intercept
e – voids ratio
E – Young modulus
e0 – initial voids ratio
$e_{\sigma'vm}$ – voids ratio at the preconsolidation stress
K – flow stress
k – permeability
M – stress ratio
p' – average effective stress
p0'/2 – Yield surface size
q – deviator stress
R – cap eccentricity
s' – (σ'1 + σ'3)/2
t – (σ'1 - σ'3)/2
wf – final water content
wi – initial water content
β – MCM parameter for the friction angle
γw – specific weight of wetting liquid
κ – Log Bulk Modulus
λ – Bulk Modulus
ϕ' – effective friction angle
Ψ – Dilation angle
Δu – porepressure variation
γn – natural unit weight
ρ – density
σ'vm – preconsolidation stress
σ'3 – confining stress
υ – Poisson ratio

Soils and Rocks
An International Journal of Geotechnical and Geoenvironmental Engineering
www.soilsandrocks.com
ISSN 1980-9743
ISSN-e 2675-5475

New modeling approach for tunnels under complex ground and loading conditions

Osvaldo Paiva Magalhães Vitali[1#], Tarcisio Barreto Celestino[2], Antonio Bobet[1]

Technical Note

Keywords
Tunnel misalignment
Stress anisotropy
Rock anisotropy
3D FEM
Numerical modeling
3D face effects

Abstract

The behavior of tunnels in anisotropic rock masses is highly complex and heavily dependent on the orientation of the tunnel axis with respect to the geostatic principal stress directions and to the rock structural planes. 2D solutions cannot capture the 3D face effects of such complex scenario; thus, 3D numerical modeling is required. The modeling of such tunnels using conventional boundary conditions may be cumbersome since the tunnel may not be parallel to the boundaries. The issue is further complicated if the principal far-field stresses are not parallel to the principal axes of material anisotropy. In this case, the use of conventional boundary conditions may be problematic. In this paper, a new approach is presented to impose the boundary conditions and the far-field stresses on 3D numerical models of tunnels under complex ground and loading conditions. With the proposed approach, it is possible to easily simulate any orientation of the tunnel with respect to the principal directions of stress and material anisotropy. The numerical results obtained with the proposed approach were validated with an analytical solution and with numerical results using traditional boundary conditions.

1. Introduction

Rock masses may present pronounced stress and material anisotropy. Stress measurements in rock masses show that stress anisotropy may be highly pronounced, as shown by McGarr & Gay (1978). Also, the data compiled by Brown & Hoek (1978) show that large horizontal stresses are common at shallow depths. According to Brady & Brown (2006), the major horizontal stress (σ_H) and the minor horizontal stress (σ_h) rarely have the same magnitude. Large and highly anisotropic horizontal stresses were reported by Haimson et al. (2003) and Park et al. (2014) in gneissic and granitic rock masses in South Korea. Those stresses were associated with the intense tectonic activity in the area. Rock masses may present pronounced fabric structure; thus, anisotropic mechanical behavior is expected. The data compiled by Worotnicki (1993) in metamorphic rocks showed that the ratio between the Young modulus perpendicular to the rock structure and parallel to the rock structure was larger than 2 for more than 50% of the rocks tested (e.g. schists, slates, quartzites, mudstones and phyllites), and the largest stiffness ratio was 6. This is relevant because anisotropic rock properties strongly affect the behavior of tunnels and should be considered in tunnel design (Fortsakis et al., 2012; Wittke, 1990; Armand et al., 2013; Bobet, 2011, 2016; Bobet & Yu, 2016; Vitali et al., 2020a, b, c; Vitali, 2020; Goricki et al., 2005; Schubert & Mendez, 2017, Klopčič & Logar, 2014).

In anisotropic rock masses, the tunnel alignment with one of the principal directions of stress and material anisotropy is unlikely. In this case, asymmetric displacements are induced near the face and anti-symmetric axial displacements occur far-behind the face of the tunnel (Vitali et al. 2019b, 2020a, c; Vitali, 2020). The asymmetric displacements near the face affect the performance of the support and rock surrounding the excavation and may produce asymmetric plastic deformations around the tunnel (Vitali et al., 2019b, c, 2020a). Further, asymmetric displacements and asymmetric failure at the tunnel walls are commonly observed (Schubert & Budil, 1995; Goricki et al., 2005; Schubert et al., 2005; Schubert & Moritz, 2011; Klopčič & Logar, 2014; Lenz et al., 2017).

2D analyses cannot capture the 3D face effects that occur in tunnels during construction and, in particular, when the tunnel axis is not one of the principal directions of material anisotropy or a principal far-field stress; thus, 3D analyses are required. Because of recent advances in hardware and software, 3D FEM modeling is nowadays possible in the practice of engineering. However, the numerical modeling of tunnels not aligned with one of the principal directions of material anisotropy may be cumbersome and time consuming.

[#]Corresponding author. E-mail address: opmvitali@gmail.com
[1]Purdue University, Lyles School of Civil Engineering, West Lafayette, IN, USA.
[2]Universidade de São Paulo, Escola de Engenharia de São Carlos, São Carlos, SP, Brasil.

Submitted on June 8, 2020; Final Acceptance on September 30, 2020; Discussion open until May 31, 2021.

DOI: https://doi.org/10.28927/SR.2021.052120

Traditionally, for deep tunnels, the geostatic stress field is generated by applying a uniform pressure perpendicular to the boundaries of the model. With this approach, different 3D FEM meshes need to be created for each attempted orientation of the tunnel with respect to the principal stress directions (Vitali et al., 2018b). Also, if the principal stress directions are not aligned with the principal material directions, displacements parallel to the boundaries are induced, which may be problematic.

In this paper, a new approach for general numerical modeling of tunnels under complex anisotropic conditions is presented. The basic idea is to impose body forces to all the FEM elements to generate the geostatic stress field and to constrain the displacements at the boundaries. Because no displacements are expected far from the tunnel, fixing the nodes at the boundaries is acceptable, with the assumption that the boundaries are sufficiently far from the tunnel. The paper shows that the numerical results obtained with the 3D FEM model imposing the proposed boundary conditions match the analytical results (Vitali et al., 2020b) and the results of 3D FEM models with traditional boundary conditions (Vitali et al., 2020a).

2. 3D FEM mesh

Figure 1 shows the 3D FEM mesh used with the proposed boundary conditions. The tunnel is assumed deep. The geostatic stress field is generated by imposing appropriate body forces in the 3D FEM elements that discretize the rock mass; thus, any initial stress state can be easily created. Midas GTS NX, which is the FEM code used in this paper, has a feature that allows the user to impose body forces into 3D finite elements by providing the components of the Cauchy stress tensor (σ_{xx}, σ_{yy}, σ_{zz}, τ_{yz}, τ_{xz}, τ_{xy}). A similar feature exists in other FEM codes. The nodes at the boundaries are fixed, as illustrated in Figures 1c and 1d. Consequently, external forces are generated at these nodes (i.e. the reaction forces) that ensure equilibrium of the imposed geostatic stress field. Also, this boundary condition is reasonable since no displacements are expected far from the tunnel. Obviously, to achieve accurate numerical results, the model should be large enough, and the mesh properly refined.

The tunnel investigated numerically was circular with 5m radius (r_0). The 3D FEM mesh had a cylindrical shape with $100r_0$ diameter and $120r_0$ length. The adopted size of the FEM mesh ensured accurate results even for highly

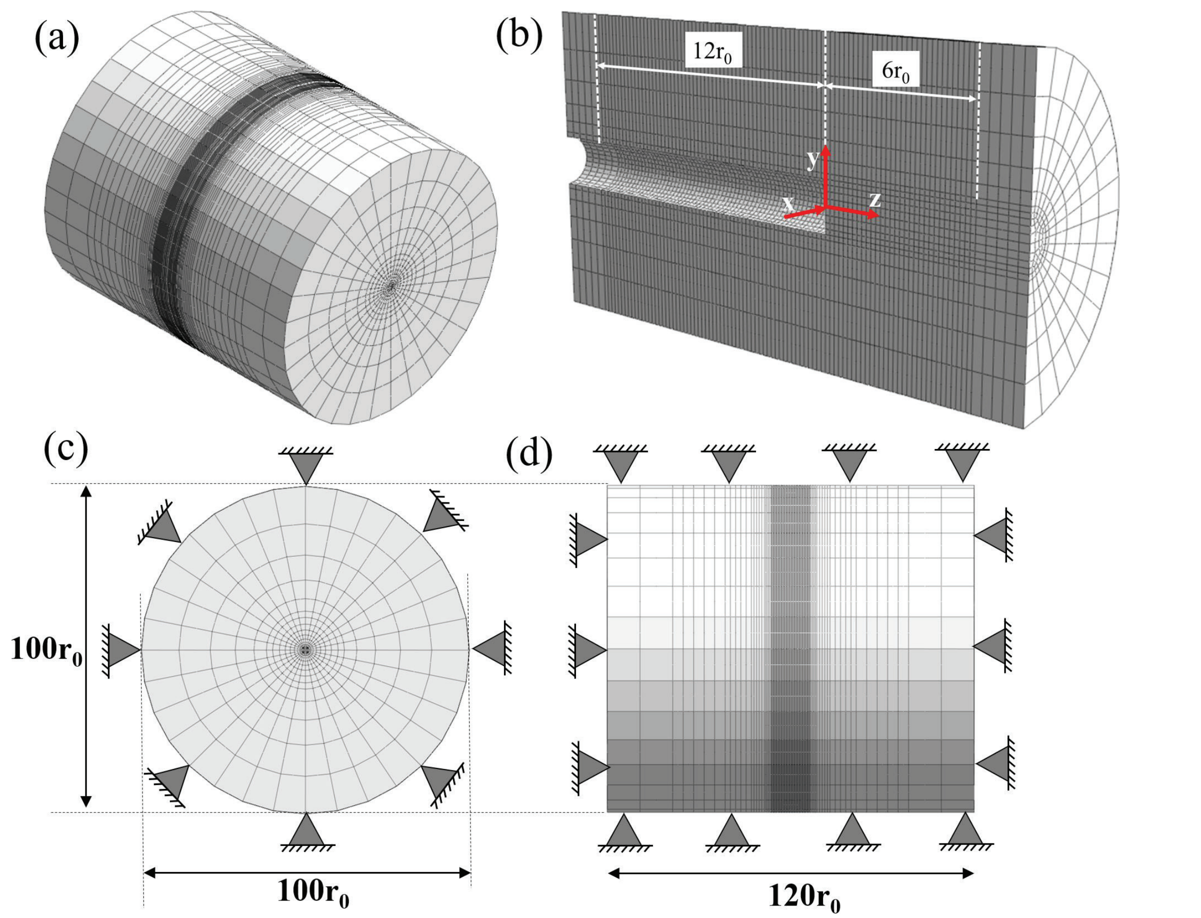

Figure 1. 3D FEM mesh with proposed boundary conditions. (a) mesh; (b) refined mesh at the core, where the results are extracted; (c) front view of the mesh with boundary conditions; (d) top view of the mesh with boundary conditions.

nonlinear material (Vitali et al., 2018a). The mesh was refined near the tunnel face and was gradually coarsened towards the boundaries. The mesh refinement adopted follows the recommendations by Vitali et al. (2018a). 2nd order hexahedron elements were adopted. The FEM mesh shown in Figure 1 has around 300,000 nodes and 76,000 elements. The results from the simulations were extracted from a refined mesh at the core of the model (Figure 1b). The length of the hexahedron elements at the core was $0.2r_0$ in the axial direction, as recommended by Vitali et al. (2018a). To ensure the accuracy of the numerical results, the refined mesh was extended to a distance of $6r_0$ ahead the face and $12r_0$ behind the face, as illustrated in Figure 1b. The results far-behind the face presented in this paper were extracted at a distance of $8r_0$ behind the face, which is far enough from the face such that the 3D face effects are negligible and the results can be compared with the analytical solution. The first phase of the analyses imposed the body forces in the 3D finite elements that discretize the rock mass, to generate the far-field stresses, while the displacements at the boundaries of the model were constrained. After this stage, the elements inside the tunnel were deactivated to simulate the tunnel excavation. Although the results presented in this paper were obtained with the FEM code Midas GTS NX, this modeling approach is general; thus, any FEM code that allows the user to impose body forces in the elements may be used. Note that the presented new approach is valid for elastoplastic rock masses, tunnels with support systems and for any geometry and construction sequence.

3. Verification of the proposed boundary conditions

3.1 Tunnel in anisotropic rock and complex geostatic stress field

To verify the accuracy of the 3D FEM mesh with the proposed boundary conditions, as shown in Figure 1, the displacements and stresses at the tunnel perimeter were compared with those obtained with the analytical solution proposed by Vitali et al. (2020b). The transversely anisotropic elastic model was selected to represent the rock mass. The anisotropic rock properties are: Young modulus parallel to the rock structure, 2.67GPa, and perpendicular to the rock structure, 1.33GPa; shear modulus parallel to the rock structure, 1GPa, and perpendicular to the rock structure, 0.76GPa; Poisson's ratio parallel to the rock structure, 0.33, and perpendicular to the rock structure, 0.25. The dip angle was 64° and the strike direction, 37°. The tunnel was assumed aligned with the North (i.e. it is assumed that the z-axis is parallel to the North); thus, the axis of the tunnel is not parallel to any of the principal directions of material anisotropy. The strike direction is measured from the positive z-axis towards the positive x-axis (coordinate system shown in Figure 1). A highly complex geostatic stress field was selected. The far-field stresses with respect to the tunnel coordinate system (Figure 1b) were $\sigma_{xx,ff}$=7.5MPa; $\sigma_{yy,ff}$=5MPa; $\sigma_{zz,ff}$=7.5MPa; $\tau_{yz,ff}$=2.5MPa; $\tau_{xz,ff}$=2.5MPa and; $\tau_{xy,ff}$=-1.25MPa, where positive normal stresses denote compression. Using the proposed approach, such complex geostatic stress field was easily generated by imposing the body forces into the 3D elements. The nodes at the boundaries of the model were fixed; that is, the displacements at the boundaries were zero and the reaction forces balanced the (complex) geostatic stress field. Note that, in this scenario, the geostatic principal stress directions and the principal directions of material anisotropy are not aligned; thus, the use of traditional boundary conditions (Vitali et al., 2018a, b, 2020a) could be problematic. Also, if traditional boundary conditions were used, the tunnel would not be aligned with the boundaries. Each tunnel orientation attempted would thus require a different mesh (Vitali et al., 2018b), which is a time-consuming task.

Figure 2 presents the normalized stresses and displacements at the tunnel perimeter obtained with the 3D FEM model

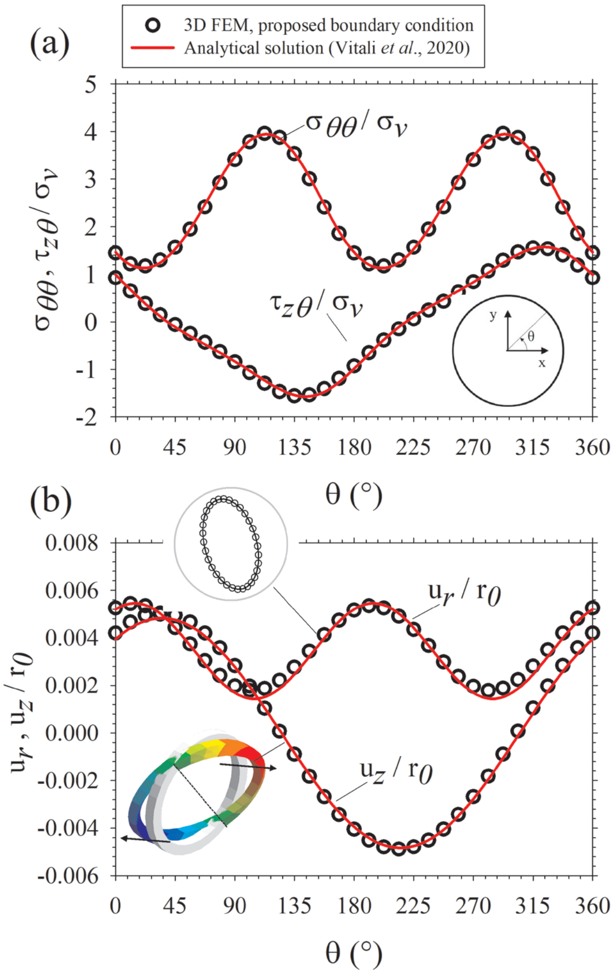

Figure 2. Comparison between numerical and analytical results: (a) tangential stress ($\sigma_{\theta\theta}$) and tangential axial shear stress ($\tau_{\theta z}$), normalized with respect to the vertical stress (σ_v), at the tunnel perimeter; and (b) radial (u_r) and axial (u_z) displacements, normalized with the tunnel radius (r_0), at the tunnel perimeter.

with the proposed boundary conditions (Figure 1) and with the analytical solution (Vitali et al., 2020b). Positive radial displacements are towards the inside of the tunnel. The axial displacements sign convention is consistent with the z-axis direction (i.e. negative axial displacements are towards the excavated tunnel and positive towards the rock mass ahead of the face of the tunnel). As one can see, analytical and numerical results match, which shows that the proposed boundary conditions work well. The stresses and the displacements at the tunnel perimeter are not symmetric with respect to the horizonal and vertical axes as a consequence of the stress and material anisotropy. Anti-symmetric axial displacements and anti-symmetric tangential axial shear stresses ($\tau_{\theta z}$) are induced around the tunnel perimeter. The tunnel cross-section is distorted in the axial direction about the axis of anti-symmetry at θ=126°, as illustrated in Figure 2b. Note that the tangential axial shear stresses are larger at the locations where the axial displacements are zero and are smaller where the axial displacements are maximum (i.e. maximum axial displacement refers to the magnitude regardless of the direction). Also, the tangential stresses are larger where the radial displacements are minimum and are smaller where the radial displacements are maximum. The deformed tunnel cross-sections are shown in Figure 2b, that illustrates the axial distortion of the tunnel cross sections and the ellipsoidal shape of the deformed cross section.

3.2 Tunnel in vertically-foliated rock mass

The cases investigated by Vitali et al. (2020a) of tunnels in vertically-foliated rock masses were selected for further verification of the proposed method to impose initial/geostatic stress conditions. The cases were assessed using a 3D FEM model and the proposed method and boundary conditions (Figure 1). The results were compared with those from the analytical solution presented by Vitali et al. (2020b) and with the 3D FEM model using traditional boundary conditions (Figure 3), from Vitali et al. (2020a). The same geostatic stress field selected by Vitali et al. (2020a) was adopted (i.e. major horizontal stress, σ_H, of 10MPa; minor horizontal stress, σ_h, of 5MPa and; vertical stress, σ_v, of 5MPa). The tunnel was at an angle of 45° with the major horizontal stress. Two orientations of the major horizontal stress with respect to the rock structure were considered: major horizontal stress, σ_H, perpendicular to the strike, and major horizontal stress, σ_H, parallel to the strike. In these cases, the principal directions of stress and material anisotropy are aligned, which is ideal for the use of traditional boundary conditions (Vitali et al., 2020a); note that, when those directions are not aligned, the use of traditional boundary conditions may be difficult.

The far-field stresses and the rock structure are shown in Figure 4. The rock properties selected were the same as the previous case. With the tunnel angle at 45°, the far-field stresses $\sigma_{xx,ff}$, $\sigma_{yy,ff}$, and $\sigma_{zz,ff}$, in the coordinate system attached to the tunnel, were: $\sigma_{xx,ff}$ = $\sigma_{yy,ff}$=5MPa, $\sigma_{zz,ff}$=7.5MPa, and $\tau_{xz,ff}$ = ±2.5MPa, with the sign of the far-field shear stress being the only difference between the cases, as one can see in Figure 4. The figure also shows that the tunnel orientation, with respect to the rock structure, was the same in both cases. The mesh shown in Figure 1 was used for all the cases. This is an advantage of the proposed technique: the same 3D FEM mesh can be used to analyze the tunnel excavation under any geostatic stress state in any full anisotropic rock mass, which is not the case when using traditional boundary conditions.

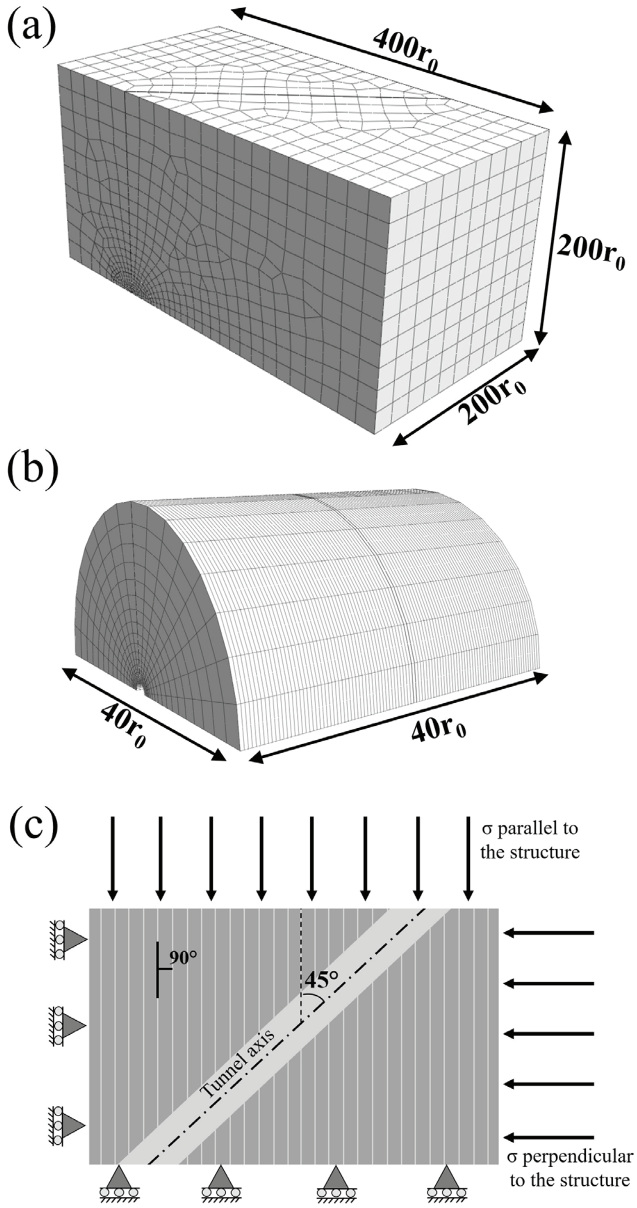

Figure 3. 3D FEM model with traditional boundary conditions. (a) mesh and dimensions; (b) mesh at the core, where the results are extracted; and (c) plan view with boundary conditions.

The FEM model with traditional boundary conditions is presented in Figure 3. This was the same 3D FEM model used by Vitali et al. (2020a). As one can see, the mesh was rather large, to prevent effects from the boundaries. All elements used were 2nd order hexahedron elements, and the

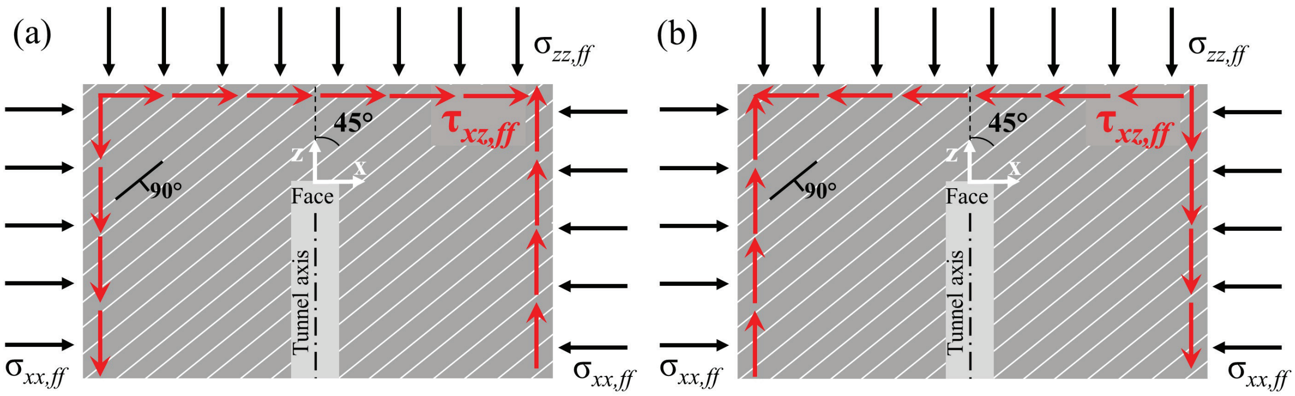

Figure 4. Plan view of the far-field stresses and rock structure with respect to the tunnel coordinate system. (a) major horizontal stress perpendicular to the rock structure; and (b) major horizontal stress parallel to the rock structure.

mesh refinement and the size of the model (Figure 3) were selected to ensure the accuracy of the results, following the recommendations provided by Vitali et al. (2018a). Figure 3b shows the refined mesh at the core of the model where the results were extracted. Figure 3c illustrates the plan view of the mesh with the boundary conditions. The rock structure was aligned with the sides of the discretization. Note that the tunnel was not aligned with the mesh, but at an angle Ψ=45°. The far-field stresses, as shown in Figure 3c, were applied to the boundaries of the discretization. At the faces of the mesh, opposite to where the stresses were applied, rollers were used. This was the first stage of the simulation, where far-field stresses were imposed, and all displacements were zeroed. That is, the geostatic stress conditions were imposed. In the second stage of the simulation, the elements of the tunnel were deactivated, without changing the boundary conditions imposed in the first stage.

The normalized stresses and displacements along the tunnel perimeter, far-behind the face, are presented in Figure 5. As one can see, the results obtained with different methods are the same (i.e. 3D FEM model with the proposed boundary conditions, Figure 1; analytical solution, Vitali et al. (2020b); and 3D FEM model with traditional boundary conditions, Figure 3). The consistency of the results with all three different methods indicates that the new approach is essentially correct. Anti-symmetric tangential axial shear stresses ($\tau_{\theta z}$) and anti-symmetric axial displacements (u_z) were induced far-behind the face, as illustrated by the axially deformed tunnel cross-sections shown in Figures 5a.2 and 5b.2 (i.e. the tunnel cross-section is distorted about the vertical axis). Note that the direction of the axial distortion is not the same for the two cases investigated. The axial and the radial displacements are larger for the case where the major horizontal stress is perpendicular to the strike (Figure 5a.1) than for the case where it is parallel (Figure 5b.2). As discussed by Vitali et al. (2020a, b, c) and Vitali (2020), when the major horizontal stress is perpendicular to the strike, the axial distortion produced by the material anisotropy and by the stress anisotropy have the same tendency; thus, axial and radial displacements are increased. The opposite occurs when the major horizontal stress is parallel to the strike direction. Note that, as shown by Vitali et al. (2018b, 2019a, b), if the rock mass is isotropic and elastic and the tunnel is unsupported, the far-field shear stress does not affect the radial and the tangential displacements far-behind the face because the in-plane displacements do not depend on the axial stresses. However, if the rock mass is anisotropic or the tunnel is not aligned with the principal axes of material anisotropy, the far-field axial shear stresses ($\tau_{xz,ff}$ and $\tau_{yz,ff}$) induce displacements on the plane of the tunnel cross section (Vitali et al., 2020b). The far-field axial shear stress did not affect the tangential stresses ($\sigma_{\theta\theta}$) at the tunnel perimeter, as one can see by comparing Figures 5a.1 and 5b.1. In contrast, the tangential axial shear stresses ($\tau_{\theta z}$) were affected by the far-field shear stress.

Figure 6 shows the normalized radial and axial displacements at the face of the tunnel for the two cases investigated. As one can see, the results with both 3D FEM models are the same (i.e. the 3D FEM model with the proposed boundary conditions, Figure 1, and the 3D FEM model with traditional boundary conditions, Figure 3). This is further evidence that the proposed method provides accurate results. As one can see in Figure 6, the displacements at the face are highly asymmetric. For the case where the major horizontal stress is perpendicular to the strike (Figure 6a), the tunnel cross section translates to the right (i.e. towards the positive x-axis) and, for the case where it is parallel (Figure 6b), to the left. The asymmetric displacements are more pronounced, and the axial displacements larger, when the major horizontal stress is perpendicular to the strike. Also, the location where the radial and axial displacements are maximum is the same in both cases analyzed, as well as the location where radial and axial displacements are minimum. For instance, for the case where the major horizontal stress is perpendicular to the strike (Figure 6a), the maximum axial and radial displacements occur at the

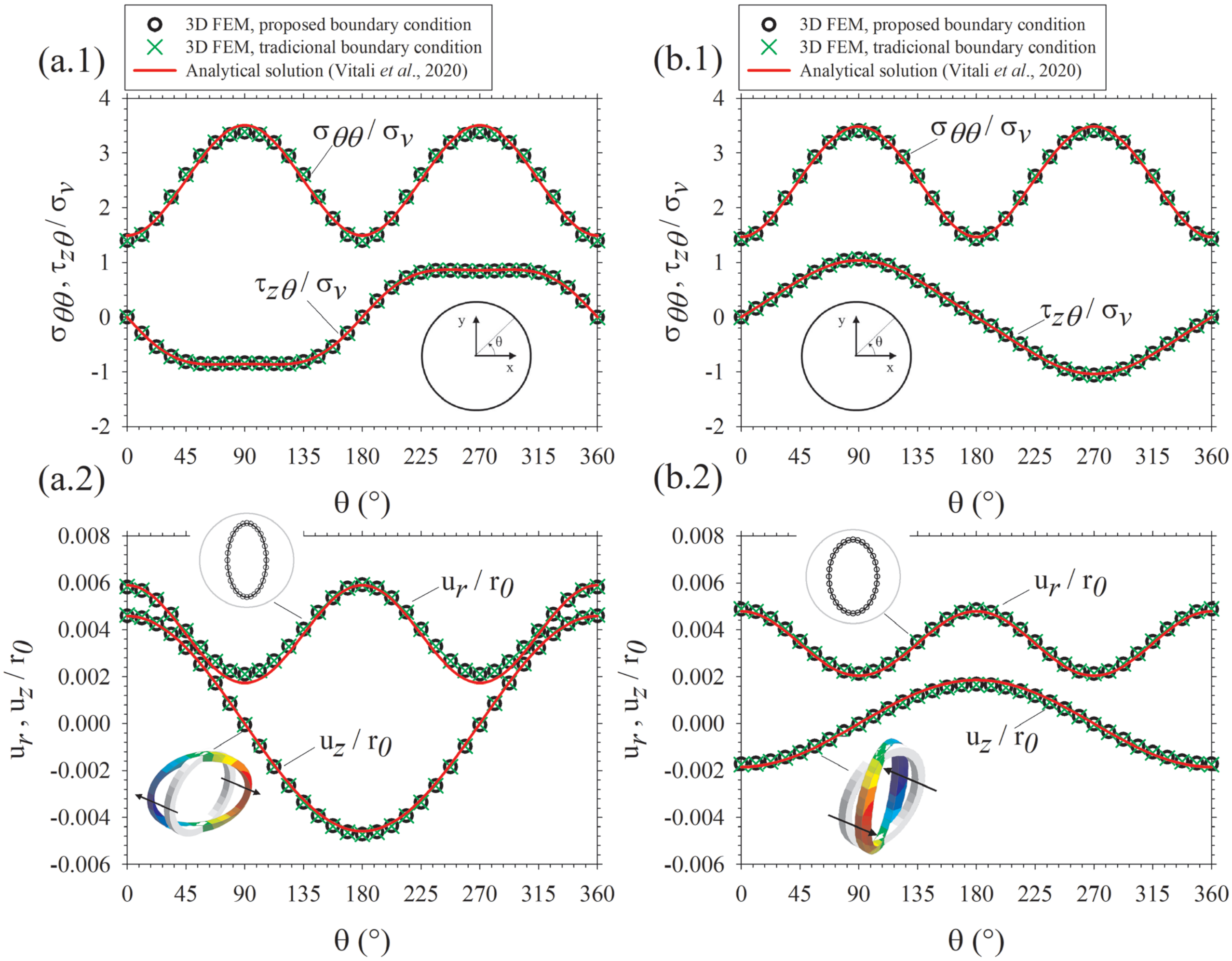

Figure 5. Displacements and stresses along the tunnel perimeter far-behind the face. (1) tangential stresses ($\sigma_{\theta\theta}$) and tangential axial shear stresses ($\tau_{\theta z}$) normalized with respect to the vertical stress (σ_v); and (2) radial (u_r) and axial (u_z) displacements normalized with the tunnel radius (r_0) along the tunnel perimeter. (a) major horizontal stress perpendicular to the rock structure; and (b) major horizontal stress parallel to the rock structure.

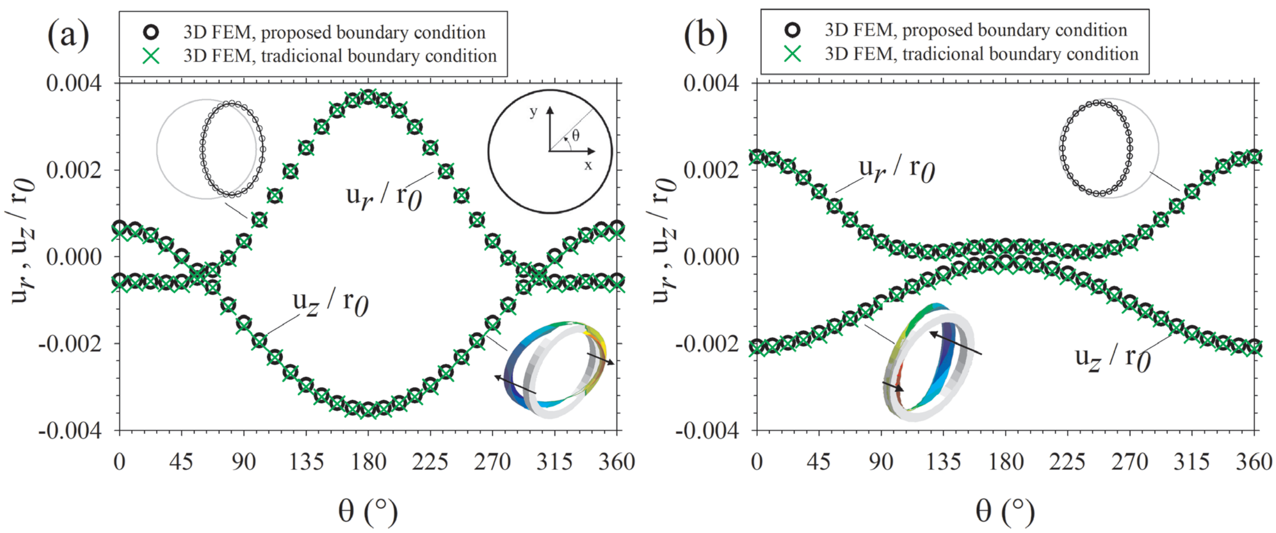

Figure 6. Normalized radial (u_r) and axial (u_z) displacements with respect to the tunnel radius at the face of the tunnel, for: (a) major horizontal stress perpendicular to the strike; and (b) major horizontal stress parallel to the strike.

right springline, and the minimum, at the left springline. The opposite is observed when the major horizontal is parallel to the strike (Figure 6b). Thus, as one can see in Figure 6, the tunnel cross section translates towards the location where the axial displacement is smaller. Note that negative axial displacements are towards the excavated tunnel and positive, towards the rock mass ahead of the face of the tunnel. The anti-symmetric axial displacements are partially constrained at the face, which may explain the asymmetric deformations near the face. A detailed discussion on the influence of the stress and rock anisotropy on tunnel behavior is provided by Vitali et al. (2020a).

4. Conclusions

A new approach for 3D numerical modeling of tunnels in complex conditions is proposed. The geostatic stress field is generated by imposing body forces to the elements, while the boundaries of the model are fixed. The proposed approach is validated by comparing its results with those of a 3D FEM model where conventional boundary conditions are used (Vitali et al., 2020a), and with results from an analytical solution (Vitali et al., 2020b). The results from all three different methods are the same; thus, when the mesh is properly refined and the model sufficiently large, the numerical results obtained should be correct. The approach is well-suited for the design of tunnels under complex loading and/or ground properties.

Acknowledgements

The research is being partially supported by the research funding agency of the Brazilian government CNPq ("Conselho Nacional de Desenvolvimento Científico e Tecnológico"). The authors acknowledge the support from CNPq and from Midas company, which kindly provided the license of Midas GTX NX software, used in the present work.

Declaration of interest

The authors certify that they have no affiliations with or involvement in any organization or entity with any financial interest (such as honoraria; educational grants; participation in speakers' bureaus; membership, employment, consultancies, stock ownership, or other equity interest; and expert testimony or patent-licensing arrangements), or non-financial interest (such as personal or professional relationships, affiliations, knowledge or beliefs) in the subject matter or materials discussed in this paper.

Author's contributions

Osvaldo Paiva Magalhães Vitali: conceptualization of the new modelling approach, numerical and analytical validation, figures preparation, writing. Tarcisio Barreto Celestino: Orientation and supervision of the research work, reviewing, editing and writing. Antonio Bobet: Orientation and supervision of the research work, reviewing, editing and writing.

References

Armand, G., Noiret, A., Zghondi, J., & Seyedi, D.M. (2013). Short- and long-term behaviors of drifts in the Callovo-Oxfordian claystone at the Meuse/Haute-Marne Underground Research Laboratory. *Journal of Rock Mechanics and Geotechnical Engineering*, 5(3), 221-230. http://dx.doi.org/10.1016/j.jrmge.2013.05.005.

Bobet, A. (2011). Lined circular tunnels in elastic transversely anisotropic rock at depth. *Rock Mechanics and Rock Engineering*, 44(2), 149-167. http://dx.doi.org/10.1007/s00603-010-0118-1.

Bobet, A. (2016). Deep tunnel in transversely anisotropic rock with groundwater flow. *Rock Mechanics and Rock Engineering*, 49(12), 4817-4832. http://dx.doi.org/10.1007/s00603-016-1118-6.

Bobet, A., & Yu, H. (2016). Full stress and displacement fields for steel-lined deep pressure tunnels in transversely anisotropic rock. *Tunnelling and Underground Space Technology*, 56, 125-135. http://dx.doi.org/10.1016/j.tust.2016.03.005.

Brady, B.H.G., & Brown, E.T. (2006). *Rock mechanics for underground mining* (3rd ed.). New York: Springer. https://doi.org/10.1007/978-1-4020-2116-9.

Brown, E.T., & Hoek, E. (1978). Trends in relationships between measured in-situ stresses and depth. *International Journal of Rock Mechanics and Mining Sciences*, 15(4), 211-215. http://dx.doi.org/10.1016/0148-9062(78)91227-5.

Fortsakis, P., Nikas, K., Marinos, K.V., & Marinos, P. (2012). Anisotropic behavior of stratified rock masses in tunnelling. *Engineering Geology*, 141-142, 74-83. http://dx.doi.org/10.1016/j.enggeo.2012.05.001.

Goricki, A., Button, A.E., Schubert, W., Pötsch, M., & Leitner, R. (2005). The influence of discontinuity orientation on the behaviour of tunnels. *Felsbau*, 23(5), 12-18.

Haimson, B.C., Lee, M.Y., & Song, I. (2003). Shallow hydraulic fracturing measurements in Korea support tectonic and seismic indicators of regional stress. *International Journal of Rock Mechanics and Mining Sciences*, 40(7-8), 1243-1256. http://dx.doi.org/10.1016/S1365-1609(03)00119-9.

Klopčič, J., & Logar, J. (2014). Effect of relative orientation of anisotropy planes to tunnel axis on the magnitude of tunnelling displacements. *International Journal of Rock Mechanics and Mining Sciences*, 71, 235-248. http://dx.doi.org/10.1016/j.ijrmms.2014.02.024.

Lenz, G., Kluckner, A., Holzer, R., Stadlmann, T., Schachinger, T., & Gobiet, G. (2017). Prediction of fault zones based on geological and geotechnical observations during tunnel construction. *Geomechanics and Tunneling*, 10(4), 366-379. http://dx.doi.org/10.1002/geot.201700014.

McGarr, A., & Gay, N.C. (1978). State of stress in the earth's crust. *Annual Review of Earth and Planetary Sciences*, 6(1), 405-436. http://dx.doi.org/10.1146/annurev.ea.06.050178.002201.

Park, E.S., Choi, B.H., Bae, S.H., & Jeon, S. (2014). Horizontal stresses at shallow depths in Seoul (Korea) gneissic region. In *Proceedings of EUROCK 2014, ISRM European Regional Symposium* (pp. 399-404), Vigo, Spain.

Schubert, W., & Budil, A. (1995) The importance of longitudinal deformation in tunnel excavation. In *Proceedings of 8th ISRM Congress on Rock Mechanics* (pp. 1411-1414), Tokyo, Japan.

Schubert, P., Klopčič, J., Štimulak, A., Ajdič, I., & Logar, J. (2005). Analysis of characteristic deformation patterns at the Trojane tunnel in Slovenia. *Felsbau*, 23(5), 25-30.

Schubert, W., & Moritz, B. (2011). State of the art in evaluation and interpretation of displacement monitoring data in tunnels. *Geomechanics and Tunneling*, 4(5), 371-380. http://dx.doi.org/10.1002/geot.201100033.

Schubert, W., & Mendez, J.M.D. (2017). Influence of foliation orientation on tunnel behavior. *Procedia Engineering*, 191, 880-885. http://dx.doi.org/10.1016/j.proeng.2017.05.257.

Vitali, O.P.M., Celestino, T.B., & Bobet, A. (2018a). 3D finite element modelling optimization for deep tunnels with material nonlinearity. *Underground Space*, 3(2), 125-139. http://dx.doi.org/10.1016/j.undsp.2017.11.002.

Vitali, O.P.M., Celestino, T.B., & Bobet, A. (2018b). Analytical solution for tunnels not aligned with geostatic principal stress directions. *Tunnelling and Underground Space Technology*, 82, 394-405. http://dx.doi.org/10.1016/j.tust.2018.08.046.

Vitali, O.P.M., Celestino, T.B., & Bobet, A. (2019a). Shallow tunnel not aligned with the geostatic principal stress directions. In *Proceedings of Eighth International Conference on Case Histories in Geotechnical Engineering (Geo-Congress 2019)* (Geotechnical Special Publication, No. 313, pp. 214-222), Philadelphia.

Vitali, O.P.M., Celestino, T.B., & Bobet, A. (2019b). Shallow tunnels misaligned with geostatic principal stress directions: analytical solution and 3D face effects. *Tunnelling and Underground Space Technology*, 89, 268-283. http://dx.doi.org/10.1016/j.tust.2019.04.006.

Vitali, O.P.M., Celestino, T.B., & Bobet, A. (2019c) Progressive failure due to tunnel misalignment with geostatic principal stresses. In *Proceedings of ISRM 14th International Congress on Rock Mechanics* (pp. 2292-2299), Foz do Iguaçu.

Vitali, O.P.M. (2020). *Tunnel behavior under complex anisotropic conditions* [PhD thesis]. Lyles School of Civil Engineering, Purdue University. https://doi.org/10.25394/PGS.12302600.v1.

Vitali, O.P.M., Celestino, T.B., & Bobet, A. (2020a). Tunnel misalignment with geostatic principal stress directions in anisotropic rock masses. *Soils and Rocks*, 43(1), 123-138. http://dx.doi.org/10.28927/SR.431123.

Vitali, O.P.M., Celestino, T.B., & Bobet, A. (2020b). Analytical solution for a deep circular tunnel in anisotropic ground and anisotropic geostatic stresses. *Rock Mechanics and Rock Engineering*, 53(9), 3859-3884. http://dx.doi.org/10.1007/s00603-020-02157-5.

Vitali, O.P.M., Celestino, T.B., & Bobet, A. (2020c). Deformation patterns and 3D face effects of tunnels misaligned with the geostatic principal stresses in isotropic and anisotropic rock masses. In *Proceedings of 54th US Rock Mechanics /Geomechanics Symposium (ARMA 2020)*, Golden, Colorado.

Wittke, W. (1990). *Rock mechanics: theory and applications with case histories*. Switzerland: Springer. (English translation of Wittke, 1984, Felsmechanik).

Worotnicki, G. (1993). CSIRO triaxial stress measurement cell. In J. A. Hudson (Ed.), *Rock testing and site characterization: principles, practice, and projects* (Chap. 13, pp. 329-394). Oxford: Pergamon Press.

Soils and Rocks
An International Journal of Geotechnical and Geoenvironmental Engineering
www.soilsandrocks.com
ISSN 1980-9743
ISSN-e 2675-5475

A proposal for static load tests on piles: the Equilibrium Method

Francisco R. Lopes[1#], Paulo Eduardo L. Santa Maria[1], Fernando A. B. Danziger[1], Ian S. M. Martins[1], Bernadete R. Danziger[2], Michel C. Tassi[3]

Technical Note

Keywords
Pile load tests
Equilibrium Method
Pile foundations
Pile bearing capacity
Soil viscosity

Abstract

This note presents an alternative method for static load tests on piles (and caissons). Called Equilibrium Method by its first proponents, the method was applied in some load tests in Brazil, in addition to being the object of theoretical studies conducted at the Federal University of Rio de Janeiro. The method consists, in each step, to keep the load constant for a period of time and then let it relax (not pumping the jack) until the displacement and the load reach mutual equilibrium. The stabilized displacement and the relaxed load (the so-called *load and displacement in equilibrium*) are considered for the load-displacement curve. The method has the advantage of producing the load-displacement curve close to that of a slow, stabilized test (incremental slow maintained load test), but with a shorter total execution time. The paper includes a short theoretical background and a review of the Brazilian experience.

1. Introduction

Soils, most notably clayey, saturated, exhibit viscous behaviour, that is, a time-dependent behaviour which is not associated with water migration to equilibrate pore-pressures – *consolidation* –. Viscosity manifests itself in some conditions, such as *creep* (deformation under constant loading conditions), *stress relaxation* (change in stress under sustained displacement) and the *effect of loading rate* on shear strength. These occurrences or phenomena were recognized a long time ago, as in the work of Buisman (1936), who described what became known as *secondary consolidation* (which would be *creep*), and in those of Casagrande & Wilson (1951) and Bjerrum (1973), in which a variation in the shear strength of clays was observed with the variation of *loading rate*. Viscosity is also responsible for increasing the thrust on retaining structures, evolving to an *at-rest condition*, if these are prevented from displacing (e.g., Bishop, 1957). Early works, such as Hvorslev (1937, 1960) and Terzaghi (1941), attributed these phenomena to the viscous nature of the adsorbed water film involving soil particles.

1.1 An approach to soil viscosity and its effects on pile capacity

A viscosity model developed at the Graduate School of Engineering, Federal University of Rio de Janeiro assumes that the shear stress in clayey soils has two components: one of frictional nature and the other of viscous nature, i.e. (Martins, 1992):

$$\tau = \tau_f + \tau_\eta \tag{1}$$

It turns out that the frictional component of the shear stress depends on the effective solid-solid stress, σ'_s, and on the mobilized friction angle, ϕ'_{mob}, with the mobilized friction angle being, in turn, a function of the distortion, γ . Thus, the friction component is written:

$$\tau_f = \sigma'_s \tan\phi'_{mob}(\gamma) \tag{2}$$

On the other hand, the viscous component, τ_η , is a function of a soil viscosity coefficient, η (e), – in its turn a function of the void ratio, *e*, – and of the rate of distortion, $d\gamma/dt$. Thus, the viscous component of the shear stress can be written as:

$$\tau_\eta = \eta(e)\frac{d\gamma}{dt} \tag{3}$$

Therefore, the shear stresses mobilized, during pile loading, both along the shaft and in the soil region that produces base or tip resistance, can be expressed by the sum of τ_f and τ_η.

[#]Corresponding author. E-mail address: flopes@coc.ufrj.br
[1]Universidade Federal do Rio de Janeiro, Rio de Janeiro, RJ, Brasil.
[2]Universidade do Estado do Rio de Janeiro, Rio de Janeiro, RJ, Brasil.
[3]Instituto Militar de Engenharia, Exército Brasileiro, Rio de Janeiro, RJ, Brasil.

Submitted on September 23, 2020; Final Acceptance on January 20, 2021; Discussion open until May 31, 2021.
DOI: https://doi.org/10.28927/SR.2021.057920

This means that the expression for the mobilized shaft load capacity must be written, taking into account the rate effect (viscosity), as:

$$Q_s = U\int_0^L K.\sigma_v^{'}(z).tan\phi_{mob}^{'}.dz + U\int_0^L \eta\left(e(z)\right)\frac{d\gamma}{dt}dz \quad (4)$$

The friction angle, as it is usually determined, is also affected by rate effects, and, therefore, the tip resistance is also a function of the loading rate in the load test, that is, the higher the loading rate – or the shorter the time taken to produce failure –, the greater the tip resistance. In relation to the pile tip, there is the opposite time effect due to the consolidation (dissipation of excess pore-pressures generated by soil compression under the tip). But it can be said that the total load capacity (shaft + tip capacities), measured in a load test, increases with loading rate.

2. Loading rate effects on pile bearing capacity

The behaviour observed in pile load tests is typical of loading rate effects on soil resistance, that is, the faster a pile is loaded – or the shorter the duration of load stages – the greater the resistance. This behaviour of piles, in which quick loadings bring about higher capacities than slow loadings, is opposed to that of plates on saturated clayey soils in which fast loading tends to be critical. This is explained by the stress-paths followed at representative points around these foundations (Figure 1). Under a plate, stress paths are close to that of a triaxial test, in which there is an increase in mean normal stress accompanying the increase in shear stress (Figure 1b); thus, there is an increase in pore-pressures with loading, which – if dissipated in a slow loading process – lead to higher resistance. On the other hand, in the soil around the pile shaft, the stress path is vertical, indicating a loading mode called *simple shear* (Figure 1a); thus, unless the soil is contractive, there will be practically no excess pore-pressure generation during loading. If there is no water migration process (consolidation) in this region, it can be concluded that viscosity dominates the time dependent behaviour of the soil around the pile shaft. Under the tip of the pile, the stress path is similar to that of the soil under plates, but this resistance is only a fraction of the total pile resistance (unlike the plate). In other words, in piles, which are long elements, there is a large portion of soil subject to an increase in resistance with an increase in rate, therefore, there is a predominance of viscous effects over consolidation.

The assumption that quick loading leads to lower load capacity – which is only valid for plates – served to postulate the load test known in Brazil as the *mixed method*. In this method, loading up to the service load follows a

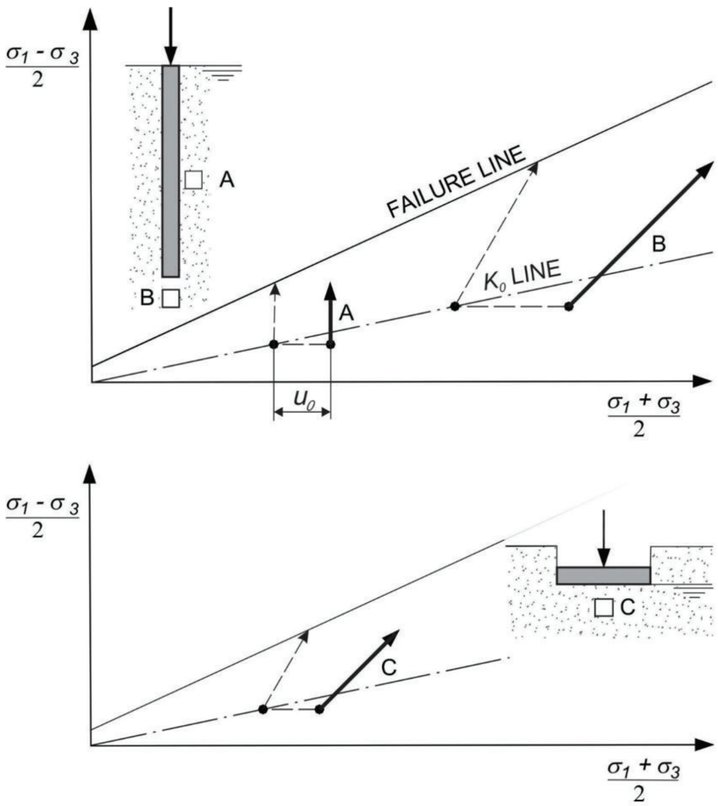

Figure 1. Total (solid lines) and effective stress paths (dashed lines) at points (a) around a pile and (b) under a plate, during loading (adapted from Lopes, 1979, 1985).

stabilization criterion (i.e., in a slow loading rate) in order to determine the displacement for the service load, and then it proceeds with short duration load increments (i.e., in a quick loading rate), assuming that the ultimate load capacity obtained is on the safe side (lower than that under slow loading).

Pore-pressure generation around the pile shaft during load tests should not be mistaken for pore-pressure generation when installing driven piles, which is significant. The dissipation of installation pore-pressures is the main cause of the gain in pile capacity with time after installation, known as *set-up*.

The issue of quick tests, an example being the CRP (Constant Rate of Penetration) test, indicating load capacities greater than slow tests, was discussed by several authors, such as Whitaker & Cooke (1966), Lopes (1985, 1989), Ferreira & Lopes (1985), Burland & Twine (1988), Patel (1992) and England & Fleming (1994). These latter authors stated:

> *It has been shown that the effect of the rate of penetration (normally approximately 1 mm/min) is to enhance pile shaft capacities in clay soils, but the same is also probable with regard to friction in a wider range of soils and also to base capacities.*

2.1 Loading rate effect on displacements

In relation to the displacement for service loads, there is no doubt that a slow, stabilized load is that representative of a foundation – plate or pile – under maintained load.

2.2 Methods for obtaining a stabilized load-displacement curve

The *fully stabilized* load-displacement curve corresponds to the *zero loading rate curve*. The question is how to arrive at this curve in load tests, in which, invariably, the load is applied in stages. There are two ways (see Figure 2): (i) applying a load increment and keeping it constant until displacements cease (path A-B) or (ii) applying an increase in load and allowing both displacements and loads to stabilize (path A-C). In option (ii), stabilization will imply load relaxation. The study of the Appendix shows that the path via relaxation is faster.

Experience shows that the time for stabilization under constant load increases as the loading level increases. At the higher load stages, several hours are required for rigorous stabilization. In the Equilibrium Method, according to Mohan et al. (1967), stabilization is achieved 'in a matter of minutes'.

3. The Equilibrium Method

The Equilibrium Method consists, in each step, of keeping the load constant for a period of time and then let it relax (not pumping the jack) until the displacement and the load reach mutual equilibrium. The stabilized displacement and the relaxed load (the so-called *load and displacement in equilibrium*) are considered for the load-displacement curve. The set of graphs produced by the method is shown

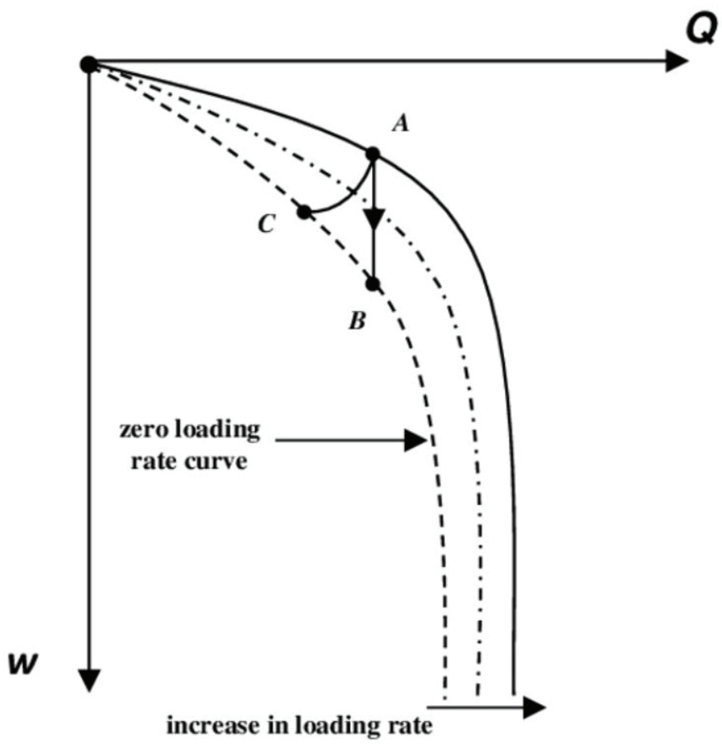

Figure 2. Possible load (Q) vs. displacement (w) curves in load tests and paths to reach the zero loading rate curve (Martins, 2006).

in Figure 3, where t_1 is the time interval under constant load and t_2 is the time interval of load relaxation.

4. Brazilian experience with the Equilibrium Method

4.1 Load tests at Santos-São Vicente Bridge (DERSA)

Ferreira (1985) analyzed 6 load tests carried out on 2 steel pipe piles of a bridge between Santos and São Vicente. The piles were 65 cm in diameter and 42 and 50 m long. Soil profile was a sequence of layers of soft clay and low density clayey fine sand, until nearly 40m, where residual soil was found (dense sandy silt).

The service load of the piles was 2500 kN and the maximum loads in the tests reached 6000 kN. Three procedures, applied in sequence, were followed for each of the piles:

(i) incremental load until a rigorous stabilization, maximum load of 5000 kN, in 10 stages of 16 hours each;
(ii) Brazilian standard NBR 6121 (ABNT, 1980), maximum load of 3750 kN, in 8 stages;
(iii) Equilibrium Method, maximum load of 6000 kN, in 10 stages.

The load tests lasted about 50 total hours in the last two procedures and about 200 hours in the more rigorous stabilization procedure.

In terms of displacements, for the 3000 kN stage (the closest to the service load, 2500 kN), displacements were small and close in the 3 methods: 8mm for PV-02 and 6mm for PV-03. These displacements reflect the fact that the piles had their tips driven into very dense material, which was also reflected in the small load relaxation in the stages of the Equilibrium Method.

Five load-displacement curves did not indicate a clear failure and extrapolations by Van der Veen's (1953) method indicated unrealistic load capacities, around 9000 kN. Only the Equilibrium Method curve of PV-02 showed 80 mm displacement for the maximum load, indicating failure for practical purposes (~ 6000 kN). Figure 4 shows the results of PV-02 for the more rigorous stabilization procedure and for the Equilibrium Method (with the rigorous stabilization curve extrapolated).

4.2 Load test on model pile in soft clay in Rio de Janeiro

Francisco (2004) performed load tests on a steel model pile, 11.5 cm diameter, driven in soft clay to a depth of 3.5 m, at Sarapuí II test site, Rio de Janeiro metropolitan region. The pile was subject to a quick load test and to 2 equilibrium tests (Figure 5). Failure loads were in the proximity of 7.2 kN for the quick test and between 5.5 and 6.5 kN for the equilibrium tests. The test program also included a long term creep test and the thesis presents a theoretical approach to pile behavior considering soil viscosity.

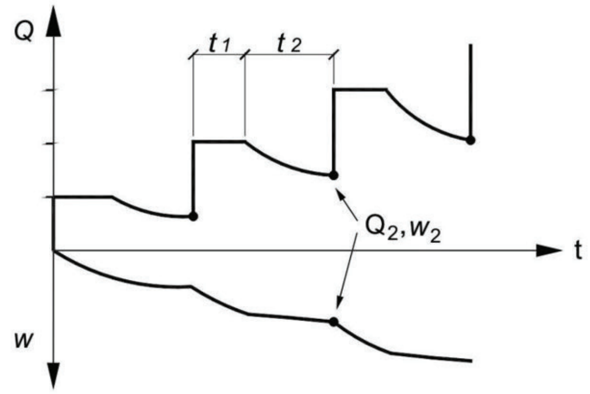

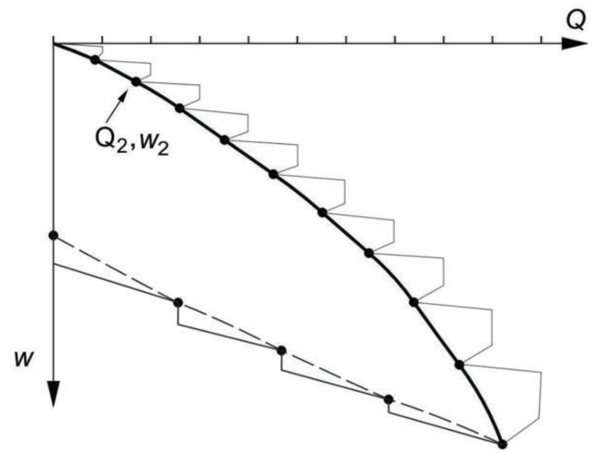

Figure 3. Typical graphs produced in the application of the Equilibrium Method.

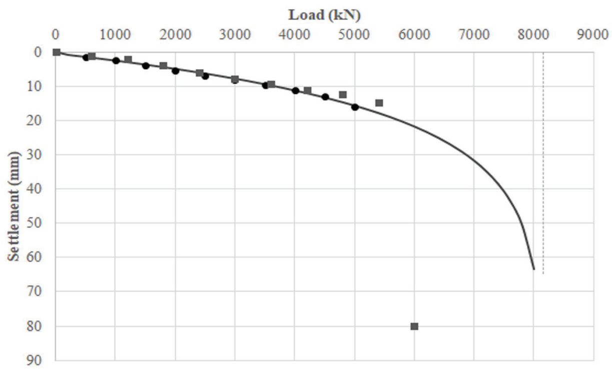

Figure 4. Load-displacement curves obtained with incremental load maintained until rigorous stabilization (circles) - with extrapolation - and by the Equilibrium Method (squares), PV-02 (Ferreira, 1985).

4.3 Load tests at USP/São Carlos test site

Benvenutti (2001) performed load tests on two caissons, 50 cm shaft diameter, 1.5 m base diameter, length 5.1 m, installed in collapsible soil at the São Carlos Test Site, State of São Paulo. On each caisson, 4 tests were performed: 3 quick and then 1 by the Equilibrium Method. One caisson was tested in natural water content conditions and the other after flooding. Results for the natural water content conditions are shown in Figure 6. It can be seen that the Equilibrium Method produced load-displacement curves with less stiffness in the first-loading segment.

4.4 Load tests on model plates at University of São Paulo/São Carlos

Almeida (2009) carried out load tests – although on plates – in the laboratory, on undisturbed block-type samples of partially saturated soils. Sets of three samples were taken next to each other, presenting the same matrix suction. On each sample one of the following test methods was applied: (i) slow maintained load, (ii) quick maintained load and (iii) Equilibrium Method (with 5 minutes of maintained load and 10 minutes of load relaxation). It was concluded that the load-displacement curves obtained with the Equilibrium Method were closer to those of the slow maintained load tests than those of the quick tests, as shown in Figure 7 for one of the test sets.

5. Proposed procedure for the Equilibrium Method

Based on the published data on the Equilibrium Method, the following procedure is proposed (see Figure 3):

a) loading must be carried out in 10 equal stages, each one corresponding to 20% of the expected service load;
b) the load of each stage must be kept constant for 20 min, taking displacement readings at 2, 5, 10, 15 and 20 min;
c) after 20 min, the load is allowed to relax for a period of 15 min, noting displacements and loads at 2, 5, 10, 15 min;
d) at 15 min, stabilization is verified by the criterion described below; if the criterion is met, the stage ends; if not, the stage continues up to a maximum of 30 min, checking the stabilization criteria at 20 and 25 min;
e) the load and displacement after relaxation will be considered for the load-displacement curve;
f) unloading may be carried out in 4 short duration stages, such as 10 min each one.

5.1 Criterion to end the relaxation period

During relaxation, the load variation *(ΔQ in Figure 8)* is more pronounced than the displacement variation (Δw_2), therefore, the stabilization criterion is applied to the former. The proposed criterion compares the load variation that occurred up to a given time to the variation in the previous time (see Figure 8). If the ratio between the 2 load variations is less than 5%, the stage is terminated. The application of this criterion starts at 15 min. Therefore, if

$$\Delta Q_{15} \leq 1{,}05 \Delta Q_{10} \tag{5}$$

the stage ends; if not, go on to 20 min, and so on for up to 30 min (maximum relaxation time).

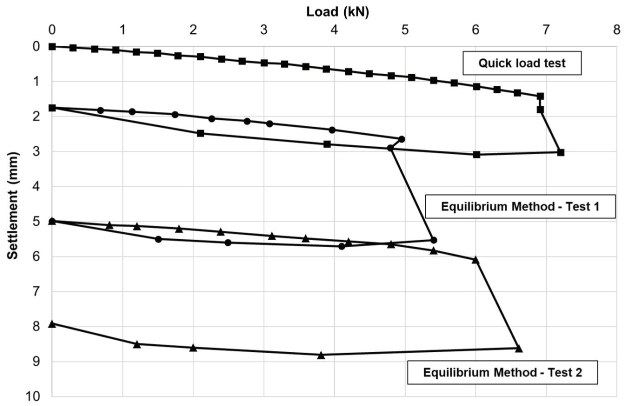

Figure 5. Load-displacement curves for a model pile subjected to different loading procedures (Francisco, 2004).

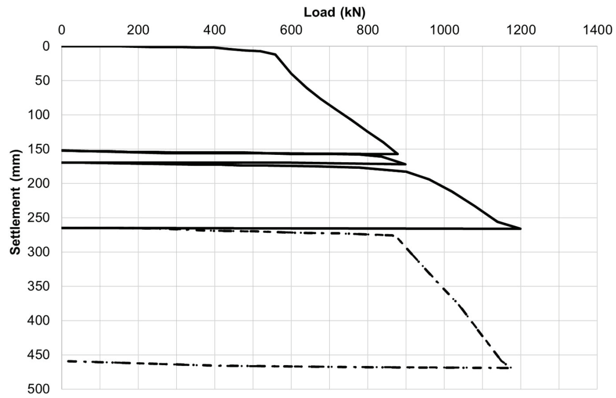

Figure 6. Load-displacement curves from quick tests (solid line) and Equilibrium Method (dash-dotted line) in natural water content conditions (Benvenutti, 2001).

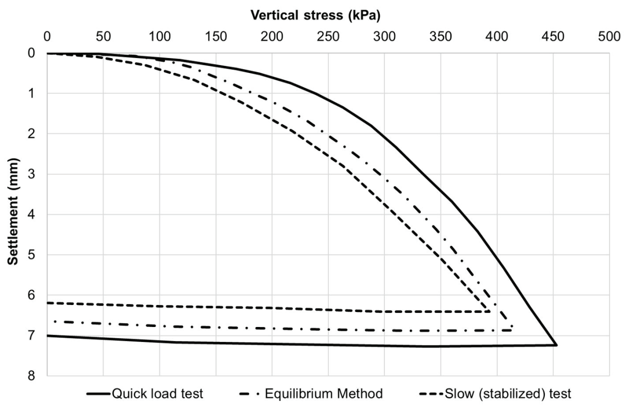

Figure 7. Pressure-displacement curves from plate load tests: quick test, slow test and Equilibrium Method (Almeida, 2009).

For the interpretation of the ultimate pile capacity, any procedure from the local Foundation Code or established in the literature can be applied, as in any other type of test method.

This procedure should be evaluated with the experience gathered with new load tests.

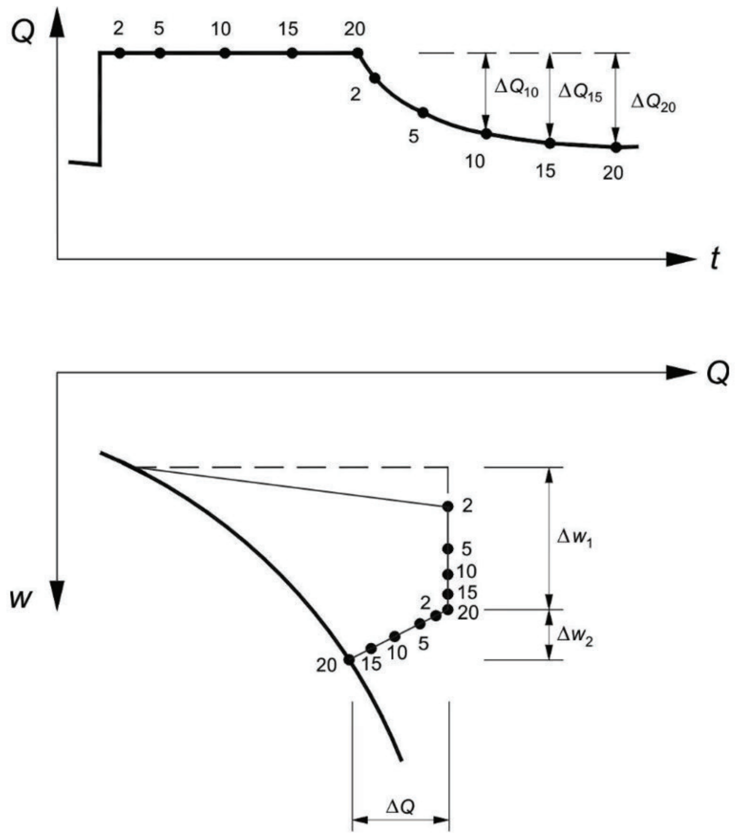

Figure 8. Details of a loading stage – Equilibrium Method – with reading times (in min) indicated.

6. Concluding remarks

This note aims to stimulate the discussion of procedures for carrying out load tests on piles and caissons. There is an interest in limiting the time spent on load tests, for various reasons, such as interference in the construction schedule, labor safety and costs. The method discussed here, called the Equilibrium Method by its first proponents (Mohan et al., 1967), can lead to displacements very close to those of a fully stabilized test in a predictable execution time.

It is noteworthy that the choice of the load test method must be made by the Designer and/or Consultant, taking into account the particularities of the load to which the pile/caisson will be subjected under the structure. Among the methods is the quick test, which should not be understood as a static load test, but a test that reflects the behaviour of the pile under fast acting loads, such as wind and wave actions on power transmission towers and marine structures.

Acknowledgements

The authors benefited from discussions with members of the review committee of the Brazilian Load Test Standard, in particular Paulo J.R. Albuquerque, Guilherme Soler and Gentil Miranda Jr. Extrapolations by Van der Veen's method made use of a spreadsheet by Prof. José Antonio Schiavon, Technological Institute of Aeronautics. This study was partly financed by CAPES - Coordenação de Aperfeiçoamento de Pessoal de Nivel Superior, Brazil, under Finance Code 001.

Declaration of interest

There is no conflict of interests in the material presented.

Author's contributions

Francisco R. Lopes: conceptualization, methodology, writing - original draft preparation. Paulo Eduardo L. Santa Maria: conceptualization, formal analysis. Fernando A.B. Danziger: investigation, discussion of results, review and approval of the final version of the manuscript. Ian S. M. Martins: conceptualization, investigation. Bernadete R. Danziger: discussion of results, writing - reviewing and editing. Michel C. Tassi: visualization, discussion of results, review and approval of the final version of the manuscript.

References

ABNT NBR 6121 (1980). NBR 6121: *Pile and Caisson - Load test*. ABNT - Associação Brasileira de Normas Técnicas, Rio de Janeiro, RJ (in Portuguese).

Almeida, M.P.B. (2009). *Quick load test with equilibrium settlement* [Unpublished master's dissertation]. Escola de Engenharia de São Carlos, Universidade de São Paulo (in Portuguese).

Benvenutti, M. (2001). *Caissons to improve load capacity on collapsible soils* [Unpublished master's dissertation]. Escola de Engenharia de São Carlos, Universidade de São Paulo (in Portuguese).

Bishop, A.W. (1957). Discussion, Session 8 - Earth Pressure on Structures and Tunnels. In *Proceedings of the 4th International Conference on Soil Mechanics and Foundation Engineering* (pp. 242-243). London: ISSMGE - International Society for Soil Mechanics.

Bjerrum, L. (1973). Problems of soil mechanics and construction on soft clays and structurally unstable soils. In *Proceedings of the 8th International Conference on Soil Mechanics and Foundation Engineering* (pp. 111-189). Moscow: ISSMGE - International Society for Soil Mechanics.

Buisman, A.S.K. (1936). Results of long duration settlement tests. In *Proceedings of the 1st International Conference on Soil Mechanics and Foundation Engineering* (Vol. 1, pp. 103-106). Cambridge, Mass: ISSMGE - International Society for Soil Mechanics.

Burland, J.B., & Twine, D. (1988). The shaft friction of bored piles in terms of effective strength. In *Proceedings of the Seminar on Deep foundations on bored and auger piles* (pp. 411-420). Ghent: Balkema, Rotterdam .

Casagrande, A., & Wilson, S. (1951). Effect of rate of loading on the strength of clays and shales at constant water content. *Geotechnique*, 2(3), 251-263. http://dx.doi.org/10.1680/geot.1951.2.3.251.

England, M., & Fleming, W.G.K. (1994). Review of foundation testing methods and procedures. *Proceedings of ICE. Geotechnical Engineering*, 107(3), 135-142. http://dx.doi.org/10.1680/igeng.1994.26466.

Ferreira, A.C. (1985). *Loading rate effects and the question of pile settlements in load tests* [Unpublished master's dissertation]. Universidade Federal do Rio de Janeiro (in Portuguese).

Ferreira, A.C., & Lopes, F.R. (1985). Contribution to the study of loading rate effects on the behaviour of test piles. *Proceedings of the 1st Seminar on Special Foundations*. São Paulo: ABEF - Associação Brasileira de Empresas de Engenharia de Fundações.

Francisco, G.M. (2004). *Study of time effects on foundation piles in clayey soils* [Unpublished DSc Thesis]. Universidade Federal do Rio de Janeiro.

Hvorslev, M.J. (1937). *Physical properties of remolded cohesive soils (Uber die festigkeitseigenschaften gestorter bindiger boden* [Unpublished Doctoral thesis]. U. S. Army Engineer Waterways Experiment Station.

Hvorslev, M.J. (1960). Physical components of the shear strength of saturated clays. In *Proceedings of the ASCE Research Conference on Shear Strength of Cohesive Soils* (pp. 169-273). Boulder: University of Colorado.

Lopes, F.R. (1979). *The undrained bearing capacity of piles and plates studied by the finite element method* [Unpublished PhD thesis]. Imperial College, University of London.

Lopes, F.R. (1985). Lateral resistance of piles in clay and possible effect of loading rate. In *Proceedings of the Symposium on Theory and Practice of Deep Foundations* (Vol. 1, pp. 53-68). Porto Alegre: ABMS - Associação Brasileira de Mecânica dos Solos e Engenharia Geotécnica.

Lopes, F.R. (1989). Discussion to Session 15. In *Proceedings of the 12th International Conference on Soil Mechanics and Foundation Engineering* (Vol. 5, pp. 2981-2983). Rio de Janeiro: ISSMGE - International Society for Soil Mechanics.

Martins, I.S.M. (1992). *Fundamentals of a model for the behaviour of saturated clayey soils* [Unpublished Doctoral thesis]. Universidade Federal do Rio de Janeiro (in Portuguese).

Martins, I.S.M. (2006). On the viscous behaviour od soils. Lecture. In *Proceedings of the 13th Brazilian Conference Soil Mech*. Curitiba: ABMS - Associação Brasileira de Mecânica dos Solos e Engenharia Geotécnica.

Mohan, D., Jain, G.S., & Jain, M.P. (1967). A new approach to load tests. *Geotechnique*, 17(3), 274-283. http://dx.doi.org/10.1680/geot.1967.17.3.274.

Patel, D.C. (1992*).* Interpretation of results of piles tests in London Clay. In *Piling: European Practice and Worldwide Trends*. London: Thomas Telford.

Terzaghi, K. (1941). Undisturbed clay samples and undisturbed clays. *Journal of the Boston Society of Civil Engineers*, 28(3), 211-231.

Van der Veen, C. (1953). The bearing capacity of a pile. In: *Proceedings of the 3rd International Conference on Soil Mechanics and Foundation Engineering* (vol. 2, pp. 84-90). Zurich: ISSMGE - International Society for Soil Mechanics.

Whitaker, T., & Cooke, R.W. (1966). An investigation of the shaft and base resistances of large bored piles in London Clay. In *Proceedings of the Large Bored Piles* (pp. 7-49). London: Institution of Civil Engineers.

Appendix. Comparison of evolution towards stabilization under maintained load and by load relaxation by Linear Viscoelasticity Theory

This appendix presents a comparative analysis of static load tests using the maintained load method and Equilibrium Method.

The resistance of a pile when subjected to generic external loads can be represented by the equation:

$$R = f1(w) + f2(\dot{w}) + f3(\ddot{w}) \tag{A1}$$

where $f1$, among other variables, is a function of the displacement w, $f2$ of the displacement rate (or velocity) $\dot{w}$ and $f3$ of the acceleration $\ddot{w}$. In the case of static load tests, $f3(\ddot{w})$ can be neglected but not $f2(\dot{w})$. Although the second component is, in general, much less representative than $f1(w)$, it is important for understanding the process and its interpretation.

In order to better understand the displacement vs time behaviour and load vs time behaviour of piles during load test stages in the maintained load method and in the Equilibrium Method, a simple mathematical model of these tests was elaborated considering:

The use of Linear Viscoelasticity Theory;

The soil represented by the constitutive relations of Kelvin's viscoelastic model;

The test reaction structure represented by the linear elastic model.

Two important aspects should also be highlighted:

It is a very simple model and, therefore, the absolute values obtained are not relevant;

The objective is to compare the two load pile test procedures in terms of time to stabilize each process.

Figure A1 shows displacement development in a maintained load test in a 1000 kN loading stage. Figures A2 to A4 show the variation of load with time in a test by the Equilibrium Method, considering different stiffnesses of the reaction system (1K, 2K, ..., 5K). In Figure A2, a displacement was applied such that the load value after stabilization was approximately equal to the loading stage of the maintained load test (~ 1000 kN). Figure A3 is the same as Figure A2, with an amplified time scale. In Figure A4, displacements were applied such that the initial load value was equal (for all stiffnesses of the reaction system) to the load in the maintained load test (1000 kN).

Appendix conclusions

1. It was observed that the time required for load stabilization in the load test by the Equilibrium Method varied relatively little when the stiffness of the reaction system varied from 1K to 5K.
2. The displacement stabilization time in an incremental maintained load test was approximately equal to three times the load stabilization time in the Equilibrium Method.

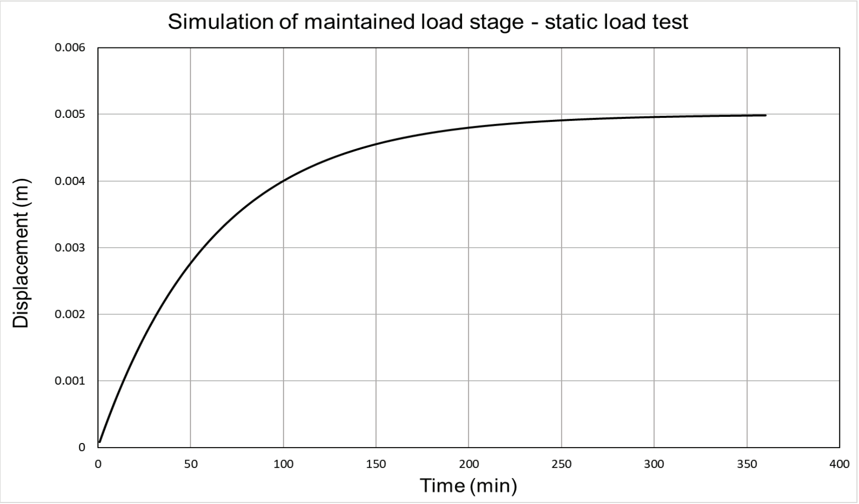

Figure A1. Simulation of (incremental) maintained load stage, conventional static load test.

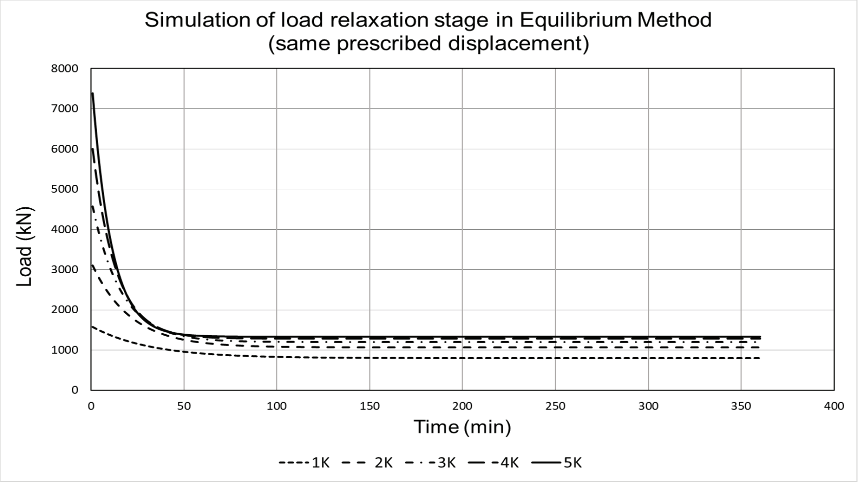

Figure A2. Simulation of load relaxation stage in Equilibrium Method, same prescribed displacement.

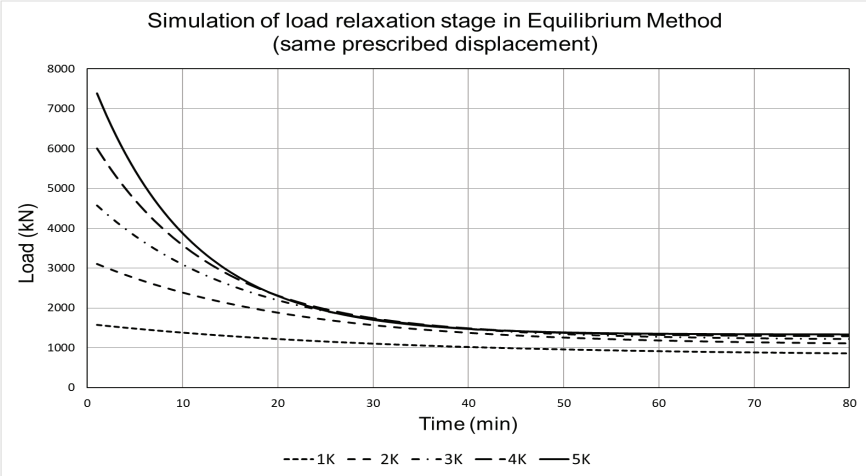

Figure A3. Simulation of load relaxation stage in Equilibrium Method, same prescribed displacement (first 80 minutes).

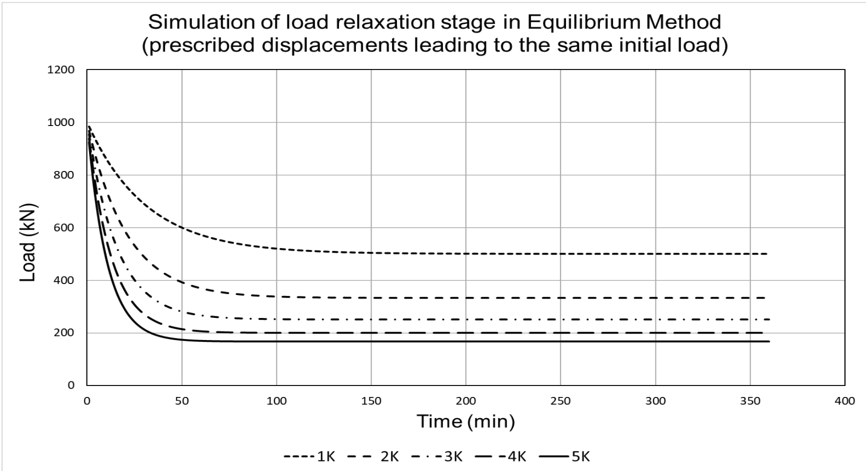

Figure A4. Simulation of load relaxation stage in Equilibrium Method, displacements leading to the same initial load.

List of Symbols

Q = load
w = displacement
Q_s = pile shaft load capacity
U = pile perimeter
L = pile length
z = depth below ground level
u = pore-pressure
K = earth pressure coefficient after pile installation
K_o = coefficient of earth pressure at rest
e = void ratio
t = time
t_1 = time under constant load
t_2 = time of load relaxation
ΔQ = load variation in a stage
Δw = displacement variation in a stage
R = pile resistance
$f1$ = displacement dependent factor
$f2$ = rate (or velocity) dependent factor
$f3$ = acceleration dependent factor
$\dot{w}$ = velocity
$\ddot{w}$ = acceleration
ϕ'_{mob} = mobilized angle of shearing resistance
τ = shear stress
τ_f = friction component of shear stress
τ_η = viscous component of shear stress
σ'_s = effective solid-solid stress
σ'_v = effective vertical stress
γ = shear strain or distortion
η = soil viscosity coefficient
σ_1 = major principal stress
σ_3 = minor principal stress

Soils and Rocks
An International Journal of Geotechnical and Geoenvironmental Engineering
www.soilsandrocks.com
ISSN 1980-9743
ISSN-e 2675-5475

Numerical analysis of cyclic loading effect on progressive failure of an earth dam upon a multi-laminate framework

Hamzeh Rahimi Dadgar[1#], Mohamad Ali Arjomand[2], Ali Arefnia[1]

Technical Note

Keywords
Earth dam
Progressive failure
Multi-Laminate framework
Cyclic loading

Abstract

In this paper, the progressive failure in an earth dam is evaluated upon a Multi-Laminate framework by considering 10 historical earthquakes in the world, along with their equivalent harmonic cyclic loading. Whenever the framework is given for any suggested plane by direction cosines, it has its certain direction, so, on this basis, the activation order of planes represents the direction and next step of progressive failure. The numerical integration comprises a function that is determined by distributing in sphere area including a radius of one, which can be approximated with several planes, tangential to different points in the sphere area. By calculating numerical integration, the quantity, spread on the sphere, achieved in the aforesaid points to predict fabric anisotropy effects. The framework efficiency is proved by evaluation of removal constants, such as confining pressure, and void ratio. The effects of driven anisotropy studied on all planes of the framework in 10 earthquakes to determine the effects of induced anisotropy on activated and no activated planes, in order to evaluate the progressive failure. Then, the model is capable to predict the coordinate of node of each brick element of the earth dam for next failure.

1. Introduction

Progressive failure appears whereas the average driven resistance, on a sliding surface, is less than the average peak resistance at the time of failure (La Rochelle, 1960). Typical slopes failure appears on any occasion that the strength reduction exceeds in post-peak zones; however, it increases in the driven resistance in the pre-peak parts (Bishop, 1971). This phenomenon causes sudden instability and larger post-failure movements. Some experimental evidence clarified that the average driven resistance is crucial in examining progressive failure (Peck, 1967; Rowe, 1969). A few numerical methods used to analyze cases associated to long slopes (Bernander & Olofsson, 1981; Palmer & Rice, 1973). Part of numerical analyses presented by considering softening phenomena and a non-linear finite element analysis has been performed (Biondi et al., 1976; Prévost & Höeg, 1975).

The analyses express the impact of progressive failure and exhibit various modes of slope and earth dam behavior. Subsequent researches have been carried out to study the issues concerning the progressive failure conditions especially in sand particles by numerical frameworks (Sadrnejad & Labibzadeh, 2006). In this research, the weight coefficient and direction cosines of seventeen planes are calculated using Multi-Laminate theory; the effect of planes is transferred to the middle points of them by numerical integration. Constitutive relations corrected by the method of reducing the number of soil constants, using hypo-plasticity theory (Dafalias, 1986; Dafalias & Manzari, 2004; Manzari & Dafalias, 1997; Taiebat et al., 2010; Wang et al., 1990). Therefore, a constant value at 0.65 is increased by a constant scale used (Halyan, 2001). To determine the number of cycles equivalent to the acceleration of the mappings proposed (Seed & Bruce, 1976), a special method is employed for the time history of shear stress, resulted from the ground motions recorded.

In Multi-Laminate, the equations of the planes and the model constants implemented and calibrated. On each plane the important effects of the applied anisotropy analyzed to evaluate the progressive failure. Evaluating Crack propagation in Earth Dams upon a mixture of Multi-Line technic and Multi-Laminate theory clarified the order of planes activation and progressive failure due to cyclic triaxial test with the same dimensions and boundary conditions and confining pressure for dynamic loading state investigated and compared to laboratory tests (Rahimi Dadgar et al., 2019a, 2019b) and finally the model constants modified based on constitutive relations obtained from elasto-plastic theory (Dashti et al., 2017, 2019).

The major innovative point of this numerical study is that the model is able to predict progressive failure in the earth dam in an equivalent cyclic loading. In this study, to learn the progressive failure, the effect of cyclic loading

[#]Corresponding author. E-mail: st.h_rdadgar@riau.ac.ir
[1]Islamic Azad University, Roudehen Branch, Department of Civil Engineering, Roudehen, Iran.
[2]Shahid Rajaee Teacher Training University, Department of Civil Engineering, Tehran, Iran.

Submitted on August 13, 2020; Final Acceptance on January 27, 2021. Discussion open until: May 31, 2021.

DOI: https://doi.org/10.28927/SR.2021.056720

is applied. For this purpose, the response spectrum of ten important earthquakes caused serious damages is studied. Then, the aforesaid response ranges, being converted to harmonic charges are studied in numerical method. In this paper, due to the breadth and complexity of earthquake records, as well as the diversity of soil structures' response to each of these applied loads, historical earthquakes and their equivalent cyclic loads at maximum Different ranges, as a factor of the max acceleration of the relevant record, are studied.

2. Materials and method

The numerical relationship between micro-scale behaviors and engineering mechanical properties (macro-scale behavior) due to constitutive equation is the basis of the Multi-Laminate theory. The numerical integration, from a mathematical function, is obtained from sphere area, and the planes are in contact with points of the sphere.

2.1 The framework relations and parameters

The given model has remarkable features and consisting with the principles of advanced soil mechanics. By definition of constitutive relation in the planes and the dilatancy surface and bounding surface and their changes during cyclic loading-unloading and the corresponding match to the critical surface in failure condition, prediction of progressive failure due to order of planes activation is possible. In the following part, governing equations on planes and modifications are considered:

$$G_{(P)} = (2.83 - e)^2 / (1 + e)\left(\frac{\sigma_{n(P)}}{P_{atm}}\right)^{1/2} G_{0P} P_{atm} \tag{1}$$

$$K_{(P)} = \frac{2(1 + v_p)}{3(1 - 2v_p)} G_{(P)} \tag{2}$$

For determination of critical state line and yield surface, considering the state parameter for all the planes, the following relations used four main surfaces of the numerical applied model at every node of brick elements.

$$e_{c(P)} = e_{0P} - \lambda_{cp}\left(\frac{\sigma_{n(P)}}{P_{atm}}\right)^{\xi_P} \tag{3}$$

$$Cog_{(P)} = \left[\left(Dev_{(P)} - \sigma_{n(P)}\alpha_{(P)}\right) : \left(S_{(P)} - \sigma_{n(P)}\alpha_{(P)}\right)\right]^{1/2} - \sqrt{5/7\sigma_{n(P)}}\, m_P = 0 \tag{4}$$

$$Dev_{(P)} = \sigma_{(P)} - \sigma_{n(P)} I_{(P)} \tag{5}$$

$$I_{(P)} = \begin{bmatrix} 1 & 0 & 0 \\ 0 & 0 & 0 \\ 0 & 0 & 0 \end{bmatrix} \tag{6}$$

$$r_{(P)} = Dev_{(P)} / \sigma_{n(P)} \tag{7}$$

According to the equation of $Cog_{(P)}$, $L_{(P)}$ and $n_{(P)}$ are obtained as follows:

$$L_{(P)} = \partial Cog_{(P)} / \partial \sigma_{(P)} \tag{8}$$

$$n_{(P)} = \frac{r_{(P)} - \alpha_{(P)}}{r_{(P)} - \alpha_{(P)}} \tag{9}$$

If non-associated flow rule is the dominant plasticity behavior, the following relation used in modeling the progressive failure:

$$R_{(P)} = R'_{(P)} + \frac{1}{3} Di_{(P)} I_{(P)} = B_{(P)} n_{(P)} + C_{(P)}\left(n^2_{(P)} - \frac{1}{3} I_{(P)}\right) + \frac{1}{3} Di_{(P)} I_{(P)} \tag{10}$$

$C_{(P)}$ and $g_{(P)}$ is obtained from the following equations:

$$C_{(P)} = 3.5 \times \frac{(1 - C_P)}{C_p} \times g_{(P)} \tag{11}$$

$$g_{(P)} = \frac{2C_P}{5Cos3\theta_{(P)}} \tag{12}$$

The plane dilatiancy is determined by the following relation:

$$Di_{(P)} = A_{d(P)}\left(\alpha^d_{\theta(P)} - \alpha_{(P)}\right) : n_{(P)} \tag{13}$$

The dilatancy surface is defined as follows:

$$\alpha^d_{\theta(P)} = 0.8 \times \left[g_{(P)} \times M_P \times exp\left(n^d_P \times \psi_{(P)}\right)\right] n_{(P)} \tag{14}$$

The cyclic loading parameter is defined as the following relation:

$$\begin{aligned} CLP_{(P)} = {} & \left(3 \times G_{(P)} n_{(P)} : de_{(P)} - n_{(P)} : r_{(P)} d\varepsilon_{V(P)} \times K_{(P)}\right) / (K_{P(P)} + \\ & 2G_{(P)}\left(B_{(P)} + C_{(P)} trn^3_{(P)}\right) - K_{(P)} Di_{(P)} n_{(P)} : r_{(P)}) \end{aligned} \tag{15}$$

Whereas, the elastic deviatoric strain is determined by the following equation:

$$de^e_{(P)} = ds_{(P)} / \left(2G_{(P)}\right) \tag{16}$$

The framework plastic coefficient is calculated as follows:

$$K_{P(P)} = 0.8 \times \sigma_{n(P)} \times h_{(P)}\left(\alpha^b_{\theta(P)} - \alpha_{(P)}\right) : n_{(P)} \tag{17}$$

2.2 Equivalent cyclic loading

Considering earthquake acceleration record, Fourier spectrum, and the equivalent harmonic load of ten important earthquakes, according to the number of equivalent cycles offered for different magnitudes, the highest equivalent cycle obtained in each range is selected as the number of cycles, equivalent to its characteristic. Frequency content is so effective on obtained equivalent cyclic load and consequently, number of equivalent cycles determines by considering Fourier amplitude. According to the Fourier spectrum of the selected earthquake recordings, it was observed that high duration with closed frequency content causes fewer equivalent cycles than low duration with open frequency content. Equivalent cyclic load specifications of earthquakes with different range of magnitude, fore earthquake with magnitude of 6-6.5, and N considered equal to 0.45 and 10 respectively, and for earthquake with magnitude of 6.5-7, C_{eq} and N considered equal to 0.65 and 15 orderly, and finally fore magnitude of 7-8, C_{eq} considered equal to 0.75 and chosen N is 20. The characteristics of earthquake records of Chichi, Tabas, Kocaeli, Duzce, Northridge, Loma Prieta, Kobe, Imperial Valley, Palm Spring and Whittier used development of the model for purpose of progressive failure occurrence evaluation due to seismic excitation.

2.3 Earth dam modeling

Roudbar-Lorestan earth dam is located at 32.9032° N, 49.6833° E, in western Iran. This earth dam is located on the Roudbar River, a tributary of the East Dez River, about 511 km south of Aligudarz city in Lorestan province and the Zagros Mountain. Some technical specifications of the ECRD dam body are normal water level of 1756 m, and dam crest level of 1766 m above sea level, crest length of 185 m, crest width of 15 m, earth dam height of 153 meters, tunnel overflow, average annual flow of 30.2 cubic meters per second, maximum monthly flow of 250.5 cubic meters per second and minimum monthly flow of 4.1 cubic meters per second. Zones used for the analysis of Roudbar-Lorestan earth dam based on 16 layer construction modeling are shown in Figure 1.

The parameters of the materials of the earth dam are given in Table 1. 8-point brick elements are used for analysis. The structure has 570 elements and 1260 nodes. It is assumed that the earth dam foundation is solid, so the nodes on the base are considered to be fixed.

3. Results

Based on mathematical relations mentioned and material properties of the earth dam and boundary conditions and finite element method relations and standard brick element used and layers of construction considered, and equivalent cyclic loading of earthquake spectrums, the Multi-Laminate constants used in the evaluation of progressive failure is 110 for G_0^p, 0.4 for v_P, 0.65 for M_P, 0.85 for c_P, 0.02 for λ_{CP} 1.05 for e_{0P}, 0.78 for ξ_P, 0.03 for m_P, 4 for h_{0P}, 0.9 for C_{hP}, 1.1 for n_P^d, 0.5 for A_{0P}, and 3.5 for n_P^d. Using the failure point coordinates and prediction of next failure point by the framework, progressive failure evaluated in full reservoir state of the dam. Progressive failure, due to seismic excitation by earthquake with magnitude of 7 to 8,and considering 5, 10, 15 and 20 as N, illustrated in Figures 2 to 5.

4. Discussion

In high-magnitude earthquakes, the exciting frequency content had high amplitude over an extensive rate of frequencies. However, the higher the energy level, the higher the number of cycles equivalent to an earthquake, and depending on the prevailing period of the studied soil barrier, it will be able to create larger deformations. In the range of plastic strains, the number of cycles affects the decrease and increase of

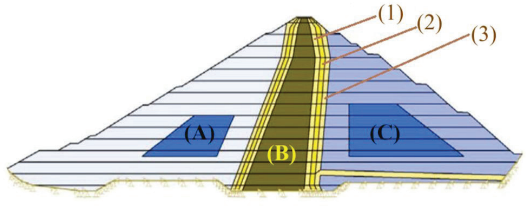

Figure 1. Construction layers and Zones of the earth dam.

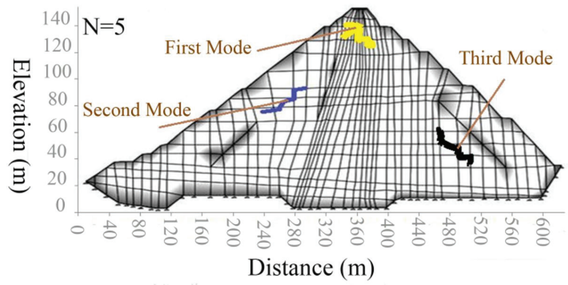

Figure 2. First step of progressive failure.

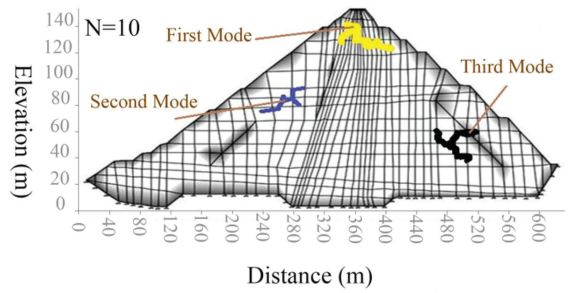

Figure 3. Second step of progressive failure.

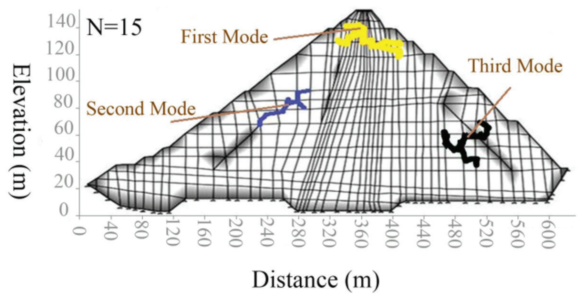

Figure 4. Third step of progressive failure.

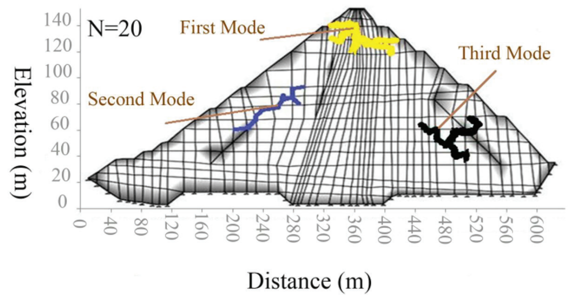

Figure 5. Fourth step of progressive failure.

Table 1. Parameters of Roudbar-Lorestan earth dam materials.

Material Description of Zones	v	E	γ_{dry}	γ_{wet}	γ_{sat}	C'	$\varnothing'$	Hydraulic Conductivity
		kPa	kN/m^3	kN/m^3	kN/m^3	kPa	(°)	(cm/sec)
Upstream- (A)	0.25	70	21.5	22.5	23.5	0	45	1.0×10^{-1}
Impervious Core- (B)	0.35	35	21.5	23.1	23.4	50	25	1.0×10^{-6}
Downstream Rock fill-(C)	0.25	70	21.0	22.0	23.0	0	45	1.0×10^{-1}
Fine Filter-(1)	0.33	70	19.0	20.0	21.9	0	37	5.0×10^{-4}
Drainage Transition-(2)	0.25	70	21.0	22.0	23.2	0	45	1.0
Coarse Filter-(3)	0.30	70	19.5	20.5	22.2	0	39	5.0×10^{-2}
Random Rock fill	0.25	50	20.5	21.5	22.9	0	42	1.0×10^{-2}

plastic modules and as the number of cycles increases, their rate of change will also increases. According to the Fourier transform of selected earthquake records, it was observed that the number of harmonic load cycles equivalent to earthquake records depends on the frequency content and the time of its continuation. High continuity time with closed frequency content causes lower number of equivalent cycles compared with low duration mode with open frequency content.

The acceleration coefficients and the number of equivalent cycles are 0.45, 10, plus 0.65, 15, which are respectively compliant to the earthquake Magnitude at 6-6.5 and 6.5-7 on (the Richter scales). Furthermore, the number of cycles compliant to earthquakes Magnitude at 7-8 (Richter scales) is 20 and its acceleration coefficient is 0.75 respectively. In the study of progressive failure, it is found that among the three main modes of failure that are considered upstream, downstream, and the crest of the earth dam, the first mode is related to the crest of earth dams. Progressive failure at Roudbar-Lorestan earth dam in earthquakes with magnitudes of 6 to 6.5 and also 6.5 to 7 Richter, does not leading to the formation of the failure surface. However, in earthquakes with a magnitude of 7 to 8 Richter, with increasing step-by-step harmonic load cycle, wedge rupture is formed in the crest of the dam, and according to the results of numerical modeling, the rupture is more likely due to the progress of cracks in the dam crest.

5. Conclusion

Achieving a reliable numerical method to evaluate the progressive failure of earth dams due to seismic excitation has always been a challenging target for geotechnical engineers. For solving this problem, Conversion of seismic spectra to equivalent harmonic loads and their application to the desired earth dam and evaluation the surface of rupture created and the consequent progressive failure is so considerable. The Multi-Laminate framework basis is the calculating the numerical relationship between micro-scale behaviors and engineering mechanical properties in constitutive equations. So, the framework was chosen because of its high accuracy and calibrated by the most reliable previous numerical and experimental researches. By considering 10 main historical earthquakes in the world, and their equivalent harmonic loading and the related factors, the purpose of the research was implemented.

Finite Element Method Considering directional cosines and weight coefficient of 17 planes and constant parameters related to elasticity, plastic modulus, critical state line and yield surface in each plane led to the correct diagnosis of progressive failure. A magnitude 7 earthquake struck on November 12, 2017 at 18:18 UTC, in Ezgeleh, Iran. As a result of this earthquake, Roudbar-Lorestan earth dam was also damaged, due to which the failure surface was propagated resulting in the progressive failure, with a behavior similar to the 3 main modes of damage predicted in full reservoir state of the dam in this paper. Although Ezgeleh earthquake record is not mentioned in 10 historical earthquakes of this study, it is worth mentioning, the progressive failure caused by this earthquake at 7.3 Magnitude showed a failure compatible to what the numerical analysis predicted in Figure 5, and the critical major rupture occurred on the crest of the dam considering that the rupture was 140 m high from the foundation and the movement was towards downstream. In 2 other failure modes, the behavior of the dam was similar to the behavior, predicted by numerical modeling through a Multi-Laminate framework. The numerical method used in this research can be used as a remarkable method for rapid and reliable evaluation to detect progressive failure due to seismic excitation in future geotechnical researches.

Declaration of interest

The authors have no conflicts of interest to declare. All co-authors have observed and affirmed the contents of the paper and there is no financial interest to report. We assure that the paper is original and is not under review at any other Journal.

Author's contributions

Hamzeh Rahimi Dadgar: Conceptualization, Data Curation, Methodology, Validation. Mohamad Ali Arjomand: Supervision. Ali Arefnia: Project Administration.

References

Bernander, S., & Olofsson, I. (1981). On the formation of progressive failure in slopes. In *Proceedings of the 10th International Conference of Soil Mechanics and Foundation Engineering* (pp. 357-362). Stockholm: Balkema.

Biondi, P., Manfredini, F., Martinetti, S., Rickbackhi, R., & Riccioni, R. (1976). Limit load of a foundation in a strain-softening soil. In *Proceedings of the International Conference on Numerical Methods in Geomechanics* (pp. 591-596). Blacksburg: ASCE.

Bishop, A.W. (1971). The influence of progressive failure on the choice of the method of stability analysis. *Geotechnique*, 21(2), 168-172. https://doi.org/10.1680/geot.1971.21.2.168.

Dafalias, Y.F. (1986). Bounding surface plasticity. I: mathematical foundation and hypoplasticity. *Journal of Engineering Mechanics*, 112(9), 966-987. https://doi.org/10.1061/(ASCE)0733-9399(1986)112:9(966)

Dafalias, Y.F., & Manzari, M.T. (2004). Simple plasticity model accounting for fabric changes effect. *Journal of Engineering Mechanics*, 130(6), 622-634. http://dx.doi.org/10.1061/(ASCE)0733-9399(2004)130:6(622).

Dashti, H., Sadrnejad, S. A., & Ganjian, N. (2019). A novel semi-micro multilaminate elasto-plastic model for the liquefaction of sand. *Soil Dynamics and Earthquake Engineering*, 124, 121-135. https://doi.org/10.1016/j.soildyn.2019.05.031.

Dashti, H., Sadrnejad, S.A., & Ganjian, N. (2017). Modification of a constitutive model in the framework of a multilaminate method for post-liquefaction sand. *Latin American Journal of Solids and Structures*, 14(8), 1569-1593. http://dx.doi.org/10.1590/1679-78253841.

Halyan, M. (2001). Fully coupled earthquake response analysis of earth dams using a critical state sand model. *International Journal of Seismic Design*, 1(3), 23-31.

La Rochelle, P. (1960). *The short term stability of slopes in London Clay*. University of London.

Manzari, M.T., & Dafalias, Y.F. (1997). A critical state two-surface plasticity model for sands. *Geotechnique*, 47(2), 255-272. http://dx.doi.org/10.1680/geot.1997.47.2.255.

Palmer, A.C., & Rice, J.R. (1973). The growth of slip surfaces in the progressive failure of overconsolidated clays. *Royal Society of London*, 332(1591), 527-548. https://doi.org/10.1098/rspa.1973.0040.

Peck, R.B. (1967). Stability of natural slopes. *Journal of the Soil Mechanics and Foundations Division*, 93(4), 403-417.

Prévost, J.H., & Höeg, K. (1975). Soil mechanics and plasticity analysis of strain softening. *Geotechnique*, 25(2), 279-297. http://dx.doi.org/10.1680/geot.1975.25.2.279.

Rahimi Dadgar, H., Arjomand, M.A., & Arefnia, A. (2019a). Crack Detection in Earth Dams upon a Multiline-Multilaminate Model. *IACSIT International Journal of Engineering and Technology*, 11(3), 445-455. http://dx.doi.org/10.21817/ijet/2019/v11i3/191103030.

Rahimi Dadgar, H., Arjomand, M.A., & Arefnia, A. (2019b). Numerical analysis of cyclic loading effect on progressive failure in earth dams upon a multiline-multilaminate model. *IACSIT International Journal of Engineering and Technology*, 11(3), 492-504. http://dx.doi.org/10.21817/ijet/2019/v11i3/191103038.

Rowe, P.W. (1969). Progressive failure and strength of a sand mass. In *Proceedings of the 7th international Conference of Soil Mechanics and Soil Foundations Engineering* (pp. 341-349). Mexico: ISSMGE.

Sadrnejad, S.A., & Labibzadeh, M. (2006). A continuum/discontinuum micro plane damage model for concrete. *International Journal of Civil Engineering*, 4(4), 296-313.

Seed, H.B., & Bruce, R. (1976). Stabilization of potentially liquefiable sand deposit using Gravel Drain System. *Earthquake Engineering Research Journal*, 2(4), 104-111.

Taiebat, M., Jeremić, B., Dafalias, Y.F., Kaynia, A.M., & Cheng, Z. (2010). Propagation of seismic waves through liquefied soils. *Soil Dynamics and Earthquake Engineering*, 30(4), 236-257. http://dx.doi.org/10.1016/j.soildyn.2009.11.003.

Wang, Z., Dafalias, Y.F., & Shen, C. (1990). Bounding surface hypoplasticity Model for Sand. *Journal of Engineering Mechanics*, 116(5), 983-1001. http://dx.doi.org/10.1061/(asce)0733-9399(1990)116:5(983).

List of Symbols and Acronyms

$A_{d(P)}$: Dilatancy Constant of the framework

C' : Cohesion Parameter

C_{eq} : Equivalent Acceleration Coefficient

$CLP_{(P)}$: Cyclic loading Plastic coefficient

$Cog_{(P)}$: Cone geometry in the deviatoric stress space of the plane

$Dev_{(P)}$: Deviatoric stress tensor in the plane

$Di_{(P)}$: Dilation parameter for the plane

$de^{e}_{(P)}$: Elastic deviatoric strain

E: Elasticity Modulus

ECRD: Earth Core rockfill Dam

e: Void ratio

$e_{c(P)}$: Critical void ratio

$G_{(P)}$: Elastic shear modulus

G_0^P, v_P : Model Constants in plane related to elasticity

$g_{(P)}$: Interpolation function for stress path

h_{0P}, C_{hP}, n_P^b: Model Constants in plane related to plastic modulus

$K_{(P)}$: Elastic bulk modulus

$K_{P(P)}$: Framework plastic coefficient

$L_{(P)}$: Yield surface gradient in space

$M_P, C_P, \lambda_{CP}, e_{0P}, \xi_P$: Model Constants in plane related to critical state

m_P : Model Constant in plane related to yield surface

N: Number of Equivalent Cycles

$S_{(P)}$: Deviatoric stress parameter

$n_{(P)}$: Tensor perpendicular to the yield surface

P_{atm} : Atmospheric pressure

R_P : Direction vector

$R'_{(P)}$: Deviatoric part of R_P

$r_{(P)}$: Stress ratio tensor in the plane

$\alpha_{(P)}$: Deviatoric back stress ratio tensor

$\alpha^d_{\theta(P)}$: Dilatancy surface

γ_{dry} : Dry unit weight

γ_{wet} : Wet unit weight

γ_{sat} : Saturated unit weight

θ : Angle of Orientation

v : Poisson's ratio

$\sigma_{n(p)}$: Normal stress in plane

$\varnothing'$: Drained angle of internal friction

ψ_p : Dilatancy parameter of the plane

Soils and Rocks
An International Journal of Geotechnical and Geoenvironmental Engineering
www.soilsandrocks.com
ISSN 1980-9743
ISSN-e 2675-5475

Stiffness, compressibility, and hydraulic conductivity of compacted soil mixtures submitted to acidic percolation

Franciele Noll da Silva[1], Pedro Domingos Marques Prietto[1#], Márcio Felipe Floss[1]

Technical Note

Keywords
Contaminant barriers with and without cement
Long-term hydraulic conductivity
Bender element test

Abstract

The inadequate disposal of hazardous solid waste has become a potential issue, mainly because of the impacts on the environment and human health. This occurs mainly through the contamination of subsurface soil and groundwater by leachates, which are often of the acidic constitution. To prevent such situations, the study of more efficient waste containment techniques has become opportune. In this way, this work was aimed to investigate the mechanical and hydraulic behavior of compacted clayey soil, with and without the addition of Portland cement (0 and 2%), submitted to the action of a sulfuric acid solution (2% volume concentration) and to a constant static vertical load (280 kN/m^2), aiming at its prospective application as containment barrier. The experimental program comprised a few tests performed in an instrumented rigid-wall permeameter, during which the variations in hydraulic conductivity, shear modulus, and settlements were measured. The results showed that the hydraulic conductivity increased with cement addition when only water was percolated. During the acidic percolation, however, a reduction was observed only for the cemented soil. The acidic attack caused, almost instantaneously, an increase in the settlement rate and a reduction in stiffness, although a trend of stabilization was observed afterward.

1. Introduction

Industrial landfills and tailing dams generate leachates, which potentially impact the environment, sometimes due to their strong acidic nature and the presence of toxic inorganic substances, as in the leaching of corrosive wastes from metallurgical industrial processes and the acid mine drainage from metal or coal mining operations.

The construction of engineered waste disposal systems is one of the ways to avoid the problem. Particularly, impervious barrier systems have been used to minimize the migration of contaminants into the soil and the groundwater (e.g., Daniel, 1993; Rowe et al., 1995).

However, an aggressive contaminant can modify the physical-chemical characteristics of barriers, affecting their mechanical and hydraulic behavior (Knop et al., 2008; Hamoi & Srasra, 2012; Gratchev & Towhata, 2013, 2016; Bakhshipour et al., 2016, 2017; Agbenyeku et al., 2016; Chavali & Ponnapureddy, 2018a, b; Chavali et al., 2017; Lui & Gao, 2018; Ferrazzo et al., 2020; Korf et al., 2020). Strong acids can dissolve materials in the soil and form preferential flow channels (Daniel, 1993). Also, the vertical load from the waste deposited above the barrier might favor the migration of contaminants due to structural changes.

In recent years, efforts have been made to develop optimized barriers to simultaneously provide low permeability and structural durability. In this sense, physical-chemical stabilization through the addition of Portland cement or other cementing agents has been studied (Morandini & Leite, 2015; Gueddouda et al., 2016), given its potential to preserve the barrier structure, without compromising the hydraulic conductivity (Knop et al., 2008). Therefore, the generation of useful knowledge for the design of more efficient and durable soil barriers is necessary, minimizing their impacts and guaranteeing their applicability as a waterproofing system.

In this context, the objective of the present study was to investigate the hydraulic and mechanical behavior of a compacted clayey soil, with and without the addition of Portland cement, subjected to an acidic solution percolation.

2. Materials and methods

The experimental program included permeability tests under constant load lasting more than 30 days, in which saturated specimens were percolated by distilled water followed by a sulfuric acid solution. During the tests, the stiffness and the settlements were continuously measured.

2.1 Experimental variables

The variables investigated were the type of percolating liquid (water and sulfuric acid solution) and the cement content (0 and 2%). Other variables were kept fixed: hydraulic gradient; static vertical load; curing period; water content and

#Corresponding author. E-mail address: pdmp@upf.br
[1]Universidade de Passo Fundo, Programa de Pós-graduação em Engenharia Civil e Ambiental, Passo Fundo, RS, Brasil.

Submitted on February 24, 2020; Final Acceptance on December 30, 2020; Discussion open until May 31, 2021.

DOI: https://doi.org/10.28927/SR.2021.047720

specific weight of the specimens. The response variables were the hydraulic conductivity coefficient, the shear deformation modulus (stiffness), and the settlement (compressibility).

2.2 Soil

The residual basalt clayey soil comes from the Experimental Geotechnical Field of the University of Passo Fundo, located in Passo Fundo - RS. The sample was collected at a depth of 1.2 meters and is classified (Streck et al., 2008), as a humic dystrophic red latosol. This soil is predominant in the north of Rio Grande do Sul and is suitable for use as a compacted barrier. It is 68% clay, 5% silt, and 27% sand, presenting a plasticity index of 11% (liquid limit of 53 and plasticity limit of 42%), specific gravity of 26.7 kN/m^3, and organic matter content lesser than 0.8%.

2.3 Cement and contaminant solution

Portland cement CP-V was used to mold the cemented specimens. Its average composition comprises 0-5% of mineral additions and 95-100% of clinker, with a nominal compression strength of 40 MPa at 28 days.

For the acidic percolation, a solution of 2% by volume of sulfuric acid (H_2SO_4) (Merck® 95-97%), diluted in distilled water was prepared. The average pH of the solution was 1.31.

2.4 Testing apparatus

The testing apparatus was developed by Santos (2012) at the Environmental Geotechnical Laboratory of the University of Passo Fundo. It has six independent test cells, in which the application of static vertical loads is made, independently, through a system of pneumatic cylinders powered by an air compressor and controlled by pressure regulators and transducers connected to a data acquisition system. The vertical displacements are measured by LVDT transducers. Each of the six cells functions as a downward-flow rigid wall permeameter. In the present work, one of the cells was adapted with piezoceramic bender elements, which allowed to continuously evaluate the stiffness of the tested specimens.

The use of bender elements is one of the most popular non-destructive techniques for the determination of maximum shear modulus (G_{max}) in soils at the small strain range (Viggiani & Atkinson, 1995; Lee & Santamarina, 2005).

The bender elements were adapted in such a way that the free portions of the transducers (approx. 7mm) are completely inserted into the test specimen at its ends (top and base). The G_{max} value can be measured at any stage of the test by applying an electrical signal to one of the transducers (transmitter), which emits a mechanical shear wave (S wave) through the specimen, and by determining the time of arrival of the wave at the other end of the specimen, using the electrical signal produced by the second transducer (receiver).

2.5 Molding of specimens

The specimens were compacted in three layers, directly on the cell pedestal, in which the receiving bender element was adapted. The specimens, with 6 cm in height and 7 cm in diameter, were molded with a dry specific weight of 14.5 KN/m^3 and water content of 26%, defined from the compaction curves of the soil. After compaction, it was necessary to carve a groove at the top of the specimen to insert the transmitting bender element. For the transducer to be in complete contact with the specimen material, a filling paste was used.

To ensure a uniform distribution of the percolating liquid and prevent preferential paths, separating filter papers were placed at the top and bottom interfaces between the specimen and the perforated metal plates.

After molding, the test cell was filled with distilled water, and the specimen was subjected to a 48-hour resting period. The cell was then coupled to the equipment for the application of the vertical static load and the beginning of the saturation/percolation phase. The vertical load applied was 280 kPa, to simulate a constant load over a hypothetical bottom liner in a waste disposal site.

2.6 Saturation, percolation, and hydraulic conductivity determination

The saturation was started by percolating distilled water for approximately 5 days. The minimum volume percolated was 6 void volumes, and the hydraulic gradient used was 33, defined from preliminary tests. The total curing period for the samples with cement addition was approximately 7 days (48 hours at rest plus the time needed for the percolation of distilled water). The degree of saturation obtained was greater than 95%.

After the percolation with water, the acidic solution percolation was started, lasting for approximately 30 days. The variation of the hydraulic conductivity coefficient (k) was determined by the direct application of Darcy's Law and from the continuous monitoring of the percolated volumes.

2.7 Maximum shear modulus determination

The maximum shear module ($G_{máx}$) is obtained by Equation 1 (Viggiani & Atkinson, 1995). The speed of the shear wave (sinusoidal with frequencies from 2 to 10 kHz) is obtained from the division of the distance traveled by the wave between the bender elements, corrected by the settlement value) by the propagation time, which was determined by the procedure proposed by Lee & Santamarina (2005).

$$G_{máx} = \rho . V_s^2 \tag{1}$$

in which:
V_s is the shear wave velocity; and
ρ is the apparent specific mass of the soil.

3. Results and discussion

Figure 1 shows the variation in hydraulic conductivity and the evolution of settlements for the specimens tested with and without cement. The arrows indicate the start of the acidic percolation.

Before the acidic percolation phase, it is observed that the addition of cement resulted in an increase in hydraulic

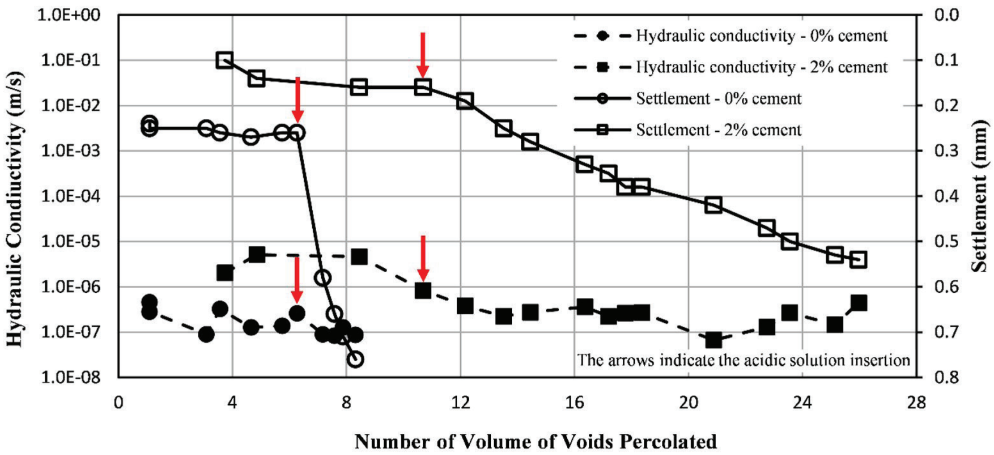

Figure 1. Variation of hydraulic conductivity and settlement.

conductivity of approximately one order of magnitude. It is also observed that the specimens did not show significant settlements under the action of the vertical load. In fact, the addition of Portland cement can increase the hydraulic conductivity of clay soils, due to hydration and solubilization reactions (Sharma & Reddy, 2004; Knop et al., 2008). In addition, it could be attributed to the physical-chemical interaction between the clay particles and the calcium present in the Portland cement solution, which is expected to induce flocculation due to the reduction in the double layer thickness of the clay particles (e.g., Mitchell & Soga, 2005).

Korf et al. (2016), for the same soil of the present study, also observed an initial increase in permeability followed by a reduction after the percolation with a solution of nitric acid.

For the soil without cement, the hydraulic conductivity was apparently not affected by acidic percolation, being around 10^{-7}m/s at the end of the test. For the soil with 2% cement, there is a reduction in hydraulic conductivity, showing the effect of the acidic percolation. The hydraulic conductivity did not show significant variations throughout the test but in the end, it was between 10^{-6} and 10^{-7} m/s, above the value obtained for the soil without cement. These values are high for use in containment barriers since the minimum recommended value is 10^{-9} m/s (Daniel, 1993).

The analysis indicates a remarkable effect of the acid solution insertion. There is a sudden increase in the rate of settlement under the constant load of 280 kN/m^2, characterizing a collapse of the material structure. However, the evolution of settlements should result in a reduction in hydraulic conductivity. As described in the preceding paragraph, this reduction was observed only for the cemented soil.

The observed behavior is possibly related to the different interaction mechanisms between the soil structure, including the cementing bonds and the acid solution, with antagonistic effects on hydraulic conductivity. On the one hand, the reduction in the void ratio, due to the collapse of soil structure. On the other hand, the probable formation of preferential paths at the end of the process (after 21 volumes of voids percolated). The behavior observed would, therefore, be the sum of these antagonistic effects. Timbola (2014), who studied the hydraulic response of the same material, reported a very similar pattern of behavior.

Finally, it appears that the settlement rate was higher for the soil without cementation, indicating that the acidic attack to the soil structure occurred with greater intensity and that the presence of cementation may have helped, at least partially, in preserving soil structure during acidic percolation.

Figure 2 shows the results of the stiffness measurements during the percolation tests with distilled water and sulfuric acid solution. The arrows indicate the insertion of the sulfuric acid solution.

The soil with 2% cement showed values of shear modulus in the range of 60 to 120 MPa, while the soil without cement presented values from 18 to 46 MPa, demonstrating the effect of cement addition on the stiffness of the compacted soil. These ranges are similar to the modules (20 to 251 MPa) obtained for similar clayey materials (e.g., Vardanega & Bolton, 2013).

With the insertion of the acid solution, there was an immediate increase followed by a drop in stiffness, more clearly observed for the cemented soil. However, when comparing the responses before and after the acidic solution insertion, for both uncemented and cemented specimens, the relative impact of the acidic percolation is greater for the soil without cement, which presented a reduction in shear modulus of about 34%, comparing the values at the start and at the end of the test. For the cemented soil, the observed reduction was of about 10%.

The most plausible hypothesis is that the variation in stiffness during acidic percolation results from the superposition of different mechanisms, often with antagonistic effects: the gradual degradation of cementation, the reduction of the average void ratio, and the formation of localized zones of higher hydraulic conductivity.

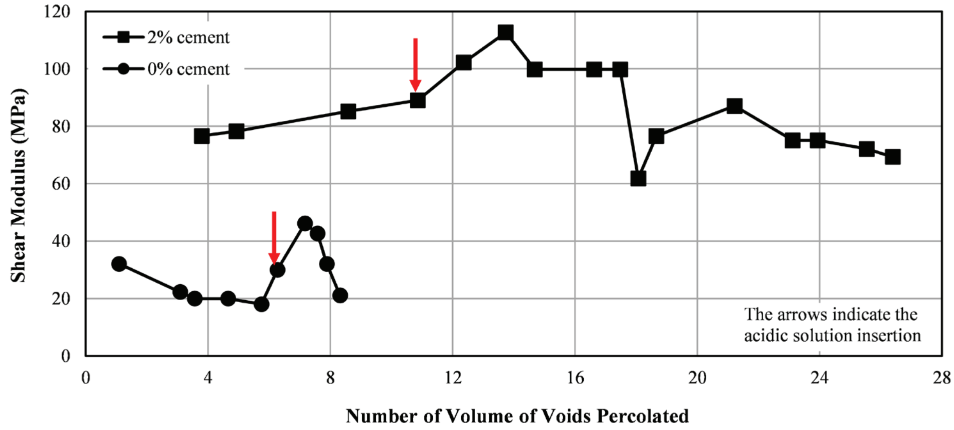

Figure 2. Variation of shear modulus.

In fact, one of the possible outcomes of strong acid percolation is the dissolution of the cementing compounds formed among particles, causing loss of rigidity.

Silva et al. (2009) studied artificially cemented soils and reported a degradation in stiffness with the increase of the confinement stress. Consoli et al. (2000) investigated the usual procedure for obtaining the stiffness of cemented soils in conventional triaxial tests, focusing on the influence of the confining stresses before and after cementation formation. The authors found that the degradation of cementation occurred only in specimens cured without confinement, whereas in samples cured under tension, there was an increase in stiffness with the confining stress.

In the present study, however, cementation degradation is not related to changes in the state of stresses but results from the physical-chemical interaction between the acidic solution and the soil compounds.

The cementation degradation, however, does not explain the immediate increase in stiffness after the insertion of the acidic solution, nor the reduction in stiffness observed for the soil without cement (Figure 2). As for the immediate increase in stiffness, this can be explained by the collapse of the soil structure and reduction of the void's ratio, as indicated by the evolution of settlements in Figure 1. On the other hand, the reduction in stiffness of the non-cemented soil observed during acidic percolation can be credited to structural changes such as the formation of localized areas of higher porosity (preferential paths).

4. Conclusions

The present work evaluated the hydraulic and mechanical behavior of a compacted clayey soil, with and without Portland cement, when percolated with distilled water and sulfuric acid solution, aiming at its use in impermeable barriers to contain hazardous industrial and mining solid waste.

The analysis of the results allowed to infer that the acidic percolation affected more the hydraulic conductivity of the cemented soil, from the occurrence of two antagonistic mechanisms: the collapse of soil structure, evidenced by the sharp increase in the settlement rate, which reduces hydraulic conductivity, and the possible formation of preferential percolation paths, with the opposite effect.

Regarding stiffness, the results showed an immediate increase and a subsequent reduction in the shear modulus with the acidic percolation, again indicating the occurrence of different mechanisms: the gradual degradation of cementation, the reduction of the average void ratio, and the possible formation of preferential percolation paths.

As a final remark, it is expected that the results reported herein contribute to establishing patterns for geotechnical materials under acidic percolation that can serve as a basis for the design of bottom barriers used in landfills and tailing dams, providing experimental evidence that allows the development of prediction models.

Acknowledgements

This study was financed in part by the Coordenação de Aperfeiçoamento de Pessoal de Nível Superior - Brazil (CAPES) - Finance Code 001. The authors are also grateful for the financial support of CNPq (Grants 312756/2017-8 and 438328/2018-3).

Declaration of interest

The authors declare that they have NO affiliations with or involvement in any organization or entity with any financial interest or non-financial interest (such as personal or professional relationships, knowledge, or beliefs) in the subject matter or materials discussed in this manuscript.

Author's contributions

Franciele Noll da Silva: conceptualization, investigation, writing of the original draft. Pedro Domingos Marques Prietto: project administration, supervision, writing, review and editing. Márcio Felipe Floss: supervision, writing, review and editing.

References

Agbenyeku, E.E., Muzenda, E., & Msibi, M.I. (2016). Chemical alterations in three clayey soils from percolation and interaction with acid mine drainage (AMD). *South African Journal of Chemical Engineering*, 21(C), 28-36. http://dx.doi.org/10.1016/j.sajce.2016.04.003.

Bakhshipour, Z., Asadi, A., Huat, B.B., Sridharan, A., & Kawasaki, S. (2016). Effect of acid rain on geotechnical properties of residual soils. *Soil and Foundation*, 56(6), 1008-1019. http://dx.doi.org/10.1016/j.sandf.2016.11.006.

Bakhshipour, Z., Asadi, A., Sridharan, A., & Huat, B. (2017). Acid rain intrusion effects on the compressibility behaviour of residual soils. *Environmental Geotechnics*, 6(7), 1-38. http://dx.doi.org/10.1680/jenge.15.00081.

Chavali, R.V.P., & Ponnapureddy, H.P.R. (2018a). Swelling and compressibility characteristics of bentonite and kaolin clay subjected to inorganic acid contamination. *International Journal of Geotechnical Engineering*, 12(5), 500-506. http://dx.doi.org/10.1080/19386362.2017.1299418.

Chavali, R.V.P., & Ponnapureddy, H.P.R. (2018b). Volume change behavior of phosphogypsum treated clayey soils contaminated with inorganic acids: a micro level study. *Journal of Environmental Engineering and Landscape Management*, 26(1), 8-18. http://dx.doi.org/10.3846/16486897.2017.1331168.

Chavali, R.V.P., Ponnapureddy, H.P.R., Murthya, V.R., & Sivapullaiahb, P.V. (2017). Swelling characteristics of soils subjected to acid contamination. *Soil and Foundation*, 58(1), 110-121. http://dx.doi.org/10.1016/j.sandf.2017.11.005.

Consoli, N.C., Rotta, G.V., & Prietto, P.D.M. (2000). The influence of curing under stress on the triaxial response of cemented soils. *Geotechnique*, 50(1), 99-105. http://dx.doi.org/10.1680/geot.2000.50.1.99.

Daniel, D.E. (1993). Clay liners. In D.E. Daniel (Ed.), *Geotechnical practice for waste disposal* (pp. 137-163). London: Chapman & Hall.

Ferrazzo, S.T., Timbola, R.S., Bragagnolo, L., Prestes, E., Korf, E.P., Prietto, P.D.M., & Ulsen, C. (2020). Effects of acidic attack on chemical, mineralogical, and morphological properties of geomaterials. *Environmental Science and Pollution Research International*, 27(2), 37718-37732. http://dx.doi.org/10.1007/s11356-020-09834-6.

Gratchev, I., & Towhata, I. (2013). Stress-strain characteristics of two natural soils subjected to long-term acidic contamination. *Soil and Foundation*, 53(3), 469-476. http://dx.doi.org/10.1016/j.sandf.2013.04.008.

Gratchev, I., & Towhata, I. (2016). Compressibility of soils containing kaolinite in acidic environments. *KSCE Journal of Civil Engineering*, 20(2), 623-630. http://dx.doi.org/10.1007/s12205-015-0141-6.

Gueddouda, M.K., Goual, I., Benabed, B., Taibi, S., & Aboubekr, N. (2016). Hydraulic properties of dune sand-bentonite mixtures of insulation barriers for hazardous waste facilities. *Journal of Rock Mechanics and Geotechnical Engineering*, 8(4), 541-550. http://dx.doi.org/10.1016/j.jrmge.2016.02.003.

Hamoi, N., & Srasra, E. (2012). Hydraulic conductivity study of compacted clay soils used as landfill liners for an acidic waste. *Waste Management*, 33(1), 60-66. http://dx.doi.org/10.1016/j.wasman.2012.08.012.

Knop, A., Vangulck, J., Heineck, K.S., & Consoli, N.C. (2008). Compacted artificially cemented soil-acid leachate contaminant interactions: breakthrough curves and transport parameters. *Journal of Hazardous Materials*, 155(1-2), 269-276. http://dx.doi.org/10.1016/j.jhazmat.2007.11.056.

Korf, E.P., Prietto, P.D.M., & Consoli, N.C. (2016). Hydraulic and diffusive behavior of a compacted cemented soil. *Soils and Rocks*, 39(3), 325-331.

Korf, E.P., Prietto, P.D.M., Silveira, A.A., Ulsen, C., Consoli, N.C., & Bragagnolo, L. (2020). Modifications in the chemical and mineralogical composition of compacted mature residual soil submitted to the percolation of acidic leachates. *Soils and Rocks*, 43(1), 159-167. http://dx.doi.org/10.28927/SR.431159.

Lee, J., & Santamarina, J.C. (2005). Bender elements: performance and signal interpretation. *Journal of Geotechnical and Geoenvironmental Engineering*, 131(9), 1063-1070. http://dx.doi.org/10.1061/(ASCE)1090-0241(2005)131:9(1063).

Lui, J., & Gao, Y. (2018) Effects of acid and base contamination on geotechnical properties of Shanghai remolded silty clay. In *Proceedings of the GeoShanghai International Conference* (Vol. 1, pp. 611-619), Singapore.

Mitchell, J.K., & Soga, K. (2005). *Fundamentals of soil behavior*. Hoboken: John Wiley & Sons.

Morandini, T.L.C., & Leite, A.L. (2015). Characterization and hydraulic conductivity of tropical soils and bentonite mixtures for CCL purposes. *Engineering Geology*, 196, 251-267. http://dx.doi.org/10.1016/j.enggeo.2015.07.011.

Rowe, R.K., Quigley, R.M., & Booker, J.R. (1995). *Clayey barrier systems for waste disposal facilities*. London: E&FN Spon.

Santos, V.C. (2012). *Development of a column apparatus for long-term hydraulic conductivity tests on compacted barriers* [M.Sc. Dissertation]. Univesity of Passo Fundo]. (in Portuguese). Retrieved in February 24, 2020, from https://secure.upf.br/pdf/2013ValterCaetanodosSantos.pdf

Sharma, H.D., & Reddy, K.R. (2004). *Geoenvironmental engineering: site remediation, waste containment, and emerging waste management technologies*. Hoboken: John Wiley & Sons.

Silva, S., Fonseca, A.V., & Consoli, N.C. (2009). Strength and stiffness properties of mixtures of granitic soil-cement. In *Proceedings of the 17th International Conference on Soil Mechanics and Geotechnical Engineering* (Vol. 1, pp. 312-315), Alexandria.

Streck, E.V., Kämpf, N., Dalmolin, R.S.D., Klamt, E., Nascimento, P.C., Schneider, P., Giasson, E., & Pinto, L.F.S. (2008). *Solos do Rio Grande do Sul*. Porto Alegre: EMATER/RS-ASCAR. (in Portuguese).

Timbola, R.S. (2014). *Hydraulic conductivity of compacted soil-cement mixtures submitted to the action of acidic leached in long-term tests* [M.Sc. Dissertation]. Univesity of Passo Fundo. (in Portuguese). Retrieved in February 24, 2020, from https://secure.upf.br/pdf/2014RafaelSouzaTimbola.pdf

Vardanega, P.J., & Bolton, M.D. (2013). Stiffness of clays and silts: normalizing shear modulus and shear strain. *Journal of Geotechnical and Geoenvironmental Engineering*, 139(9), 1575-1589. http://dx.doi.org/10.1061/(ASCE)GT.1943-5606.0000887.

Viggiani, G., & Atkinson, J.H. (1995). Interpretation of bender elements tests. *Geotechnique*, 47(4), 873-877. http://dx.doi.org/10.1680/geot.1995.45.1.149.

List of symbols

k = hydraulic conductivity of the porous media (distance/time)
Gmáx = maximum shear modulus
Vs = seismic wave propagation velocity
ρ = apparent specific mass of the soil

Case study

Soils and Rocks
An International Journal of Geotechnical and Geoenvironmental Engineering
www.soilsandrocks.com
ISSN 1980-9743
ISSN-e 2675-5475

Assessment of potential surface degradation resulting from erosion processes in environmentally protected area

Ana Patricia Nunes Bandeira[1#], Cícera Camila Alves Macedo[2], Gerbeson Sampaio Clarindo[1], Maria Gorethe de Sousa Lima[1], João Barbosa de Souza Neto[1]

Case Study

Keywords
Erodibility
Soil loss
Field tests on erosion
Geotechical investigaton
Inderbitzen test

Abstract

Erosion processes occur in several locations, causing impacts on the environment. This article analyzes the soil erodibility potential of the conservation unit of Timbaúbas municipal natural reserve, located in Juazeiro do Norte, in the southern mesoregion of Ceará, northeastern Brazil. It also addresses geotechnical characterization tests and field tests on erosion. In the field tests on erosion, huge volumes of soil loss were found caused by the action of rainfall and simulated surface flows. The results of the geotechical investigaton revealed silty sand soil, low values resistance parameters, has high erosion potential. The reduced rate of soil vegetation cover associated with the mechanical characteristics of the aggregate increases susceptibility to erosion processes, also intensified by anthropic intervention and construction of buildings on the site, without proper action to discipline the runoff. This work enables us to conclude that natural factors together with unsuifigure anthropic factors have been the causes of erosion of the conservation unit in question.

1. Introduction

Although erosion processes are considered natural phenomena, they are now a problem for environmental resources when soil loss rates exceed the natural levels of soil generation (Jorge & Guerra, 2013). In urban areas, one of the main problems related to the increased erosion processes is the possible destruction of community assets, resulting from geohazard events leading to necessary land use planning to prevent such problems (Camapum de Carvalho et al., 2006). The problem is even more severe since erosion processes are not restricted only to where erosion scars exist, but also to where materials are deposited, in some cases, for example, water bodies, possibly causing local siltation and pollution concentration.

Guerra & Hoffmann (2006) discuss studies in several Brazilian locations degraded by several surface erosion types (gullies), mainly caused by deforestation, lack of urban planning, absence of storm water drains and no drainage elements, or by poor design. According to Camapum de Carvalho et al. (2006), some places in Maranhão state evidence severe erosion phenomena, especially ravines in the Bacanga river basin (Coeduc, Batatã, Gapara, Itaqui, Maracanã, Posto, Sacavém, Torre and Vila Maranhão), aggravated by high urbanization rate and the physical, chemical and environmental characteristics of the basin. In the satellite towns of Ceilândia (DF) and Jardim Ingá (GO), by the end of the 1980s, erosion had destroyed towns and damaged roads.

Soil erosion depends on the active forces of rainfall and slope characteristics, and or by intrinsic factors linked to the soil and vegetation density (Bertoni & Lombardi Neto, 1999). Disordered growth and inappropriate land use are the prime aggravating factors of erosion, major capitals and several other locations in Northeast Brazil, as has been observed in Ceará's hinterland, where erosion processes occur in urban areas, roadsides and legally protected areas (Lafayette, 2006; Meira, 2008; Macedo, 2019). The purpose of this paper is to present a study of the potential soil erodibility of the Timbaúbas Municipal Nature Reserve in Juazeiro do Norte (CE), in support of the area's rehabilitation project.

2. Erodibility potential indicator parameters

Field and laboratory testing can be done in order to achieve erodibility potential indicator parameters. Geotechnical characterization testing (soil size analysis, liquid limit, plasticity limit, shear strength, permeability) and other more specific tests (e.g., slaking, crumb, Inderbitzen) could provide information on the hydraulic and mechanical behavior of the soil and, in turn, be directly related to the erodibility potential, making it easier to understand the erosion processes.

[#]Corresponding author. E-mail address: ana.bandeira@ufca.edu.br
[1]Universidade Federal do Cariri, Centro de Ciências e Tecnologia, Juazeiro do Norte, CE, Brasil
[2]Universidade Federal do Cariri, Centro de Ciências Agrárias e da Biodiversidade, Juazeiro do Norte, CE, Brasil

Submitted on June 16, 2020; Final Acceptance on December 22, 2020. Discussion open until: May 31, 2021.

DOI: https://doi.org/10.28927/SR.2021.052420

The finer particles (clay) are easily displaced and transported when the cohesive force is overcome. Larger particles (coarse sand, gravel) are more resistant to erosion and tend to accumulate on the surface, due to the relationship with the frictional force. Soils with high silt content generally have high erodibility (Llopis Trilho, 1999). Ramidan (2003) finds that the soils more resistant to erosion have 30%-35% clay in their composition, due to the cohesive nature of the clay and contributing to dispersion resistance.

In the opinion of Bender (1985) the erosion resistance and shear strength depend on the cohesive behavior of the soil. Bastos (1999) states that when the variation in cohesion (Δc) is more than 85%, obtained from a soil sample in natural moisture in relation to the value of the cohesion obtained in that same sample in the saturated condition, the soil may be considered erodible.

The slaking test allows us to observe the stability of an undisturbed soil sample, when immersed in distilled water, estimating the capacity of the water to disperse the soil. Bastos (1999) believes that soils that crumble completely in water are considered highly erodible. However, there is no direct relationship of intermediary and low levels of erodibility with this test.

The crumb test helps classify the reaction of a soil plot in relation to dispersion when immersed in water. The soil may be classified as dispersive (susceptible to erosion) or non-dispersive (possibly erodible or not). The standard ABNT (1996) determines four (4) degrees of dispersibility, as follows: Degree 1 - non-dispersive, where the clod may fracture or crumble, but there is no turbidity; Degree 2 - slightly dispersive, where signs of turbidity are seen in the water; Degree 3 - moderately dispersive, observing turbidity with colloidal particles; and Degree 4 - highly dispersive, with thick turbidity of colloidal particles.

Inderbitzen tests were performed on undisturbed test specimens in order to assess soil mass loss due to surface runoff. The test is performed on an articulated hydraulic ramp, which may have an adjustable slope, fitted with a central orifice in which a soil sample is enclosed (Nagel et al., 2009).

Through testing, quantified hydraulic shear stresses, using hydraulic parameters, can be related to soil loss (per unit area and time). A graph of this relationship can obtain an erodibility rate (K) representing a soil loss rate in g/cm^2/min/Pa. It is also possible to obtain a critical hydraulic shear stress (τ_{hcrit}), understood as the lowest hydraulic shear stress capable of producing decomposition (Bastos et al., 2017). Bastos (1999) proposes classification of soil erodibility, based on the erodibility rate (K) in g/cm^2/min/Pa, as follows - low erodibility for soils that have $K<1\text{x}10^{-3}$; medium erodibility for $1\text{x}10^{-3}<K<1\text{x}10^{-1}$, and high erodibility for $K>1\text{x}10^{-1}$.

Soil permeability is closely related to its erodibility potential. Water seepage is a problem in soils with low permeability, since the surface or subsurface runoff is greater, as is its erosion potential, due to the direction of particles dragged by the force of the water. On the other hand, highly permeable soils easily suffer leaching processes, losing nutrients to support the vegetation, important for protecting against erosion processes.

An erodibility study in pilot tests is designed to measure the surface runoff and amount of transported soil. It is possible to quantify the soil losses and onsite crumbling rate (Lafayette, 2006; Meira, 2008; Inácio et al., 2007). The relationship between rainfall intensity and soil loss is useful information for decision makers.

3. Characteristics of the investigated area

The subject of this paper is the area of Timbaúbas Municipal Nature Reserve, located in the municipality of Juazeiro do Norte (Figure 1). The municipality of Juazeiro

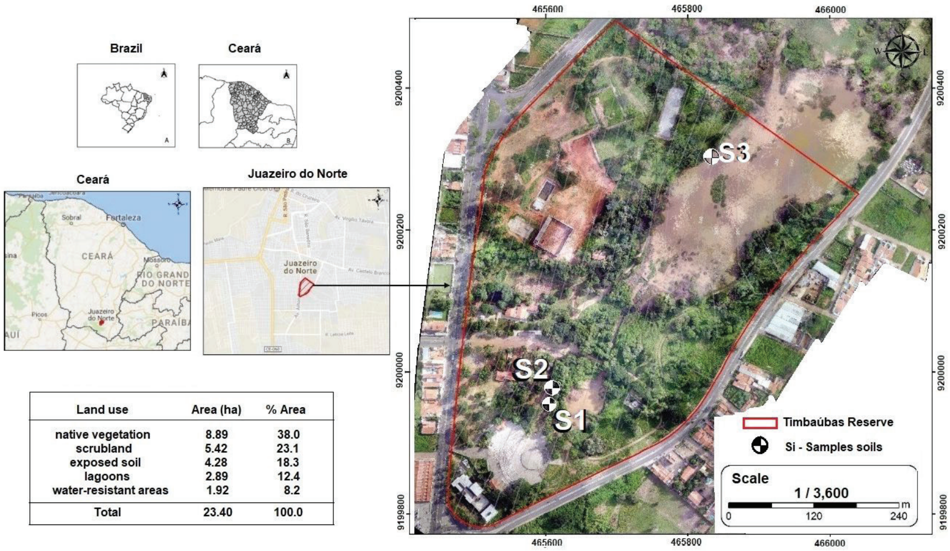

Land use	Area (ha)	% Area
native vegetation	8.89	38.0
scrubland	5.42	23.1
exposed soil	4.28	18.3
lagoons	2.89	12.4
water-resistant areas	1.92	8.2
Total	23.40	100.0

Figure 1. Location of the Timbaúbas municipal nature reserve. Sources: Macedo (2019), IBGE (2010), IPECE (2017).

do Norte, in turn, is located in the southern mesoregion of Ceará, northeastern Brazil, between the coordinates latitude (S) 7º12'47" and longitude (WGr) 39º18'55" covering an area of 248.8 km^2 with a population of 249,939 inhabitants (Ceará Research Institute on Economic Strategy-IPECE, 2017).

According Köppen & Geiger (1928), the region has a semiarid hot tropical climate, with 925 mm average annual precipitation. The annual average temperature varies between 24°C and 26°C. The wet season is January to May (FUNCEME, 2006).

Timbaúbas municipal natural reserve was created in 1997 in order to "ensure preservation and restoration of the margins of the Rivers Salgadinho and Timbaúbas" (Juazeiro do Norte, 1997). In 2017, the area was classified as a conservation unit and defined as an Integral Protection Area, in order to protect the water table comprising the Salgado river basin (Juazeiro do Norte, 2017). The reserve currently has a total area of 23.40 ha.

The area's predominant soils are alluvial neosols, consisting of coarse and fine sand, mostly quartz, thick well drained and with low natural fertility (FUNCEME, 2012). Costa et al. (2013) studied the hydrosedimentological parameters of the São José catchment area (location of study area) and prepared a GIS-based erosion-prone soil map using the Universal Soil Loss Equation (USLE). They found that the Timbaúbas Municipal Nature Reserve soils with medium to high erodibility potential predominate. This area has laminar erosion shown by exposed tree roots on the surface, and linear erosion in the form of furrows, ravines and gullies.

4. Materials and methods

4.1 Morphometric characterization and land occupation and use

The morphometric characterization of the microbasin in the study area was done using software QGIS v. 2.14, based on domain images of Google Earth and the Brazilian Institute of Geography and Statistics (IBGE), and an aerial survey using unmanned aerial vehicles (UAV). This work was designed to obtain the following parameters: area, perimeter, length of watercourses, compactness coefficient, shape coefficient, circularity and sinuosity index and drainage density; whose formulations were based in the studies by Villela & Mattos (1975), Cardoso et al. (2006) and Silva Neto et al. (2013). The aerial survey (May 2018) helped toward estimating the areas of vegetation, exposed soil and built up areas.

4.2 Methods for geotechnical characterization

4.2.1 Laboratory tests

For geotechnical characterization of the study area, soil mechanics laboratory tests were performed on three samples (Figure 1) collected from different points in the municipal reserve close to an area of severe erosion processes.

The tests were as follows:

a) Basic physical characterization tests: Soil grading analysis, by sieving and sedimentation (ABNT, 2016a); specific particle weight based on ABNT (2017) (soil particles passing through the 4.8 mm sieve – Determining the specific density); liquid limit (ABNT, 2016b); plasticity limit (ABNT, 2016c);
b) Erosion susceptibility test: Slaking test, Crumb test (ABNT, 1996);
c) Inderbitzen tests. The tests were performed in three different surface runoff flows (3.5 L/min, 6 L/min and 7 L/min), when adopting a ramp gradient of 30º, based on the procedures applied by Lafayette (2006). The samples were tested under two initial conditions, starting with natural moisture and then a 24-hour saturated condition. The water flow was measured using Arduino hardware.
d) Shear strength tests using a direct shearing press on previously saturated test specimens in natural moisture and previously saturated.

4.2.2 In situ tests

4.2.2.1 Permeability testing

In situ permeability was tested close to the three sampling sites, using the Guelph constant head permeameter. Heads referring to the 5 cm and 10 cm water columns were adopted by monitoring water columns (cm/s) in the *R1* and *R2* tanks, respectively. Hydraulic conductivity saturated on site (K_{fs}) was calculated by using Equation 1.

$$Kfs=[(0.0041).(x).(R2)]-[(0.0054).(x).(R1)] \tag{1}$$

where: Kfs is the hydraulic conductivity (cm/s); x is the tank constant, namely 35.22 cm^2 in the case of interconnected tanks; *R1* is the waterfall rate obtained from the first load applied (cm/s); *R2* is the waterfall rate obtained from the second load applied (cm/s).

4.2.2.2 Erodibility study in pilot tests

Pilot tests were carried out to understand the erosion processes in the form of furrows. In the study area, three pilot tests were performed (pilot tests I, II and III), all close to the Sample 2 site (area with the highest concentration of erosion in furrows). The methodological procedures were based on the studies from Inácio et al. (2007), Meira (2008) and Lafayette (2006). Pilot test I was used in the soil loss study due to the rainfall in April 2018; and Pilot tests II and III (Figure 2) were used for simulated runoffs situated between two erosion furrows, one in soil protected by natural vegetation and plant litter; and the other in unprotected soil. For the pilot tests, the plots were defined by 0.4 m high zinc metal plates, 0.2 m of this being driven into the ground, and rectangular in shape (0.5 m wide x 1.5 m long - Figure 2). Rainfall volumes were obtained from the readings of a rain gauge. Further details can be obtained from studies in Macedo (2019).

Figure 2. Pilot tests: II (vegetation), III (without vegetation).

The Rational Method (Equation 2) was applied in order to estimate the test flow, and the rainfall intensity was obtained from Equation 3. The values 28.337; 0.104; 10.845; 0.813 and -2.750 were assigned to the maximum rainfall intensity for empirical parameters a, b, c, n and s, respectively, as proposed by Sobrinho et al. (2014). A 50-year return period (*Tr*) was adopted, in these conditions, the calculated flow used in the tests was 1.0 L/min. In order to estimate the soil loss (*SL*, in kg/m) and soil dispersion rate (*D*, in kg / m^2 x s), Equations 4 and 5 were used, respectively, quoted by Meira (2008) and Inácio et al. (2007).

$$Q = \frac{CIA}{360} \tag{2}$$

where: Q is the flow (L/s); C is the runoff coefficient; I is the rainfall intensity (mm/h); A is the area (ha).

$$I = \frac{\left[a\left(Tr - s\right)^{b}\right]}{c^{n}} \tag{3}$$

where: I is the rainfall intensity (mm/min); Tr is the return period (years); *a, b, c, n* and *s* are the empirical parameters for each location.

$$SL = \frac{\Sigma\left(Q.Cs.t\right)}{Ap} \tag{4}$$

where: SL is the soil loss (kg/m); Q is the flow (L/s); Cs is the concentration of soil (kg/L); t is the time between collections (min); Ap is the plot area (m^2);

$$D = \frac{Mss}{\left(Ap.Dc\right)} \tag{5}$$

where: D is the inter-furrow dispersion rate (kg / m^2.s); Mss is the dispersed dry soil mass (kg);

Ap is the plot area (m^2); Dc is the collection duration in (s).

5. Results and discussion

5.1 Morphometric characterization and land occupation and use

The results of the morphometric characterization show that the micro basin is prone to flooding, according to the figures presented in the compactness coefficient (*kc*) of 1.17, shape coefficient (*kf*) 0.62 and circularity index (*Ic*) 0.48, referring to a more circular shape of basin. On the other hand, the shape index suggests a basin prone to average flooding, since the distance of the index figure is one (1) (Magalhães Filho et al., 2013, p. 42). Likely flooding is somehow related to water concentration and, consequently, to the concentration of transported sediments.

The drainage density was 0.92 km/km^2, classified as average drainage capacity with few ramifications, according to Strahler (1953). Villela & Mattos (1975) affirm that basins with poor drainage systems vary from 0.1 to 0.5 km/km^2 and well-drained basins vary from at least 3.5 km/km^2. In light of this, the emphasis is on how important it is to mitigate the severe erosion processes in the area, since they could cause aggradation and contamination of nearby water bodies. The sinuosity of the drainage system was low (0.33), signifying straight channels, that is, channels that encourage greater sediment transport (Antoneli & Thomaz, 2007).

With regard to land occupation and use, it was found that 8.89 ha (38%) are covered wtih native vegetation, 5.42 ha (23%) with scrubland, and the total value of exposed soil and water-resistant areas is 6.2 ha (26.5%) in addition to the existence of two shallow lagoons.

5.2 Results of geotechnical characterization

5.2.1 Laboratory tests

The soil samples from Timbaúbas Nature Reserve revealed predominantly sandy soils with medium particles (53%-65.2%). Figure 3 shows that the materials passing

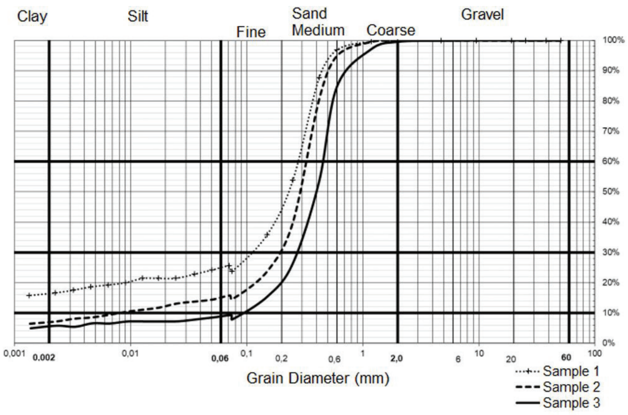

Figure 3. Grading curves of samples.

through the sieve 0.075 mm varied from 10% to 26%. The clay percentages were 16.7%, 8% and 6.8% for Samples 1, 2, and 3, respectively.

The relative particle densities of the soil samples were 2.61 to 2.67. According to Camapum de Carvalho et al. (2015), the values allow to conclude that the sand is predominantly quartz, confirming what was mentioned earlier.

With regard to soil consistency limits, the samples were classified as non liquid and non plastic, allowing classification of the samples in the *SM* (silty sand) group, showing high soil erosion potential (Llopis Trilho, 1999).

In the slaking tests Samples 2 and 3 were found to have disintegrated completely after total immersion (Table 1), indicating the frailty of the material when immersed in water, typical of highly erodible soils (Bastos, 1999). Sample 1, however, remained practically undisturbed throughout the test, associated with the higher concentration of clay content (16.7%) compared to the other samples (8% and 6.8%).

In crumb tests, the lumps of soil were immersed in a vessel with 150 ml of distilled water. One hour later, the sample reactions were observed to attribute the degree of dispersibility. According to the classification in ABNT NBR 13601/1996, Sample 1 falls into Degree 1 class (non-dispersive), showing to be fractured but with no turbidity in the water; Samples 2 and 3, however, are in the Degree 2 class (slightly dispersive), since the samples are fractured and the water slightly cloudy.

The Inderbitzen tests of the three soil samples, in natural moisture and pre-saturation conditions, showed that the soil mass is mostly lost in the test specimen condition with initial natural moisture. In this condition, the mass losses of the samples varied from 8.2×10^{-3} to 1.3×10^{-2} g/mm^2. In the saturated soil the mass losses of the samples varied from 7.8×10^{-3} to 1.1×10^{-2} g/mm^2. Only the saturated Sample 1, tested in the smallest flow (3.5 L/min), showed less mass loss of 4.3×10^{-3} g/mm^2, after 20 minutes testing - around 50% of the natural soil mass loss (8.2×10^{-3} g/mm^2). The mass losses were higher with the increase in runoff flow (Table 2). The results obtained in the study herein are in the same order of magnitude as Fácio's studies (Fácio, 1991) for the locations of Ceilândia I, Sobradinho I and Samambaia, in the Federal District, which present intense erosion processes. From this study, it is found that erosion control interventions must be made before the first rains, when the erosion process would be more severe.

For Bastos (1999), the mass loss is greater in the soil in natural moisture due to the intra-aggregate suction parameter (negative neutral pressure) of non-saturated soils, hampering the water seepage process and, consequently, increasing surface runoff.

The erodibility rate (K) of all three samples in natural moisture, obtained in the Inderbitzen tests, were from 0.105 to 0.108 g/cm^2/min/Pa, suggesting that they are highly erodible soils. Bastos (1999) believes that the most erodible soils, in the natural moisture condition, have a higher K value than 0.1 g/cm^2/min/Pa.

Table 1. Soil behavior in slaking test stages

Water phases in test	Sample 1	Sample 2	Sample 3
Test specimen base	Intact with 80% rise of sample	Intact with full rise of sample	Fracture of sample with full rise
h/3 test specimen	Intact with full rise of sample	Start of dispersion	Advanced dispersion
2h/3 test specimen	Slight dispersion	Dispersion advance	New fractures
Complete immersion of test specimen	Slight dispersion	Formation of a pile of unstructured material (Reduction)	Formation of pile of unstructured material (Reduction)

Table 2. Loss of soil mass in the Inderbitzen test

Amostra	Loss of soil mass ($\times 10^{-3}$ g/mm^2)					
	Flow of 3.5 L/min		Flow of 6.0 L/min		Flow of 7.0 L/min	
	Natural	Immersed	Natural	Immersed	Natural	Immersed
1	8.2	4.3	11.0	7.8	12.0	8.0
2	9.5	7.8	11.0	8.5	13.0	10.5
3	9.0	8.0	11.7	10.0	12.5	11.0

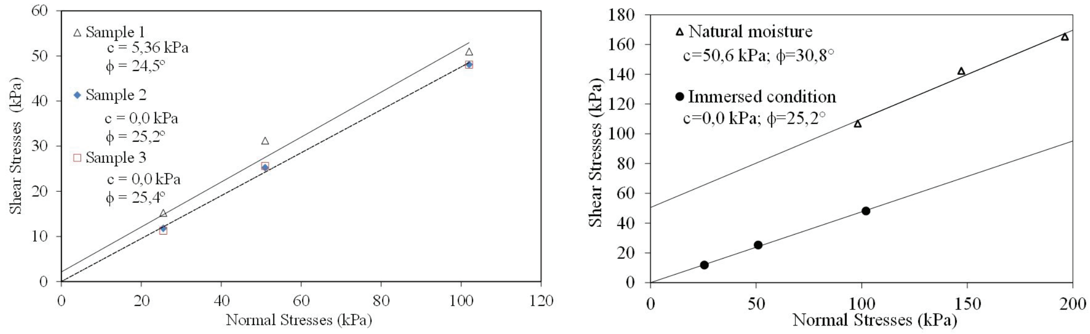

a) Samples in the immersed condition

b) Sample 2 in the immersed condition and natural moisture

Figure 4. Shear stress x Normal stress. Source: Adapted from Clarindo (2018, *apud* Sobrinha, 2019)

With respect to the shear strength of the soils (Figure 4a), the tests on immersed test specimens provided cohesion intercept low values. Concerning friction angles, the values in the saturated samples are close, with a slight variation (24.5° - 25.4°). In order to evaluate the cohesive behavior for samples in natural and saturated moisture, and their relationship in the erodibility potential, resistance tests were performed in the natural moisture condition of, only in Sample 2, as it has a higher clay content (Figure 4b). For the natural moisture condition, the cohesion was 50.55 kN/m^2, while in the saturation moisture the cohesion was zero. According to the proposal by Bastos (1999), Sample 2 has high erosion potential (Δc> 85%). This fact was confirmed in the study area, where there is a deep erosion scar near the sample extraction site. The friction angle decreased 18% compared to the result obtained in natural moisture (30.8°) with the saturated sample (25.2°). The same behavior is expected in Samples 1 and 3, which have smaller clay contents.

5.2.2 In situ tests

5.2.2.1 Permeability testing

The Guelph permeameter tests provided permeability coefficient values of 10^{-5} m/s, in places near the collection sites of Samples 1 and 3, typical of sandy soils. However, in the vicinity of the Sample 2 site, the permeability coefficient was negative, and may be related to the hydraulic discontinuity in the soil profile or permeability beyond the top limit of the equipment capacity, because roots and ant holes are found around the hole where the test was performed.

5.2.2.2 Erodibility Study in Pilot tests

During the experiment, daily rainfall of 7.0 mm (04/14/2018) was able to erode 73.5 g of soil (Pilot test I, Figure 5). On the other hand, 29 mm daily rainfall was logged (04/09/2018) causing 221.37g of soil to be dragged, while heavier rainfall of 50 mm (04/05/2018) eroded 407.9 g of soil. The quantity of soil loss due to natural rainfall provided values that reinforce the alert for the area degraded by erosion will require rehabilitation.

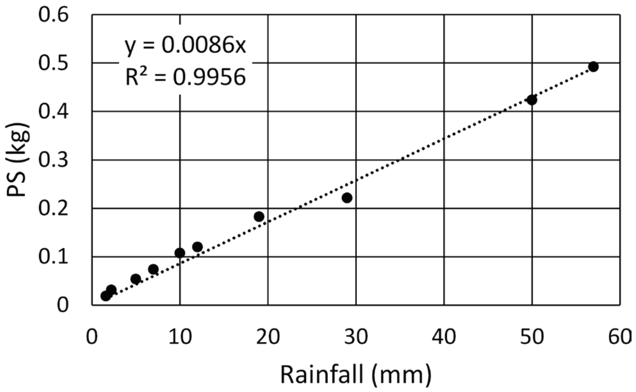

Figure 5. Soil loss x rainfall (Pilot test I).

Pilot tests II and III were installed between two erosion furrows in order to estimate the soil mass loss due to surface runoff, over a stretch of land with a gradient of 17%. In Pilot test II (with vegetation), the transported material was first collected an hour and a half after the start of the test, at a measured surface runoff velocity of 0.070 m/s. In Pilot test III (exposed soil), the first collection of the transported material was faster (51 minutes after the start of the test), and the runoff velocity was 0.133 m/s. From the results, a 52.63% drop was observed in the runoff velocity, when the soil is protected by vegetation, implying less pulling power of the runoff and consequently less erosion.

With regard to the dispersion rates given in kg/m^2.s, and soil losses in kg/m^2, higher values in the pilot test without vegetation were logged (Figures 6a and 6b). In this pilot test, the dispersion rate was 10 times more than the value obtained in the pilot test with vegetation (Table 3). Inácio et al. (2007) and Meira (2008) also observed this fact. Mannering & Meyer (1963) explain that the vegetation on the ground surface prevents the direct impact of raindrops and dissipates their energy, reducing the dispersion of particles, corroborating the results obtained in this study. The surface soil of the pilot test with vegetation had moisture content of 21.5% in the end, higher than that of the soil in the pilot test

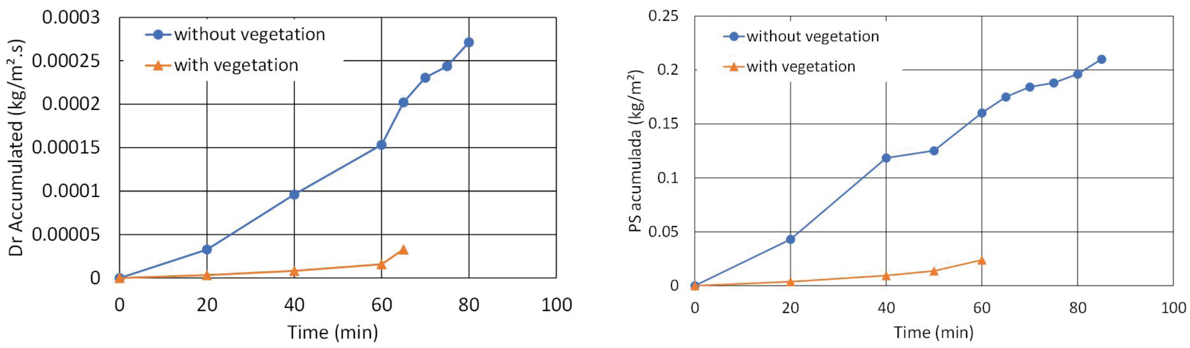

a) Accumulated dispersion rate of soil b) Accumulated soil loss

Figure 6. Accumulated dispersion rate and accumulated soil loss in the Pilot test.

Table 3. Parameters obtained in simulated runoff in Pilot tests

Parameters	Pilot test of soil with no vegetation	Pilot test of soil with vegetation
Gradient	17.25%	17.25%
Initial runoff velocity	0.133 m/s	0.070 m/s
Soil collection duration	51 minutes	1h 30 minutes
Initial soil moisture	9.0%	9.3%
Final soil moisture	14.6%	21.5%
Soil loss (kg/m^2) in 1h	0.1603	0.0238

without vegetation (14.6%). These results show that the soil with vegetation cover facilitates the water seepage process, increasing the degree of saturation, reducing the runoff and surface dispersion rate.

The higher dispersion rates in the soil without vegetation may be associated with the higher values of matrix suction of the undiscovered soil, in the as yet unsaturated state, which hinders seepage. When the soil is covered with vegetation, roots can help in seepage. Almeida (2014), in his studies on the influence of suction in the loss of eroded total mass, commented on a direct relationship between the initial soil suction and the eroded mass. This result shows the need to implement rehabilitation projects in the area, considering planting medium-size and small native species, as well as scrubland vegetation.

6. Conclusions

Timbaúbas municipal nature reserve presents several factors that contribute to the occurrence of erosion processes. This study addressed the morphometric characteristics that favor the rapid water flow and potential drag on solids. The reduced rate of soil vegetation cover associated with the mechanical characteristics of the aggregate increases susceptibility to erosion processes, also intensified by anthropic intervention, removal of vegetation and construction of buildings on the site, without proper action to discipline the runoff. The exposed soil area and water-resistant areas (6.2 ha) are 26.5% of the Reserve's total area (23.4 ha). The area covered by native vegetation (8.89 ha) represents only 38%. These facts alert to the need to consider the area's geomorphological, geotechnical and hydrological characteristics, to implement projects to rehabilitate the area degraded by erosion, involving implementation of proper drainage systems; planting native species and outher structural and non structural measures. It is the adoption of non-structural measures, such as, for example, educational actions for Reserve users, could contribute to prevent the emergence of new erosion processes in the area.

Declaration of interest

There is no conflicting interests.

Authors' contributions

Ana Patricia Nunes Bandeira: investigation, validation, discussion of results, review and approval of the final version of the manuscript. Cícera Camila Alves Macedo: investigation, validation, original draft preparation. Gerbeson Sampaio Clarindo: investigation and validation. Maria Gorethe de Sousa Lima: discussion of results, writing – reviewing. João Barbosa de Souza Neto: investigation, validation, discussion of results, writing - reviewing.

References

ABNT NBR 13601. (1996). *Soil – Standard test methods for determining dispersive characteristics of clayey soil by the Crumb test*. ABNT - Associação Brasileira de Normas Técnicas, Rio de Janeiro, RJ (in Portuguese).

ABNT NBR 6458. (2017). *Gravel grains passing through the 4.8 mm mesh sieve - Determination of bulk specific gravity*. ABNT - Associação Brasileira de Normas Técnicas, Rio de Janeiro, RJ (in Portuguese).

ABNT NBR 7181. (2016a). *Soil - Grain size analysis*. ABNT - Associação Brasileira de Normas Técnicas, Rio de Janeiro, RJ (in Portuguese).

ABNT NBR 6459. (2016b). *Determining the liquid limit*. ABNT - Associação Brasileira de Normas Técnicas, Rio de Janeiro, RJ (in Portuguese).

ABNT NBR 7180. (2016c). *Determination of plastic limit*. ABNT - Associação Brasileira de Normas Técnicas, Rio de Janeiro, RJ (in Portuguese).

Almeida, J.G.R. (2014). *Erodibilidade de solos tropicais não saturados nos municípios de Senador Canedo e Bonfinópolis (Goias)* [Unpublished master's dissertation]. Universidade Federal de Goiás.

Antoneli, V., & Thomaz, E.L. (2007). Caracterização do meio físico da bacia do Arroio Boa Vista, Guamiranga-PR. *Caminhos de Geografia*, 8(21), 46-58.

Bastos, C.A.B. (1999). *Estudo geotécnico sobre a erodibilidade de solos residuais não saturados* [Doctoral thesis, Universidade Federal do Rio Grande do Sul]. Lume Repositório Digital UFRGS. https://www.lume.ufrgs.br/handle/10183/2978

Bastos, C.A.B., Gitirana Junior, G.F.N., & Kühn, V.O. (2017). Solos não saturados e os processos erosivos. In M.M. Sales, J. Camapum de Carvalho, M.M.A. Mascarenha, M.P. Luz, N.M. Souza & R.R. Angelim (Org.), *Erosão em Borda de Reservatório* (1 ed., v. 1, p. 91-126, Cap. 5, 584 p.). Goiânia: Universidade Federal de Goiás.

Bender, H. (1985). Erosion: un probleme de résistance au cisaillement en fonction du chemin des contraintes pendant ínfiltration. In *International Conference on Geomechanics in Tropical Lateritic and Saprolitic Soils* (pp. 15-25). ABMS.

Bertoni, J., & Lombardi Neto, F. (1999). *Conservação do solo* (8. ed., 360 p.). São Paulo.

Camapum de Carvalho, J., Barbosa, M.C., Mendonça, R.M.G., Farias, W.M., & Cardoso, F.B.F. (2015). Propriedades químicas, mineralógicas e estruturais de solos naturais e compactados. In J. Camapum de Carvalho, G.F.N. Gitirana Junior, S.L. Machado, M.M.A. Mascarenha & F.C. Silva Filho (Org.), *Solos não saturados no contexto geotécnico* (1 ed, v.1, p. 39-78, 759 p.). São Paulo: ABMS.

Camapum de Carvalho, J., Sales, M.M., Mortari, D., Fácio, J.A., Motta, N.O., & Francisco, R.A. (2006). Processos Erosivos. In J. Camapum de Carvalho, M.M. Sales, N.M. Souza & M.T.S. Melo, (Org.). *Processos erosivos no centro oeste brasileiro* (1ed., v. 1, p. 39-91, Cap. 2, 464 p.). Brasília: FINATEC.

Cardoso, C.A., Dias, H.C.T., Soares, C.P.B., & Martins, S.V. (2006). Caracterização Morfométrica da Bacia Hidrográfica do Rio Debossan, Nova Friburgo, RJ. *Revista Árvore*, 30(2), 241-248.

Clarindo, G.S. (2018). *Avaliação da Erodibilidade do solo do Parque Natural Municipal das Timbaúbas* [Monograph]. Universidade Federal do Cariri.

Costa, K.V.M., Barreto, A.C., Fontenele, S.B., & Mendonça, L.A.R. (2013). Estimativa de perda de solo distribuída em uma bacia hidrográfica de pequeno porte através de técnicas de geoprocessamento. In *XVI Simpósio Brasileiro de Sensoriamento Remoto.* Foz do Iguaçu, PR.

Fácio, J.A. (1991). *Proposição de uma metodologia de estudo da erodibilidade dos solos do Distrito Federal*. [Unpublished master's dissertation]. Universidade de Brasília.

Fundação Cearense de Meteorologia e Recursos Hídricos – FUNCEME. (2006). *Zoneamento Geoambiental do Estado do Ceará - Parte II: Mesorregião do Sul Cearense*. FUNCEME.

Fundação Cearense de Meteorologia e Recursos Hídricos – FUNCEME. (2012). *Levantamento de reconhecimento de média intensidade dos solos* (280 p.). FUNCEME.

Guerra, A.J.T., & Hoffmann, H. (2006). Urban gully erosion in Brazil. *Geography Review, Oxford*, 19(3), 26-29.

Inácio, E.S.B., Cantalice, P.G.S.N., Araujo, Q.R., & Barreto, A.C. (2007). Quantificação da erosão em pastagem com diferentes declives na microbacia do Ribeirão Salomea. *Revista Brasileira de Engenharia Agrícola e Ambiental*, 11(4), 355-360.

Instituto Brasileiro de Geografia e Estatística – IBGE. (2010). *Cidades, 2010*. Retrieved in December 23, 2018, from http://www.ibge.gov.br/cidadesat/topwindow.htm?1

Instituto de Pesquisa e Estratégia Econômica do Ceará – IPECE (2017). *Juazeiro do Norte: perfil básico do município*. Retrieved in December 20, 2018, from www.ipece.ce.gov.br/.../ perfil_basico/PBM.../Juazeiro%20do%20Norte.pdf

Jorge, M.C.O., & Guerra, A.J.T. (2013). Erosão dos solos e movimentos de massa - recuperação de áreas degradadas com técnicas de bioengenharia e prevenção de acidentes. In A.J.T. Guerra & M.C.O. Jorge, (Org.). *Processos erosivos e recuperação de áreas degradadas* (Vol. 1, pp. 7-30). 1ª ed. São Paulo: Oficina de Textos.

Juazeiro do Norte. (1997). Decreto Municipal n°. 1183, de 16 de Junho de 1997. Delimita o Parque Ecológico das Timbaúbas, área de proteção de mananciais e do meio ambiente. *Diário Oficial do Município*.

Juazeiro do Norte. (2017). Decreto Municipal nº. 352, de 23 Outubro de 2017. Cria o Parque Natural Municipal das Timbaúbas, no Município de Juazeiro do Norte, no Estado do Ceará, e dá outras providências. *Diário Oficial do Município*.

Köppen, W. & Geiger, R. (1928). *Klimate der Erde.* Gotha: Verlag Justus Perthes [Wall-map 150 cm x 200 cm].

Lafayette, K.P.V. (2006). *Estudo geológico – geotécnico do processo erosivo em encostas no Parque Metropolitano Armando de Holanda Cavalcanti - Cabo de Santo Agostinho/ PE* [Unpublished doctorate thesis]. Universidade Federal de Pernambuco.

Llopis Trilho, G. (1999). Control de la erosión y obras de desague. In C. L. Jimeno (Ed.), *Manual de estabilización* *y revegetación de taludes* (704 p.). Entorno Grafico S. L. Madrid.

Macedo, C.C.A. (2019). *Diagnóstico da erodibilidade e da qualidade hídrica em uma unidade de conservação municipal* [Unpublished master's dissertation]. Universidade Federal do Cariri.

Magalhães Filho, L.L., Marinho Filho, G.M., Maciel, G.F., Dias, R.R., Rezende, C.D.S.A., Figueroa, F.E.V., & Moura Oliveira, L. (2013). Avaliação de características morfométricas da bacia hidrográfica do Rio Formoso–TO. *Revista de Ciências Ambientais, Canoas*, 7(1), 37-48.

Mannering, J.V., & Meyer, L.D. (1963). The effects of various rates of surface mulch on infiltration and erosion. *Soil Science Society of American Proceeding*, 27(1), 84-86.

Meira, F.F.A. (2008). *Estudo do processo erosivo em encostas ocupadas* [Unpublished doctorate thesis]. Universidade Federal de Pernambuco.

Nagel, F., Storgatto, G., Basso, L., Nummer, A.V., & Pinheiro, R.J.B. (2009). Ensaio Interbitzen: estudo da erodibilidade de solos e rochas sedimentares. In *5º Seminário de Engenharia Geotécnica do Rio Grande do Sul* (9 p.). Retrieved in August 19, 2018, from https://www.abms.com.br/links/bibliotecavirtual/geors2009/2009-nagel-storgatto.pdf

Silva Neto, A.F., Guimarães, C.L., de Araújo, J.S., & Araújo, J.S. (2013). Geotechnologies for morphometric characterization of a river basin. In *Proceedings of the XVI Brazilian Remote Sensing Symposium* (pp. 5483-5490). Foz do Iguaçu, Paraná, Brazil.

Ramidan, M.A.S. (2003). *Estudo de um processo de voçorocamento próximo a UHE de Itumbiara-GO* [Unpublished master's dissertation]. Pontifícia Universidade Católica do Rio de Janeiro.

Sobrinha, M.A.S.M. (2019). *Avaliação da erodibilidade de um solo da região do Cariri* [Monograph]. Universidade Federal do Cariri.

Sobrinho, V.F., Rodrigues, J.O., Mendonça, L.A.R., Andrade, E.M.A., & Tavares, P.R.L. (2014). Desenvolvimento de equações Intensidade-Duração-Frequência sem dados pluviográficos em regiões semiáridas. *Revista Brasileira de Engenharia Agrícola e Ambiental*, 18(7), 727-734.

Strahler, A.N. (1953). Hypsometric (area-altitude) analysis and erosional topography. *Geological Society of America Bulletin*, 63, 1117-1142.

Villela, S.M., & Mattos, A. (1975). *Hidrologia aplicada* (239 p.). São Paulo: McGraw-Hill do Brasil.

List of Symbols

A Area
a, b, c, n, s Empirical parameters for each location.
Ap plot area
API Integral Protection Area
c Cohesion intercept
C Runoff coefficient
Cs Concentration of soil
D Inter-furrow dispersion rate
Dc Collection duration
GIS Geographic information systems
I Rainfall intensity
Ic Circularity index
IBGE Brazilian Institute of Geography and Statistics
IPECE Ceará Research Institute on Economic Strategy
K Erodibility rate
kc Compactness coefficient
kf Shape coefficient
K_{fs} Hydraulic conductivity saturated on site
Mss Dispersed dry soil mass (kg)
Q Flow
R1 Waterfall rate obtained from the first load applied in the in situ permeability
R2 Waterfall rate obtained from the second load applied in the in situ permeability
SL Soil loss
SM Silty sand
t Time between collections
Tr Return period
UAV Unmanned aerial vehicles
USLE Universal Soil Loss Equation
x Tank constant
Δc Variation in cohesion
ϕ Friction angles
τ_{hcrit} Critical hydraulic shear stress


PIONEERING
AND INNOVATION
SINCE 1921
LICENCE NO. 24 - PUB
TEIXEIRA DUARTE
ENGENHARIA E CONSTRUÇÕES, S.A.
PORT FACILITY CONSTRUCTION
NACALA - MOZAMBIQUE
Building a better world.
teixeiraduarteconstruction.com

The Best Solution!

***Tecnilab Portugal, S.A.** will provide you with answers to your Geotechnical engineering needs.*

Tecnilab Portugal, S.A. is a professional Geotechnical engineering company and has a lot of experience as a professional group that mainly engages in measurement engineering in dam, subway(Metro), harbor, power plant, soft ground and structure construction.

WE ARE THE DISTRIBUTOR OF PORTUGAL OF ACE INSTRUMENT CO., LTD. IN KOREA.

ACE INSTRUMENT CO., LTD. is a company that obtains worldwide reputation for supplying high precision, high reliability products in all Geotechnical instruments, data logger and in-situ test equipments. Independently developed automatic monitoring system can be used anywhere in the world, including buildings, bridges, ground and any constructions.

Data Acquisition System & Web Monitoring Program

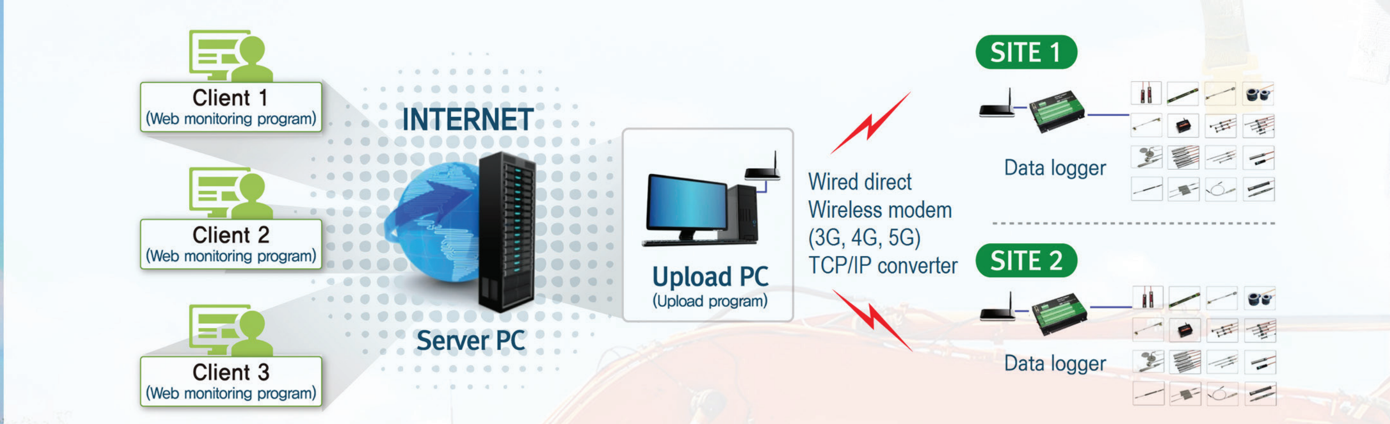

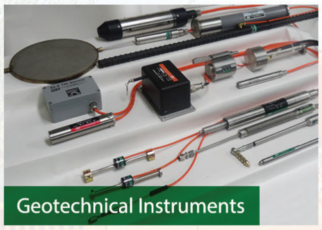
Geotechnical Instruments


Digital Inclinometer Set


Dataloggers, Indicators

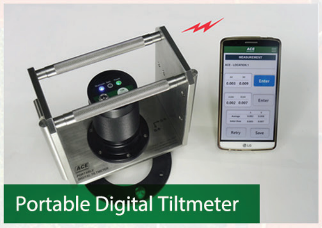
Portable Digital Tiltmeter

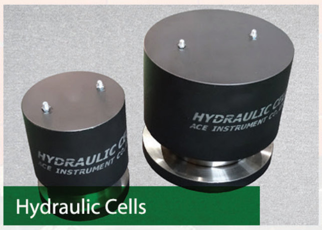
Hydraulic Cells


Inclinometer Casings

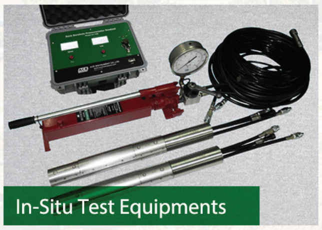
In-Situ Test Equipments


Pendulum System

Sales company

Tecnilab Portugal, S.A.
A: Rua Gregorio Lopes, Lote 1512B 1449-041 Lisboa Portugal
T: +351 217 220 870 F: +351 217 264 550
www.tecnilab.pt

Manufacturer

ACE INSTRUMENT CO., LTD.
The first value in Geotechnical & Structural Instrumentation
A: 9, Dangjung-ro 27 beon-gil, Gunpo-si, Gyeonggi-do, Korea
T: +82 31 459 8753-7 F: +82 31 459 8758 E: acens@naver.com
www.aceinstrument.com

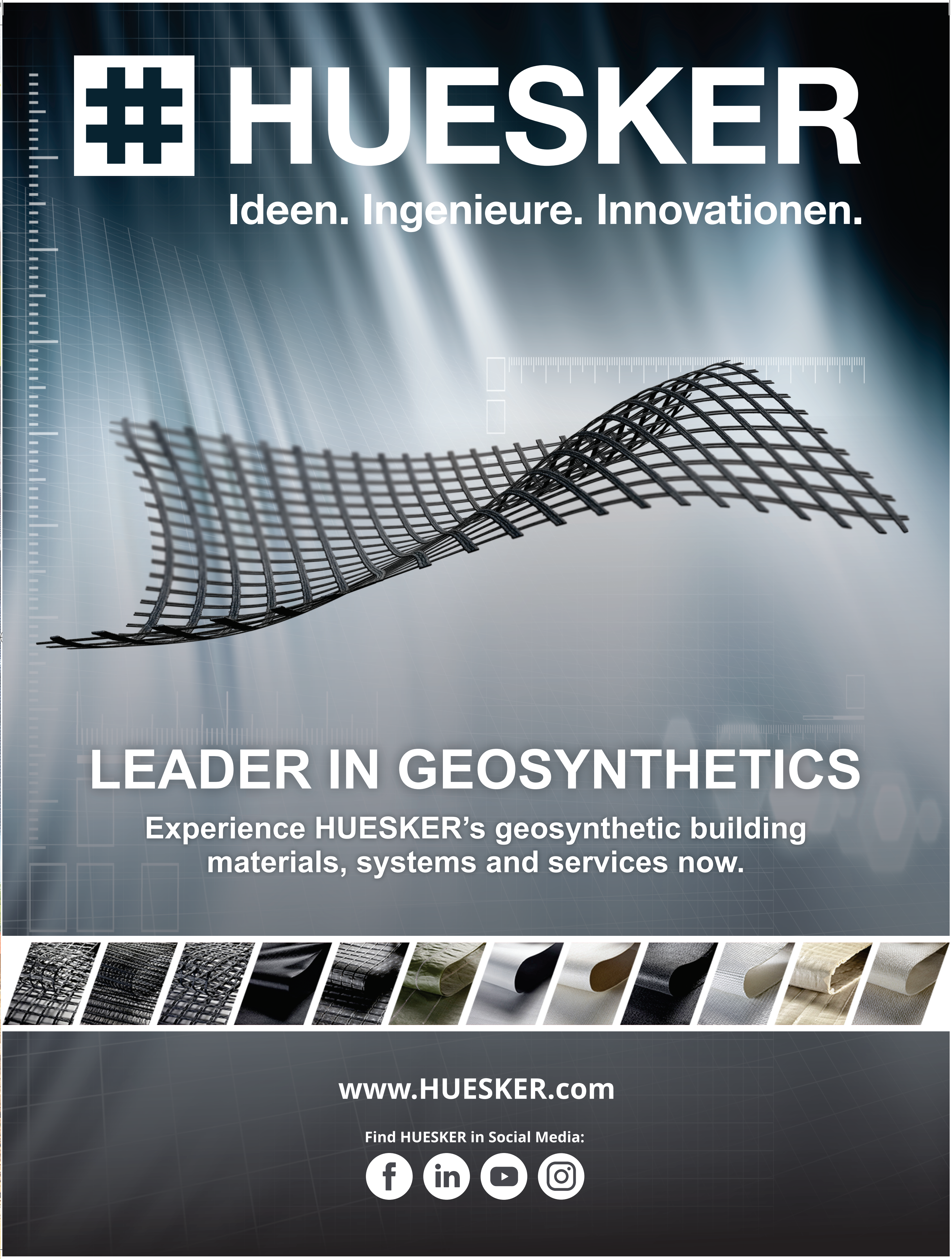
HUESKER
Ideen. Ingenieure. Innovationen.
LEADER IN GEOSYNTHETICS
Experience HUESKER's geosynthetic building materials, systems and services now.
www.HUESKER.com
Find HUESKER in Social Media:

Guide for Authors

Soils and Rocks is an international scientific journal published by the Brazilian Association for Soil Mechanics and Geotechnical Engineering (ABMS) and by the Portuguese Geotechnical Society (SPG). The aim of the journal is to publish original papers on all branches of Geotechnical Engineering. Each manuscript is subjected to a single-blind peer-review process. The journal's policy of screening for plagiarism includes the use of a plagiarism checker on all submitted manuscripts.

Soils and Rocks embraces the international Open Science program and is striving to meet all the recommendations. However, at this moment, the journal is not yet accepting preprints and open data, and has not adopted open peer reviews.

Soils and Rocks provides a manuscript template available at the journal's website.

1. Category of papers

Submissions are classified into one of the following categories:

Article – an extensive and conclusive dissertation about a geotechnical topic, presenting original findings.
Technical Note – presents a study of smaller scope or results of ongoing studies, comprising partial results and/or particular aspects of the investigation.
Case Study – report innovative ways to solve problems associated with design and construction of geotechnical projects. It also presents studies of the performance of existing structures.
Review Article – a summary of the State-of-the-Art or State-of-the-Practice on a particular subject or issue and represents an overview of recent developments.
Discussion – specific discussions about published papers.

Authors are responsible for selecting the correct category when submitting their manuscript. However, the manuscript category may be altered based on the recommendation of the Editorial Board. Authors are also requested to state the category of paper in their Cover Letter.

When submitting a manuscript for review, the authors should indicate the category of the manuscript, and is also understood that they:

a) assume full responsibility for the contents and accuracy of the information in the paper;
b) assure that the paper has not been previously published, and is not being submitted to any other journal for publication.

2. Paper length

Full-length manuscripts (Article, Case Study) should be between 4,000 and 8,000 words. Review articles should have up to 10,000 words. Technical Notes have a word count limit of 3,500 words. Discussions have a word count limit of 1,000 words. These word count limits exclude the title page, notation list (e.g., symbols, abbreviations), captions of tables and figures, acknowledgments and references. Each single column and double column figure or table is considered as equivalent to 150 and 300 words, respectively.

3. Scientific style

The manuscripts should be written in UK or US English, in the third person and all spelling should be checked in accordance with a major English Dictionary. The manuscript should be able to be readily understood by a Civil Engineer and avoid colloquialisms. Unless essential to the comprehension of the manuscript, direct reference to the names of persons, organizations, products or services is not allowed. Flattery or derogatory remarks about any person or organization should not be included.

The author(s) of Discussion Papers should refer to himself (herself/themselves) as the reader(s) and to the author(s) of the paper as the author(s).

The International System (SI) units must be used. The symbols are recommended to be in accordance with Lexicon in 14 Languages, ISSMFE (2013) and the ISRM List of Symbols. Use italics for single letters that denote mathematical constants, variables, and unknown quantities, either in tables or in the text.

4. Submission requirements and contents

A submission implies that the following conditions are met:

- the authors assume full responsibility for the contents and accuracy of the information presented in the paper;
- the manuscript contents have not been published previously, except as a lecture or academic thesis;
- the manuscript is not under consideration for publication elsewhere;
- the manuscript is approved by all authors;
- the manuscript is approved by the necessary authorities, when applicable, such as ethics committees and institutions that may hold intellectual property on contents presented in the manuscript;
- the authors have obtained authorization from the copyright holder for any reproduced material;
- the authors are aware that the manuscript will be subjected to plagiarism check.

The author(s) must upload two digital files of the manuscript to the Soils and Rocks submission system. The size limit for each submission file is 20 MB. The manuscript should be submitted in docx format (Word 2007 or higher) or doc format (for older Word versions). An additional PDF format file of the manuscript is also required upon submission. Currently, the journal is not accepting manuscripts prepared using LaTeX.

The following documents are required as minimum for submission:

- cover letter;
- manuscript with figures and tables embedded in the text (doc or docx format);

manuscript with figures and tables embedded in the text for revision (PDF format);

- permission for re-use of previously published material when applicable, unless the author/owner has made explicit that the image is freely available.

4.1 Cover letter

The cover letter should include: manuscript title, submission type, authorship information, statement of key findings and work novelty, and related previous publications if applicable.

4.2 Title page

The title page is the first page of the manuscript and must include:

- A concise and informative title of the paper. Avoid abbreviations, acronyms or formulae. Discussion Papers should contain the title of the paper under discussion. Only the first letter of the first word should be capitalized.
- Full name(s) of the author(s). The first name(s) should not be abbreviated. The authors are allowed to abbreviate middle name(s).
- The corresponding author should be identified by a pound sign # beside his/her and in a footnote.
- The affiliation(s) of the author(s), should follow the format: Institution, (Department), City, (State), Country.
- Affiliation address and e-mail must appear below each author's name.
- The 16-digit ORCID of the author(s) – mandatory
- Main text word count (excluding abstract and references) and the number of figures and tables

4.3 Permissions

Figures, tables or text passages previously published elsewhere may be reproduced under permission from the copyright owner(s) for both the print and online format. The authors are required to provide evidence that such permission has been granted at the moment of paper submission.

4.4 Declaration of interest

Authors are required to disclose conflicting interests that could inappropriately bias their work. For that end, a section entitled "Declaration of interest" should be included following any acknowledgments and prior to the "Authors' contributions" section. In case of the absence of conflicting interests, the authors should still include a declaration of interest.

4.5 Authors' contributions

Authors are required to include an author statement outlining their individual contributions to the paper according to the CASRAI CRediT roles (as per https://casrai.org/credit). The minimum requirements of contribution to the work for recognition of authorship are: a) Participate actively in the discussion of results; b) Review and approval of the final version of the manuscript. A section entitled "Authors' contributions" should be included after the declaration of interest section, and should be formatted with author's name and CRediT role(s), according to the example:

Samuel Zheng: conceptualization, methodology, validation. Olivia Prakash: data curation, writing - original draft preparation. Fatima Wang: investigation, validation. Kwame Bankole: supervision. Sun Qi: writing - reviewing and editing.

Do not include credit items that do not follow the Taxonomy established by CASRAI CRediT roles.

The authors' contributions section should be omitted in manuscripts that have a single author.

5. Plagiarism checking

Submitted papers are expected to contain at least 50 % new content and the remaining 50 % should not be verbatim to previously published work.

All manuscripts are screened for similarities. Currently, the Editorial Board uses the plagiarism checker Plagius (www.plagius.com) to compare submitted papers to already published works. Manuscripts will be rejected if more than 20 % of content matches previously published work, including self-plagiarism. The decision to reject will be under the Editors' discretion if the percentage is between 10 % and 20 %.

IMPORTANT OBSERVATION: Mendeley software plug-in (suggested in this guide) for MS-Word can be used to include the references in the manuscript. This plug-in uses a field code that sometimes includes automatically both title and abstract of the reference. Unfortunately, the similarity software adopted by the Journal (Plagius) recognizes the title and abstract as an actual written text by the field code of the reference and consequently increases considerably the percentage of similarity. Please do make sure to remove the abstract (if existing) inside Mendeley section where the adopted reference is included. This issue has mistakenly caused biased results in the past. The Editorial Board of the journal is now aware of this tendentious feature.

6. Formatting instructions

The text must be presented in a single column, using ISO A4 page size, left, right, top, and bottom margins of 25 mm, Times New Roman 12 font, and line spacing of 1.5. All lines and pages should be numbered.

The text should avoid unnecessary italic and bold words and letters, as well as too many acronyms. Authors should avoid to capitalize words and whenever possible to use tables with distinct font size and style of the regular text.

Figures, tables and equations should be numbered in the sequence that they are mentioned in the text.

Abstract

Please provide an abstract between 150 and 250 words in length. Abbreviations or acronyms should be avoided. The abstract should state briefly the purpose of the work, the main results and major conclusions or key findings.

Keywords

A minimum of three and a maximum of six keywords must be included after the abstract. The keywords must represent the content of the paper. Keywords offer an opportunity to include synonyms for terms that are frequently referred to in the literature using more than one term. Adequate keywords maximize the visibility of your published paper.

Examples:

Poor keywords – piles; dams; numerical modeling; laboratory testing

Better keywords – friction piles; concrete-faced rockfill dams; material point method; bender element test

List of symbols

A list of symbols and definitions used in the text must be included before the References section. Any mathematical constant, variable or unknown quantity should appear in italics.

6.1 Citations

References to other published sources must be made in the text by the last name(s) of the author(s), followed by the year of publication. Examples:

- Narrative citation: […] while Silva & Pereira (1987) observed that resistance depended on soil density
- Parenthetical citation: It was observed that resistance depended on soil density (Silva & Pereira, 1987).

In the case of three or more authors, the reduced format must be used, e.g.: Silva et al. (1982) or (Silva et al., 1982). Do not italicize "et al."

Two or more citations belonging to the same author(s) and published in the same year are to be distinguished with small letters, e.g.: (Silva, 1975a, b, c.).

Standards must be cited in the text by the initials of the entity and the year of publication, e.g.: ABNT (1996), ASTM (2003).

6.2 References

A customized style for the Mendeley software is available and may be downloaded from this link.

Full references must be listed alphabetically at the end of the text by the first author's last name. Several references belonging to the same author must be cited chronologically.

Some formatting examples are presented here:

Journal Article

Bishop, A.W., & Blight, G.E. (1963). Some aspects of effective stress in saturated and partly saturated soils. *Géotechnique*, 13(2), 177-197. https://doi.org/10.1680/geot.1963.13.3.177

Castellanza, R., & Nova, R. (2004). Oedometric tests on artificially weathered carbonatic soft rocks. *Journal of Geotechnical and Geoenvironmental Engineering*, 130(7), 728-739. https://doi.org/10.1061/(ASCE)1090-0241(2004)130:7(728)

Fletcher, G. (1965). Standard penetration test: its uses and abuses. Journal of the Soil Mechanics Foundation Division, 91, 67-75.

Indraratna, B., Kumara, C., Zhu S-P., Sloan, S. (2015). Mathematical modeling and experimental verification of fluid flow through deformable rough rock joints. *International Journal of Geomechanics*, 15(4): 04014065-1-04014065-11. https://doi.org/10.1061/(ASCE)GM.1943-5622.0000413

Garnier, J., Gaudin, C., Springman, S.M., Culligan, P.J., Goodings, D., Konig, D., ... & Thorel, L. (2007). Catalogue of scaling laws and similitude questions in geotechnical centrifuge modelling. *International Journal of Physical Modelling in Geotechnics*, 7(3), 01-23. https://doi.org/10.1680/ijpmg.2007.070301

Bicalho, K.V., Gramelich, J.C., & Santos, C.L.C. (2014). Comparação entre os valores de limite de liquidez obtidos pelo método de Casagrande e cone para solos argilosos brasileiros. *Comunicações Geológicas*, 101(3), 1097-1099 (in Portuguese).

Book

Lambe, T.W., & Whitman, R.V. (1979). *Soil Mechanics, SI version*. John Wiley & Sons.

Das, B.M. (2012). *Fundamentos de Engenharia Geotécnica*. Cengage Learning (in Portuguese).

Head, K.H. (2006). *Manual of Soil Laboratory Testing - Volume 1*: Soil Classification and Compaction Tests. Whittles Publishing.

Bhering, S.B., Santos, H.G., Manzatto, C.V., Bognola, I., Fasolo, P.J., Carvalho, A.P., ... & Curcio, G.R. (2007). *Mapa de solos do estado do Paraná*. Embrapa (in Portuguese).

Book Section

Yerro, A., & Rohe, A. (2019). Fundamentals of the Material Point Method. In *The Material Point Method for Geotechnical Engineering* (pp. 23-55). CRC Press. https://doi.org/10.1201/9780429028090

Sharma, H.D., Dukes, M.T., & Olsen, D.M. (1990). Field measurements of dynamic moduli and Poisson´s ratios of refuse and underlying soils at a landfill site. In *Geotechnics of Waste Fills - Theory and Practice* (pp. 57-70). ASTM International. https://doi.org/10.1520/STP1070-EB

Cavalcante, A.L.B., Borges, L.P.F., & Camapum de Carvalho, J. (2015). Tomografias computadorizadas e análises numéricas aplicadas à caracterização da estrutura porosa de solos não saturados. In *Solos Não Saturados no Contexto Geotécnico* (pp. 531-553). ABMS (in Portuguese).

Proceedings

Jamiolkowski, M.; Ladd, C.C.; Germaine, J.T., & Lancellotta, R. (1985). New developments in field and laboratory testing of soils. *Proc. 11th International Conference on Soil Mechanics and Foundation Engineering,* San Francisco, August 1985. Vol. 1, Balkema, 57-153.

Massey, J.B., Irfan, T.Y. & Cipullo, A. (1989). The characterization of granitic saprolitic soils. *Proc. 12th International Conference on Soil Mechanics and Foundation Engineering*, Rio de Janeiro. Vol. 6, Publications Committee of XII ICSMFE, 533-542.

Indraratna, B., Oliveira D.A.F., & Jayanathan, M. (2008b). Revised shear strength model for infilled rock joints considering overconsolidation effect. *Proc. 1st Southern Hemisphere International Rock Mechanics Symposium*, Perth. ACG, 16-19.

Barreto, T.M., Repsold, L.L., & Casagrande, M.D.T. (2018). Melhoramento de solos arenosos com polímeros. *Proc. 19º Congresso Brasileiro de Mecânica dos Solos e Engenharia Geotécnica*, Salvador. Vol. 2, ABMS, CBMR, ISRM & SPG, 1-11 (in Portuguese).

Thesis

Lee, K.L. (1965). *Triaxial compressive strength of saturated sands under seismic loading conditions* [Unpublished doctoral dissertation]. University of California at Berkeley.

Chow, F.C. (1997). *Investigations into the behaviour of displacement pile for offshore foundations* [Doctoral thesis, Imperial College London]. Imperial College London's repository. https://spiral.imperial.ac.uk/handle/10044/1/7894

Araki, M.S. (1997). *Aspectos relativos às propriedades dos solos porosos colapsíveis do Distrito Federal* [Unpublished master's dissertation]. University of Brasília (in Portuguese).

Sotomayor, J.M.G. (2018). *Evaluation of drained and non-drained mechanical behavior of iron and gold mine tailings reinforced with polypropylene fibers* [Doctoral thesis, Pontifical Catholic University of Rio de Janeiro]. Pontifical Catholic University of Rio de Janeiro's repository (in Portuguese). https://doi.org/10.17771/PUCRio.acad.36102*

* *official title in English should be used when available in the document.*

Report

ASTM D7928-17. (2017). Standard Test Method for Particle-Size Distribution (Gradation) of Fine-Grained Soils Using the Sedimentation (Hydrometer) Analysis. *ASTM International, West Conshohocken, PA.* https://doi.org/10.1520/D7928-17

ABNT NBR 10005. (2004). Procedure for obtention leaching extract of solid wastes. *ABNT - Associação Brasileira de Normas Técnicas*, Rio de Janeiro, RJ (in Portuguese).

DNIT. (2010). Pavimentação - Base de solo-cimento - Especificação de serviço DNIT 143. *DNIT -Departamento Nacional de Infraestrutura de Transportes*, Rio de Janeiro, RJ (in Portuguese).

USACE (1970). Engineering and Design: Stability of Earth and Rock-Fill Dams, Engineering Manual 1110-2-1902. Corps of Engineers, Washington, D.C.

Web Page

Soils and Rocks. (2020). *Guide for Authors*. Soils and Rocks. Retrieved in September 16, 2020, from http://www.soilsandrocks.com/

6.3 Artworks and illustrations

Each figure should be submitted as a high-resolution image, according to the following mandatory requirements:

- Figures must be created as a TIFF file format using LZW compression with minimum resolution of 500 dpi.
- Size the figures according to their final intended size. Single-column figures should have a width of up to 82 mm. Double-column figures should have a maximum width of 170 mm.
- Use Times New Roman for figure lettering. Use lettering sized 8-10 pt. for the final figure size.
- Lines should have 0.5 pt. minimum width in drawings.
- Titles or captions should not be included inside the figure itself.

Figures must be embedded in the text near the position where they are first cited. Cite figures in the manuscript in consecutive numerical order. Denote figure parts by lowercase letters (a, b, c, etc.). Please include a reference citation at the end of the figure caption for previously published material. Authorization from the copyright holder must be provided upon submission for any reproduced material.

Figure captions must be placed below the figure and start with the term "Figure" followed by the figure number and a period. Example:

Figure 1. Shear strength envelope.

Do not abbreviate "Figure" when making cross-references to figures.

All figures are published in color for the electronic version of the journal; however, the print version uses grayscale. Please format figures so that they are adequate even when printed in grayscale.

Accessibility: Please make sure that all figures have descriptive captions (text-to-speech software or a text-to-Braille hardware could be used by blind users). Prefer using patterns (e.g., different symbols for dispersion plot) rather than (or in addition to) colors for conveying information (then the visual elements can be distinguished by colorblind users). Any figure lettering should have a contrast ratio of at least 4.5:1

Improving the color accessibility for the printed version and for colorblind readers: Authors are encouraged to use color figures because they will be published in their original form in the online version. However, authors must consider the need to make their color figures accessible for reviewers and readers that are colorblind. As a general rule of thumb, authors should avoid using red and green simultaneously. Red should be replaced by magenta, vermillion, or orange. Green should be replaced by an off-green color, such as blue-green. Authors should prioritize the use of black, gray, and varying tones of blue and yellow.

These rules of thumb serve as general orientations, but authors must consider that there are multiple types of color blindness, affecting the perception of different colors. Ideally, authors should make use of the following resources: 1) for more information on how to prepare color figures, visit https://jfly.uni-koeln.de/; 2) a freeware software available at http://www.vischeck.com/ is offered by Vischeck, to show how your figures would be perceived by the colorblind.

6.4 Tables

Tables should be presented as a MS Word table with data inserted consistently in separate cells. Place tables in the text near the position where they are first cited. Tables should be numbered consecutively using Arabic numerals and have a caption consisting of the table number and a brief title. Tables should always be cited in the text. Any previously published material should be identified by giving the original source as a reference at the end of the table caption. Additional comments can be placed as footnotes, indicated by superscript lower-case letters.

When applicable, the units should come right below the corresponding column heading. Horizontal lines should be used at the top and bottom of the table and to separate the headings row. Vertical lines should not be used.

Table captions must be placed above the table and start with the term “Table” followed by the table number and a period. Example:

Table 1. Soil properties.

Do not abbreviate “Table” when making cross-references to tables. Sample:

Table 1. Soil properties

Parameter	Symbol	Value
Specific gravity of the sand particles	G_s	2.64
Maximum dry density (Mg/m^3)	$\rho_{d(max)}$	1.554
Minimum dry density (Mg/m^3)	$\rho_{d(min)}$	1.186
Average grain-size (mm)	d_{50}	0.17
Coefficient of uniformity	C_u	1.97

6.5 Mathematical equations

Equations must be submitted as editable text, created using MathType or the built-in equation editor in MS Word. All variables must be presented in italics.

Equations must appear isolated in a single line of the text. Numbers identifying equations must be flushed with the right margin. International System (SI) units must be used. The definitions of the symbols used in the equations must appear in the List of Symbols.

Do not abbreviate “Equation” when making cross-references to an equation.